

---

# HRMOS

A High-Resolution Multi-Object Spectrograph for the VLT

White Paper

Science Motivation

---

July 7, 2026

## Authors

Laura Magrini<sup>1</sup>, Thomas Bensby<sup>2</sup>, Sofia Randich<sup>1</sup>, Andrea Bianco<sup>3</sup>, Oscar Gonzalez<sup>4</sup>, Emma Fernández-Alvar<sup>5,6</sup>, Sergio G. Sousa<sup>7</sup>, Letizia Caito<sup>8</sup>, Marco Riva<sup>3</sup>, Vardan Adibekyan<sup>7,9</sup>, Anish M. Amarsi<sup>10</sup>, Maria Teresa Belmonte<sup>11</sup>, Maria Benito<sup>5,6</sup>, Christian P. Clear<sup>12</sup>, Camilla Danielski<sup>13,1</sup>, Valentina D'Orazi<sup>14</sup>, Riano Giribaldi<sup>1</sup>, Camilla J. Hansen<sup>15</sup>, Vanessa Hill<sup>16</sup>, Robin D. Jeffries<sup>17</sup>, Georges Kordopatis<sup>16</sup>, Andrea Miglio<sup>18,19</sup>, Dinko Milaković<sup>20,21</sup>, Germano Sacco<sup>1</sup>, José Schiappacasse-Ulloa<sup>1</sup>, Ása Skúladóttir<sup>22,1</sup>, Rodolfo Smiljanic<sup>23</sup>, Maria Tsantaki<sup>1</sup>, Almudena Arcones<sup>24,25,26</sup>, José Maria Arroyo-Polonio<sup>5,6</sup>, Martina Baratella<sup>27</sup>, Beatriz Barbuy<sup>28</sup>, John R. Barnes<sup>29</sup>, Giuseppina Battaglia<sup>5,6</sup>, Holger Baumgardt<sup>30</sup>, Katia Biazzo<sup>31</sup>, Manuela Bischetti<sup>32,20</sup>, Angela Bragaglia<sup>19</sup>, Tobias Buck<sup>33,34</sup>, Sven Buder<sup>35</sup>, Sema Caliskan<sup>10,36</sup>, Gabriele Cescutti<sup>37,20</sup>, Andrew Collier Cameron<sup>38</sup>, Ryan Cooke<sup>39,40</sup>, Sergio Cristallo<sup>41,42</sup>, Francesco Damiani<sup>43</sup>, Arnas Drazdauskas<sup>44</sup>, Heitor Ernandes<sup>2,23</sup>, Antonio Frasca<sup>45</sup>, Mark Gieles<sup>46,47</sup>, Valeria Grisoni<sup>20</sup>, Moira Jardine<sup>38</sup>, Evan N. Kirby<sup>48</sup>, Jonas Klevas<sup>44</sup>, Andreas Korn<sup>10</sup>, Ioanna Koutsouridou<sup>22,1</sup>, Cis Lagae<sup>49,50</sup>, Nadege Lagarde<sup>51</sup>, Romain Lucchesi<sup>22,1</sup>, Francesca Lucertini<sup>27</sup>, Luca Malavolta<sup>52,57</sup>, Fabiola Marino<sup>57</sup>, Tadafumi Matsuno<sup>53</sup>, Thibault Merle<sup>54,55</sup>, Sapna Mishra<sup>56</sup>, Marta Molero<sup>25</sup>, Mario Montalto<sup>52</sup>, Michele Moresco<sup>18</sup>, Alessio Mucciarelli<sup>18,19</sup>, Domenico Nardiello<sup>52,57</sup>, Valerio Nascimbeni<sup>52</sup>, Brunella Nisini<sup>31</sup>, Joana Oliveira<sup>17</sup>, Elenia Pacetti<sup>58</sup>, Marco Palla<sup>1</sup>, Marco Pignatari<sup>59,60,61</sup>, Danae Polychroni<sup>58</sup>, Federico Rizzuti<sup>62,20</sup>, Donatella Romano<sup>18</sup>, Stefania Salvadori<sup>22,1</sup>, Luca Sbordone<sup>27</sup>, Emanuele Spitoni<sup>20</sup>, Matthew R. Standing<sup>63</sup>, Grazina Tautvaišienė<sup>44</sup>, Yuan-Sen Ting<sup>64,65,66</sup>, Andrea Travascio<sup>20</sup>, Diego Turrini<sup>58</sup>, Sophie Van Eck<sup>53</sup>, Kim Venn<sup>67</sup>, Diego Vescovi<sup>41,42</sup>, C. Clare Worley<sup>68</sup>, Nick Wright<sup>17</sup>, Robert Yates<sup>69,70</sup>, Alice Zocchi<sup>71</sup>, Laura Affer<sup>43</sup>, Carlos Allende<sup>6</sup>, Paul Barklem<sup>10</sup>, Michele Bellazzini<sup>18</sup>, Serena Benatti<sup>43</sup>, Leda Berni<sup>1</sup>, Francesco Borsa<sup>3</sup>, Maurizio Busso<sup>42</sup>, Tiago Campante<sup>7</sup>, Roberta Carini<sup>31</sup>, Brad Carter<sup>72</sup>, Giada Casali<sup>73,18</sup>, Mario Damasso<sup>54</sup>, Elisa Delgado Mena<sup>74</sup>, Ignacio Del Moral Castro<sup>75</sup>, Silvano Desidera<sup>57</sup>, Maria Pia Di Mauro<sup>76</sup>, Ana Escorza<sup>5,6</sup>, Sergio Fonte<sup>76</sup>, Elena Franciosini<sup>1</sup>, Xiaoting Fu<sup>77,18</sup>, Paolo Giacobbe<sup>54</sup>, Terese Thidemann Hansen<sup>78</sup>, Henrik Hartman<sup>79,2</sup>, Keith Hawkins<sup>80</sup>, Neda Heidari<sup>81,82</sup>, Krzysztof Helminiak<sup>22</sup>, H. Jens Hoeijmakers<sup>2</sup>, Stavro Lambrov Ivanovski<sup>20</sup>, Pascale Jablonka<sup>83,84</sup>, Chiaki Kobayashi<sup>85</sup>, Arunas Kucinskas<sup>44</sup>, Carmela Lardo<sup>18,19</sup>, Sebastiano Ledda<sup>86</sup>, Alesandra Lehtmetts<sup>87</sup>, Karin Lind<sup>78</sup>, João J.G. Lima<sup>7,9</sup>, Sara Lucatello<sup>57</sup>, Fatemeh Zahra Majidi<sup>88</sup>, Sarah Martell<sup>89</sup>, Anna McLeod<sup>39</sup>, Sergio Molinari<sup>76</sup>, Stephanie Monty<sup>90</sup>, Benjamin Montet<sup>91</sup>, Michael T. Murphy<sup>92</sup>, Henryka Netzel-Ilkiewicz<sup>23</sup>, Belinda Nicholson<sup>93</sup>, Patrick Palmeri<sup>94</sup>, Luca Pasquini<sup>1</sup>, Lorenzo Pino<sup>1</sup>, Romolo Politi<sup>76</sup>, Francesca Primas<sup>95</sup>, Pascal Quinet<sup>96,97</sup>, Monica Rainer<sup>3</sup>, Heleri Ramler<sup>87</sup>, Yassin Rany Khalil<sup>22,98</sup>, Martina Rossi<sup>18</sup>, Eugenio Schisano<sup>58</sup>, Federico Sestito<sup>85</sup>, Paolo Simonetti<sup>20</sup>, Arianna Vasini<sup>99</sup>, Silvia Vicente<sup>100</sup>, Carlos Viscasillas Vazquez<sup>44</sup>, Manuela Zocchi<sup>75</sup>, Michele Zusi<sup>58</sup>, Andrea Baruffolo<sup>57</sup>, Martin Black<sup>4</sup>, Anna Brucalassi<sup>1</sup>, Simone D'Auria<sup>1</sup>, Vincenzo De Caprio<sup>88</sup>, Michele Frangiamore<sup>3</sup>, Enrico Giro<sup>20</sup>, Robert J. Harris<sup>101</sup>, Alen Khanbekyan<sup>1</sup>, Enrique Joven<sup>6</sup>, Tom Louth<sup>4</sup>, Matteo Munari<sup>45</sup>, Graham J. Murray<sup>101</sup>, Luis Fernando Rodriguez Ramos<sup>6</sup>, Bernardo Salasnich<sup>57</sup>, William Taylor<sup>4</sup>, Andrea Tozzi<sup>1</sup>, Steven Watson<sup>4</sup>

## Executive Summary

This White Paper presents the updated scientific rationale and instrument concept for HRMOS (High-Resolution Multi-Object Spectrograph), a next generation instrument that will be proposed for the European Southern Observatory (ESO) Very Large Telescope (VLT) in the context of the VLT 2030 call and roadmap.

Over the past decades, large spectroscopic surveys have transformed our understanding of Galactic and extragalactic astrophysics, while ultra-high-resolution spectrographs have delivered unprecedented precision for individual targets, opening new frontiers in precision radial velocity for exoplanet detection and detailed chemical profiling. New multi-object spectrographs (MOS) and surveys are starting or are proposed; however, no existing or planned instrument at ESO and, more in general in the international landscape, combines these complementary capabilities: MOS capability and very high resolution. This is not only a technical gap, but a scientific need.

HRMOS is conceived to bridge this gap; by combining very high spectral resolution, multi-object observing capability, and stability, it will enable statistically significant studies, in a variety of Galactic and extra-galactic environments, requiring both spectral fidelity and observational efficiency.

The baseline design delivers a resolving power of  $R = 80\,000$ , radial velocity precision of  $10\text{ m s}^{-1}$  (with a goal of  $5\text{ m s}^{-1}$ ), simultaneous observations of 50–60 targets, and broad wavelength coverage across three optical spectral windows down to 385 nm. These capabilities will allow highly precise measurements of elemental abundances, isotopic ratios, line profiles, and radial velocities for large samples of stars, including in crowded stellar fields, members of star clusters, the Galactic bulge, and nearby dwarf galaxies that will not practically be feasible with current or upcoming very high-resolution facilities.

HRMOS will solve fundamental questions in astrophysics that we expect to be still open when it will be operating. Specifically, it will enable the precise and accurate determination of the ages of the oldest globular clusters through nucleocosmochronology, and thereby place independent and robust constraints on the age of the Galaxy, the timeline of cosmic evolution, and  $H_0$ ; it will allow surveys of hot Jupiters in complete samples of star cluster members, testing how planets form and survive in different environments; it will probe hierarchical galaxy assembly in the Milky Way satellite galaxies, identifying relics of ancient accretion events; it will trace the astrophysical sites responsible for the production of the heaviest elements, unveiling the contribution of neutron star mergers; it will advance studies of star clusters and stellar physics; it will characterize the interstellar and circumgalactic gas through absorption spectroscopy, revealing the chemical composition, physical conditions, and gas flows that regulate the exchange of matter between stars, galaxies, and their surroundings. HRMOS occupies a unique region of the parameter space, complementing both current and forthcoming multi-object survey facilities and single-object high-resolution spectrographs. In particular, it will provide an essential bridge between large spectroscopic surveys and the capabilities of the next generation of extremely large telescopes, maximizing scientific return through strong synergies with facilities such as 4MOST, *Gaia*, TESS, PLATO, the proposed Haydn space mission and the future ELT instrumentation.

Noticeably, to ensure the success of this science framework, the HRMOS initiative proactively integrates two key components directly into its deployment: namely, *i* laboratory astrophysics and a collaboration with atomic theory and experimental groups to deliver highly accurate atomic data before first light; *ii* advanced atmospheric modelling: Expanding grids of full 3D

Radiation-Hydrodynamics (RHD) stellar atmospheres and multi-element non-LTE codes. Finally, HRMOS represents the natural technological evolution and heritage of the VLT/FLAMES instrument, upgrading its capabilities to meet the challenges of the 2030s. The proposed instrument builds upon proven technologies, while introducing innovative solutions for fibre positioning, atmospheric dispersion correction, and fibre scrambling. Together, these developments enable the radial velocity stability and spectroscopic precision required by the ambitious science goals, while maintaining operational efficiency and compatibility with the VLT infrastructure. Overall, we believe that it represents a strategic investment in the future of European astronomy.

# Contents

<b>1 Introduction</b>	<b>7</b>
1.1 Preface and history . . . . .	7
1.2 The need for an HRMOS-like instrument . . . . .	8
1.3 The HRMOS instrument . . . . .	9
1.3.1 Top level requirements and efficiency . . . . .	9
1.3.2 Basic design elements . . . . .	10
1.3.3 Front-End Architecture . . . . .	11
1.3.4 Atmospheric Dispersion Correction Strategy . . . . .	13
1.3.5 Fibre Link . . . . .	14
1.3.6 Spectrographs . . . . .	14
1.3.7 Calibration Unit . . . . .	16
1.3.8 Radial-Velocity Error Budget . . . . .	16
1.4 HRMOS in context . . . . .	18
1.5 Structure and aim of this document . . . . .	19
<b>2 Exoplanets across Galactic environments</b>	<b>21</b>
2.1 Scientific context . . . . .	21
2.2 Formation and evolution of planetary systems . . . . .	23
2.2.1 The role of the environment in planetary formation . . . . .	24
2.2.2 Stellar evolution and the long-term evolution of planetary systems . . . . .	25
2.2.3 The star-planet interplay . . . . .	26
2.3 The potential of HRMOS . . . . .	27
2.4 Simulations and feasibility . . . . .	27
2.4.1 Expected Detectability with HRMOS . . . . .	27
2.4.2 HRMOS-like spectra translator . . . . .	28
2.4.3 Young stars: RV simulations and activity de-trending . . . . .	31
2.5 Expected Scientific Outcomes . . . . .	33
2.5.1 Environmental dependence of planet formation rates at Galactic scale . . . . .	33
2.5.2 Observational constraints of planetary systems evolution . . . . .	36
2.6 Potential targets . . . . .	36
2.6.1 Stars in open clusters . . . . .	36
2.6.2 Giants in the Bulge, globular clusters, and local dwarf galaxies . . . . .	38
2.6.3 Possible other targets . . . . .	39
2.7 The unique role of HRMOS . . . . .	41

<b>3 Origin of the elements and nucleosynthesis</b>	<b>42</b>
3.1 Scientific context	42
3.2 Chemical evolution of the carbon isotopes	43
3.3 The Galactic chemical evolution of sulphur	44
3.4 Abundances and isotopes of heavy neutron-capture elements	45
3.4.1 r-process elements: constraining rates and yields of compact-object mergers	45
3.4.2 Other neutron capture processes	47
3.4.3 Barium isotopes	47
3.4.4 Heavy elements detectable with HRMOS	51
3.4.5 Simulations with HRMOS-like spectra.	51
<b>4 Hierarchical formation and evolution of nearby galaxies</b>	<b>57</b>
4.1 Scientific context	57
4.1.1 Hierarchical galaxy formation and dark matter microphysics	57
4.1.2 Star formation histories of the host and accreted galaxies	60
4.1.3 Nucleosynthesis in the MW satellites	61
4.1.4 Descendants of zero-metallicity Pair-Instability Supernovae	62
4.1.5 Binary properties	62
4.2 Simulations	64
4.3 Potential targets	65
<b>5 Nucleocosmochronology: Constraining Cosmology from the Ages of the Oldest Milky Way Stars</b>	<b>68</b>
5.1 Scientific context	68
5.2 The method: Nucleocosmochronology	69
5.3 Feasibility of high-precision Th and Eu abundance measurements	70
5.3.1 Thorium abundances	70
5.3.2 Uranium detection with HRMOS	72
5.4 Systematic uncertainties affecting Th and Eu abundance determinations	72
5.5 Theoretical considerations: the Th/Eu production ratio	73
5.6 Possible targets: ages of globular clusters and of old stars in the field	74
5.6.1 Globular Clusters	74
5.6.2 Giant stars in the Milky Way field	75
<b>6 High-resolution spectroscopy of star clusters</b>	<b>77</b>
6.1 Scientific context	77
6.2 Young clusters as tracers of magnetic activity	78
6.2.1 Doppler tomography	79
6.2.2 Magnetic activity and planet detection	80
6.2.3 Impact of magnetic activity on abundance measurements	80
6.3 Star-disc interaction and tests of magnetospheric accretion	81
6.3.1 Magnetospheric accretion	81
6.3.2 Disc winds and jets	81
6.4 From cosmic dawn to today: the origin of multiple populations in globular clusters	82
6.4.1 High-precision abundances of light and heavy elements in globular clusters	83
6.4.2 Magnesium isotopes and the nature of globular-cluster polluters	84
6.5 Cluster stars as tracers of surface-composition evolution	86
6.5.1 The role of atomic diffusion	87

6.5.2	Demographics of lithium-rich giants . . . . .	87
6.6	Dynamics and kinematics of star clusters . . . . .	91
6.6.1	Cluster rotation and anisotropy . . . . .	91
6.6.2	Dynamics of multiple populations . . . . .	91
6.6.3	Binaries . . . . .	91
6.6.4	Simulations . . . . .	92
<b>7</b>	<b>Galactic and extragalactic gas reservoirs</b>	<b>94</b>
7.1	Scientific context . . . . .	94
7.2	The interstellar medium in the Galaxy . . . . .	95
7.2.1	Products, potential targets and synergies for the Galactic case . . . . .	96
7.3	Extragalactic gas reservoirs . . . . .	97
7.3.1	Products, potential targets, and synergies for the extragalactic case . . . . .	98
<b>8</b>	<b>Atomic data for high-precision spectroscopy</b>	<b>100</b>
8.1	Scientific context . . . . .	100
8.2	Capabilities: Delivering Atomic Data at the Accuracy HRMOS Demands . . . . .	101
8.2.1	Experimental atomic data . . . . .	101
8.2.2	Theoretical atomic data . . . . .	105
8.3	State of the field and data needs for HRMOS . . . . .	108
8.3.1	Synergies and products . . . . .	110
<b>9</b>	<b>Advanced stellar atmosphere and radiative transfer models for high-precision spectroscopy</b>	<b>112</b>
9.1	Scientific context . . . . .	112
9.2	Grids of 3D RHD model atmospheres expanded across stellar parameter space . . . . .	113
9.3	Model atoms with more complete and more accurate atomic data . . . . .	115
9.4	1D non-LTE and 3D LTE grids expanded across the periodic table . . . . .	117
9.5	Full 3D non-LTE calculations . . . . .	117
<b>10</b>	<b>Synergies and complementarities with present and forthcoming instrumentation</b>	<b>119</b>
10.1	Large spectroscopic surveys follow-up . . . . .	119
10.2	Present and future space missions . . . . .	120
10.2.1	TESS . . . . .	120
10.2.2	PLATO . . . . .	121
10.2.3	<i>Gaia</i> . . . . .	121
10.2.4	The ESO Extremely Large Telescope . . . . .	122
10.2.5	HAYDN . . . . .	123
<b>11</b>	<b>Target selection: Crowded stellar fields in the Milky Way and nearby dwarf galaxies</b>	<b>125</b>
11.1	Open clusters . . . . .	125
11.1.1	Observational strategy in a Benchmark open cluster . . . . .	125
11.2	Globular clusters . . . . .	126
11.2.1	Observational strategy in a Benchmark globular cluster . . . . .	128
11.3	The Galactic bulge and nearby dwarf galaxies . . . . .	128
11.3.1	Observational strategies in the Sagittarius dwarf galaxy and the LMC . . . . .	129
11.3.2	Observational strategy in the Galactic bulge . . . . .	130
<b>12</b>	<b>Appendix</b>	<b>132</b>
12.1	Estimating the precision in abundances and abundance ratios . . . . .	132

**List of Acronyms** 135

**References** 139

**Affiliations** 159

**Acknowledgements** 163

# 1 Introduction

## 1.1 Preface and history

The High-Resolution Multi-Object Spectrograph (HRMOS) initiative emerges from a shared scientific vision within the European astronomical community to equip the European Southern Observatory's (ESO) Very Large Telescope (VLT) with new capabilities enabling pivotal science that would otherwise remain unexplored. Indeed, over the past decades, ESO has delivered exquisite high-resolution and multi-object spectrographs, and new ones are coming online, but never both at once. HRMOS is devised to close this gap.

More in general, in the last three decades or so, large spectroscopic surveys and advanced instrumentation have transformed Galactic and extragalactic astrophysics by mapping the properties of vast target samples. Focusing on stellar surveys, the new generation ones will build on these early efforts in terms of statistical reach and depth, delivering spectra for millions of stars across the full sky and across a wide range of environments. These developments, combined with astrometric and photometric missions, ensure that the next era of astrophysics will be rich in data volume and diversity. What remains conspicuously missing from this coherent progression is a comparable leap in spectral resolving power, still combined with multiplex capabilities. This next logical step was identified a few years ago and presented at the ESO Workshop "The VLT in the 2030<sup>1</sup>" (Randich 2019; Tolstoy 2019) on behalf of a group of people that had started brainstorming around this idea; at the time, it was also stressed that a very high resolution multi-object spectrograph may represent the heritage of the VLT/FLAMES instrument. The Scientific Prioritization Community Poll organised by ESO after the workshop (Mérand et al. 2021) confirmed the increasing interest of the community in this concept.

Following the positive response from the ESO community, it was decided to develop these initial ideas into a comprehensive instrument concept, with the goal of submitting a proposal for the VLT once ESO opened a call for new instrumentation. A consortium and a science team were put together which have grown through the years, now comprising more than 180 people in Europe and oversea. The instrument was named High-Resolution Multi-Object Spectrograph, HRMOS, and the ambition was (and still is) to combine very high spectral resolution, stability and radial velocity precision with good multiplex capabilities.

As detailed in this document, HRMOS will allow one to address a variety of science questions in different areas. A first science workshop<sup>2</sup> was held in Firenze (Italy) and in parallel in Sydney (Australia) in October 2021. The meeting brought together a very large number of participants who proposed and discussed science projects where HRMOS would have a strong impact; following the conference and the ideas presented there, a first White Paper was published (Magrini et al. 2023). During the last two years, the science case has been both refined and expanded to new areas; in parallel, the science requirements have been further discussed and defined and the instrument design has now moved from an initial concept (Brucalassi et al. 2022) to a solid design (Riva et al. 2026, e.g.). This second version of the White Paper therefore presents those technical and science updates, illustrates the expected synergies between HRMOS and other current or planned facilities and instruments, and includes key discussions on the need for state-of-the-art model atmospheres

<sup>1</sup><https://www.eso.org/sci/meetings/2019/VLT2030.html>

<sup>2</sup><https://indico.ict.inaf.it/event/1547/>

and atomic data to best exploit the instrument potential.

This document is published after the workshop “*The VLT beyond 2030*”<sup>3</sup>, organised by ESO, where the HRMOS project has been presented and further captured the community interest. Following the opening of the ESO White Paper call in February 2026, this document is meant as a community contribution to the ongoing process leading to the submission of the White Paper in January 2027. By providing a coordinated consortium perspective at this stage, we seek to ensure that the transformative potential of high-resolution, multi-object spectroscopy is properly represented in the forthcoming ESO-wide discussions on next-generation instrumentation. In this context, we stress that the science team remains open to new contributors, who are welcome to join it via the HRMOS website<sup>4</sup>.

## 1.2 The need for an HRMOS-like instrument

Since the launch of the 2DF Galaxy survey and Sloan almost 30 years ago (Colless et al. 2001; Abazajian et al. 2009), large-scale ground-based spectroscopic surveys have become increasingly central to cosmology, extragalactic science, and Galactic astrophysics, with their impact now widely recognised. Focusing on the Galactic stellar populations, prominent surveys such as the Radial Velocity Experiment (RAVE, Steinmetz et al. 2020), Gaia-ESO (Gilmore et al. 2022; Randich et al. 2022), the Apache Point Observatory Galactic Evolution Experiment (APOGEE, Majewski et al. 2017), the GALactic Archaeology with HERMES (GALAH, De Silva et al. 2015), and the Large Sky Area Multi-Object Fibre Spectroscopic Telescope (LAMOST, Zhao et al. 2012) provided radial velocities that extend *Gaia* measurements to fainter stars, along with detailed atmospheric parameters and comprehensive elemental abundances across different environments. Collectively, these datasets have substantially deepened our understanding of key astrophysical processes, including star and stellar cluster formation, stellar evolution, and the formation and chemical enrichment history of the Milky Way and its companions. In the coming years, a new generation of multi-object spectroscopic (MOS) facilities and large-scale surveys—operating at low, medium, and relatively high spectral resolution ( $R \simeq 20,000$  for the approved instruments) will extend those efforts to much larger samples and areas on sky and/or fainter stars and/or larger volumes and/or different wavelength regimes. Surveys and facilities such as the 4-metre Multi-Object Spectroscopic Telescope (4MOST, de Jong et al. 2019), the WHT Enhanced Area Velocity Explorer (WEAVE, Dalton et al. 2014; Jin et al. 2022), the Multi-Object Optical and Near-infrared Spectrograph (MOONS, Cirasuolo et al. 2020; Gonzalez et al. 2020), the Milky Way Mapper (MWM) survey of SDSS-V (Almeida et al. 2023), the Dark Energy Spectroscopic Instrument (DESI Cooper et al. 2023), the Multi-Object Spectrograph for the ELT (MOSAIC, Hammer et al. 2021) and the proposed Wide-field Spectroscopic Telescope (WST, Bacon et al. 2023) will greatly amplify the scientific return of imaging and astrometric surveys, enabling detailed chemo-dynamical follow-up studies based on stellar samples of unprecedented size and diversity.

While MOS spectrographs provide information for large statistical samples, very high resolution spectroscopy remains crucial to deliver precise (or very precise) Doppler shifts and radial velocities, to derive high precision elemental abundances, to resolve line profiles, to precisely measure weak and/or blended spectral lines and isotope ratios, which is essential for the investigation of stellar, Galactic, and exoplanet science. Complementarily with the development of MOS and spectroscopic surveys, a number of high resolution spectrographs targeting individual objects have come on line in the last 20-30 years; focusing on the European instruments, we mention HARPS (Mayor et al.

<sup>3</sup>[https://www.eso.org/sci/meetings/2026/VLT\\_beyond\\_2030.html](https://www.eso.org/sci/meetings/2026/VLT_beyond_2030.html)

<sup>4</sup><https://www.hrmos.eu>

2003), UVES (Dekker et al. 2000), ESPRESSO (Pepe et al. 2021), CRIRES+ (Dorn et al. 2023) at ESO and HARPS-N (Cosentino et al. 2012) at the Italian TNG. Indeed ESO offers a unique battery of high-resolution spectrographs that serves a very wide scientific community, with the ELT/ANDES clearly representing the next technological and scientific frontier (Marconi et al. 2022a).

In summary, the present and the coming decades promise substantial advances in MOS and high spectral resolution instrumentation, which will considerably broaden the accessible parameter space. Nevertheless, despite this anticipated progress, to our knowledge the current international landscape lacks plans for an instrument on an 8-metre-class telescope that combines the statistical power of a MOS with very high resolution. While such an instrument poses significant technological challenges (see Section 1.3), it appears essential for the efficient delivery of very precise information for large numbers of targets across diverse environments and crowded fields. Providing this capability, in synergy with forthcoming ground- and space-based facilities, will allow us to address some of the most compelling astrophysical questions of the coming decades, as we showcase in this document. We mention that such a need is highlighted in the ASTRONET Roadmap 2022-2035<sup>5</sup> for Astronomy, which includes a HRMOS-like instrument among the "*exciting concepts in development that will provide important capabilities*". The recent post-Sloan V report<sup>6</sup> emphasises as well the need for high-multiplex, high-resolution spectroscopy to tackle a broad range of Galactic and extragalactic science cases,

HRMOS is conceived to cover this gap and to offer the community an instrument that will deliver unique capabilities to address a variety of science cases that require high precision information for sizeable samples of targets (Randich et al. 2026, see). This document is meant to describe these science drivers.

## 1.3 The HRMOS instrument

### 1.3.1 Top level requirements and efficiency

HRMOS will take advantage of the large collecting area of the VLT and will provide an upgraded version of the existing FLAMES instrument. The main characteristics and top level requirements (TLR) of HRMOS have been defined starting from the high priority science cases (see also Magrini et al. 2023); the final TLRs resulting from a number of trade-offs, performance goals, and constraints that guide the instrument design and development are presented in Tab. 1.1. As mentioned above, the primary science requirement for HRMOS is the combination of a very high spectral resolution with MOS capabilities. A radial-velocity precision of  $10 \text{ m s}^{-1}$  or better is a key requirement, as well as coverage of the blue spectral range down to about 385 nm.

The table shows that, although fundamental optical design constraints limit the multiplex to values well below those of instruments such as MOONS or 4MOST, the instrument will still enable the simultaneous observation of at least 50 targets (with a goal of 60), representing a significant improvement over current facilities such as UVES-FLAMES. Also, it will operate at a very high resolving power ( $R = 80\,000$ ), approximately a factor of two higher than that of UVES-FLAMES.

We also stress that HRMOS will provide a wide spectral coverage, encompassing three key spectral regions, including the critical lines identified by the primary science drivers. The simultaneous wavelength coverage of about 130 nm is sufficiently broad to allow high radial velocity precision ( $10 \text{ m s}^{-1}$ , with a goal of  $5 \text{ m s}^{-1}$ ).

Finally, in the inner area the instrument will be capable of observing targets separated by 10 arcsec, enabling efficient observations in extremely crowded fields, such as the cores of Galactic

<sup>5</sup>[https://www.astronet-eu.org/?page\\_id=521](https://www.astronet-eu.org/?page_id=521)

<sup>6</sup><https://www.sdss.org/future/>

**Table 1.1.** HRMOS baseline top level requirements

	Requirement	Goal
Resolving power	80 000	
Central Wavelength ( $\lambda_C$ )	402 nm	
$\lambda_C$	501 nm	
	650 nm	
Spectral intervals	$\lambda_C/12$	
Total coverage	129.5 nm	
Radial velocity precision	10 m s <sup>-1</sup>	5 m s <sup>-1</sup>
Number of fibres	50	60
Minimum object separation	30 arcsec outer regions; 10 arcsec inner regions	

globular clusters.

Figure 1.1 shows the SNR per resolution element obtained for an one-hour exposure using a preliminary version of the instrument Exposure Time Calculator (ETC), adopting conservative values for the efficiencies of the different sub-systems and the overall throughput. A detailed description of the ETC is given in Schiappacasse et al. (2026, in preparation). The figure demonstrates that the instrument is highly efficient. For solar-type stars, the limiting magnitude for a SNR of 10 in one hour for a G2V-type star is  $G = 17.2, 18.1, \text{ and } 18.5$  in the blue, green, and red bands, respectively.

### 1.3.2 Basic design elements

A detailed description of the HRMOS technical concept, the spectrograph optical design and the positioner are provided in Bianco et al., Brucalassi et al, Gonzalez et al. (2026, in preparation). We summarise below the main aspects.

The instrument is proposed to be mounted on the Nasmyth platform of one of the VLT units, providing a stable, side-mounted configuration that accommodates the complex optical and mechanical subsystems. It will consist of four primary components, illustrated schematically in Figure 1.2.

The **Front End** will position between 50–60 optical fibres. It will also correct for telescope aberrations, derotate the field to compensate for sky rotation, and provide the injection of calibration light. The design of the Front End builds substantially on the MOONS project, leveraging its proven rotating-platform architecture and field-corrector optics, while incorporating adaptations to meet the more stringent proximity and precision requirements of HRMOS (see Section 1.3.3).

The **Fibre Link** will collect the light from each fibre and deliver it to the spectrographs with minimal losses, while preserving the uniformity required for high-precision radial-velocity measurements. It incorporates a double-scrambling stage to homogenise both near-field and far-field illumination, wavelength-splitting dichroics, and an image-slicing subsystem designed to match the telescope 'etendue.

The **Spectrographs** will disperse the collected light into high-resolution spectra across the three selected wavelength ranges, using volume phase holographic (VPH) gratings as the primary dispersing elements. The spectrograph bench will be maintained under active thermal and pressure control in order to minimise spectral drifts.

Complementing these subsystems, the **Calibration Unit** will project well-characterised artificial light onto the focal plane, enabling precise wavelength and flux calibration across all fibres (see

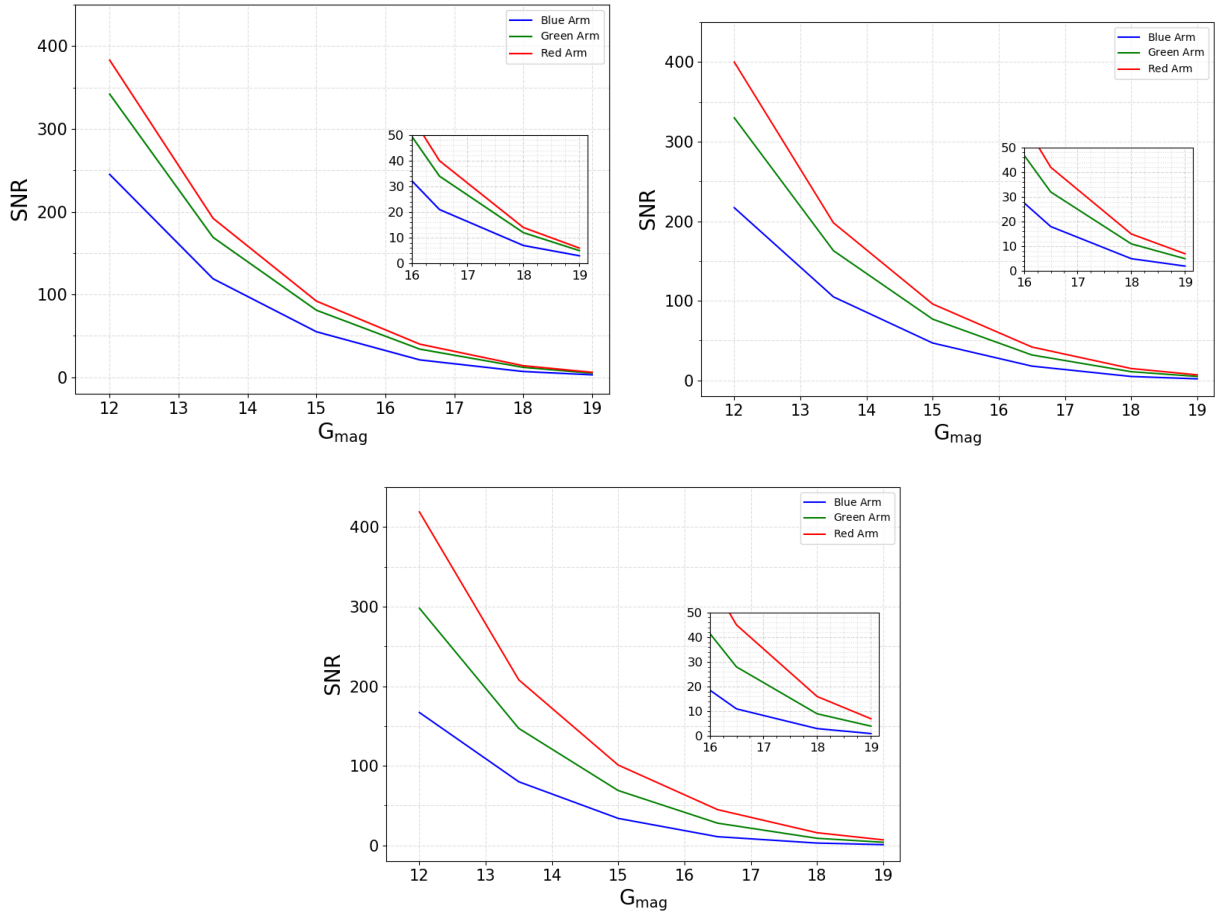


**Figure 1.1.** SNR per resolution element for **F4V-, G2V, and K4V-type** stars (left upper panel, right upper left and bottom panels, respectively) as a function of G magnitudes (**Vega system**) for 1 hr of exposure time (airmass 1, dark sky condition, seeing=0.8”).

Section 1.3.7).

The radial-velocity error budget for HRMOS is designed to meet a precision requirement of  $10 \text{ m s}^{-1}$ . According to technical simulations, the current estimated total error is approximately  $8.2 \text{ m s}^{-1}$ , comprising a random component of  $1.4 \text{ m s}^{-1}$  and a systematic component of  $6.7 \text{ m s}^{-1}$  (see Section 1.3.8 for the full derivation).

### 1.3.3 Front-End Architecture

**Overall layout.** HRMOS will exploit the full 25' field of view of the VLT through a field corrector closely based on that developed for MOONS, mounted at the Nasmyth focus and supported by a rotating front-end platform inherited from MOONS. The multiplex of 50–60 targets requires a fibre-positioning architecture that differs from that adopted by MOONS, both to accommodate the more compact fibre-head spacing required for crowded-field science and to enable per-fibre ADC correction (see below). Calibration light is injected into the fibres via a fibre-switching mechanism integrated within the Front End.

**Fibre-positioning concepts.** Two fibre-positioning concepts have been evaluated, as illustrated in Figure 1.3. The  $r$ - $\theta$  positioner (Figure 1.3, left), derived from MOONS and KMOS designs, combines a rotation axis with a linkage mechanism enabling radial extension. It allows rapid field

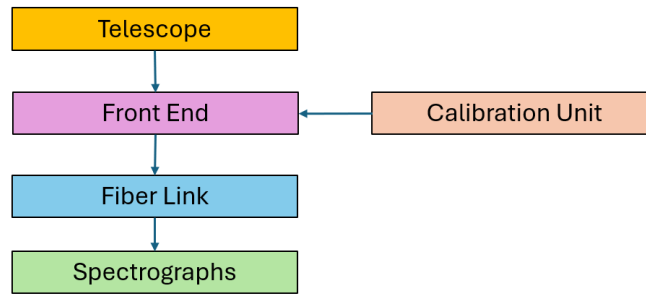


**Figure 1.2.** High-level block diagram of the HRMOS instrument, comprising the Front End, Fibre Link, Spectrographs, and Calibration Unit.

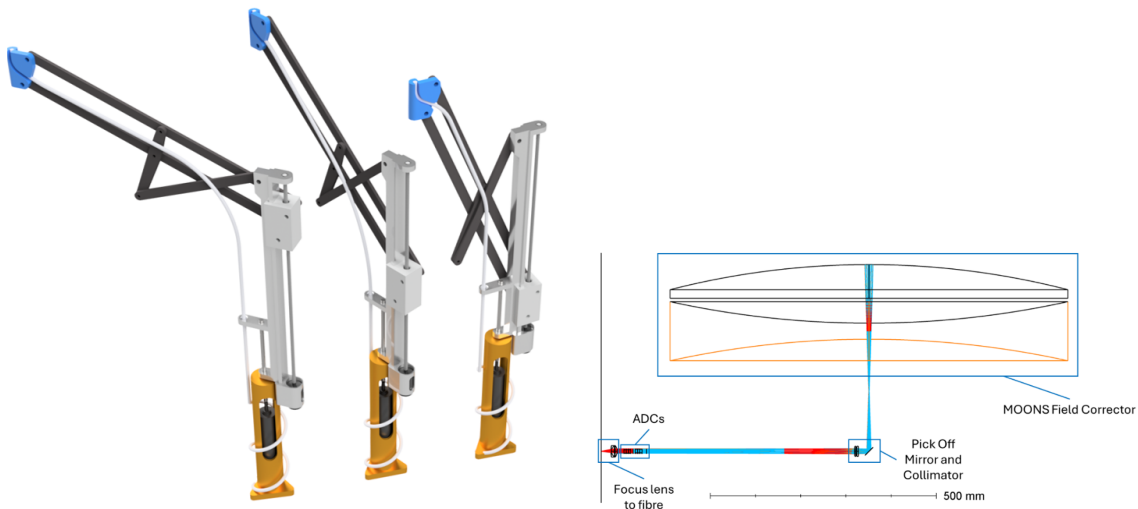


**Figure 1.3.** *Left:* The  $r$ - $\theta$  positioner concept (derived from MOONS and KMOS designs) combines a rotation axis with a linkage mechanism enabling radial extension. *Right:* The novel pick-and-place concept with integrated miniaturised ADCs.

reconfiguration and high fibre packing density; however, it would require a single, traditional telescope level ADC placed upstream of all fibres. This would likely require refractive optics approaching 1.5 m in diameter. Such optics are expensive, heavy, difficult to manufacture, and introduce additional optomechanical complexity.

The *pick-and-place system* (Figure 1.3, right) (see Gonzalez et al. 2026, in preparation) uses passive configurable pick-off mirror units, each providing tip-tilt, rotation, and collimation. ADC and fibre-injection optics are housed in fixed receivers distributed around the focal plane; active alignment within each sub-module is performed by integrated cameras. Pick-off units are oriented at a docking point and then translated to the required position on the focal plane. This architecture natively accommodates individual compact ADCs on each receiver, making it better suited to the close-proximity science requirements of HRMOS.

The selected solution, described in detail in Section 1.3.4, is a *hybrid* approach that combines features of both concepts in order to balance science requirements, technological readiness, operational complexity, and optical performance across the full field.

**1.3.4 Atmospheric Dispersion Correction Strategy**

Considering the simultaneous observation in the B, V and R spectral bands, accurate atmospheric dispersion correction is essential for HRMOS, both to maintain high coupling efficiency into the science fibres and to avoid wavelength-dependent flux losses that would degrade radial-velocity precision. Two competing constraints drive the ADC design: the need to cover the full spectral range (385–677 nm) with high correction quality, and the need to position fibres as close as 10–15 arcsec apart in crowded fields.

**The Dual ADC solution.** The adopted strategy is a dual two-zone architecture that consider the  $r-\theta$  concept for the fibre positioning:

- **Central zone (separation  $\geq 10$  arcsec):** A single, moderately sized ADC covers the central region of the focal plane. Fibres deployed in this zone do not carry individual ADCs and rely on the common upstream element. This configuration allows a minimum fibre separation of 10 arcsec, which is essential for studying the cores of globular clusters and other crowded-field science cases.
- **Peripheral zone (separation  $\geq 30$  arcsec):** Fibres in the outer field are equipped with dedicated compact ADCs integrated into the pick-off sub-modules. The larger inter-fibre spacing in this region makes individual ADC packaging physically feasible.

The optical design of each peripheral ADC unit consists of a pair of counter-rotating prisms placed downstream of the pick-off mirror and collimator, operating in a converging beam. The prism size is constrained by the available envelope within the Nasmyth focal-plane assembly; ray-trace analysis confirms that the correction residuals remain within the acceptable budget for fibres in the outer field (Figure 1.4).

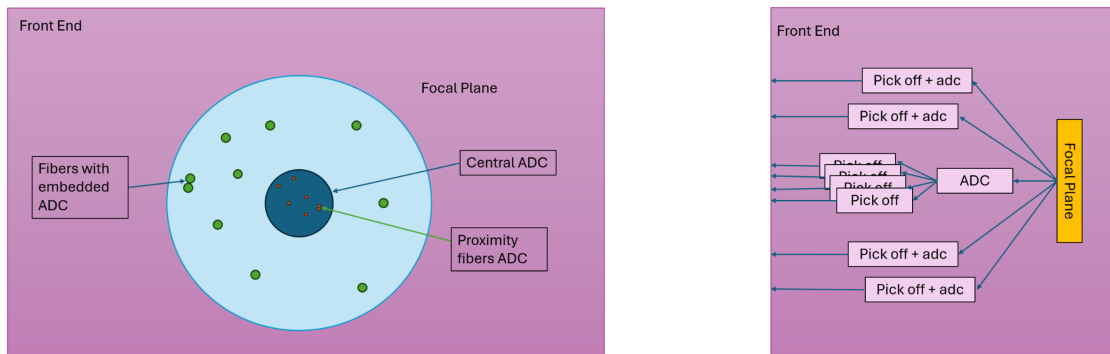


**Figure 1.4.** Optical layout of the pick-and-place ADC sub-module for the peripheral zone (left: full collimator–ADC–camera train; right: pupil-concentric focal-plane arrangement within the Nasmyth rotator envelope).

This hybrid solution represents the best compromise between two extremes: a single large ADC and a fully distributed system with one ADC per fibre. impractical at the scale of the central field. The technology readiness of all components is high, drawing on proven ADC designs from ESPRESSO, MOONS, and KMOS; the main operational complexity lies in the target-allocation software, which must account for the different ADC correction performance in the two zones when optimising fibre configurations.

### 1.3.5 Fibre Link

As mentioned, the fibre link is the subsystem that physically connects the Front End to the spectrographs, performing distinct optical functions.

**Modular architecture.** The fibre link is organised as 50 (goal: 60) identical modules, one per observed target. Within each module the light path proceeds as follows. A single-mode connector at the Front End focal plane injects the starlight into the first fibre segment. A *double scrambler* then homogenises both the near field (focal-plane illumination) and the far field (pupil illumination). Dichroic beam-splitters split the scrambled beam into the three spectral channels each routed to a dedicated *slicer* module. Each slicer subdivides the fibre image into  $N_{\text{slice}} = 19$  sub-pupils, reformatting the circular fibre output into a pseudo-slit that is optimally matched to the spectrograph collimator. A simultaneous calibration fibre (*Sym Calib*) runs in parallel with each science channel, delivering a stable wavelength reference that follows the same optical path as the starlight up to the spectrograph entrance.

**Hardware components.** The key hardware elements of the fibre link are discussed in detail in Bianco et al. (2026, in preparation). Briefly we recall here that they include:

*Connectors.* The fibre-link connectors interface the Front End with the fibre bundle and must preserve the scrambling quality achieved downstream. Custom connectors implement the double-scrambling function and route the fibre stress-relief bundles towards the spectrograph room.

*Double scramblers.* The double-scrambler units suppress the modal noise and illumination asymmetries induced by variable telescope guiding. By combining two consecutive scramblers oriented at  $90^\circ$  to each other, both the near-field (focal-plane intensity distribution) and the far-field (pupil intensity distribution) are homogenised. The gain factor achieved by this arrangement is of order  $10^4$ , reducing guiding-induced RV systematics to the sub- $\text{cm s}^{-1}$  level (see Section 1.3.8).

*Slicers.* Each slicer module subdivides the circular fibre output into 19 sub-pupils using a microlens array. The resulting rectangular pseudo-slit matches the spectrograph collimator acceptance and improves the spatial uniformity of the illumination entering the disperser, which is critical for high-fidelity spectral extraction.

The complete fibre-link assembly for 50 modules fits within a standard instrument rack platform close to the spectrograph enclosure to minimise the fibre run length and associated transmission losses.

### 1.3.6 Spectrographs

HRMOS employs three spectrograph arms — blue (B), green (V), and red (R) — one per spectral window, each receiving the pre-sliced and pre-scrambled light from the corresponding dichroic channel of the fibre link. The three arms share a common optical design and are housed within a single temperature- and pressure-stabilised enclosure.

**Optical functions.** Each spectrograph performs four sequential operations (Figure 1.5):

1. *Pseudo-slit formation.* The 19-slice output of each fibre module is stacked into a pseudo-slit by the slit-forming optics at the spectrograph entrance. For each star, the 19 slices are arranged in a column, separated from adjacent stars by a small inter-object gap to prevent cross-contamination during spectral extraction.

2. *Collimation.* A collimator lens group converts the diverging beam from the pseudo-slit into a well-defined parallel beam of diameter matched to the disperser.
3. *Dispersion.* A VPH grating acts as the main dispersing element, offering high-diffraction efficiency (typically  $>80\%$  at blaze) combined with the large format and low scattered-light level required for precision spectroscopy at  $R = 80\,000$ .
4. *Detection.* A multi-element camera focuses the dispersed spectra onto the detector mosaic.

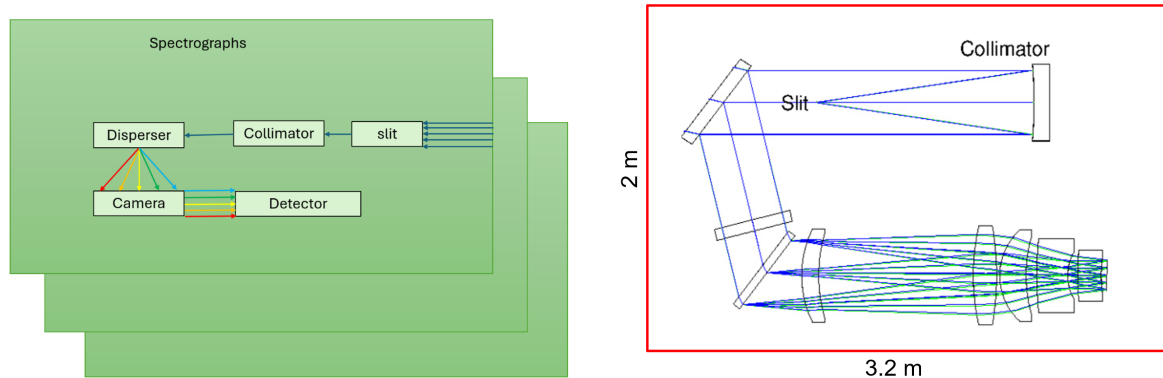


**Figure 1.5.** *Left:* Block diagram of the HRMOS spectrographs. *Right:* Optical ray-trace layout of one HRMOS spectrograph arm, showing the pseudo-slit, collimator, VPH grating, and camera–detector assembly. The overall footprint is approximately  $3.2 \times 2.0$  m

**Key design parameters.** The main numerical parameters of each spectrograph arm are listed below.

- Resolving power:  $R = 80\,000$
- Number of slices per science object: 19
- Simultaneous calibration fibres: 1 per object per arm (*Sym Calib*)
- Inter-object gap on slit: equivalent to one fibre width
- Detector format:  $2 \times 1$  mosaic of  $9k \times 9k$  CCDs; pixel size =  $10\mu$
- Number of objects per detector mosaic: 52 (example value within the range 50–60)
- Spectral sampling: 2.7 pixels per resolution element
- Camera focal ratio: F/2.96
- Overall spectrograph footprint:  $\sim 3.2 \times 2.0$  m (length  $\times$  height)

The detector mosaic of  $2 \times (9k \times 9k)$  pixels provides the spatial and spectral real estate required to accommodate 52 objects (example value within the range 50–60) with 19 slices each, plus inter-object gaps and simultaneous calibration traces, at 2.7-pixel sampling. The camera operates at F/2.96 to keep the overall spectrograph length within the Nasmyth platform envelope. Whilst current design is based on CCDs, use of CMOS detectors is under study.

**Environmental control.** To achieve the extreme stability required by the scientific goals, each spectrograph arm will be housed within a thermally insulated enclosure maintained at controlled temperature and pressure. Active environmental control, combined with double scrambling in the fibre link, minimises spectral shifts induced by mechanical and thermal variations. The temperature stability requirement is set by the thermo-mechanical contribution to the RV error budget: thermal drifts of the optical bench must be kept at the level of a few  $\text{mK h}^{-1}$  in order to maintain the residual calibratable systematic error below the  $6.7 \text{ m s}^{-1}$  budget (see Table 1.2). This level of environmental control is well established in existing high-precision spectrographs (HARPS, ESPRESSO) and is adopted here as a proven baseline.

### 1.3.7 Calibration Unit

The Calibration Unit delivers calibration light to the focal plane in a manner that mimics the illumination of science targets, so that the calibration light follows the same optical path as starlight collected by the fibres. A dedicated injection system formats the calibration light and projects it onto the focal plane with the correct spatial distribution to match the fibre positions and slicing configuration. This approach — referred to as *symmetric calibration* (*Sym Calib*) in the fibre-link description (Section 1.3.5) — ensures that each fibre receives a well-characterised reference signal, enabling accurate wavelength calibration, throughput monitoring, and correction of instrumental drifts at every position in the focal plane.

A laser frequency comb (LFC) is considered the baseline simultaneous reference source for the radial-velocity programme, given its unparalleled line-spacing regularity and long-term absolute stability. The LFC comb lines are injected into the *Sym Calib* fibres and propagate alongside the science signal through the scrambler and slicer stages to the detector, providing a wavelength grid that is insensitive to spectrograph drifts occurring between daytime and nighttime calibration sequences. Alternative or complementary sources (Fabry–Pérot etalons, hollow-cathode lamps) can be accommodated for flat-field and arc-line calibrations, or as a backup in case the LFC is not operational.

The injection system is fed from the Calibration Unit via a dedicated fibre switching mechanism located in the Front End, which allows the calibration source to illuminate the focal plane without any mechanical intervention in the science beam path. This design choice ensures that the calibration and science exposures can be interleaved with minimal overheads and that the calibration light path is stable with respect to the science light path at the sub-pixel level.

By delivering highly uniform, precise, and stable reference light to every science fibre, the Calibration Unit ensures that all spectroscopic measurements maintain the high precision and repeatability required for the demanding science applications described in this White Paper, including radial-velocity measurements at the level of a few metres per second and abundance analyses requiring signal-to-noise ratios in excess of 200.

### 1.3.8 Radial-Velocity Error Budget

A key requirement for HRMOS is a radial-velocity (RV) precision of  $10 \text{ m s}^{-1}$  (goal:  $5 \text{ m s}^{-1}$ ), needed to detect Jupiter-mass planets around solar-type stars in open clusters and to measure precise stellar kinematics in crowded fields. This section summarises the error-budget analysis underpinning the estimate quoted in Section 1.3.2.

**Guiding and scrambling assumptions.** Experience from testing of the MOONS fibre positioner demonstrates that a peak-to-valley centring error of  $60 \mu\text{m}$  can be routinely achieved. At the

HRMOS front-end plate scale this corresponds to a centring uncertainty of  $\sim 100$  mas. This is compatible with the guiding error of the VLT. Without scrambling, such a centring error would translate directly into an illumination gradient across the fibre face and hence into a systematic RV shift. The double-scrambling stage in the fibre link provides a suppression factor of  $\sim 10^4$ , reducing this contribution to the  $\text{sub-cm s}^{-1}$  level.

**Systematic error budget.** The dominant systematic contributions are thermo-mechanical drifts of the spectrograph bench (thermal stability of the disperser, grating evolution, pressure variations) and detector-related effects (charge-transfer inefficiency, readout thermal changes). When these are calibrated with a simultaneous reference source (e.g., a laser frequency comb, LFC), the residual calibrable systematic is reduced by a factor of  $\sim 3$  (assuming 30% calibration residuals as a conservative estimate). The resulting systematic budget is summarised in Table 1.2.

**Table 1.2.** HRMOS radial-velocity error budget. Random and systematic contributions are listed before calibration; the final row gives the quadrature sum after applying the calibration residual factor.

Error source	Random ( $\text{cm s}^{-1}$ )	Systematic ( $\text{cm s}^{-1}$ )
Instrument (uncalibrable)	12.0	9.3
Calibration source	4.0	4.0
External errors	500	25.0
Instrument calibration	4.0	2236
<b>Total (final)</b>	<b>500</b>	<b>670</b>

**Random (photon-noise) limit.** The photon-noise contribution to the RV measurement is evaluated using the standard line-width formalism:

$$\sigma_{\text{line}}(\text{RV}) = A \times \text{FWHM} \times \text{SNR}^{-1} \times N_{\text{samp}}^{-0.5} \quad (1.1)$$

where  $A = 0.41$  (appropriate when a laser frequency comb is used as simultaneous reference),  $\text{FWHM} = c/R = 3750 \text{ m s}^{-1}$  at  $R = 80\,000$ ,  $\text{SNR} = 25$  per resolution element in the G band (average value, is adopted here—see Table 2.1), and  $N_{\text{samp}} = 2.7$  pixels. This yields  $\sigma_{\text{line}} = 37.4 \text{ m s}^{-1}$  per spectral line (Equation 1.1).

$$\sigma_{\text{tot}} = (\sigma_{\text{instr}}^2 + \sigma_{\text{lines}}^2)^{0.5}. \quad (1.2)$$

Combined in quadrature (Equation 1.2) with the instrumental random floor of  $\sigma_{\text{instr}} = 20 \text{ m s}^{-1}$  (including a contingency margin over the budget value), the per-line total is  $\sigma_{\text{tot}} = 42.4 \text{ m s}^{-1}$ .

**Multi-line combination.** The final RV precision is obtained by averaging over all usable spectral lines,

$$\sigma_{\text{final}} = \sigma_{\text{tot}} \times N_{\text{lines}}^{-0.5}. \quad (1.3)$$

For HRMOS, the three spectral windows (total 130 nm) at  $R = 80\,000$  contain approximately  $N_{\text{lines}} = 800$  lines suitable for RV work—compared with  $\sim 5000$  for ESPRESSO over 200 nm at  $R = 100\,000$ . Inserting these numbers into Equation (1.3) gives:

$$\sigma_{\text{final}}^{\text{rand}} = 1.5 \text{ m s}^{-1}, \quad (1.4)$$

$$\sigma_{\text{final}}^{\text{syst}} = 6.7 \text{ m s}^{-1}, \quad (1.5)$$

yielding an overall precision of  $8.2 \text{ m s}^{-1}$ , comfortably within the  $10 \text{ m s}^{-1}$  requirement.

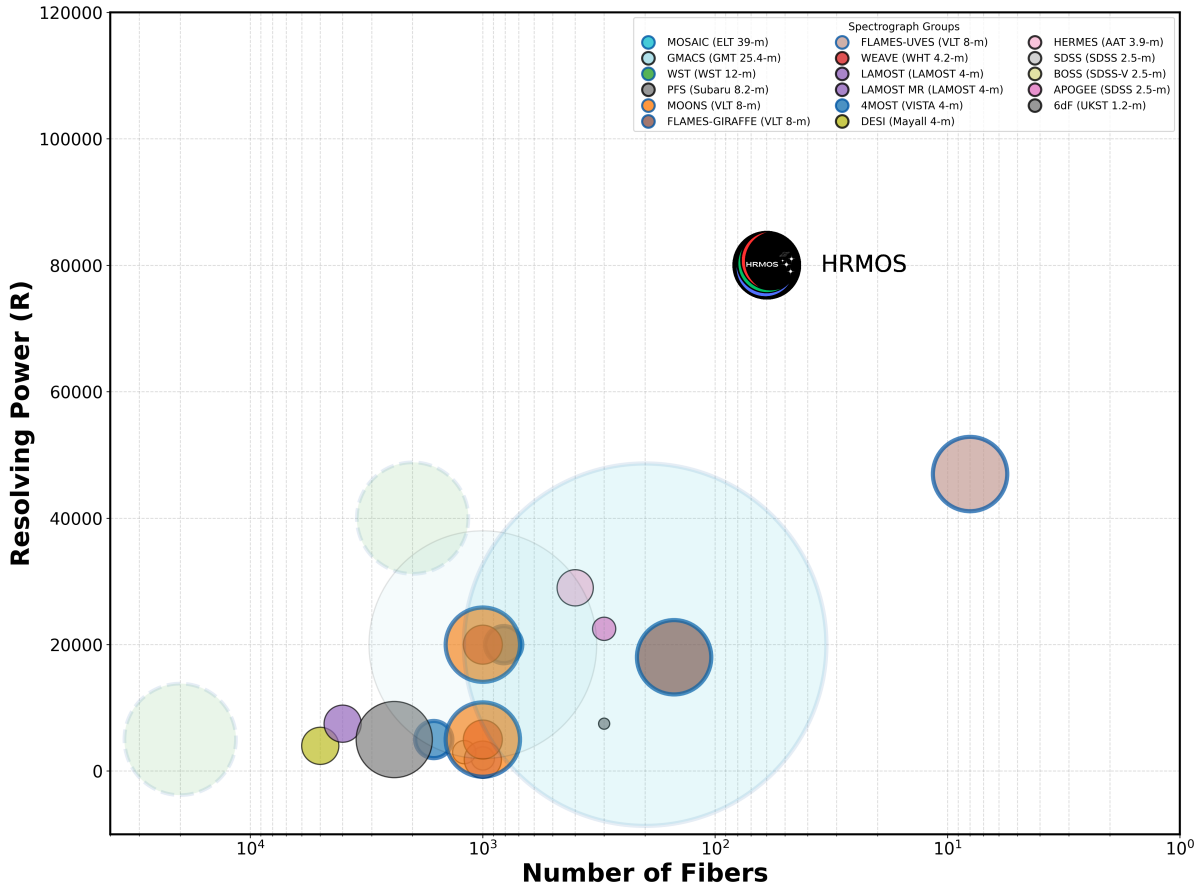


**Figure 1.6.** HRMOS in the context of multi-object spectrographs. The resolving power  $R$  is shown as a function of the number of fibres, with the symbol sizes proportional to the collecting area of the corresponding telescope. HRMOS is represented by its logo, positioned at  $R \approx 80,000$  and a multiplex of 60 fibres (within the range 50–60). Future instruments are represented with transparent circles; proposed facilities are denoted with dashed contours, while ESO instruments are highlighted with blue contours.

### 1.4 HRMOS in context

Figure 1.6 shows the resolving power as a function of the number of fibres for current, upcoming, and proposed MOS instruments and facilities; HRMOS clearly occupies a region of parameter space unmatched by any existing or planned facility. As already stressed, to our knowledge, no comparable instrument is currently operational or in development in the near term.

Focusing on the suite of ESO VLT instrumentation, illustrated in Fig. 1.7—where resolving power, spectral coverage, and the distinction between integral-field, single-object, and multi-object capabilities are compared—it is clear that no existing instrument offers such a combination of capabilities. This leaves a critical gap in the available observational parameter space, one which HRMOS is specifically designed to address.

Looking ahead to the ELT era, HRMOS will provide a complementary capability: whereas ANDES will deliver unprecedented sensitivity and spectral resolution for individual targets, HRMOS will enable large, statistically significant surveys that are crucial for addressing key questions in our Galaxy and beyond. In this context, HRMOS represents not only a natural evolution of the VLT spectrograph suite, but also a pivotal facility for bridging the gap between current surveys and the groundbreaking science anticipated with next-generation extremely large telescopes.

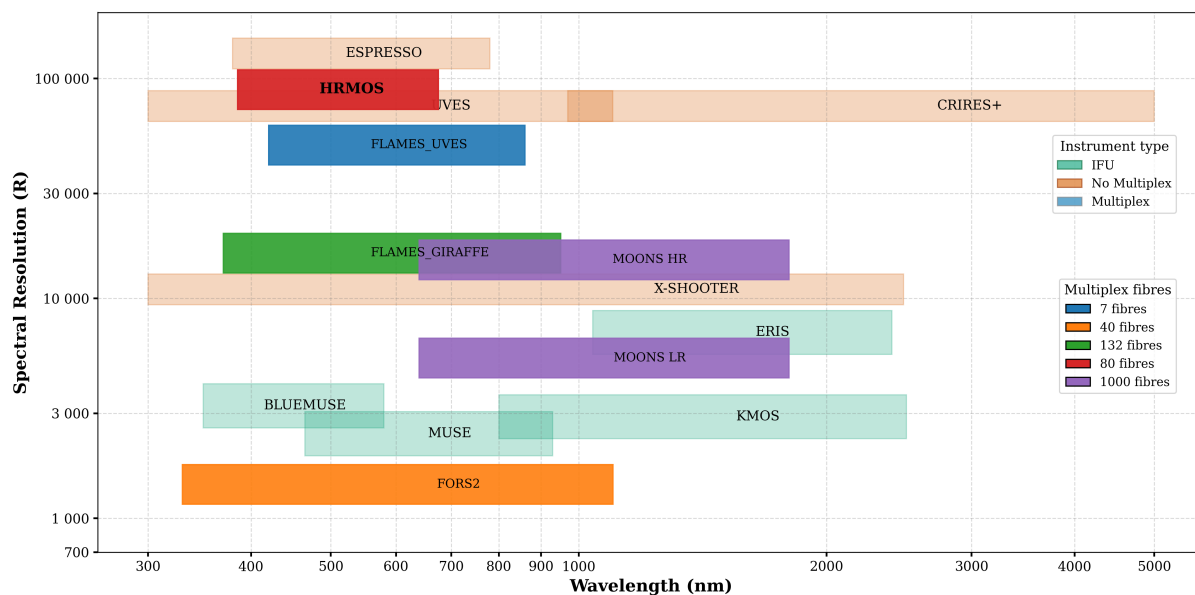


**Figure 1.7.** Positioning of HRMOS within the landscape of current and forthcoming ESO spectroscopic instrumentation in the optical and near-infrared ranges for VLT. The multi-object facilities are colour coded by the number of fibres or slits, which is reported in the legend. Single object and integrated field spectrographs are shown with different colours, as indicated in the top-right legend. The y axis is represented with a scale, which is approximately logarithmic but visually compressed to enhance readability of both high- and low-resolution instruments.

The unique combination of very high spectral resolution, stability and radial velocity precision, multi-object capability offered by HRMOS is not merely an instrumental advance; as we aim to showcase in this document, it is a scientific necessity. Many pressing open questions in astrophysics and cosmology –and that will remain open in the 2030’s when HRMOS, if selected, will be operational– do require these capabilities: from establishing model-independent ages of the oldest stellar populations, to reconstructing the assembly history of the Milky Way and nearby galaxies, to the origin of elements, to tracing the role of environment in shaping planetary systems.

The science cases presented in this White Paper are only a subset of the opportunities that HRMOS can address. Owing to its natural complementarity with current and forthcoming ground- and space-based facilities (see Chapter 10), and its synergy with the rapid advances in laboratory atomic physics and the dynamical, non-equilibrium modelling of stellar atmospheres that enable spectroscopic analyses of ever improving accuracy (Chapters 8 and 9), the scientific reach of HRMOS will continue to expand over time. As new discoveries emerge, HRMOS will provide a flexible and powerful platform capable of responding to evolving scientific priorities in the decades ahead.

## 1.5 Structure and aim of this document

This document does not aim to provide an exhaustive overview of all the potential scientific applications of HRMOS. Rather, its purpose is to outline a set of representative, high-impact science cases that illustrate the unique capabilities of the instrument, and to derive from them the corresponding technical requirements.

The document is structured as follows. Chapter 1 provides an overview of the HRMOS project and its scientific motivation within the current observational landscape. The following chapters present the driving science cases for HRMOS. Chapter 2 outlines the potential of HRMOS for

detecting massive planets in diverse environments. Chapter 3 focuses on key elemental abundance and isotopic ratio studies, covering light elements such as carbon and sulphur, as well as s- and r-process elements. Chapter 4 examines hierarchical assembly processes in the context of the formation and evolution of dwarf galaxies. Chapter 5 discusses the use of radioactive isotopes to constrain stellar ages, and thereby the age of the Universe. Chapter 6 examines open and globular cluster science, including detailed chemical and dynamical studies. Chapter 7 addresses studies of the interstellar medium, both within our Galaxy and in an extragalactic context. Chapters 8 and 9 describe complementary resources, including atomic data and model atmospheres required for high-precision spectroscopic analyses. Chapter 10 highlights synergies between HRMOS and other facilities, and Chapter 11 discusses possible target strategies.

## 2 Exoplanets across Galactic environments

Star clusters offer uniquely well-characterised environments, where ages, metallicities, and stellar densities can be independently constrained, providing an essential benchmark for understanding how planet formation and dynamical evolution depend on environment. By exploiting its high radial-velocity precision and multiplexing capability, and complementarily with respect to other space and ground-based facilities, HRMOS will enable statistically robust measurements of giant planet occurrence rates in open and globular clusters, but also in other crowded fields, such as the Galactic Bulge and dwarf galaxies.

### 2.1 Scientific context

The study of exoplanets has advanced rapidly, yet our understanding remains constrained by the limited range of environments explored so far and by the fact that individual studies have been carried out, while *population level* studies are less frequent. In fact, the properties of exoplanetary systems are expected to be strongly linked both to those of their host stars and to the environments in which the stars formed and reside, while the systems themselves are also expected to evolve significantly over their lifetimes (e.g. Turrini et al. 2022; Biazzo et al. 2022). Hence, in order to robustly determine how planetary systems form and evolve, we must systematically probe environments with distinct chemical and dynamical properties, also extending our investigations beyond the familiar regions of the Milky Way. By detecting planets in these diverse settings, we can isolate the factors that influence planet occurrence, composition, and system architecture. Expanding our observational reach in this way is essential for building a more complete and predictive framework for planetary science. It is within this context that HRMOS will play a unique role: a facility designed to expand our observational horizons and enable the next phase of comparative planetary science, also on a Galactic scale. We stress that the HRMOS effort would be mainly devoted to hot and warm giant planets, from sub-Saturns to super-Jupiters and brown dwarfs, and with partial sensitivity to Neptune-mass planets on short-period orbits. This approach is complementary to searches of Earth-like and habitable planets and detailed studies of exoplanet atmospheres.

**State of the art of Galactic exoplanets** At the time of writing, the NASA Exoplanet Archive reports more than 6,300 confirmed exoplanets<sup>1</sup>. These detections have been accomplished via a variety of methods, probing distances of up to 3–4 kpc in the case of transit surveys in the Kepler field, and typically 6–10 kpc toward the Galactic bulge for microlensing observations. In terms of Galactic altitude, the majority of the discovered systems lie close to the Galactic plane, the highest two systems being a microlensing (inner disc), and a radial velocity (outer disc) detection at about 3 kpc and 1.3 kpc above the Plane, respectively. So far, no searches outside the Milky Way have been performed.

**Diversity of planetary systems** This spatial coverage has enabled us to identify different classes of exoplanets, system architectures, and correlations between star and planet properties.

---

<sup>1</sup>June 2026 - source: <https://exoplanetarchive.ipac.caltech.edu>

Nonetheless, there are observational biases and hindrances, for instance the focus on nearby field/main sequence/single stars, which prevent us from establishing whether the Galactic planetary population as a whole is consistent with that observed in the Solar neighbourhood. Taking our own Solar System as an example, we know that the gas giants were born in a primordial disc, probably via the core accretion (CA) process, during the first 10 Myr (e.g. Pollack et al. 1996; Ida & Lin 2004, see Sirono & Turrini 2025 for the most recent dating of Jupiter’s formation at about 2 Myr and Bernabò et al. 2022 for the similar timescale revealed by protoplanetary discs). Over the next 10 – 100 Myr, the terrestrial planets built up from rocky debris through a process of accretion, agglomeration and punctuated by collisions (e.g. Morbidelli et al. 2012). Throughout this process and afterwards, it is likely that the orbital radii of the planets have changed and that the Solar System was strongly affected by external radiation and close encounters with other stars (e.g. Adams 2010; Pirani et al. 2019; Turrini et al. 2022; Rickman et al. 2023; Przyłuski et al. 2025). For many years, it has been quite clear that our planetary system cannot be considered the only typical outcome of planetary system formation pathways (e.g. Turrini et al. 2018, and references therein). Indeed, the discovery of thousands of planetary systems through transit and radial velocity surveys, but also direct imaging and microlensing, has uncovered a rich variety of properties (see Fig. 2.1), system architectures and chemical evidence in both star and planets, which demands explanation. The problem is inherently non-trivial, owing to the complex interaction of multiple factors that influence the present-day diversity of systems. In the following, we outline the key variables that may contribute to this complexity.

**Exoplanets in star clusters** Star clusters provide an important testbed for exoplanet studies, allowing us to explore how planetary systems form and evolve in different stellar environments. Early searches for exoplanets in stellar clusters yielded very few detections. The most prominent examples are the HST photometric campaigns targeting the globular clusters 47 Tucanae and NGC 6397, finding no close-in giant planets despite monitoring large stellar samples (Gilliland et al. 2000; Nascimbeni et al. 2012). These null results suggested that metal-poor and/or dynamically dense environments may suppress either the formation or survival of hot Jupiters<sup>2</sup>. Subsequent ground-based transit surveys targeted a number of open clusters, including NGC 2099 (M 37) (Hartman et al. 2009), NGC 2168 (M 35) and NGC 2158 (Mochejska et al. 2006; Nardiello et al. 2015), NGC 2682 (M 67) (Nardiello et al. 2016), NGC 1245 (Burke et al. 2006), NGC 7789 (Bramich & Horne 2006), and NGC 6791 (Bruntt et al. 2003; Montalto et al. 2007), among others. These surveys demonstrated that ground-based photometry can reach the precision required for transit detections in cluster environments, but produced only a small number of weak or unconfirmed candidates. Overall, they pointed toward a low occurrence rate of short-period giant planets in clusters.

This picture was later revised by RV surveys. The first planet discovered in an open cluster,  $\epsilon$  Tau b, was a long-period giant orbiting a red giant in the Hyades cluster (Sato et al. 2007). RV monitoring of M 67 main sequence and giant stars revealed several giant planets and suggested a hot-Jupiter occurrence rate of  $\sim 4\text{--}6\%$  in this intermediate-age (4.5 Gyr), solar-metallicity cluster (Pasquini et al. 2012; Brucalassi et al. 2014, 2017).

With the advent of space-based missions such as Kepler, K2, and TESS, the search for exoplanets in star clusters entered a new phase. Kepler revealed the first sub-Neptune planets in clusters, including NGC 6811, demonstrating that small planets can form and survive in cluster environments. K2 expanded the census to nearby young and intermediate-age clusters, including the Hyades, Praesepe, the Pleiades, Ruprecht 147, M 35, NGC 2158, and M 67 (e.g. Libralato et al. 2016a,b;

---

<sup>2</sup>Hot Jupiters are gas giant exoplanets with masses similar to Jupiter, orbiting very close to their host star (orbital periods of a few days)

Nardiello et al. 2016; Mann et al. 2017; Gaidos et al. 2017; Curtis et al. 2018). These discoveries enabled RV follow-up of both transiting and non-transiting cluster members, including the multi-planet system Pr 0211 in Praesepe (Malavolta et al. 2016).

In parallel, RV surveys of evolved intermediate-mass stars ( $>2 M_{\odot}$ ) in open clusters identified additional giant planet candidates and highlighted the importance of long temporal baselines to disentangle stellar variability from Keplerian signals (Lovis & Mayor 2007; Delgado Mena et al. 2018, 2023).

In the TESS era, dedicated projects such as PATHOS (A PSF-based Approach to TESS High quality data Of Stellar clusters) and CDIPS (the Cluster Difference Imaging Photometric Survey) have enabled systematic transit searches in crowded cluster fields, yielding tens of candidates and several confirmed planets, including TOI-837 b in the young cluster IC 2602 (Nardiello et al. 2019; Bouma et al. 2019; Barragán et al. 2024; Damasso et al. 2024). In parallel, spectroscopic programmes such as GAPS (Global Architecture of Planetary Systems) and THYME (TESS Hunt for Young and Maturing Exoplanets) have provided essential follow-up for validation and characterisation (Covino et al. 2013; Newton et al. 2019; Rizzuto et al. 2020; Carleo et al. 2021).

Despite recent progress, the current census of exoplanets in stellar clusters and moving groups remains highly incomplete and heterogeneous, with only  $\sim 346$  between planets and candidates currently listed in Gaia-based compilations (Dai et al. 2025). Noticeably, the number of confirmed planets in young clusters is extremely small. A complete and statistically robust census of exoplanets in stellar clusters is still lacking. Current surveys are limited by small sample sizes, heterogeneous selection functions, and restrictions to specific stellar populations and orbital regimes. A large-scale spectroscopic survey of cluster members, with high completeness within each cluster, is therefore still missing. Such a systematic investigation can only be efficiently achieved with a high-resolution, highly stable multi-object spectrograph capable of monitoring large stellar samples with the precision and temporal coverage required to derive unbiased occurrence rates across different cluster environments.

#### Key Questions:

- How do environment, density, metallicity, and stellar multiplicity affect the formation, occurrence, masses, and orbital architectures of giant planets?
- How do stellar evolution and dynamics shape the demographics of short-period giant planets, including deficit around evolved stars, potential engulfment or re-inflation processes?
- What chemical and debris signatures of planet formation and evolution—such as stellar pollution—can be detected in clusters versus field stars, and what do they reveal about planetary system architectures and dynamics?

## 2.2 Formation and evolution of planetary systems

Planetary systems are shaped by a complex interplay of processes spanning multiple scales, from the physical and chemical properties of protoplanetary discs to the broader stellar and Galactic environment. The formation, dynamical evolution, and survival of planets depend not only on their host stars but also on environmental effects. In crowded regions, close star–star encounters can perturb planetary orbits or truncate protoplanetary discs, while interactions with dense gas clouds

may alter stellar motions and local gravitational conditions. Strong radiation fields from massive stars and Galactic tidal forces can further influence disc evolution and the long-term stability of planetary systems. Understanding these factors is essential for constructing a comprehensive picture of planetary system architectures and their diversity across different environments and evolutionary stages.

### 2.2.1 The role of the environment in planetary formation

Conditions that favour or hinder planet formation are not determined solely within the protoplanetary disc itself; the wider environment surrounding the nascent planetary system also plays a key role in shaping its evolution.

Within a planetary system, the mass, accretion rate, temperature profile and dust-to-gas ratio of the native disc are key parameters in determining the incidence of giant, Neptunian and rocky planets around MS stars (Savvidou & Bitsch 2023). Alongside the physical properties of discs, their chemical composition plays a role in affecting the outcomes of planet formation. A higher overall metallicity is correlated with a greater incidence of giant planets (e.g. Fischer & Valenti 2005), particularly Hot Jupiters, typically exhibiting high surface temperatures ( $>1000$  K; e.g., Mayor & Queloz (1995)). However, the mass distribution of the planets, particularly the giant planets, is likely also shaped by the detailed relative abundances of the major elements contributing to solids. In particular, higher stellar abundances of oxygen have been shown to increase both the incidence of giant planets and the ratio between high-mass and low-mass giant planets (Biazzo et al. 2022; Filomeno et al. 2024). Although characterised by a lower incidence of giant planets, low metallicity stars host giant planets spanning most of the mass range observed around their higher-metallicity counterparts (Adibekyan 2019; Magrini et al. 2022; Tsantaki et al. 2025; Nguyen & Adibekyan 2025), raising the question of whether they form through different pathways (e.g. disc instability -DI- versus core accretion -CA) or reflect differing protoplanetary disc conditions. Also, in the regime  $[\text{Fe}/\text{H}] < -0.2$ , there are indications that host stars are, on average, more metal-poor than non-hosts; this suggests that, while planet formation is generally favoured at higher metallicities,  $[\text{Fe}/\text{H}]$  is not the dominant parameter governing planet formation in metal-poor environments, supporting the view that the overall metal content, rather than iron abundance alone, is the key factor in the formation of planets. Exploring these diverse contexts is, therefore, crucial for assessing the universality or not of the processes that shape planetary systems.

In addition to the imprint of the properties of their host stars (Pascucci et al. 2016; Testi et al. 2022), the properties of primordial discs may be significantly altered, or discs may be either dissipated or truncated, by the external radiation environment produced by nearby massive stars or by dynamical perturbations from close encounters with third bodies (e.g. Adams et al. 2004; Adams 2010; Turrini et al. 2022). As a consequence, two otherwise identical forming systems, one evolving in isolation and the other embedded in a dense stellar environment, would experience markedly different irradiation levels. These differences would naturally lead to distinct chemical structures -including vertical chemical stratification, radial compositional gradients, and snow lines- within the disc (Eistrup et al. 2016, 2018; Pacetti et al. 2022, 2025) and divergent disc-dissipation timescales, which would limit the temporal window to form planets and result in divergent mass distributions of the final planetary populations (Savvidou & Bitsch 2023). Also, planets forming or surviving in dense stellar systems may experience strong dynamical perturbations, including orbit reshaping, inward migration, or even planet exchange and ejection through close stellar encounters and tidal interactions (e.g. Davies et al. 2014; Hamers & Tremaine 2017). All these factors ultimately lead to the formation of planetary systems with different architectures, multiplicities and compositions around otherwise similar host stars.

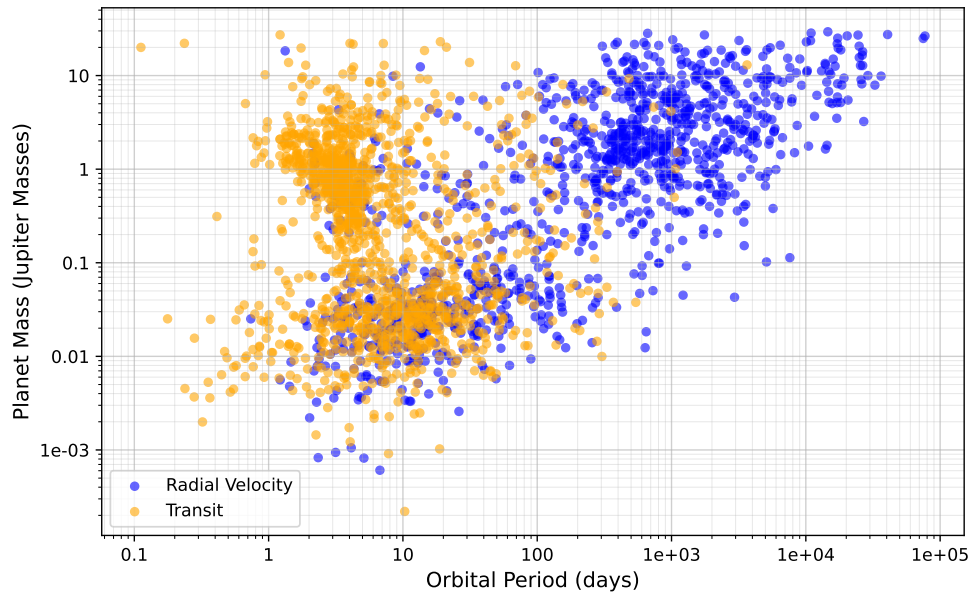


**Figure 2.1.** The planetary mass versus the orbital period for currently known exoplanets discovered either through the transit (orange) or Doppler techniques (blue) (NASA Exoplanet Archive, May 2026).

Even after their growth and accretion phases are finished, exoplanets still experience physical changes. Gas giants should cool and contract over billions of years (e.g. Fortney et al. 2007). Those that migrate close to their host stars may be subject to insolation and to inflation of their radius, or their atmospheres may be photo-evaporated, depending on their mass and the proximity of their orbit to the star (Fortney et al. 2007; Owen & Wu 2013). Whilst this latter process is likely accelerated by high levels of extreme and far ultraviolet radiation (EUV/FUV) when stars are young and fast-rotating, it may continue on Gyr timescales (King & Wheatley 2021).

### 2.2.2 Stellar evolution and the long-term evolution of planetary systems

Planetary systems evolve (Schmidt & Schlaufman 2026) and, as of today, more than one hundred planets orbiting stars ascending the RGB have been detected. When their host star(s) have sufficient initial mass, they leave the MS causing drastic changes in the dynamics and hence architecture of the systems. When stars evolve into the RGB, they cool down and undergo substantial envelope expansion while their cores contract. This, together with orbital evolution under the influence of tides, stellar mass loss and instabilities, can either cause the engulfment or disruption of those planets with insufficient mass and separation to avoid tidal engulfment (Villaver & Livio 2007; Mustill & Villaver 2012; Veras et al. 2020), and/or the ejections and/or collisions of planets (e.g., Debes & Sigurdsson 2002; Veras et al. 2011; Veras 2016; Mustill et al. 2018, and Columba et al. 2023 for the circumbinary case). One possible consequence of these severe events, is a deficit of short-period planets in this evolutionary phase (e.g., Xiao et al. 2024, and references there-in).

Nonetheless, surveying giant stars for planets offers a key advantage: detecting planets around relatively massive MS stars (from F to A spectral type) is intrinsically difficult, but these challenges can be mitigated by observing the stars after they leave the MS. As they evolve, their rotation slows due to angular momentum loss, leading to far more favourable conditions for detection. In addition, by that stage, stars have also cooled enough to develop a rich forest of spectral lines, enabling high-precision radial-velocity measurements. In this context, RV offers a clear advantage over the transit method too, given the lower probability of detecting transiting planets around giant

stars. Few planets have been detected around giant stars through the transit method (Lillo-Box et al. 2014; Jones et al. 2018; Saunders et al. 2025), yet they revealed a very interesting phenomenon of planetary radius “re-inflation” which deserves further study with larger samples.

The occurrence rate of giant planets increases with stellar mass up to intermediate-mass stars, peaking around  $1.5\text{--}2, M_{\odot}$  (Johnson et al. 2010; Jones et al. 2016a). Around evolved stars, giant planets are commonly found, with global occurrence rates of about 10% for giant stars in radial-velocity surveys (Wolthoff et al. 2022). However, this value depends strongly on sample selection, orbital period range, and planet mass limits. For low-luminosity red giant branch stars, occurrence rates of giant planets are typically in the range  $\sim 10\text{--}15\%$ , rather than significantly higher values (Jones et al. 2021; Wolthoff et al. 2022). These trends suggest that intermediate-mass stars provide favourable environments for the formation and detection of giant planets.

In parallel, theoretical and observational studies suggest that planets may be more likely to survive around compact binary systems than around single stars (Kostov et al. 2016), where survival rates reach 23%–32% around double white dwarfs (Columba et al. 2023). Yet, despite the sample of main-sequence circumbinary planets remains limited (e.g., Standing et al. 2023; Baycroft et al. 2025 for detections with RVs), their occurrence rates appear comparable to, or potentially higher than, those around single stars (Armstrong et al. 2014). Together, these findings underscore the need to broaden planet searches to include binary systems, particularly because such environments may even enable second-generation planet formation from common-envelope ejecta (Perets 2010; Ledda et al. 2023). Thus, surveying planetary systems around giant stars and binary stars together with detections in MS stars, is essential for establishing the observational constraints needed to decode how planetary architectures emerge, evolve, and persist across cosmic time.

### 2.2.3 The star-planet interplay

Exoplanets themselves may also influence the properties of the stars. Various differences in photospheric chemistry have been noted between stars with and without planets. For example, stars hosting hot Jupiters may be anomalously depleted in Li, but enhanced in C and N (e.g. Israelian et al. 2004, 2009; Delgado Mena et al. 2015; Gonzalez 2015; Suárez-Andrés et al. 2016, 2017; Spina et al. 2021). Although the latter may be simply connected with the overall correlation between metallicity and planetary incidence noted above, the former may be a more fundamental observation, showing that exoplanets may influence the internal mixing or even rotation rates of their stars via tidal interactions or interactions with the primordial accretion disc during star and planet formation (e.g. Bouvier 2008). There are suggestions of other more subtle anomalies in elements such as Al and Ba (Mishenina et al. 2016). Others have found evidence that planet-hosting stars can be more metal-rich than a binary companion, particularly in refractory elements (e.g. Saffe et al. 2017; Liu et al. 2018). This might indicate that the inward migration of planets can result in the accretion of rocky material or even the ingestion of planets during the star formation process. Star-planet interactions have also been suggested as means of altering the rotation and enhancing or suppressing magnetic activity in some stars that host hot Jupiters, either through tides or the interactions of their magnetospheres (e.g. Lanza 2009; Poppenhaeager & Wolk 2014; Pillitteri et al. 2014). A difficulty common to all these studies is firmly establishing the age of the star and obtaining a clear baseline level of chemical composition, rotation, and magnetic activity for similar stars without planets.

## 2.3 The potential of HRMOS

To explore the impact of birth environments on planet formation and evolution, HRMOS will exploit its RV precision to perform complete surveys of exoplanets in a diverse set of populations.

More specifically, HRMOS will allow, for the first time, systematic searches of high-mass planets in individual clusters (both open and globular ones), where stellar age and chemistry are tightly constrained, to isolate how stellar mass influences planet occurrence. By comparing multiple clusters with different properties (age, metallicity, density, mass), it will enable a detailed investigation of how planet demographics vary with those properties at fixed stellar mass. Finally, surveys of giant stars in the Bulge and nearby dwarf galaxies, will allow HRMOS to examine broader environmental drivers of planet formation and evolution.

**HRMOS in the 2035 landscape** By the time HRMOS achieves its first light, the exoplanet field will have been revolutionised by space missions such as *Gaia*, PLATO and the Nancy Grace Roman Space Telescope. Their observations will yield a groundbreaking number of planetary candidates, enhancing our understanding of planetary classes, and planetary system architectures. Indeed, by 2035, PLATO mission will have surveyed bright FGK stars in the field and in selected clusters with long, nearly continuous monitoring. Synergies between PLATO and 4MOST will enable the characterisation of planetary host stars, as well as the broader PLATO target sample.

*Gaia* will have delivered the first comprehensive astrometric census of giant planets around stars brighter than  $G=16$ ; and Roman will have discovered  $\sim 6 \times 10^4 - 2 \times 10^5$  transiting planets in the Bulge at near-IR wavelengths. Yet, on the one hand, key questions will remain unresolved in crowded environments (Bulge, open and globular clusters, dwarf galaxies) due to geometric bias, magnitude limits, crowding and incomplete samples. On the other hand, HRMOS will remain indispensable for confirming the candidates (particularly for *Gaia* DR5, but also for PLATO), determining precise elemental abundances of host stars – pivotal for tracing planetary migration histories– discriminating against false positives, and monitoring the long-period orbits of planets detected by *Gaia*.

## 2.4 Simulations and feasibility

### 2.4.1 Expected Detectability with HRMOS

This section presents the expected detectability of exoplanets with HRMOS, based on simulations that account for instrumental stability and observational strategy. We estimate the sensitivity to short-period giant planets and the limiting magnitudes for different spectral types, providing guidance for target selection in clusters.

Simulations assume an instrumental velocity stability of either  $10 \text{ m s}^{-1}$ , representing a more favourable scenario with respect to the conservative  $20 \text{ m s}^{-1}$  value adopted for the instrumental error in the error budget estimate (Sect. 1.3.8), or  $30 \text{ m s}^{-1}$ , representing an extreme assumption; a simple sampling strategy of 30 observations spread over 300 days and random offsets to reduce aliasing is adopted. We consider  $1 M_{\odot}$  and  $0.5 M_{\odot}$  cluster stars, with two spot-activity models: a solar-maximum type appropriate for stars of 1 – 5 Gyr, and a “super solar maximum” model for younger stars (Barnes et al. 2011), using spot/photosphere temperature ratios from Berdyugina et al. (2008). Spots on lower-mass stars are distributed over the entire surface, while solar-mass stars have spots concentrated at low and intermediate latitudes. The resulting RV jitter ranges from  $1.5 - 7 \text{ m s}^{-1}$  for  $0.5 M_{\odot}$  stars to  $7 - 44 \text{ m s}^{-1}$  for  $1 M_{\odot}$  stars, added to the instrumental noise. Fig. 2.2 illustrates the regions where exoplanets are detectable at a 0.1% false-alarm probability for

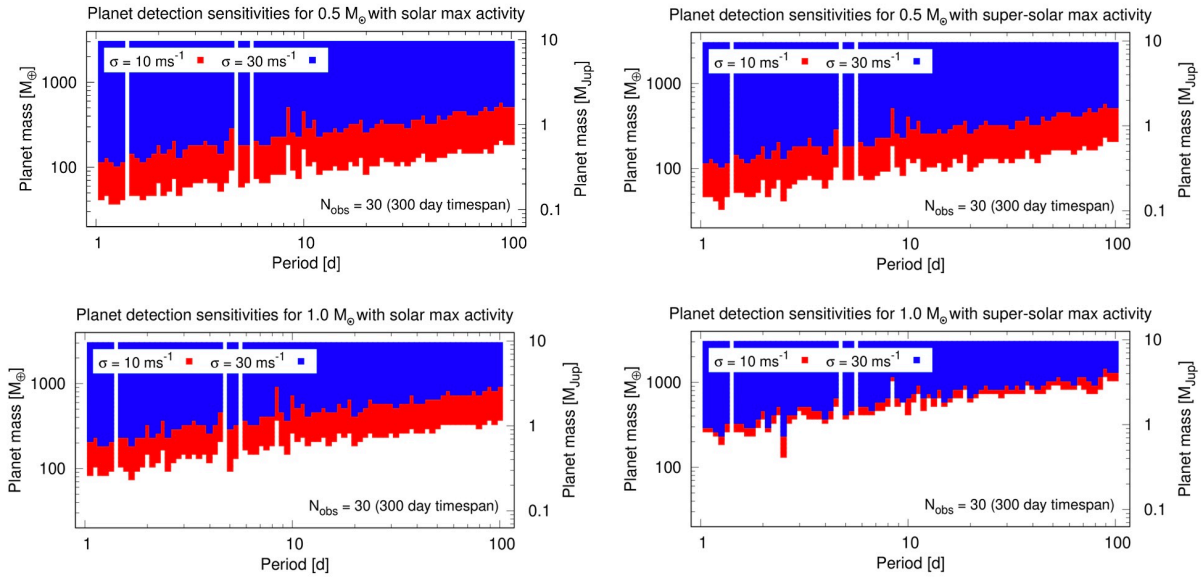


**Figure 2.2.** Simulations illustrating the regions where exoplanets become detectable with a 0.1% false alarm probability. The four simulations are labelled with the mass of star considered and the level of starspot activity assumed. In each panel, regions are shown corresponding to instrumental velocity noise of  $10 \text{ m s}^{-1}$  and  $30 \text{ m s}^{-1}$  respectively.

these conditions. An instrumental stability of  $10 \text{ m s}^{-1}$  allows detection of planets  $> 1 M_J$  over 1–100 days, and down to  $\sim 0.3 M_J$  at the shortest periods, fully exploring the region inaccessible to *Gaia* and the Nancy Grace Roman Space Telescope.

The photon-limited RV precision for different spectral types is estimated using the formula of Bouchy et al. (2001),  $\Delta RV = c/(Q\sqrt{N})$ , where the “quality factor”  $Q$  depends on spectral type, wavelength, resolving power, and rotational broadening. Table 2.1 gives the limiting  $G$  magnitudes for slowly rotating stars, of solar metallicity, that yield  $\sim 5 \text{ m s}^{-1}$  precision in a 1-hour exposure with HRMOS. The contributions to the uncertainty from all three HRMOS wavelength bands are combined with variance weighting. Faster rotators have lower limiting magnitudes due to smaller  $Q$ , and the required SNR increases approximately as  $v \sin i / (2 \text{ km s}^{-1})$ . For solar-type stars, the median  $v \sin i$  is assumed to scale as  $v \sin i \sim 2(\text{Age}/4 \text{ Gyr})^{-0.5} \text{ km s}^{-1}$ , which significantly reduces the corresponding photon-limited magnitude limit for a ZAMS stars (100 Myr) with median  $v \sin i \simeq 12 \text{ km s}^{-1}$ , as shown in Table 2.1.

These calculations indicate that slow-rotating solar-type and K-type targets should be brighter than  $G \sim 17$  to fully exploit a  $10 \text{ m s}^{-1}$  instrumental stability, with brighter limits for hotter stars and much brighter limits for young, fast-rotating stars, although the latter will be more constrained by activity-related sources of RV jitter. Chapter 11 discusses the potential targets in both open and globular clusters, and the magnitude ranges they span.

#### 2.4.2 HRMOS-like spectra translator

In this section, we present a simulator of HRMOS-like spectra, and we perform tests on real spectra to evaluate the performance of HRMOS in terms of RV precision. High-resolution spectrographs like HRMOS are designed to deliver high precision in stellar spectroscopy, enabling breakthroughs in fields such as exoplanet detection and stellar physics. However, before the instrument becomes operational, it is essential to develop and validate analysis tools and pipelines using realistic test data. To address this need, we have implemented a simulation module that generates HRMOS-like

**Table 2.1.** The limiting  $G$  magnitude for slowly rotating targets of various spectral types, that can yield a photon-limited velocity precision of  $\sim 5 \text{ m s}^{-1}$  (using data from all three arms) in a 1-hour exposure with HRMOS. The SNR columns give estimated peak values in the blue, green and red arms respectively. A further row gives an estimate for faster-rotating ZAMS solar-type stars with median  $v \sin i \simeq 12 \text{ km s}^{-1}$ .

Spectral type	SNR(B)	SNR(G)	SNR(R)	$G_{\text{lim}}$ [mag]
F2	30	50	60	15.8
G0	15	25	30	16.9
K5	8	20	32	17.2
G0 (ZAMS)	70	150	190	13.7

spectra (at current design) both from synthetic spectra and existing high-quality observations obtained with instruments such as ESPRESSO and HARPS. By transforming real spectra into a format that mimics HRMOS characteristics such as resolution, wavelength coverage, and SNR distribution, this approach provides a practical framework for testing algorithms, assessing expected performance, and refining observational strategies ahead of HRMOS deployment, in particular for exoplanet detections.

The module (in development) converts 1D echelle spectra from ESPRESSO or HARPS into a simulated HRMOS-like product. Starting from 1D FITS inputs (wavelengths in air/vacuum, flux, error, quality), it infers the original resolving power from the instrument-mode header, then degrades the spectrum to the HRMOS resolution ( $R=80,000$ ) by applying the additional Gaussian broadening. The broadened spectrum is split into four predefined HRMOS bands (B, G, R1, R2; two bands in red are included for testing purposes since it is useful to compare the results when using each different R band, moreover, the G-band is slightly shifted for HARPS data to avoid the detector gap that falls in the HRMOS defined G-band). All these bands are then interpolated onto an HRMOS-like wavelength grid whose step is defined to have the expected mean sampling of  $\sim 2.7$  pixels per resolution element. A simple curved blaze profile is applied per band to emulate order-throughput variations, and the code injects Gaussian noise to reach target per-band SNR: the user specifies a reference (interpreted as the peak SNR that is observed in the red band). This is scaled to the other bands via fixed SNR ratios expected for solar type stars following the current exposure time calculator for the HRMOS. The additional noise is added in quadrature to the original errors, so the achieved per-pixel SNR follows the intended blaze-modulated profile without creating negative variances.

The output is a multi-extension FITS file containing one binary table per band with wavelength, flux, error, blaze, dll (per-pixel spectral width) and quality (currently zeros: assuming so far perfect quality data), plus relevant headers ( $R=80,000$ ,  $\text{PixSamp}=2.7$ , and the band SNR target). The implementation is modular for its core steps (convolution, grid generation, blaze model, SNR computation, and noise injection) which are encapsulated in small functions allowing components such as the blaze model, noise law, or grid generator to be swapped or refined with minimal impact on the overall pipeline.

To validate radial velocity extraction methods for HRMOS, the simulated spectra produced by the HRMOS-like translator are processed using an Interpolated Cross-Correlation Function (iCCF<sup>3</sup>). This approach mirrors the standard procedure applied to the ESPRESSO data, ensuring consistency in methodology and enabling a more direct comparison of performance between original data and simulated/translated data. The iCCF algorithm operates on HRMOS-like spectra

<sup>3</sup><https://github.com/j-faria/iCCF>

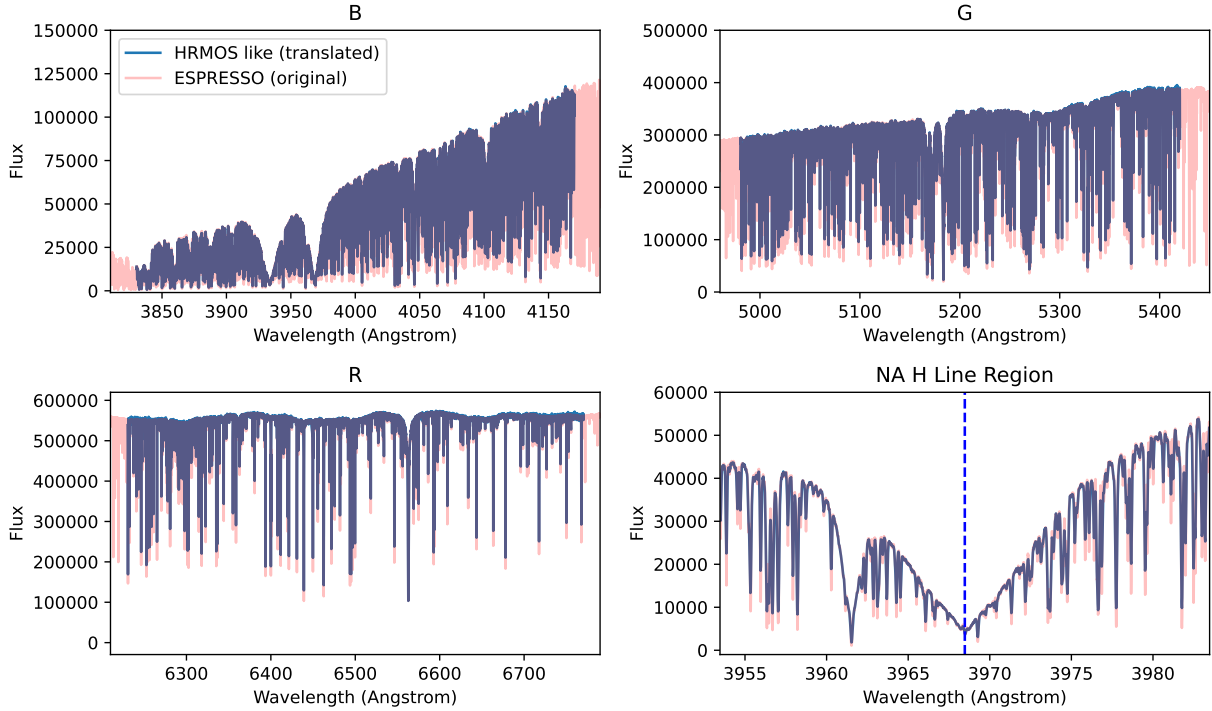


**Figure 2.3.** Comparison between original ESPRESSO spectra (an observation from Tau Ceti) and HRMOS-like simulated spectra across different wavelength regions. The panels illustrate: B-band (top left), G-band (top right), R-band (bottom left), along with a zoomed-in view of the Sodium (Na) H line region (bottom right). Flux values are shown as a function of wavelength (in  $\text{\AA}$ ), highlighting the resolution degradation and band segmentation applied during the HRMOS simulation process.

by correlating them with a predefined stellar mask—currently adopted from ESPRESSO, allowing the derivation of precise radial velocities and associated uncertainties.

The choice of iCCF methods over the traditional CCF approach is motivated by their improved handling of line asymmetries and their more accurate modelling of the correlation profile, which can lead to enhanced radial velocity precision, particularly for high-resolution spectra. By applying the same mask and correlation strategy used for ESPRESSO, the pipeline provides a realistic benchmark for HRMOS performance under comparable observational conditions. This step is essential for assessing the impact of spectral resolution, wavelength coverage, and signal-to-noise ratio on RV precision.

To assess the RV precision achievable with HRMOS-like observations, we selected Tau Ceti, a well-known RV standard star widely used as a benchmark due to its exceptional long-term stability. We retrieved a set of high-SNR ESPRESSO reduced spectra for which we selected nine observations. These high-quality spectra were used as input for the HRMOS spectral simulator, allowing us to generate realistic HRMOS-like datasets under controlled conditions. In particular, we produced two sets of simulated spectra with peak SNR values of approximately 50 and 100. The simulated spectra were then analysed using the iCCF pipeline, restricting the computation to the three wavelength bands accessible to HRMOS (B, G, and R2). From this analysis, we derived RV measurements and their corresponding uncertainties for each observation. The original ESPRESSO RVs and uncertainties were also retained for comparison. The results, summarized in Figure 2.4, aim to evaluate the expected RV precision for HRMOS observations at different SNR levels, using Tau Ceti as a stable reference. In the text box within the figure we also show the standard deviation of the calculated RVs, as well as the average of the derived uncertainties for the two cases of SNR

an the original ESPRESSO uncertainties. As expected, the RV uncertainties scale with SNR, with higher SNR spectra yielding significantly improved precision. The systematic offset is observed between the RVs derived from ESPRESSO and those obtained from the simulated HRMOS spectra. This behaviour is anticipated and can be explained by at least two main factors: (i) the HRMOS analysis uses a reduced spectral wavelength coverage compared to ESPRESSO, and (ii) differences in flux distribution across the spectral range effectively introduce different weightings in the CCF, naturally producing small shifts in the measured RVs. Despite these differences, the achieved RV precision remains within the expected performance regime, reaching uncertainties below  $\sim 8 \text{ m s}^{-1}$  even for  $\text{SNR}=50$ , and improving significantly at higher SNR. In addition, we should consider that Tau Ceti is more metal-poor than the Sun, and thus exhibits fewer spectral lines for radial velocity measurements. Metal-rich stars generally allow higher RV precision due to the larger number of usable absorption lines.

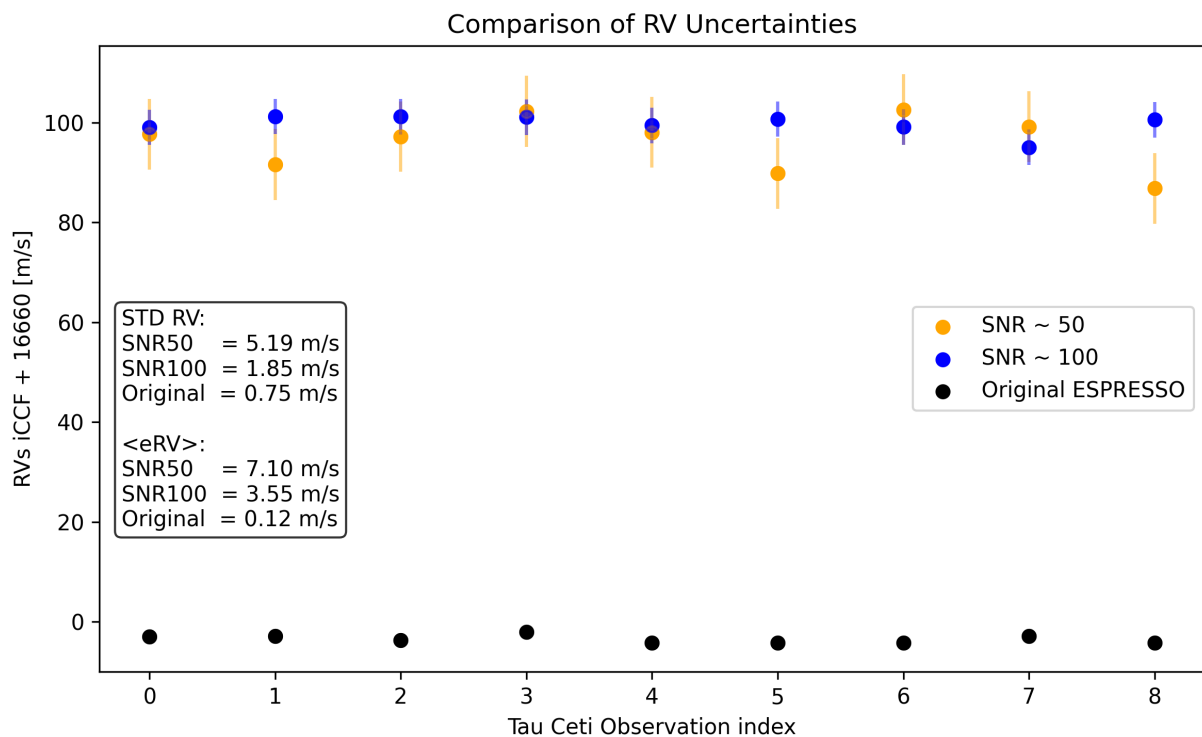


**Figure 2.4.** Comparison between the uncertainties obtained in the analysis of the original ESPRESSO spectra of Tau Ceti (black dots) and HRMOS-like simulated spectra at  $\text{SNR} = 50$  (yellow dots) and  $\text{SNR} = 100$  (blue dots). The panel shows the resulting RV uncertainties: STD RV is the standard deviation of the RVs for each observation, while  $\langle eRV \rangle$  is the average of the uncertainties of RVs for each observation. Note that the RV values and respective uncertainties were computed using iCCF (for the HRMOS simulated spectra), while the "Original" are the RV values and uncertainties from the ESPRESSO data reduction pipeline.

### 2.4.3 Young stars: RV simulations and activity de-trending

To demonstrate our ability to detect and confirm extrasolar planets also around young stars, i.e. including the most challenging cases in which stellar magnetic activity may obscure or mimic planetary signals, we conducted a series of analyses based on real observations gathered with ESPRESSO. With this approach, we do not have to rely on any assumption about the coverage and size of active regions on a star, the rotational period of the star, the reliability of the measurement and modelling of activity indexes, and ultimately, the effect of the stellar activity on the measured

RV. We can also reliably estimate the effect of the spectral range and resolution of HRMOS on the RV measurements. Furthermore, this approach naturally accounts for realistic scheduling constraints for HRMOS, as the observations were obtained with the same telescope expected for HRMOS. For this analysis, we selected two targets with candidate planets discovered by space photometry and thus targeted for an RV follow-up. The first star is TOI-451, a 120 Myr-old late-G dwarf in the Pisces-Eridanus stream known to host three sub-Neptunes (Newton et al. 2021). The second star is K2-136, a K5V 650 Myr-old late-K dwarf in the Hyades hosting two sub-Neptunes and an Earth-like planet (Mann et al. 2018; Mayo et al. 2023). We downloaded the ESPRESSO data from the ESO archive and processed them to lower the resolution and spectral range in accordance with HRMOS specifications. We then extracted the RV using the robust and well-established Cross-Correlation Function technique (Baranne et al. 1996; Pepe et al. 2002), and the chromospheric Ca II H & K (Duncan et al. 1991) and H $\alpha$  (Gomes da Silva et al. 2021, 2022) flux measurements as proxies for the stellar activity of the targets. We refrained from the use of CCF asymmetry indicators, such as the Bisector Inverse Span or the FWHM of the CCF (e.g., Queloz et al. 2001), as they require instrumental ultra-stability in order to clearly disentangle instrumental and stellar effects, while the chromospheric indexes can be reliably measured even for un-stabilised instruments (e.g., as done with the HIRES spectrograph, Vogt et al. 1994). After applying this procedure, the median RV error is  $19 \text{ m s}^{-1}$  for TOI-451 and  $12.5 \text{ m s}^{-1}$  for K2-136, compared to a RV scatter (mostly due to activity) of  $50 \text{ m s}^{-1}$  and  $15 \text{ m s}^{-1}$ , respectively. The observed scatter is consistent with the activity level expected for the age of these stars. Our goal is to determine whether HRMOS can detect a planetary companion with 30 observations over a reasonable time range. For TOI-451, we randomly selected 30 ESPRESSO observations, excluding additional observations taken on the same night. For K2-136, we only have 20 ESPRESSO observations at our disposal, so we artificially extended the dataset by randomly selecting 10 observations from the sample, and temporally displacing them to a multiple of the rotational period of the star (assumed at 13.0 days) while keeping the original cadence, in order to preserve the stellar activity signal (i.e., avoid loss of coherence in the red noise). The activity signal was modelled using a multivariate Gaussian process (Rajpaul et al. 2015) encompassing the RV, Ca II H&K S-index, and H $\alpha$  index. This approach has been successfully applied to several stars younger than 1 Gyr, yielding mass measurements with precision comparable to or better than other techniques (e.g., Barragán et al. 2019; Nardiello et al. 2022; Mantovan et al. 2024). We performed our analysis in a Bayesian framework using the publicly available code PyORBIT (Malavolta et al. 2016, 2018).

For the sake of generality, a uniform prior was assumed for the stellar rotation period. However, gyrochronology relations and ground- or space-based photometry can in principle be used to constrain the rotation period a priori, thereby improving the detection sensitivity. Uninformative priors were used for all other parameters. For our test, we did not try to model the known transiting planets, so that their contribution to the radial velocity acts as an additional noise; given the different periods of the planets, their expected RV semi-amplitude up to  $5 \text{ m s}^{-1}$ , and the random sampling of the observations, these unmodelled signals can be interpreted as random noise arising from instrumental instability. To compute the detection map from the simulated dataset, we modelled the simulated RV measurements with a circular planetary signal jointly with the stellar activity model. Since we aim to recover a planet in a dataset that does not contain any planetary signal (as the transiting planets are undetectable because their RV semi-amplitudes are smaller than the measurement uncertainties), the posterior distribution of the planetary parameters provides a direct estimate of the detection limits of the dataset. Specifically, the number of samples falling into a mass-period bin, normalised by the number of samples across all masses over the period bin, will tell us the probability that a signal due to the noise could be interpreted as a planetary signal.

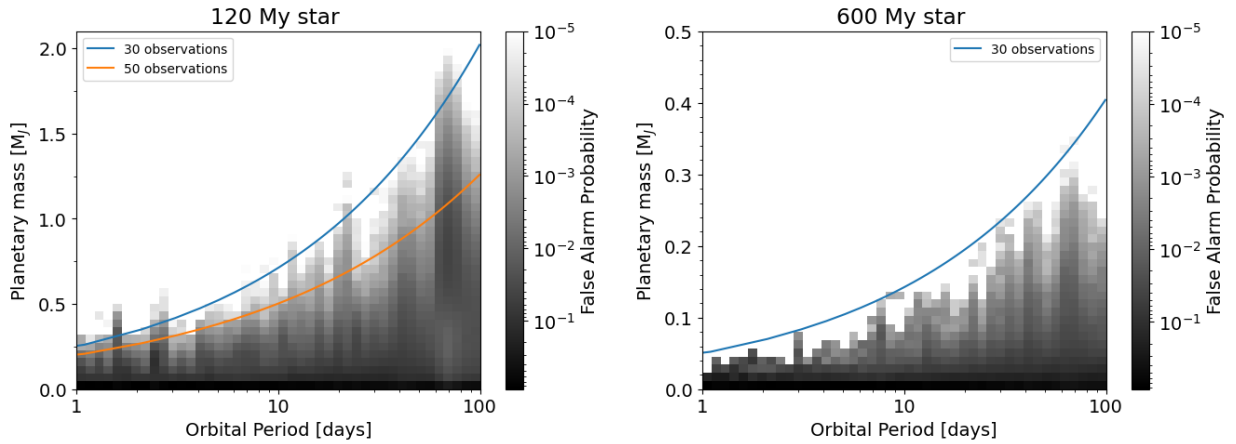


**Figure 2.5.** *Left:* False Alarm Probability of detecting a planet around a single star with age of 120 Myr and no planetary companions, based on 30 observations simulated using a real ESPRESSO dataset. The blue and orange lines represent an analytical approximation to the 0.1% FAP from 30 and 50 observations, respectively. *Right:* Same as in the left plot, using as a baseline ESPRESSO observations of a 600 Myr star.

The FAPs (False Alarm Probability) as a function of planetary period for the two cases considered in this analysis are reported in Fig. 2.5. The blue line represents an analytical approximation for the 0.01% FAP threshold, roughly corresponding to a solid detection at a  $4\text{-}\sigma$  level. For the 120 Myr case, we reported the same curve after adding 20 more observations to the original 30. For stars of about 600 Myr, with a modest investment of time, we are already able to explore the hot-Jupiter regime down to Saturn-mass planets at shorter periods, while we can confidently detect warm Jupiters and brown dwarfs at larger separations. For a slightly older star, HRMOS will be able to confidently detect either hot or warm sub-Saturn-mass planets, where ‘hot’ refers to orbital periods of a few days (typically ( $P \leq 10$  days)) and ‘warm’ to intermediate-period planets with  $10 \text{ days} \lesssim P \lesssim 100$  days.

## 2.5 Expected Scientific Outcomes

As anticipated, HRMOS will allow unique surveys of star clusters that offer an ideal laboratory to explore how planetary systems’ properties depend on their birth environments. Building large, homogeneous samples with well-determined ages, masses, densities, and chemical compositions is therefore essential for testing competing models of planet formation and evolution and for empirically constraining the timescales of key physical processes. In this section, we outline the key scientific products that HRMOS will deliver in the field of exoplanetary science.

### 2.5.1 Environmental dependence of planet formation rates at Galactic scale

The comparison of the occurrence rates of planets with the predictions of planetary population synthesis models is a crucial step to validate our global understanding of how planets and planetary systems form (see Burn & Mordasini 2024, and references therein). The demographics of giant planets in clusters spanning a range of ages and compositions will therefore constitute a major scientific product of HRMOS, providing a transformative view of planet formation across the Galaxy.

The generally accepted pathway for the formation of giant planets is core accretion (CA) (e.g. Helled et al. 2014, and references therein). In this framework, giant planets originate from the growth of solid cores through the accretion of pebbles and planetesimals embedded in protoplanetary discs.

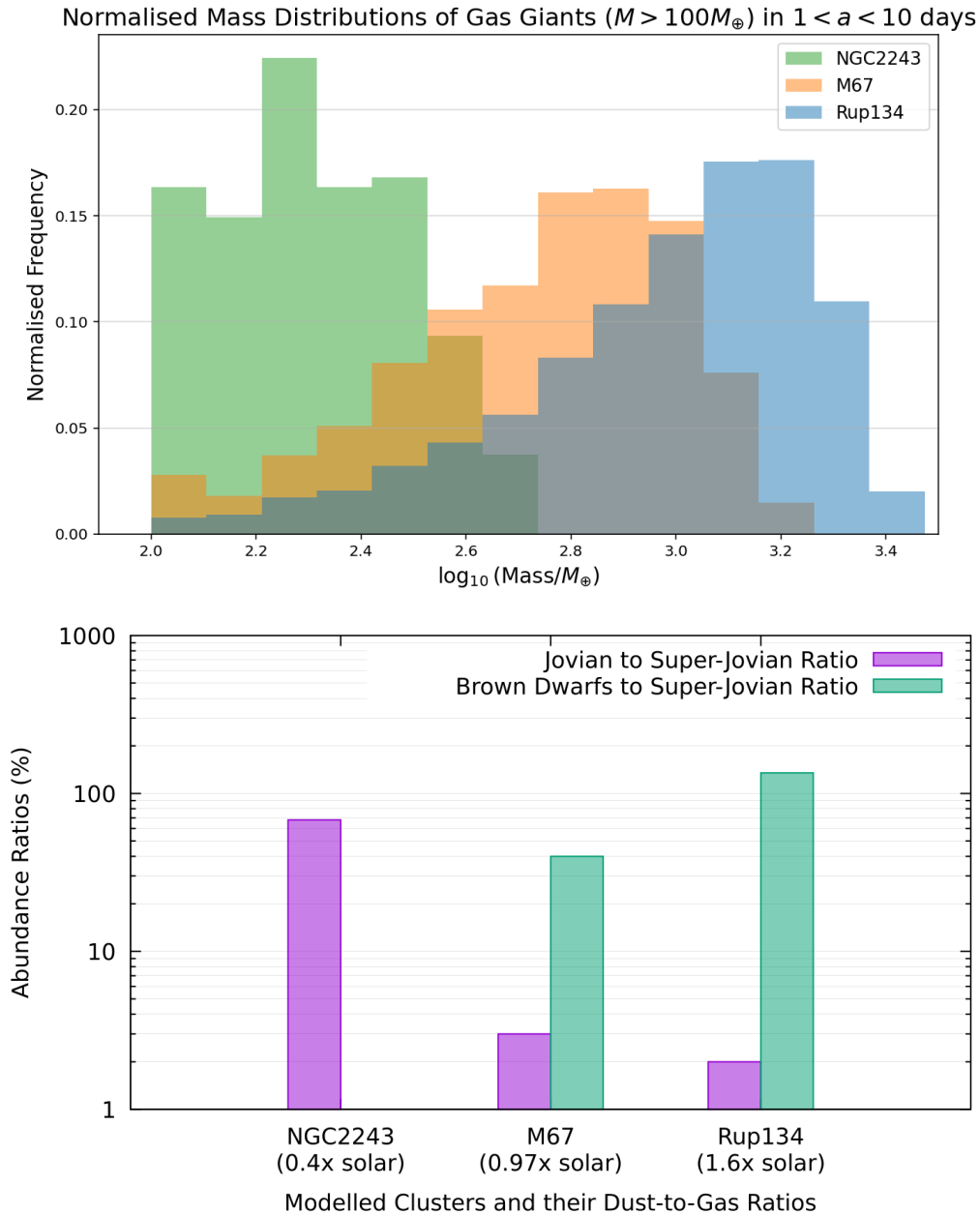


**Figure 2.6.** Predicted environmental dependence of the giant planet formation efficiency. *Top:* normalised mass distributions of giant planets with mass greater than  $0.3 M_J$  and orbiting at periods comprised between 1 and 10 days from the planetary population synthesis simulations performed for the three representative clusters NGC 2243, M67 and Rupercht 134 considering a  $0.05 M_{\odot}$  solar nebula-like disc (see main text for details). *Bottom:* relative abundance ratios of the synthetic giant planets orbiting at periods comprised between 1 and 10 days formed in the three clusters when considering a more massive  $0.1 M_{\odot}$  disc (see main text for details) after grouping each population into two mass classes: from Jovian planets ( $0.3\text{-}3 M_J$ ) to super-Jovian planets ( $3\text{-}13 M_J$ ) and from super-Jovian planets to brown dwarfs ( $> 13 M_J$ ).

Once the cores reach sufficient mass, they begin to accrete gaseous envelopes. As the envelope mass becomes comparable to that of the solid core, the system enters a runaway gas accretion phase, allowing the planet to rapidly grow to masses of several hundred to a few thousand Earth masses.

A key prediction of CA models is that higher metallicity environments, with a larger reservoir of solid material, promote faster core growth and therefore a higher efficiency in forming giant

planets. Conversely, low-metallicity environments inhibit solid accretion, leading to reduced formation efficiency and typically lower-mass giant planets. These trends are robust across CA variants, independently of whether growth is dominated by planetesimal or pebble accretion.

In contrast, disk instability (DI) models predict a much weaker dependence on metallicity. In this scenario, giant planets form via gravitational fragmentation of the gaseous disc, with the efficiency of collapse regulated primarily by disc mass and cooling timescales rather than the solid content. As a result, DI is generally expected to produce giant planets with little or only a weak dependence on metallicity. If anything, a mild increase in formation efficiency toward lower metallicity may arise in lower-opacity discs. However, DI is thought to preferentially form planets at wide orbital separations, and the occurrence of close-in giant planets would typically require subsequent inward migration or dynamical evolution.

Figure 2.6 illustrates these trends and their implications for the mass distributions of giant planets in the three clusters NGC 2243, M67, and Ruprecht 134, with metallicities  $[Fe/H] = -0.45$ ,  $0.0$ , and  $+0.27$ , respectively. For each cluster, we adopted elemental abundances from the *Gaia*-ESO Survey (Randich et al. 2022) for the main rock- and ice-forming species (Fe, Mg, Si, O, C, and N; see Lodders 2010) to derive the corresponding dust-to-gas ratios following Turrini (2023). Planetary population synthesis calculations were then performed using the pebble and gas accretion models of Polychroni et al. (2023) and Ledda et al. (2023), following the methodology of Naponiello et al. (2025). In each case, we considered solar-mass host stars embedded in protoplanetary discs with masses of  $0.05$  and  $0.1 M_{\odot}$ , consistent with observed star–disc scaling relations (Testi et al. 2022). The left panel of Fig. 2.6 shows the normalised mass distributions of giant planets ( $100\text{--}3000 M_{\oplus}$ ) for the  $0.05 M_{\odot}$  disc case. The distributions clearly shift toward higher masses with increasing metallicity and dust-to-gas ratio, although this is not the only systematic trend.

The distributions themselves, hence the planets in different mass ranges, change as a function of the cluster metallicity. The right panel of Fig. 2.6 quantifies this effect in the case of the  $0.1 M_{\odot}$  disc, grouping each planetary mass distribution in three intervals: Jovian planets ( $0.3\text{--}3 M_{J}$ ), super-Jovian planets ( $3\text{--}13 M_{J}$ ) and brown dwarfs ( $> 13 M_{J}$ ). For this example, we focus on the more massive disc since, as shown by the left panel of Fig. 2.6, the solar nebula-like one does not form brown dwarfs by core accretion at any metallicity value. The relative abundance of Jovian planets with respect to Super-Jovian planets decreases for increasing metallicity/dust-to-gas ratio values. In parallel, the abundance of brown dwarfs grows faster than that of super-Jovian planets, meaning that the ratio increases proportionally to metallicity. Differently from its higher-metallicity counterparts, NGC 2243 appears to be less efficient at forming giant planets via core accretion, likely as a consequence of its low metallicity. Should populations of brown dwarfs be observed around such low metallicity stars, their existence may indicate either that these objects did not form by core accretion or that our models are not sufficiently complete to capture their formation. As introduced in Sect. 2.1, in fact, our body of knowledge on planetary formation is shaped by our studies of the Solar System and, more recently, the solar neighbourhood. As a result, while it is expected to adequately describe planet formation as it occurs now in our Galaxy, it is not validated to describe planet formation at earlier galactic ages when it was occurring in markedly lower metallicity environments and other pathways, like the direct collapse of clumps of disc gas into planetary objects as prescribed by disc instability (DI) scenarios (e.g. Helled et al. 2014, and references therein), could have proven more efficient in producing giant planets and brown dwarfs. Furthermore, the vast majority of planet formation studies focuses on isolated protoplanetary discs around solar metallicity stars, which means we cannot directly apply the understanding we derive from them to crowded environments like clusters without expanding and consolidating it on a representative observational basis. The homogeneously characterised populations of giant planets

in clusters of different ages and chemical environments delivered by HRMOS will enable us to build the first general theory of planet formation across space and time in our Galaxy.

### 2.5.2 Observational constraints of planetary systems evolution

More in general, the capabilities of HRMOS will allow us to probe planets around stars spanning a wide range of ages and environments, from pre-MS stars—where giant planets can be detected in the most favourable cases, provided stellar activity can be mitigated and the sampling is sufficient—to evolved giant stars, revealing how system configurations shift as their hosts age and evolve. By enabling the detection of subtle dynamical features and expanding the census of planets in regimes that have been poorly sampled so far e.g., open clusters and the bulge, HRMOS will provide the statistical depth required to identify genuine evolutionary trends rather than isolated cases. In turn, this enlarged and more complete demographic landscape will allow us to chart the pathways through which planetary systems form, reshape themselves, and ultimately die.

## 2.6 Potential targets

In this section, we highlight selected aspects relevant to the selection of targets for detecting planetary systems across different environments. The discussion of a potential observational strategy is presented in Chapter 11. HRMOS is expected to observe a wide variety of open and globular clusters, crowded bulge fields, and fields in nearby satellite galaxies, spanning stars of a variety of evolutionary stages.

### 2.6.1 Stars in open clusters

As anticipated in Sect. 2.4.1 the observational strategy would typically involve 30 monitoring observations per cluster field over a period of a few years, targeting MS stars and searching for planets with periods up to  $\sim 100$  days. Beyond this range, the massive planet population is likely to be efficiently probed by *Gaia* astrometry, which, however, need a RV follow up to be confirmed. HRMOS can also perform a survey of thousands of G/K-type giants in open clusters down to  $G \sim 17$ , corresponding to distances of  $\sim 5\text{--}10$  kpc for red clump stars in the Galactic disc. The RV precision of these observations will be similar (or slightly better; e.g. Sozzetti et al. 2006) to that achievable for K dwarfs of comparable brightness (see Table 2.1), although the RV amplitudes for a given planet mass are smaller due to the higher stellar mass.

Figure 2.7 shows a simulation of the detection sensitivity, assuming an instrumental precision of either  $10 \text{ m s}^{-1}$  (the HRMOS requirement) or  $30 \text{ m s}^{-1}$  (conservative results for active/rotating stars), and that the giant contributes no intrinsic RV noise—which is unrealistic but could be partially mitigated through modelling and subtraction. The adopted sampling consists of 14 observations uniformly distributed over the first year, followed by 4 observations per year over the next 4 years, forming a 5-year monitoring programme. Figure 2.7 demonstrates that detecting a substantial fraction of the exoplanet population around giant stars requires a precision of  $10 \text{ m s}^{-1}$ , particularly for orbital periods longer than 100 days.

These detections (and non-detections), when obtained from complete and unbiased samples of cluster member stars with different properties, can provide direct constraints on the occurrence rates of giant planets and hence on the underlying planet formation mechanism. For instance, as described above, within the CA framework, a strong positive correlation with stellar metallicity is expected. Consequently, the giant planets' fraction is anticipated to be highest in the metal-rich cluster ( $[\text{Fe}/\text{H}] \sim +0.5$ ), of order  $\sim 3\text{--}5\%$ , decreasing to  $\sim 1\text{--}3\%$  at solar metallicity ( $[\text{Fe}/\text{H}] \sim 0$ ),

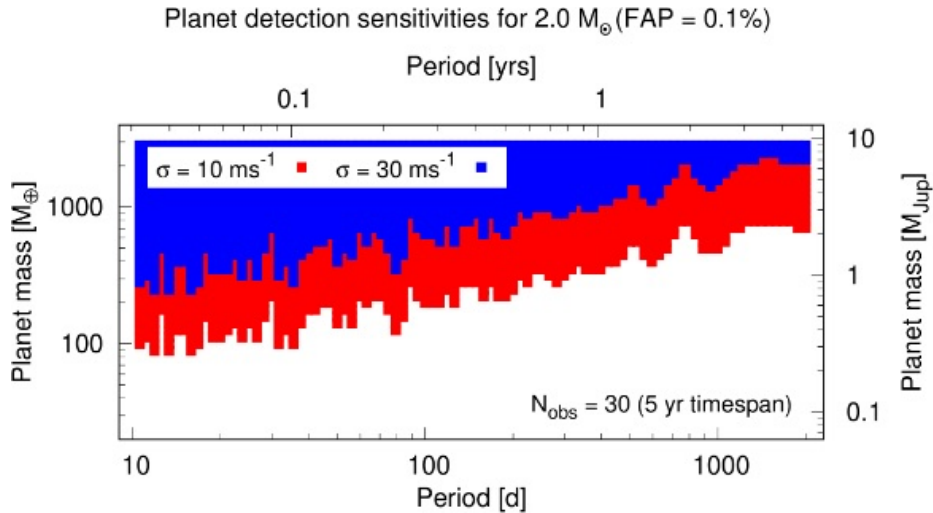


**Figure 2.7.** Detection efficiency (with a 0.1% false alarm probability) for exoplanets orbiting a  $2 M_{\odot}$  giant star. The proposed 30 observations are distributed over a 5-year period as described in the text. Simulations assuming instrumental velocity precisions of  $10 \text{ m s}^{-1}$  or  $30 \text{ m s}^{-1}$  are shown.

and dropping further to  $\lesssim 1\%$  in the metal-poor cluster ( $[\text{Fe}/\text{H}] \sim -0.5$ ), where the reduced solid content strongly inhibits efficient core growth and subsequent gas accretion.

To probe differences between CA and DI models, and the dependence of exoplanet populations on metallicity, age, and environment in a statistically robust way, we require a sample of well-populated clusters with at least 100–200 FGK stars per cluster, spanning a wide range in cluster properties. In particular, to investigate metallicity trends, one would need complete samples of  $\sim 1000$ – $2000$  stars per metallicity bin, corresponding to  $\sim 5$ – $10$  clusters per bin depending on cluster richness. Some examples of well-studied open clusters with Gaia-based membership and well-populated sequence in the FGK regime (both dwarfs and giants with  $G < 16.5$ ) include NGC 2243, Trumpler 5, Berkeley 36, and Berkeley 32 in the metal-poor regime ( $[\text{Fe}/\text{H}] \approx -0.5$  to  $-0.3$ ); NGC 2158, NGC 6633, NGC 2360, NGC 2682 (M67), and NGC 2539 in the intermediate regime ( $[\text{Fe}/\text{H}] \approx -0.3$  to  $0.0$ ); and NGC 6705, NGC 6583, Trumpler 20, and Berkeley 44 in the solar to super-solar regime ( $[\text{Fe}/\text{H}] \approx 0.0$  to  $+0.4$ ). The sensitivity of the proposed survey allows us to test differences in planet occurrence rates between CA and DI scenarios at the level of a few percent. In particular, distinguishing between an occurrence rate of  $\sim 5\%$  and  $\sim 1\%$  is statistically feasible provided sufficiently large samples per metallicity bin. Assuming binomial statistics as a first-order approximation, the uncertainty on the occurrence rate scales as  $\sigma_p \approx \sqrt{p(1-p)/N}$ , where  $N$  is the number of FGK stars per bin and  $p = N_{\text{hosts}}/N$  is the planet occurrence rate, defined as the fraction of FGK stars hosting at least one planet in the considered regime. Under this framework, a  $3\sigma$  discrimination between, e.g., 1% and 5% requires 4–15 clusters per metallicity bin. This places the survey with HRMOS in a regime where a statistically significant ( $\gtrsim 3\sigma$ ) distinction between the two occurrence-rate scenarios becomes achievable. Cluster-to-cluster variance, driven by environmental and evolutionary effects such as age and stellar density, may introduce additional covariance terms, which in turn could reveal secondary correlations between planet occurrence rates and cluster properties, providing complementary constraints on formation and evolutionary pathways. In more populated clusters, where a significant number of giant planets is expected to be detected, we also aim to investigate their mass distributions and compare them with the results of the simulations shown in Fig. 2.6.

**Table 2.2.** The  $G$  magnitude of the red clump ( $M_G \sim 0.7$ ) in two globular clusters, in the bulge, and in the Sgr dSph.

Environment	Distance [kpc]	[Fe/H] [dex]	Red clump $G$ [mag]	Target mag range [mag]
47 Tuc	4.0	-0.8	14.2	13.2-16
Omega Cen	4.9	-2.0 to -0.5	15.0	14.0-16.5
Bulge fields	8.0	-0.8 to +0.6	16.7	15.7-17.0
Sgr	20.0	-1.5 to -0.2	17.8	16.5-17.8

### 2.6.2 Giants in the Bulge, globular clusters, and local dwarf galaxies

Our goal is to select samples of red giant branch (RGB) and red clump (RC) stars that are suitable for exoplanet searches, while avoiding very luminous giants and AGB stars whose intrinsic variability precludes precise radial-velocity measurements. Based on observations of local giants, most known exoplanets around evolved stars are found in the range  $-1.5 < M_G < 1.5$ , and we aim to cover this interval whenever possible.

Sozzetti et al. (2006) have shown that a metallicity of  $[Fe/H] \approx -1$  only reduces  $Q$  by a factor of  $\sim 2$ , so the limiting magnitudes shown in Table 2.1 are still mostly applicable to these targets, although may be underestimated for some of the metal-rich bulge stars and overestimated for the most metal-poor stars, for instance, the cluster Omega Cen or the Sagittarius dwarf galaxy (Sgr dSph). There are multiple rich target fields available in all these regions and *Gaia* data is easily able to pick out largely uncontaminated samples, such that an order of 100 targets are available over the HRMOS FoV. In both 47 Tuc and Omega Cen, the range of target magnitudes easily encompasses the clump and the central part of the RGB. Single one-hour exposures in these fields should result in velocities that are limited by the instrumental precision, which for a precision of  $10 \text{ m s}^{-1}$  should identify exoplanets with masses of  $0.7 - 2 M_J$  in orbits of 100 – 1000 days ( $\sim 0.5 - 2.5$  au separation). Given a frequency for Jovian planets within 2.5 AU of field giants of  $\sim 25\%$  (e.g. Jones et al. 2021), as reported for metal-rich stellar samples and used here only for illustrative purposes, even observing single fields of 100 objects in each region should yield robust statistical conclusions about the planetary frequency. However, the true occurrence rate in fields dominated by more metal-poor stars may be lower. Such a survey would take only on the order of 4 nights per region, spread over 5 years of observation.

A more ambitious programme is to observe multiple fields in the bulge (in Baade’s window, which is also one of the main targets of the proposed HAYDN mission -see Section 10.2.5). Several fields with  $\sim 100$  RGB and RC targets have already been observed with FLAMES (e.g. Hill et al. 2011, see also Chapter 11). Even for these distant targets, one hour exposures with HRMOS should reach a SNR that is capable of reaching the  $10 \text{ m s}^{-1}$  RV precision floor dictated by the instrument stability - sufficient to probe  $> 0.7 M_J$  planets in orbits of 100 – 1000 days (where giant exoplanets are found in local field giants). Observing four fields should provide a large enough sample to see whether the frequency of giant exoplanets is a function of metallicity within the bulge.

Finally, we can consider observing giants in the nearest dwarf galaxies. Observations of clump stars will be almost impossible in Sgr dSph but it should be possible to target the upper RGB ( $-2 < M_V < 0$ ) using two hour exposures in dark conditions and reach a precision of  $\sim 10 - 20 \text{ m s}^{-1}$  that is limited by the SNR of the spectrum rather than the instrument precision. The frequency of  $> 3 - 8 M_J$  exoplanets at  $< 2.5$  au around field giants is a few percent. Observing even one carefully chosen field in each of these regions should determine whether the frequency is similar to within a factor of two. Table 2.2 lists the  $G$  magnitude of the red clump ( $M_G \sim 0.7$ ) in two globular clusters, the bulge, and nearby dwarf galaxies. It provides the magnitude range

of potential targets for HRMOS surveys in largely unexplored environments, linking detection efficiency simulations to real target selection.

### 2.6.3 Possible other targets

#### White dwarf stars

A substantial fraction of white dwarfs (WDs) show photospheric metals at  $T_{\text{eff}} \lesssim 25,000$  K, implying ongoing accretion of planetary debris and, by inference, surviving planetary architectures; yet confirmed WD planets remain rare because of faintness, sparse narrow lines, and the need for ultra-stable, high-cadence spectroscopy (Zuckerman et al. 2010; Koester et al. 2014; Veras 2021). Moreover, white dwarf photospheric metal lines are typically narrow and weak, requiring high resolving power and high SNR to measure abundances and trace multiple elements beyond calcium. The discovery of a transiting giant planet around a WD demonstrates that short-period systems can exist and motivates systematic RV searches (Vanderburg et al. 2020). Feasibility has been demonstrated with ESPRESSO, which achieves  $\text{sub-km s}^{-1}$  RV precision on polluted WDs and reveals candidate periodic signals on days–weeks timescales, validating the approach and motivating surveys beyond single-object instruments.

HRMOS will build on this with *multiplexed, high-cadence* RV campaigns targeting white dwarfs in clusters, providing key constraints on metal pollution rates in dense stellar environments. The high spectral resolution and stability of the instrument will enable the detection of weak or blended metal lines, allowing the identification of chemical species originating from the accreted material, as well as velocity shifts tracing ongoing accretion and diffusion processes in white dwarf atmospheres. From the confirmed polluted WDs (DAZ, DBZ, DZ) and WD binaries within each field, HRMOS can extract RVs from the narrow metal lines (e.g. Ca II  $\kappa$ ) to reach sensitivity to sub-Saturns at short periods and broad completeness to Jupiters up to  $\sim 50$  days (Rogers et al. 2024; Ramírez et al. 2025).

Finally, comparing the frequency of pollution of cluster WDs to the well-established rates for field WDs, will inform the community about the differences and similarities between planetary systems in their oldest evolutionary stage, driven by the environments in which these stars evolve and, potentially, by their underlying chemical composition. This will shed light on the environmental and chemical variables that regulate planetary survival, as well as on the resulting survival rates across galactic environments.

Recent studies used *Gaia*-based astrometric cluster membership and identified a total of 69 spectroscopically confirmed WDs in open clusters, of which 5 are within the range of magnitude of HRMOS (Miller et al. 2026). Future *Gaia* data releases (DR4 and DR5), together with ground-based spectroscopic surveys (e.g. WEAVE, SDSS-V, and 4MOST), are expected to substantially increase the number of spectroscopically confirmed white dwarfs (Tremblay et al. 2024). This growing sample will provide an essential target pool for HRMOS, particularly in stellar clusters, enabling searches for precise photospheric metal abundances. Such measurements serve as indirect tracers of planets, minor bodies, and planetary debris, as well as direct searches for close-in giant planets. Together, these observations will help clarify the evolutionary pathways of planetary systems, including planet survival, destruction, and ejection within the Galaxy.

#### Stellar binaries and circumbinary planets

Circumbinary planets (CBPs) provide a stringent test-bed for planet formation and migration in dynamically complex protoplanetary discs. Kepler (Borucki et al. 2010) revealed a small but compelling sample of such systems orbiting MS binaries, and debiased analyses indicate that giant CBPs with orbital periods  $P \lesssim 300$  d may be relatively common—potentially occurring at rates

comparable to those around single stars. However, transit surveys are intrinsically incomplete: large transit-timing and duration variations, together with strong viewing-geometry biases, significantly suppress detections of non-coplanar systems (Welsh et al. 2012; Orosz et al. 2012; Armstrong et al. 2014).

Recent advances in analysis techniques have demonstrated that RV detection of CBPs is now feasible in both single-lined spectroscopic binaries (SB1s) (e.g., Standing et al. 2023; Baycroft et al. 2025) and double-lined spectroscopic binaries (SB2s, e.g., Sairam et al. 2024). These developments have been enabled by dedicated RV surveys such as *The Attempt to Observe Outer-planets In Non-single-stellar Environments* (TATOOINE; Konacki et al. 2009) and *Binaries Escorted By Orbiting Planets* (BEBOP; Martin et al. 2019).

To demonstrate the sensitivity of HRMOS observations to circumbinary planets, we adapt a REBOUND (Rein & Liu 2012) circumbinary system simulation of the EBLM J0310–31 binary presented in Standing et al. (2022). The original simulation was based on HARPS radial-velocity observations obtained as part of the BEBOP programme (Martin et al. 2019). To emulate HRMOS performance, we rescale the measurement uncertainties to a median of  $10 \text{ m s}^{-1}$  and randomly select 30 and 40 observations spanning 782 and 889 days, respectively, to create two simulated datasets.

Using these simulated datasets, we derive detection and sensitivity limits following the methodology described in Standing et al. (2022) and Standing et al. (2026), and applied in (e.g. Castro-González et al. 2025; Balsalobre-Ruza et al. 2025). We analyse the data with *kima* (Faria et al. 2018), first verifying that no significant planetary signals are recovered. We then repeat the analysis with the number of planets ( $N_p$ ) fixed to one, producing posterior samples corresponding to planetary signals that are consistent with, but undetectable, in the data.

From these posteriors, we compute  $3\sigma$  upper limits within discrete period bins, shown by the green and blue lines in Figure 2.8. These lines define the HRMOS detection thresholds for the simulated 30 and 40 observations respectively. Planetary signals above them would be detected, while those below would remain hidden in the data. The current sample of circumbinary planets

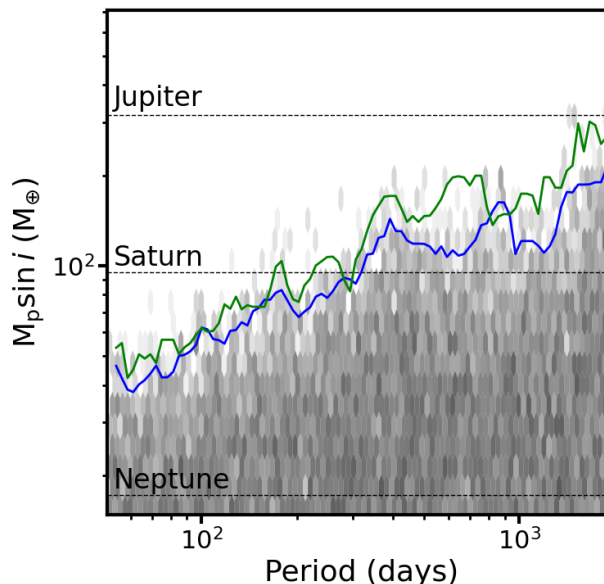


**Figure 2.8.** Hexbin plot of the *kima* posterior samples obtained from runs on simulated datasets for EBLM J0310–31, with  $N_p$  fixed to 1. The green curve shows the  $3\sigma$  sensitivity limit calculated on posterior samples obtained from a *kima* run on 30 simulated HRMOS observations, while the blue curve shows the corresponding limit computed from the plotted posterior samples obtained from a run on 40 simulated HRMOS observations. The measurement uncertainty was set to a median of  $\sim 10 \text{ m s}^{-1}$ .

demonstrates a pronounced pile-up near the instability region, at approximately  $6 \times P_{\text{bin}}$  (Winn & Fabrycky 2015; Martin 2018). For an SB1 system such as EBLM J0310–31, Figure 2.8 shows that HRMOS would be sensitive to CBPs with masses  $< 50M_{\oplus}$  out to orbital periods of  $\sim 100$  days, encompassing this pile-up region in the parameter space. The same figure also indicates sensitivity to sub-Saturn-mass planets with orbital periods  $< 300$  days, and sub-Jupiter-mass planets within  $\sim 2000$  days. Achieving an uncertainty of  $5 \text{ m s}^{-1}$ , such is the goal of HRMOS, could allow us to push the detections closed to the Neptune mass range of planets. Moreover, Sairam et al. (2024) shows that detection limits for SB2 systems are now expected to be comparable to those achieved for SB1 systems, implying similar sensitivity to CBPs across a broad range of binary architectures.

Thanks to *Gaia*, binary sequences in stellar clusters can be clearly identified in the colour–magnitude diagram, enabling a robust selection of candidate binary systems in which to search for planets. HRMOS is therefore poised to provide crucial constraints on the population of gas-giant circumbinary planets in binary systems. HRMOS will therefore probe a parameter space that transit and astrometric surveys alone are unlikely to fully characterise, given their intrinsic geometric and cadence limitations (Armstrong et al. 2014; Bouchy et al. 2001).

## 2.7 The unique role of HRMOS

Transit surveys such as Kepler, TESS, CHEOPS, and PLATO will discover large populations of predominantly close-in exoplanets ( $a < 0.1$  au), but they probe only a limited fraction of planetary systems because transits require nearly edge-on orbital geometries. Moreover, only a small subset of these planets will orbit stars in clusters, and transit surveys are inherently less sensitive to planets around evolved stars.

*Gaia* is expected to detect more than  $10^4$  exoplanets through astrometry, primarily giant planets with  $M > 3 M_J$  at orbital separations of 2–5 au around nearby field stars. Most host stars will be main-sequence stars of uncertain age, with only a relatively small number of planets expected around giant stars (Perryman et al. 2014). The Nancy Grace Roman Space Telescope will detect approximately  $10^3$  exoplanets via microlensing toward the Galactic bulge (Penny et al. 2019), many of them Jovian-mass planets at separations of 1–10 au.

HRMOS occupies a largely complementary region of parameter space. It will provide a substantially more complete survey of close-in giant planets ( $a < 0.5$  au for solar-type stars) in targeted stellar clusters with well-determined ages and chemical compositions. At the same time, it will enable planet searches around large samples of giant stars in clusters at distances and magnitudes inaccessible to both transit surveys and *Gaia*.

No existing or planned spectroscopic facility combines the key capabilities of HRMOS. Several instruments achieve superior radial-velocity precision, but they either operate on smaller telescopes (e.g. HARPS) or observe only one target at a time (e.g. ESPRESSO and, in the future, ANDES). Conversely, multi-object spectrographs such as WEAVE, 4MOST, and the proposed WST lack the wavelength stability and spectral resolution required for the science enabled by HRMOS.

The unique strength of HRMOS lies in the combination of high spectral resolution, excellent instrumental stability, large collecting area, and multiplexing capability. This combination will enable transformational surveys of stellar populations and exoplanetary systems that cannot be achieved with any existing facility alone.

### 3 Origin of the elements and nucleosynthesis

Understanding the origin of the chemical elements remains a fundamental question in astrophysics, at the interface between stellar evolution, nuclear physics, cosmic history, and multi-messenger astronomy. HRMOS will allow extremely precise measurements of key elemental abundances and isotopic ratios in well selected, large samples of stars; those abundances will cover light elements such as carbon and sulphur, as well as the heaviest species produced by slow, intermediate, and rapid neutron-capture processes, providing crucial constraints on their nucleosynthesis and on the most energetic phenomena in the Universe, including sources of gravitational waves.

#### 3.1 Scientific context

Revealing the origin of the chemical elements is one fundamental goal of astrophysics that has been pursued for many decades. It is a challenging topic that bridges nuclear physics, atomic physics, astrophysics, and cosmology. The general theoretical framework of the processes that lead to the formation of most elements was first summarised in the seminal works by Burbidge et al. (1957) and Cameron (1957). Our knowledge of these processes has evolved and improved significantly since then, but fundamental open questions remain.

Primordial nucleosynthesis after the Big Bang can produce isotopes of H and He and some amount of Li (Fields et al. 2020). Cosmic-ray spallation in the interstellar medium contributes to the production of isotopes of Li, Be, and B (Tatischeff & Gabici 2018). The production of all other elements and isotopes takes place in the interiors of stars of different masses and evolutionary stages through thermonuclear fusion or neutron-capture processes (Cowan et al. 2021; Diehl et al. 2022; Arcones & Thielemann 2023; Lugaro et al. 2023). Processes such as stellar winds, explosive events, or stellar mergers return the newly produced elements to the interstellar medium, from where they are used in the formation of the next generations of stars in a galaxy (Nomoto et al. 2013; Matteucci 2021).

We focus below on some elements and their isotopes whose production is not fully constrained and for which the very high resolution of HRMOS, along with its MOS capabilities, will open up a new parameter space for large-scale investigations into the origin.

#### Key Questions:

- What are the dominant astrophysical sources of  $^{13}\text{C}$ , and what do they reveal about Galactic chemical evolution?
- What can sulphur tell us about the production of elements in massive stars and how can it serve as a bridge between stellar nucleosynthesis and the chemical evolution of high-redshift galaxies?
- Where in the Universe are heavy elements formed, and what roles do neutron star mergers and stellar interiors play in this process?

### 3.2 Chemical evolution of the carbon isotopes

Carbon plays a fundamental role in astrophysics as it connects stellar nucleosynthesis to the chemical pathways that enable the emergence of prebiotic complexity in the Universe. It has two stable isotopes,  $^{12}\text{C}$  and  $^{13}\text{C}$ . The  $^{12}\text{C}$  isotope is produced in advanced evolutionary stages during He burning by means of the triple-alpha reaction (Hoyle 1946; Salpeter 1952). On the other hand, the  $^{13}\text{C}$  isotope is produced during H burning through the CNO cycle at the expense of  $^{12}\text{C}$ . Due to the different time scales of the reactions involved in the CNO cycle, when it is operating, the amount of  $^{12}\text{C}$  atoms decreases, although the sum of C+N+O atoms remains constant (Wiescher et al. 2010).

Although the reactions that give rise to  $^{12}\text{C}$  and  $^{13}\text{C}$  are well known, there is still discussion about the main types of objects that contribute to their enrichment in the Galaxy (Romano 2022). The production of both isotopes can take place in stars of a wide range of mass. Thus, it is not clear what fraction of their enrichment is due to stars of high mass (which end their lives as type II supernovae), stars of intermediate mass during the AGB phase, or stars that undergo nova events (Prantzos et al. 1996; Romano & Matteucci 2003; Romano 2022). The picture is further complicated by measurements of a low  $^{12}\text{C}/^{13}\text{C}$  ratio in metal-poor stars (e.g. Norris et al. 2013; Aguado et al. 2022; Molaro et al. 2023a), which requires a strong production of  $^{13}\text{C}$  from primordial massive stars by means that are still not well understood. Similarly, presolar grains condensed in the outflows of core-collapse supernovae shortly before the Sun was formed exhibit isotopic signatures suggesting vigorous  $^{13}\text{C}$  production. However, this interpretation remains controversial and is challenging to reconcile with the stellar yields typically adopted in Galactic chemical evolution models (e.g., Pignatari et al. 2015; Schofield et al. 2022; Liu et al. 2024).

To better understand the origin of  $^{13}\text{C}$  in particular, it is important to derive the  $^{12}\text{C}/^{13}\text{C}$  isotopic ratio in large samples of unevolved stars, in order to avoid contamination by the first dredge-up in red giants (e.g. Smiljanic et al. 2009; Lagarde et al. 2024, and references therein). At the same time, such abundances measured in unevolved stars supply a crucial zero point needed to calibrate computational models of the mixing processes that operate during the red giant branch phase.

Until now, observational limitations have prevented large-scale studies of carbon isotopic ratios in dwarf stars. To achieve this, one must detect the molecular lines of CH, CN, or CO in the stellar spectrum, since significant isotopic separation of the spectral features occurs only in molecular lines. These lines grow stronger as the stellar temperature decreases, making M-type dwarfs interesting targets for such studies. Nevertheless, absorption lines of several other molecular species are also present and in fact dominate the observed spectra of M-type dwarfs (Tsuji 2016). Moreover, M-type dwarfs have the disadvantage of being intrinsically faint. In warmer FGK-type stars, the lines become weaker and therefore more difficult to detect, but this kind of analysis can still be performed (Botelho et al. 2020). The bottom line is that, whatever stellar tracer is chosen, the spectra need to be of high resolution (for line separation) and high signal-to-noise ratio (for detection of weak features). This is the main reason why measurements of carbon isotopic ratios in unevolved stars are scarce in the literature.

So far, the  $^{12}\text{C}/^{13}\text{C}$  ratio has been investigated in 55 solar twin stars by Botelho et al. (2020), using optical high-resolution spectra, and by Coria et al. (2023) in six solar twins but using infrared spectra in the M band. In M-type dwarfs, measurements have been performed by González Picos et al. (2025) for 32 stars and by Xuan et al. (2024) for one binary system (composed of stars of M-type and K-type), all using infrared data. The results of these studies do not agree and further observations are required to make progress on this topic. In particular, considering the limited number of stars examined so far and the many associated uncertainties, it is necessary to obtain

measurements for larger samples of metal-rich dwarf stars, especially those with well-determined ages.

One of the three planned spectral windows of HRMOS will cover the range between 385.2 - 418.7 nm. This window includes several lines of  $^{12}\text{CH}$  and  $^{13}\text{CH}$  that offer the possibility of deriving the carbon isotopic ratio in unevolved stars. In addition, as precise ages are important for this investigation, a statistically large sample of stars can be easily obtained by focussing the observations in coeval stars belonging to open clusters. Thanks to HRMOS multiplex capabilities, several members of stellar clusters can be observed simultaneously, allowing us to place strong constraints on GCE models, which adopt different sets of yields for C isotopes from massive stars, AGB stars, and nova systems with different initial mass ranges. In addition, open clusters, spanning a wide range of metallicities and ages, will enable a systematic investigation of Galactic chemical evolution as function of both time and metallicity.

### 3.3 The Galactic chemical evolution of sulphur

Sulphur is an  $\alpha$ -element produced mainly during convective and explosive oxygen burning in massive stars and released into the interstellar medium by core-collapse supernovae (Limongi & Chieffi 2003; Kobayashi et al. 2020). Compared to iron, sulphur abundances can act as a cosmic clock, constraining both stellar nucleosynthesis and galaxy formation histories. Because of its volatile nature, sulphur is the only  $\alpha$ -element that can be reliably used as a tracer in high-redshift systems, enabling direct comparison between local stellar abundances and the gaseous phase in distant environments such as extragalactic H II regions and damped Ly $\alpha$  (DLA) systems (Matteucci et al. 1996; Bowen et al. 2005; Dessauges-Zavadsky et al. 2007). Since DLAs are likely progenitors of the Milky Way building blocks, sulphur provides a powerful link between local and high-redshift chemical evolution.

Despite this potential, the Galactic behaviour of sulphur remains uncertain. Most studies find it behaves as a typical  $\alpha$ -element, with  $[\text{S}/\text{Fe}] \sim 0.4$  at low metallicity followed by a decline toward solar values at  $[\text{Fe}/\text{H}] \sim 0$  (e.g. Nissen et al. 2004, 2007; Caffau et al. 2010; Takeda & Takada-Hidai 2011; Duffau et al. 2017). However, conflicting results exist: Israelian & Rebolo (2001) reported a continuous increase of  $[\text{S}/\text{Fe}]$  toward low metallicity up to  $\sim 0.8$  dex, possibly linked to hypernova enrichment, while Caffau et al. (2005a) suggested a bimodal halo distribution with coexisting high- and low- $[\text{S}/\text{Fe}]$  populations. In star clusters, sulphur has been measured in a limited sample of open and globular clusters (e.g. Sbordone et al. 2009; Koch & Caffau 2011; Myers et al. 2022; Kacharov et al. 2015; Caffau et al. 2014), with Duffau et al. (2017) providing the most extensive survey. It generally follows other  $\alpha$ -elements, although its role in multiple populations of globular clusters remains debated: correlations with Na were reported in 47 Tuc (Sbordone et al. 2009; Duffau et al. 2017), but not confirmed in other clusters (Kacharov et al. 2015). The Galactic homogeneity of sulphur is also debated. While some studies find standard  $\alpha$ -like behaviour in the bulge (Griffith et al. 2021), others report S-enhancement relative to the discs (Lucertini et al. 2022). In dwarf galaxies such as Sagittarius and Sculptor, low sulphur abundances are observed (Caffau et al. 2005b; Skúladóttir et al. 2015), broadly consistent with other  $\alpha$ -element trends.

Observationally, sulphur abundance determinations in stellar spectra are challenging because they rely on a limited set of lines: Multiplet 8 (675 nm), 6 (870 nm), 1 (920 nm), 3 (1045 nm), the forbidden [S I] line at 1082 nm, and near-infrared lines at 1541 and 2262 nm. Near-IR lines suffer from telluric contamination and NLTE effects, while optical lines are weak and require high resolution and S/N. Moreover, several multiplets arise from high-excitation neutral transitions, becoming weak in cool or metal-poor stars.

Large surveys faced limitations: Gaia-ESO (GES; Gilmore et al. 2022; Randich et al. 2022) at

$R \sim 47,000$  relies mainly on the strongest Multiplet 8 line and is thus limited to relatively metal-rich stars ( $[\text{Fe}/\text{H}] > -1$ ), while APOGEE (DR17; Majewski et al. 2017) used near-IR lines but suffers from significant systematics, making sulphur one of its least reliable elements. At  $R = 80,000$ , HRMOS will access the S I Multiplet 8 at 675.7 nm, enabling precise abundance measurements. These lines are relatively insensitive to NLTE effects ( $\lesssim 0.1$  dex; Korotin & Kiselev 2024) and are free from telluric contamination, making them among the most reliable sulphur diagnostics. Recent advances in oscillator strengths and 3D NLTE modelling further strengthen their robustness (Amarsi et al. 2025; Li et al. 2026), allowing accurate sulphur abundance determinations with HRMOS. HRMOS will enable homogeneous, high-precision sulphur abundances across wide metallicity ranges and Galactic populations. This will clarify whether sulphur follows the behaviour of other  $\alpha$ -elements in the metal-poor regime and will constrain nucleosynthetic yields from massive stars. In globular clusters, improved sulphur measurements will further test its role in multiple-population chemistry and help identify the progenitor processes responsible for abundance variations (see Chapter 6). More broadly, a comprehensive sulphur census will provide key constraints on its Galactic homogeneity and help to place the Milky Way in a broader extragalactic context. In particular, sulphur offers a valuable benchmark for linking local chemical evolution studies with those at higher redshift. In this context, sulphur is especially important because it is one of the few  $\alpha$ -elements that can be reliably measured in high-redshift environments, such as damped Ly $\alpha$  absorbers, where other species are often depleted onto dust or affected by complex ionisation corrections. A well-calibrated Galactic sulphur scale is therefore essential for interpreting these distant systems and for assessing whether the Milky Way chemical evolution is representative of typical galaxy assembly histories.

### 3.4 Abundances and isotopes of heavy neutron-capture elements

Iron-peak elements represent the limit of nuclear fusion reactions that release energy in stellar interiors. Beyond iron, the synthesis of heavier nuclei through charged-particle reactions becomes progressively less efficient, although still possible under extreme explosive stellar conditions (e.g., Woosley & Hoffman 1992; Roberts et al. 2010). As already pointed out in Burbidge et al. (1957), neutron-capture reactions constitute the dominant mechanism for the production of elements heavier than iron. These elements are traditionally produced through two main channels: the slow (s-process, Lugaro et al. 2023) and the rapid (r-process, Cowan et al. 2021) neutron-capture processes. The key distinction between them lies in the relative timescales of neutron captures and  $\beta$ -decays, which are governed by the neutron density and the thermodynamic conditions of the environment. Several additional nucleosynthetic processes are required to reproduce the full complexity of observed abundance patterns. These include the p-process (Arnould & Goriely 2003), neutrino-driven winds in core-collapse supernovae (e.g., Fröhlich et al. 2006; Arcones & Thielemann 2023), and other explosive or high-entropy environments. In addition, as first suggested by Cowan & Rose (1977), an intermediate neutron-capture process (the so-called i-process), characterised by neutron densities intermediate between the s- and r-process regimes, may be required to explain a number of stellar observations (see Wiedeking et al. 2025, and references therein).

#### 3.4.1 r-process elements: constraining rates and yields of compact-object mergers

One of the key questions regarding neutron-capture elements concerns their connection with the merger of compact objects, including neutron stars. In this context, their abundance patterns provide a powerful observational window into the astrophysical sites responsible for heavy-element production. In particular, the heaviest species are especially valuable, as they allow us to disentangle

the relative contributions of different nucleosynthetic channels and to place quantitative constraints on the formation rates, delay-time distributions, and evolutionary timescales of compact-object merger events, as well as other rapid enrichment sources in galaxies.

A major breakthrough in this field came from the gravitational wave event GW170817, originating from a neutron star merger (NSM), reported by Abbott et al. (2017), together with its kilonova counterpart AT 2017gfo (Valenti et al. 2017), which provided the first direct observational confirmation of an astrophysical site capable of producing r-process elements (Tanvir et al. 2017; Pian et al. 2017; Watson et al. 2019). However, owing to their intrinsically delayed occurrence and relatively low event rates, neutron star mergers alone are unlikely to account for the full Galactic inventory of r-process material (e.g., Matteucci et al. 2014; Cescutti et al. 2015; Côté et al. 2019; Kobayashi et al. 2023; Chen et al. 2025). This tension is further highlighted by the observed flat trend between the r-process element Eu and the  $\alpha$ -element Mg as a function of metallicity in metal-poor stars, which suggests that at least part of the r-process enrichment must occur on rapid timescales, comparable to those of core-collapse supernovae (da Silva & Smiljanic 2023; Monty et al. 2024). This has motivated the exploration of additional r-process production channels, including rare classes of core-collapse supernovae such as magneto-rotational supernovae (Mösta et al. 2018; Yong et al. 2021; Reichert et al. 2023), collapsars (Siegel et al. 2019), and magnetar giant flares (Cehula et al. 2024; Patel et al. 2025). In such scenarios, prompt r-process production may dominate the early chemical enrichment of galaxies (Van der Swaelmen et al. 2023; Molero et al. 2023).

Although europium is commonly used as a canonical tracer of r-process nucleosynthesis, observational evidence indicates that the apparent universality of the r-process pattern holds mainly for second-peak and heavier nuclei, while lighter neutron-capture elements exhibit significant star-to-star variations. This suggests that the r-process may not be a single universal mechanism, but instead may involve multiple astrophysical sites or physical regimes contributing differently across the full abundance pattern (Hansen et al. 2014; Kuske et al. 2025). Moreover, recent evidence points toward a possible decoupling between Eu and third-peak r-process elements, further indicating a more complex nucleosynthetic origin (Alencastro Puls et al. 2025).

In this context, robust constraints on r-process production sites require a comprehensive characterization of the full abundance pattern, spanning light neutron-capture elements, second- and third-peak species, and actinides. In particular, actinide abundances such as Th and U provide crucial complementary diagnostics, as they trace the most extreme neutron-rich conditions and encode information on neutron richness, fission cycling, and the physical conditions of the progenitor event (Kullmann et al. 2023). Beyond their role as radioactive chronometers (Chapter 5), actinide-boost stars are especially informative, as they likely probe a subset of highly neutron-rich events, possibly including neutron-star mergers or other rare compact-object environments.

Despite these advances, identifying all astrophysical sources of r-process elements and quantifying their relative contributions to Galactic chemical evolution remains an open problem (Palla et al. 2025). This highlights the need to extend observational analyses beyond Eu, targeting multiple r-process peaks simultaneously. Such measurements require high-resolution spectroscopy with sufficient blue wavelength coverage to access key transitions of light neutron-capture elements in addition to heavy species. In this context, HRMOS will provide high-resolution, multiplexed spectroscopy ideally suited to probing complete r-process abundance patterns across diverse stellar populations and environments, in particular ancient, metal-poor globular clusters and dwarf galaxies (see Chapter 4), enabling statistically robust constraints on their production sites.

### 3.4.2 Other neutron capture processes

**s-process:** The s-process is likely the best understood of the neutron-capture mechanisms, despite remaining a complex phenomenon. It is commonly divided into three components: the main, weak, and strong components. The main s-process takes place in thermally pulsing 1–4  $M_{\odot}$  AGB stars (Busso et al. 1999; Käppeler et al. 2011; Van Eck et al. 2022), which have been recognised as sources of heavy elements since the discovery of technetium in their atmospheres (Merrill 1952). Two neutron sources dominate under different physical conditions: the  $^{13}\text{C}(\alpha,n)^{16}\text{O}$  reaction and the  $^{22}\text{Ne}(\alpha,n)^{25}\text{Mg}$  reaction (see Lugaro et al. 2023, and references therein). The weak s-process operates in massive stars during core He-burning and shell C-burning phases, primarily producing elements between Fe and the first s-process peak (Sr, Y, and Zr), with neutrons mainly supplied by the  $^{22}\text{Ne}$  source (e.g. Pignatari et al. 2010). The strong component is required to account for the production of the heaviest s-process isotope,  $^{208}\text{Pb}$ , and is predominantly associated with low-metallicity AGB stars (Travaglio et al. 2001). A comprehensive census of s-process elements is therefore essential to address several open questions in Galactic chemical evolution, including the origin of neutron-capture element enhancements observed in young stellar populations (D’Orazi et al. 2009; Baratella et al. 2020), as well as the variation of these abundance patterns with Galactocentric distance and metallicity (Viscasillas Vázquez et al. 2022; Magrini et al. 2021). The HRMOS survey of open clusters (see also Chapter 2), spanning a wide range of ages, distances, and metallicities, is ideally suited to contribute significantly to this science case, thanks to its high spectral resolution and blue wavelength coverage.

**i-process:** Regarding the i-process, several key questions remain unresolved, particularly concerning its contribution to the Galactic enrichment of heavy elements and the identification of its dominant astrophysical sites. The i-process is thought to occur during proton-ingestion events (PIEs), in which protons are mixed into a convective helium-burning region (Wiedeking et al. 2025). Under these conditions, the activation of the  $^{13}\text{C}(\alpha,n)^{16}\text{O}$  reaction produces neutron densities intermediate between those of the classical s- and r-processes ( $N_n \sim 10^{13}\text{--}10^{15} \text{ cm}^{-3}$ ), leading to distinctive heavy-element abundance patterns. Possible i-process sites include AGB stars (Choplin et al. 2024), accreting CO white dwarfs (Denissenkov et al. 2019), super-AGB stars (Jones et al. 2016b), and metal-poor massive stars (Roederer et al. 2016; Clarkson et al. 2018; Banerjee et al. 2018). Since these environments predict different thermodynamic properties and chemical yields, detailed abundance measurements of many neutron capture elements are needed to provide a powerful way to constrain the physical nature of the i-process. Exploiting these diagnostics requires high-resolution, high signal-to-noise spectroscopy together with the simultaneous measurement of a broad range of neutron-capture elements, spanning the first s-process peak (Sr, Y, Zr) to the second and third peaks (Ba, La, Eu, Hf, Pb). Such abundance patterns make it possible to distinguish between pure r-process enrichment, mixed r+i signatures, and secondary pollution scenarios (see, e.g. Giribaldi et al. 2026).

### 3.4.3 Barium isotopes

Unlike atomic abundances, which trace the cumulative outcome of multiple nucleosynthetic channels, isotopic fractions retain a more direct imprint of the physical conditions under which elements are formed. A crucial diagnostic of neutron-capture nucleosynthesis is provided by the isotopic ratios of Ba. Two HRMOS spectral windows, the blue and red ones, provide access to the Ba resonance line at  $\lambda = 493.4 \text{ nm}$  and to the line at  $649.6 \text{ nm}$ , which can be used to constrain Ba isotopic ratios (Gallagher et al. 2012; Cescutti et al. 2021; Giribaldi et al. 2025; Sitnova et al. 2025). Barium has five stable isotopes ( $A = 134, 135, 136, 137, \text{ and } 138$ ), each contributing at different

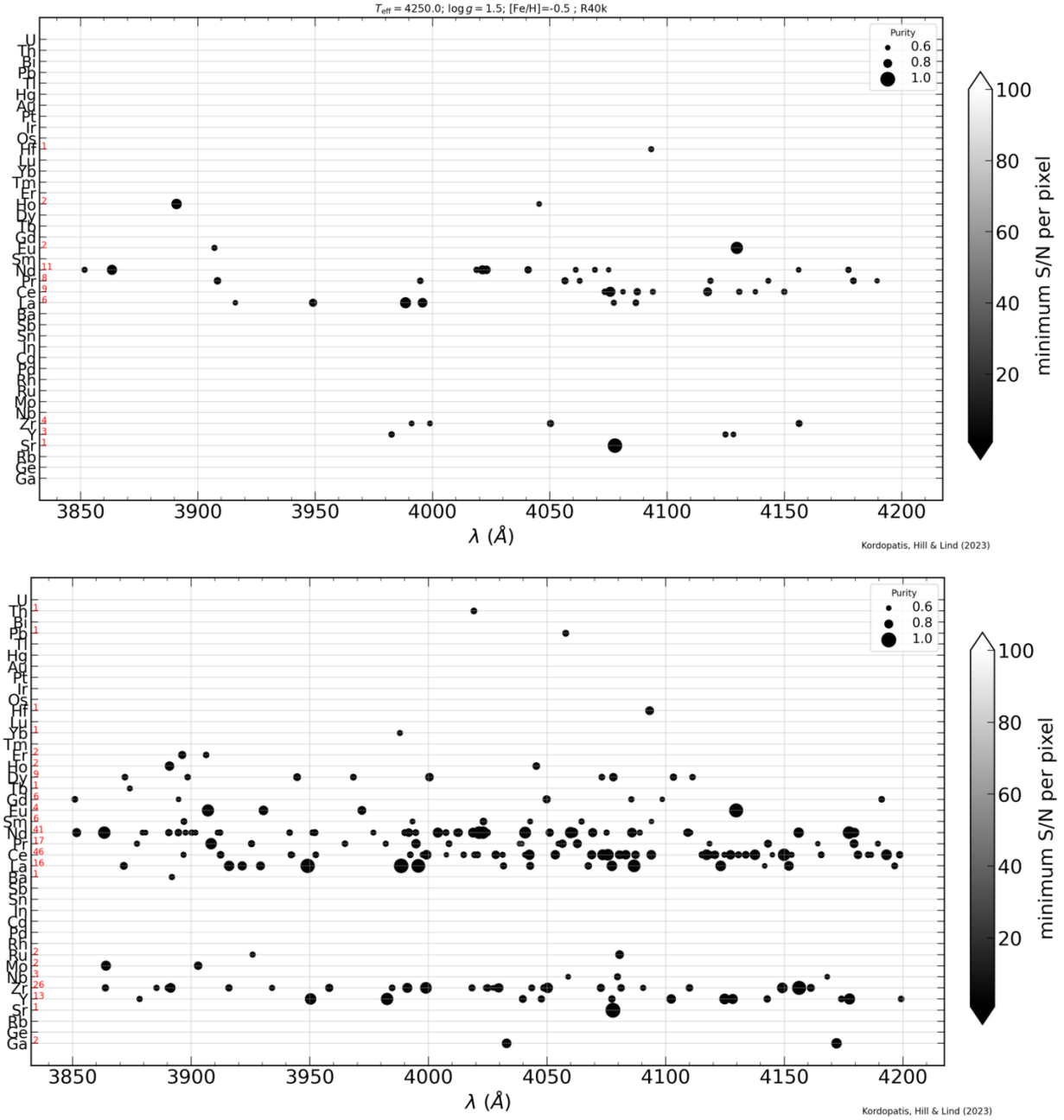


**Figure 3.1.** Spectral lines of neutron-capture elements that can be detected in the blue range of HRMOS at two resolving powers,  $R = 40k$  (top) and  $R = 80k$  (bottom). The simulations concern a no-r-process enhanced red giant of  $[\text{Fe}/\text{H}] = -0.5$ . The size of the points indicates the purity with which the line can be measured and colour is related to the minimum signal-to-noise ratio needed (per pixel). It is clear that at the resolution of HRMOS, the number of elements and of features per element increases considerably.

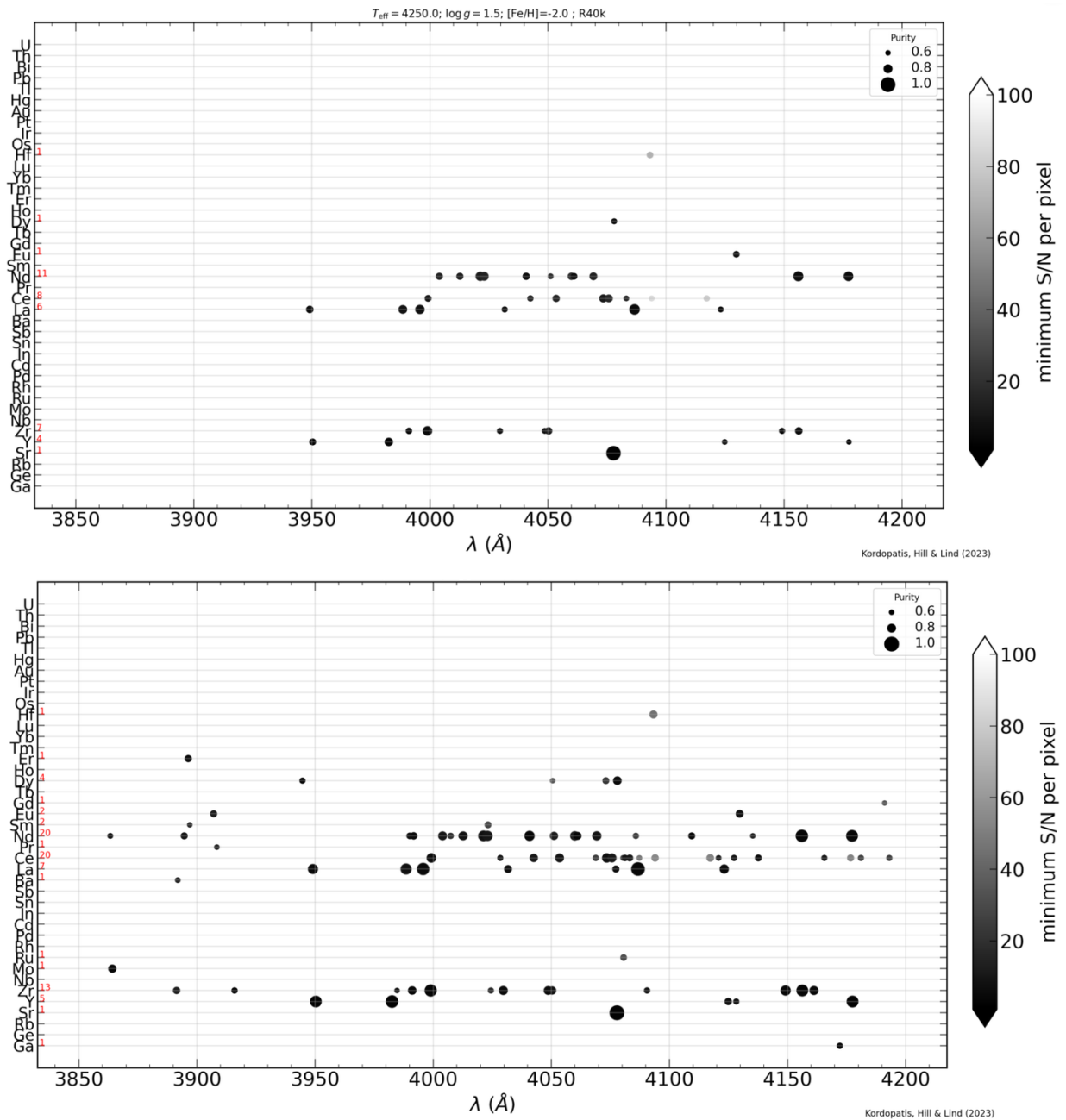


**Figure 3.2.** Same as Fig. 3.1 but the simulations for a giant with  $[\text{Fe}/\text{H}] = -2$  are shown.

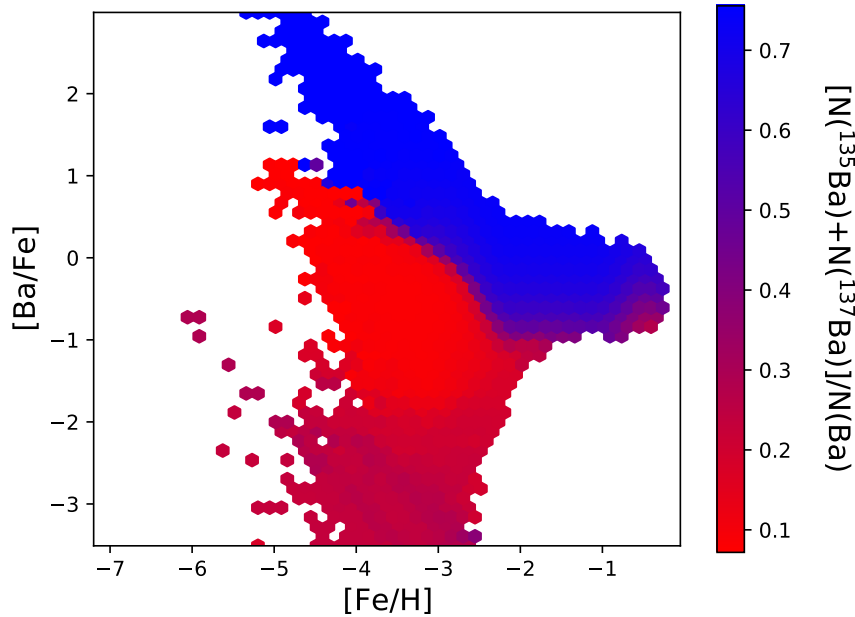


**Figure 3.3.** Theoretical predictions of the evolution of the Ba isotopes in the Galactic halo:  $[\text{Ba}/\text{Fe}]$  versus  $[\text{Fe}/\text{H}]$  with the fraction of odd Ba isotopes in colour scale, highlighting the contribution from s-process (in red) or r-process (in blue). Model obtained with the GEMS code (Rizzuti et al. 2025).

levels to the solar-system abundance. The three neutron-capture processes (s-, i-, and r-process) are expected to produce these isotopes in different proportions (see Table 5 in Giribaldi et al. 2025). In low-metallicity stars, Ba isotopic ratios can therefore be used to constrain the dominant process responsible for heavy-element enrichment. As an example, in Figure 3.3 we show the predicted behaviour of the Ba isotopic fraction in metal-poor stars, obtained with the GEMS code (Rizzuti et al. 2025). Measuring Ba isotopic ratios in a large sample of metal-poor stars will provide empirical constraints on the nucleosynthesis assumptions implemented in such theoretical models, enabling a quantitative assessment of the relative contributions of s- and r-process production channels (shown in red and blue, respectively). Recently, Giribaldi et al. (2025) demonstrated the feasibility of measuring Ba isotopic ratios in member stars of the globular cluster NGC 6752, showing that multiplexed observations of cluster members can significantly improve measurement precision. This approach is particularly well suited to HRMOS, which will enable simultaneous high-resolution spectroscopy of multiple stars in stellar clusters, thereby greatly enhancing isotopic constraints and statistical robustness.

HRMOS will deliver significantly improved precision in isotopic ratio measurements compared to UVES with the FLAMES fibre link, while also enabling much larger stellar samples in clusters. This will provide a stringent observational test of the Ba isotopic predictions presented above. Figure 3.4 shows HRMOS simulations for stars analogous to those in Fig. 9 of Giribaldi et al. (2025), for the globular cluster NGC 6752 with  $[\text{Fe}/\text{H}] \sim -1.3$  dex, allowing a direct comparison with UVES spectra at similar SNR and  $R = 47,000$ . The achieved precisions (values in brackets) are approximately a factor of two better than those obtained with UVES.

In addition, the higher resolving power of HRMOS preserves the flux contrast between s- and r-process profiles, particularly in the line wings, thereby enhancing the discrimination between different isotopic mixtures in stellar atmospheres. As illustrated in the residual panels, the wings show the largest differences between pure s- and r-process synthetic profiles (up to  $\sim 10\%$ ), producing characteristic “W”- or “M”-shaped signatures. In contrast, at UVES-like resolution the

residuals become significantly flatter, with flux differences reduced to  $\sim 5\%$  at the same SNR.

#### 3.4.4 Heavy elements detectable with HRMOS

In the blue spectral windows of HRMOS, covering between about 385-419 nm, we expect to be able to measure abundances of several heavy elements that can be used for detailed studies of neutron-capture nucleosynthesis processes; many of these lines are not detected at lower resolution. To identify the available spectral lines of these elements, we made use of the line detector tool introduced by Kordopatis et al. (2023a)<sup>1</sup>. Figures 3.1 and 3.2 exemplify the variety of elements between Ga ( $Z = 31$ ) and U ( $Z = 92$ ) that can potentially be detected in giants, depending, of course, on the metallicity of the star. Thanks to the multiplexing capability of HRMOS, it will be possible to acquire the required spectra for large sample covering a wide metallicity range, with a focus on observing stellar clusters (both open and globular) and regions of the Galactic disc. This will enable a detailed investigation of how the chemical abundances of various heavy elements vary with metallicity on a scale that has not yet been possible. The plots in Fig. 3.1 and 3.2, show that lines of several interesting elements in this context are included in the HRMOS blue spectral range: Ga ( $Z = 31$ ), Sr ( $Z = 38$ ), Y ( $Z = 39$ ), Zr ( $Z = 40$ ), Mo ( $Z = 42$ ), Ru ( $Z = 44$ ), La ( $Z = 57$ ), Ce ( $Z = 58$ ), Pr ( $Z = 59$ ), Nd ( $Z = 60$ ), Sm ( $Z = 62$ ), Eu ( $Z = 63$ ), Gd ( $Z = 64$ ), Dy ( $Z = 66$ ), Er ( $Z = 68$ ), and Hf ( $Z = 72$ ).

In Table 3.1, we summarise the astrophysical relevance of each of these elements and indicate whether the high spectral resolution of HRMOS is essential to achieve abundance measurements with a precision better than  $\sim 0.05$  dex. This highlights how HRMOS uniquely enables access to a set of difficult but decisive elements whose combined analysis is required to fully exploit neutron-capture chemistry as a probe of stellar evolution, nucleosynthesis, and Galactic chemical enrichment.

#### 3.4.5 Simulations with HRMOS-like spectra.

We computed synthetic spectra with the Turbospectrum code version 2019 (Plez 2012). The calculations assume local thermodynamic equilibrium (LTE) and use one-dimensional (1D) MARCS model atmospheres (Gustafsson et al. 2008). The data for the CH molecules are from Masseron et al. (2014). The atomic line list is the one compiled and tested in Giribaldi & Smiljanic (2023). The spectra were computed with a pixel size of 0.00185 nm and convolved with a Gaussian profile with FWHM = 0.005 nm to simulate  $R = 80\,000$  at 400 nm with a spectral sampling of 2.7 pixels. In addition, we assumed the solar values of macroturbulence and projected rotation,  $v_{\text{mac}} = 3.1 \text{ km s}^{-1}$  and  $v \sin i = 1.9 \text{ km s}^{-1}$  (Gray 1977) as typical broadening values. The signal-to-noise ratio was simulated adding Poisson noise with the MKNOISE task within IRAF (Image Reduction and Analysis Facility, Fitzpatrick et al. 2024)<sup>2</sup>.

**Carbon isotopic ratios** To evaluate the possibility of using HRMOS spectra to determine carbon isotopic ratios ( $^{12}\text{C}/^{13}\text{C}$ ) in unevolved stars, we simulated spectra for three metal-rich dwarfs were computed with the following atmospheric parameters, all with microturbulence  $\xi = 1.0 \text{ km s}^{-1}$  and the following sets of stellar parameters ( $T_{\text{eff}}, \log g, [\text{Fe}/\text{H}]$ ) = (5777 K, 4.44, 0.0), (5455 K, 4.20, +0.30), and (5000 K, 4.50, +0.15). Examples of simulated spectra are shown in Fig. 3.6. The spectral region around 386.2 is promising to allow the determination of  $^{12}\text{C}/^{13}\text{C}$  in the bluest spectral window of HRMOS.

<sup>1</sup><https://line-detector.oca.eu/>

<sup>2</sup><https://iraf.noirlab.edu/>

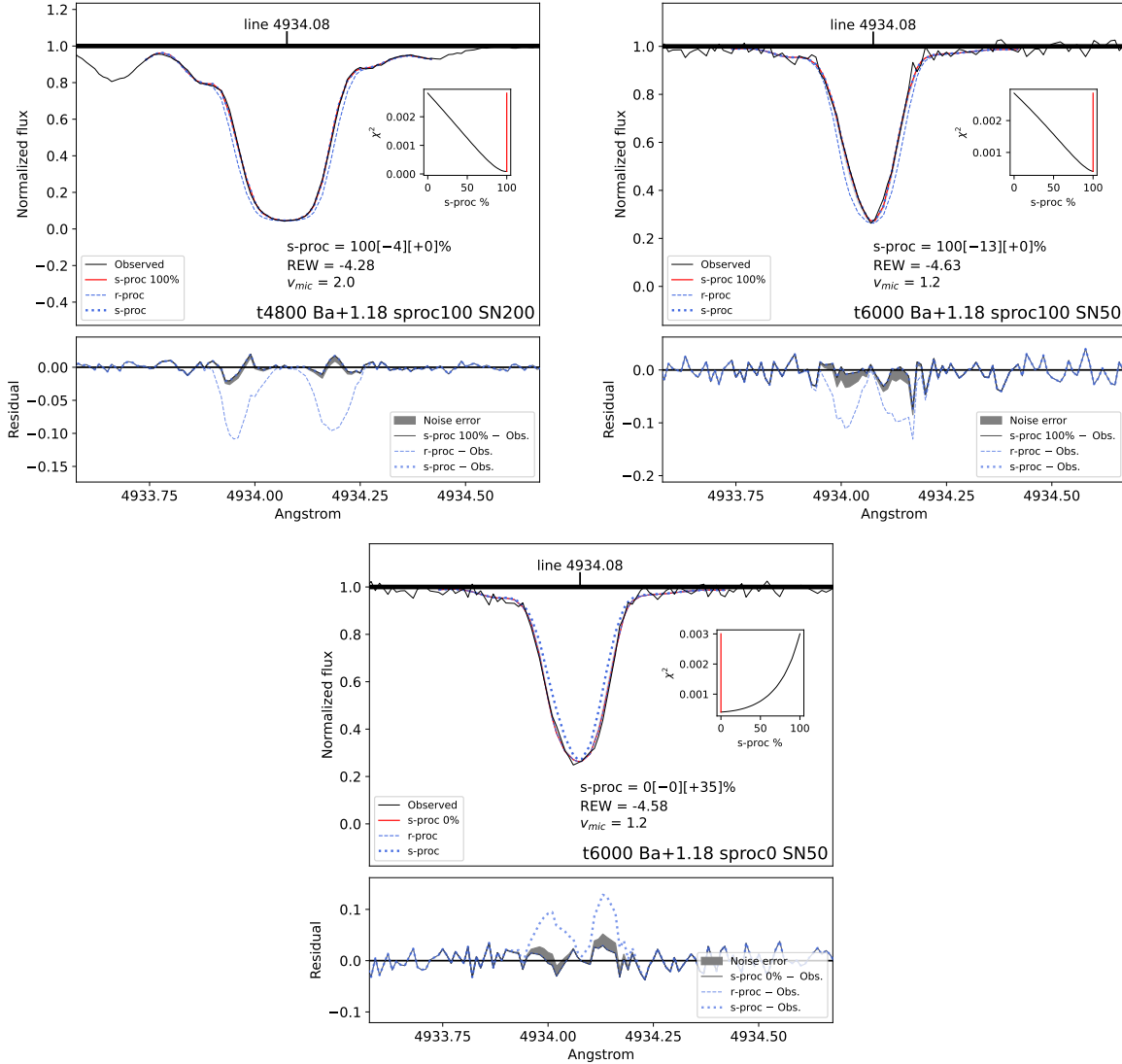


**Figure 3.4.** Fits to simulated Ba II line profiles at HRMOS resolution. The simulations were performed as described for  $[Fe/H] = -1.5$  dex. The effective temperature,  $A(Ba)$ , s-process fraction, and SNR adopted in each case are reported in the lower-right corner of the panels, and the layout follows Fig. 9 of Giribaldi et al. (2025). The simulated spectra, with 100% s-process isotopic fraction, are shown in black. Synthetic profiles representing pure s- and pure r-process isotopic mixtures are overplotted as indicated in the legend, and the best-fit solution is shown in red, with the recovered s-process fraction and its noise-related uncertainty given in parentheses. The insets display the  $\chi^2$  distributions used in the fitting, with the vertical red line marking the minimum. The residual panels include gray shaded regions denoting the flux variation related to the noise.

**Table 3.1.** Astrophysical significance of selected neutron-capture elements and requirements for high-resolution spectroscopy.

Element	Z	$R = 80,000$ critical	Expected precision	Astrophysical significance
Ga	31	Yes	$\lesssim 0.05$ dex	Light p-process tracer; useful for massive-star nucleosynthesis.
Sr	38	No	$\lesssim 0.05$ dex	First s-process peak; indicator of neutron-capture in AGB stars.
Y	39	No	$\lesssim 0.05$ dex	First s-process peak; used with Sr and Zr to calibrate s-process efficiency and Galactic chemical evolution; age tracer in open clusters.
Zr	40	No	$\lesssim 0.05$ dex	First s-process peak; sensitive to enrichment from low- and intermediate-mass AGB stars; age tracer in open clusters.
Mo	42	Yes	$\sim 0.05$ dex	Mixed s- and r-process; probes weak s-process in massive stars.
Ru	44	Yes	$\sim 0.05$ dex	r-process dominated; traces rapid neutron-capture nucleosynthesis in supernovae or neutron-star mergers.
La	57	No	$\lesssim 0.05$ dex	Second s-process peak; signature of low/intermediate-mass AGB star enrichment; age tracer in open clusters.
Ce	58	No	$\lesssim 0.05$ dex	Second s-process peak; important for Galactic chemical evolution models; age tracer in open clusters.
Pr	59	Yes	$\sim 0.05$ dex	Mixed s-/r-process; helps disentangle neutron-capture contributions.
Nd	60	Yes	$\sim 0.05$ dex	Second s-process peak with r-process component; useful for distinguishing enrichment sources.
Sm	62	Yes	$\sim 0.05$ dex	r-process dominated; indicator of early neutron-capture events.
Eu	63	No	$\lesssim 0.05$ dex	Classical r-process tracer; key for constraining neutron-star merger contributions.
Gd	64	Yes	$\sim 0.05$ dex	r-process; probes r-process universality and Galactic enrichment history.
Dy	66	Yes	$\sim 0.05$ dex	r-process; useful for testing heavy-element nucleosynthesis models.
Er	68	Yes	$\sim 0.05$ dex	r-process; probes late-time enrichment and massive-star contributions.
Hf	72	Yes	$\sim 0.05$ dex	Third s-process peak; sensitive to high-neutron exposure in AGB stars; tracer of heavy-element build-up.
Pb	82	Yes	$\sim 0.05$ dex	Third s-process peak; traces strong s-process contribution; indicator of low-metallicity AGB enrichment.
Th	90	Yes	$\sim 0.05$ dex	r-process; radioactive chronometer for stellar ages and Galactic chemical evolution.
U	92	Yes	$\sim 0.05$ dex	r-process; radioactive chronometer; constrains age of the Universe and heavy-element nucleosynthesis.

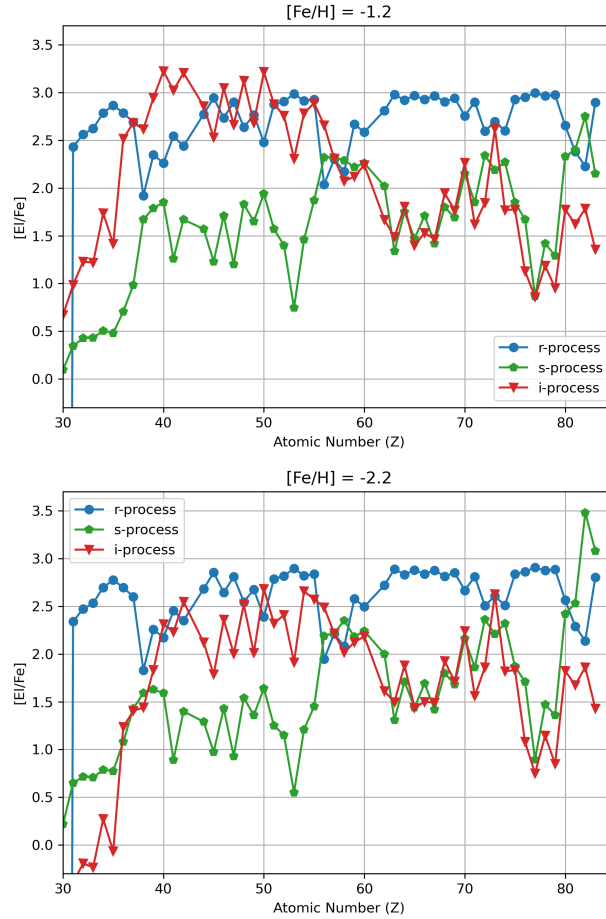


**Figure 3.5.** Nucleosynthetic signature of the three neutron capture processes for  $[\text{Fe}/\text{H}] = -1.2$  (top) and  $-2.2$  (bottom).

**Neutron-capture elements** To understand the precision of measurements of neutron-capture elements, additional simulations were performed for stars in six evolutionary stages. Three dwarfs in the main sequence with  $(T_{\text{eff}}, \log g) = (5800 \text{ K}, 3.7)$ ,  $(6400 \text{ K}, 4.1)$ , and  $(6000 \text{ K}, 4.5)$ . And three red giants with  $(T_{\text{eff}}, \log g) = (4800 \text{ K}, 1.2)$ ,  $(5000 \text{ K}, 2.0)$ , and  $(5200 \text{ K}, 2.5 \text{ dex})$ . For dwarfs and giants, microturbulence values  $1.2$  and  $2.0 \text{ km s}^{-1}$ , respectively, were assumed. For both cases, the projected rotational velocity was assumed to be zero. The grids were computed in four bins of metallicity,  $[\text{Fe}/\text{H}] = -1.0, -1.5, -2.0$  and  $-2.5$  dex. An  $\alpha$ -element enhancement of  $+0.4$  dex was assumed. A moderate carbon-to-iron ratio of  $[\text{C}/\text{Fe}] = 1.0$  dex was assumed to obtain a realistic blending of atomic lines with CH, CN, and MgH molecule features in the bluer wavelength regions. A constant carbon isotopic ratio of  $^{12}\text{C}/^{13}\text{C} = 19$  was assumed for the entire grid. Additionally, the element ratios  $[\text{Ba}/\text{Fe}]$ ,  $[\text{Ce}/\text{Fe}]$ ,  $[\text{Nd}/\text{Fe}]$  were moderately enhanced to  $+0.5$  dex. Element ratios with respect to iron of the elements of interest were chosen to cover the typical dispersions seen in the literature, i.e.  $[\text{X}/\text{Fe}] = 1.5, 1.0, 0.5, 0.0$ , and  $-1.0$  dex; where X may be Ba, Eu, La, and Pb, for example. Only for thorium, ratios of  $[\text{Th}/\text{Fe}] = 1.75, 0.75, 0.25$ , and  $0.0$  dex were assumed. The resulting simulations are shown in the Appendix in Figs. 12.5, 12.2, 12.3, and 12.4.

**Sulphur** For sulphur, we ran a series of feasibility experiments to assess the capability of measuring sulphur abundances in HRMOS-like stellar spectra. Synthetic spectra in the SI Multiplet 8 region were computed for atmospheric parameters  $T_{\text{eff}} = 5000, 4600$ , and  $4200 \text{ K}$  and  $\log g = 1.5, 2.0$ , and  $2.5$ , respectively. We adopted a microturbulence of  $1 \text{ km s}^{-1}$  and chemical compositions  $[\text{Fe}/\text{H}] = -1.0$ ,

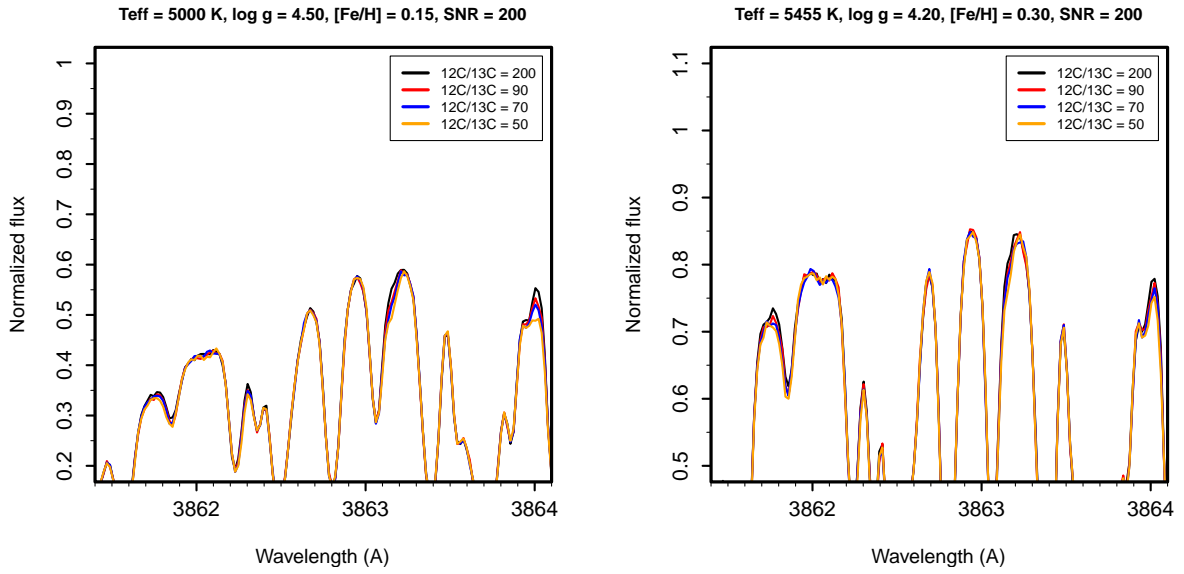


**Figure 3.6.** Simulated spectra of metal-rich dwarfs in regions containing  $^{12}\text{CH}$  and  $^{13}\text{CH}$  lines.

–1.5, and –2.0 with  $[\alpha/\text{Fe}] = 0.4$ . Figure 3.7 shows the resulting simulations, where the sulphur multiplet is clearly detectable in most cases. The line strength decreases, as expected, toward lower temperature and metallicity. Reliable sulphur abundances can be obtained for  $T_{\text{eff}} \gtrsim 4600$  K and  $[\text{Fe}/\text{H}] \gtrsim -1.5$ , while at  $T_{\text{eff}} = 4200$  K and  $[\text{Fe}/\text{H}] = -1.5$  the determination becomes uncertain but may still be feasible at higher SNR. The lowest-metallicity case ( $[\text{Fe}/\text{H}] = -2.0$ ) yields a very weak feature that is only marginally constrained, though it could be recovered with improved SNR or higher temperatures.

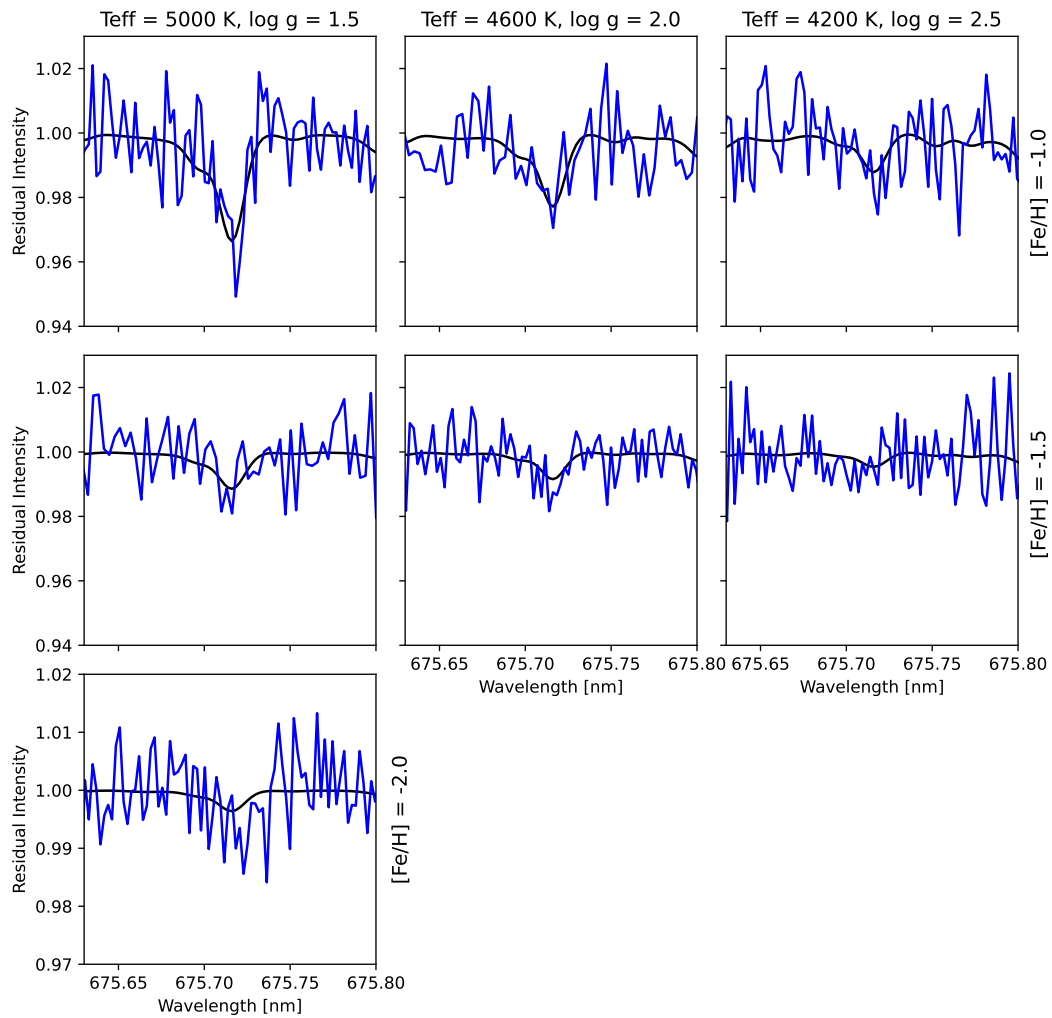


**Figure 3.7.** Simulated S I 675.7 nm line in giant stars. Synthetic broadened spectra (black) and spectra with SNR = 100 (blue) are compared in the different cases.

## 4 Hierarchical formation and evolution of nearby galaxies

The study of hierarchical galaxy formation remains one of the central open problems in astrophysics, as current observations provide only limited constraints on how merger events build up galaxies across different mass scales. In particular, while the Milky Way has revealed a rich merger history, comparable detailed constraints for its main satellites are still largely missing, leaving key questions on galaxy assembly, star formation histories, and the nature of dark matter. HRMOS will enable this leap forward by providing high-resolution, multi-object spectroscopy with the precision required to identify and chemically characterise accreted stellar populations across these systems.

### 4.1 Scientific context

#### 4.1.1 Hierarchical galaxy formation and dark matter microphysics

The standard  $\Lambda$ CDM cosmological model predicts that galaxies undergo hierarchical structure formation, where larger galaxies are gradually built through mergers and accretion events with smaller galaxies. Despite the tremendous success of  $\Lambda$ CDM, several issues have appeared, e.g. the low observed number of satellite galaxies - *The Missing Satellites Problem* (now mitigated by baryonic feedback, e.g. Homma et al. 2024; Jung et al. 2024; Kanehisa et al. 2024) - and the dark matter (DM) profiles in dwarf galaxies - *The Core Cusp Problem* (de Blok 2010). Ultimately, the hierarchical formation itself, i.e. how many galaxies of which size formed larger galaxies, remains poorly constrained from an observational point of view. In the last few years, tremendous progress has been made on this front in regards to our Milky Way. Largely thanks to the success of the *Gaia* space mission, around  $\sim 100$  potential merger events within the Milky Way have now been identified, and are currently being characterised (e.g. Ibata et al. 2021; Horta et al. 2023). These groundbreaking discoveries are revealing the hierarchical formation history of our own Galaxy, and providing an important testbed for the formation and evolution of galaxies. However, these detailed studies are mostly focused on one galaxy, our Milky Way, while other galaxies remain understudied.

#### Key Questions:

- How do galaxies form and evolve?
- What merger events shaped the formation and evolution of the Milky Way's closest companions?
- To what extent can the merger histories of galaxies reveal the microphysical properties of dark matter?
- How does the interaction with the Milky Way affect these galaxies?

**Table 4.1.** Properties of the Milky Way closest large companions (McConnachie 2012).

MW Satellite	Distance [kpc]	$M_{star}$ [ $10^6 M_{\odot}$ ]	$M_{dyn}$ [ $10^6 M_{\odot}$ ]
LMC	51	1500	$> 10^4$
SMC	64	460	$> 10^3$
Sagittarius	23	21	190

- What were the star formation histories and the chemical evolution of these galaxies and their progenitors?

The most promising way of advancing our understanding of hierarchical galaxy formation is to extend the studies done in the Milky Way to its largest companions (all conveniently located in the Southern hemisphere): the Large Magellanic Cloud (LMC), the Small Magellanic Cloud (SMC), and the Sagittarius (SGR) dwarf spheroidal (dSph) galaxies. Together with the Milky Way, these galaxies span over 3 orders of magnitude in stellar mass, see Table 4.1. The benefit of focusing on the largest satellite galaxies is clear: the larger the galaxy, the higher is the expected number of merger events (e.g., Salvadori et al. 2015). The predicted number of merger events for the three large satellite galaxies is shown in Fig. 4.1, adopting different assumptions for dark matter and galaxy evolution. These predictions are done in three main steps: 1) We first assume the theoretical prediction for the merger rate and DM halo mass growth as given in Fakhouri et al. (2010) for cold dark matter (CDM). 2) Merger rates in other DM scenarios are obtained by rescaling the CDM rate by suppression factors calculated with the Extended Press-Schechter formalism of Schneider (2015) and given in Benito et al. (2020). DM halo mass growth is assumed to be independent of DM microphysics. 3) DM mergers are transformed into galaxy mergers by adopting the galaxy occupation fractions and stellar mass-halo mass (SMHM) relations of Deason et al. (2022), bracketing uncertainties in galaxy formation models (including both high and low mass threshold for galaxy formation). The mapping between dark matter halo and galaxy mergers is inherently stochastic (see Deason et al. 2022 for details). Therefore, we repeat this step 10,000 times—obtaining 10,000 statistically identical and independent realisations—and use the median number of galaxy mergers as our final estimate.

From Fig. 4.1 emerges that the number of galaxy mergers at a given stellar mass depends both on the physics of galaxy formation models (left panels), as well as the properties of the dark matter - cold (CDM), warm (WDM) or fuzzy (FDM) and that these effects are degenerate: variations in galaxy formation efficiency can mimic or mask the effects of different dark matter models. Combined with other observable indicators (e.g. Wagner-Carena et al. 2024; Pöder et al. 2025), the merger histories of these galaxies are thus a powerful probe of both galaxy formation, as well as the dark matter physics. Currently, there are no available observational constraints on these predictions, and therefore it is quite possible that the real merger history is substantially different from our expectations. This would indicate that a serious revision of our understanding of galaxy formation and/or cosmology would be needed.

Experience from the Milky Way has taught us that to reliably identify such mergers, a combination of kinematics and precise chemical abundances is needed, for a large number of stars ( $\gtrsim 100$ ). In fact, the largest known merger event of the Milky Way, *Gaia* Enceladus (also known as the *Gaia* Sausage), was first identified through high-precision abundances of  $\sim 100$  stars with halo kinematics (Nissen & Schuster 2010, 2011). This merger event was then later confirmed by *Gaia*

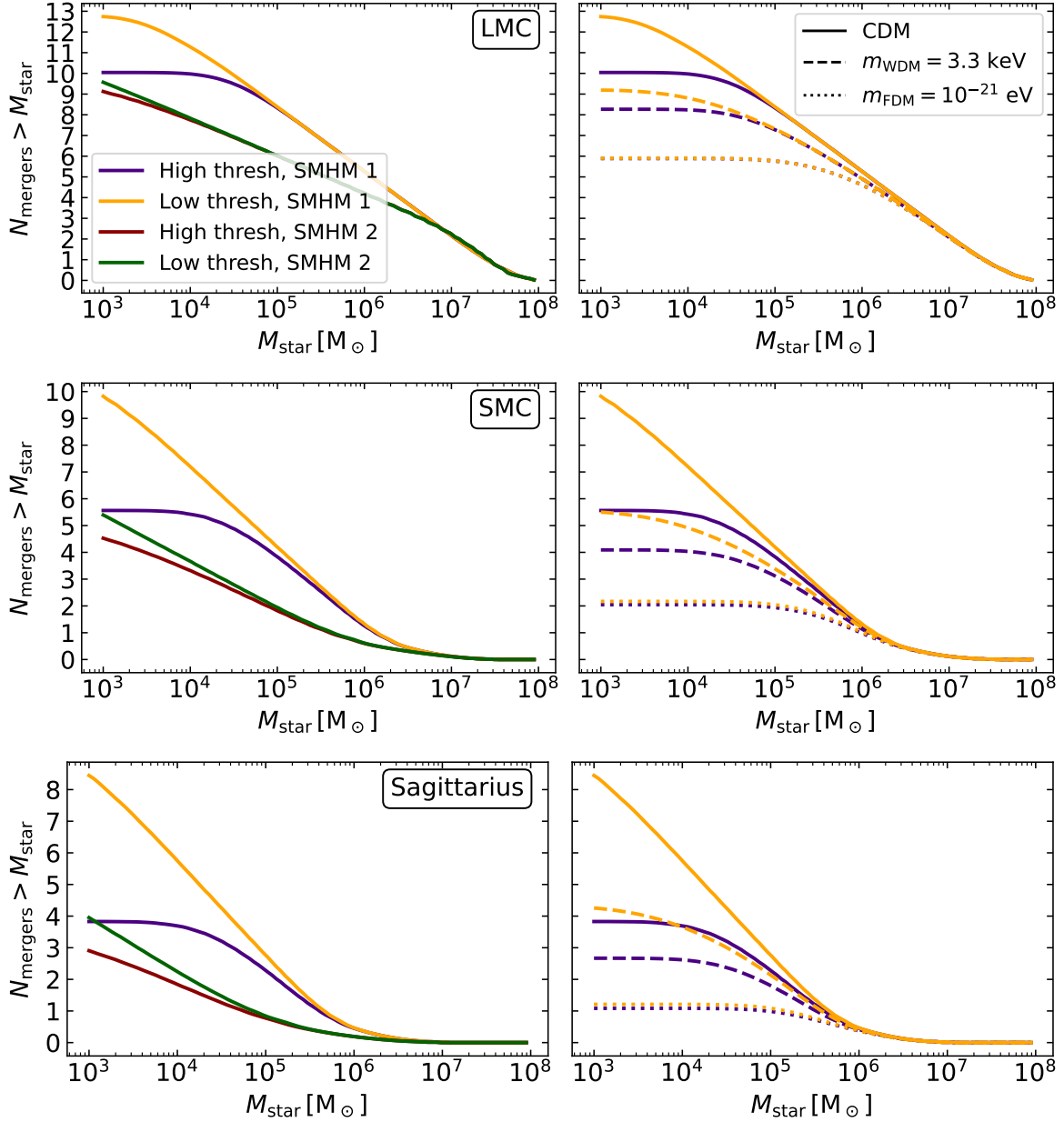


**Figure 4.1.** Predicted average number of mergers as a function of the stellar mass of the merging galaxy for the LMC (top), SMC (middle) and Sagittarius (bottom) galaxies. *Left:* CDM predictions for combinations of two galaxy occupation models (high and low threshold) and two SMHM relations (see Deason et al. 2022 for model details). *Right:* Predictions for the high and low threshold galaxy occupation models combined with the SMHM relation 1 under CDM, WDM, and FDM scenarios consistent with current observational limits (e.g. Benito et al. 2020; see Benito et al. 2025 for caveats regarding FDM).

data (e.g. Helmi et al. 2018; Belokurov et al. 2018). From studies in the Milky Way (and beyond) we have learned that candidates for merger events can be reliably pre-selected for follow-up via two main mechanisms: 1) As seen in both observations and simulations of the Milky Way, different merger events tend to cluster in kinematical spaces (e.g. energy vs. angular momentum), allowing for high probability of identifying even very small events (especially in the outskirts of galaxies). 2) Galaxies follow a very tight stellar mass-metallicity relation (e.g. Kirby et al. 2011; Tassis et al. 2012; Simon 2019), where their metallicity distribution (MDF) of stars typically has a pronounced peak around the mean-metallicity that can be predicted based on their stellar mass. Thus we can systematically search for mergers of a certain stellar mass by focusing the follow-up observations on the expected metallicity range (from the known mass-metallicity relation), where finding the merged stars will have much higher probability compared to at other metallicities (e.g. Buder et al. 2025).

At the time HRMOS is envisioned to start, we will be in an excellent position to efficiently preselect candidates of accreted stars for high-resolution follow up. At the end of the decade ( $\sim 2030$ ) the last data release of *Gaia* is envisioned, which will drastically improve the photometric and astrometric data of these relatively distant galaxies ( $\sim 20 - 60$  kpc). This will allow for a more accurate kinematical selection, and significantly improve the estimated stellar parameters and metallicities from the *Gaia* spectrophotometry. In addition, we will have spectroscopic data from two important multi-object spectrographs: 4MOST (de Jong et al. 2019) and MOONS (Cirasuolo et al. 2020). These will provide high quality metallicity measurements, which can be used to efficiently preselect stars for high-resolution follow-up observations. Furthermore, the data from these spectrographs are expected to show indications of merger events. However, to fully categorise these potential merger events (e.g. Skúladóttir et al. 2023), a higher-resolution MOS is needed with capabilities in the blue (where most diagnostics are, especially in the case of the metal-poor stars expected for smaller merger events) and with improved precision in abundance measurements (better than 0.05 dex). The HRMOS instrument will thus be a very timely addition to the ESO instruments, allowing us to build on and move beyond the science possible with the facilities currently being built.

#### 4.1.2 Star formation histories of the host and accreted galaxies

The multi-object capabilities of HRMOS will allow us to simultaneously look at the Star Formation Histories (SFH) of the main host galaxies themselves (LMC, SMC, SGR) as well as their progenitor galaxies, now merged within the main body. Chemical abundances are powerful tracers of the formation and evolution of galaxies as different elements have different timescales, e.g. Mg is formed primarily with core-collapse supernovae (ccSN,  $\sim 10^7$  yr), while Fe is formed both with ccSN and Type Ia SN (SN Ia,  $\sim 10^8-10^{10}$  yr), and heavy elements like Ba and Eu are formed on different timescales by AGB stars, and neutron star mergers (or rare supernovae), respectively (e.g. Kobayashi et al. 2020). Furthermore, the production of some elements such as Al are very metallicity dependent, giving further clues into the history of the galaxy. Abundance ratios therefore reveal details about the underlying star formation of systems, even those that are currently disrupted (e.g. Fernandes et al. 2024). The detailed abundance information can then be combined with kinematics and estimates of the stellar ages for an even more complete picture.

With unprecedented precision, HRMOS can measure spatial gradients of metallicity and chemical abundance ratios, tracing back the spatially resolved SFH of the host galaxies. Thus, HRMOS will reveal the universality of star formation and galaxy evolution, by showing whether these galaxies show signs of inside out formation, and spatially varying star formation. Furthermore, all these three galaxies are in a stage of varying interaction with the Milky Way: The Magellanic

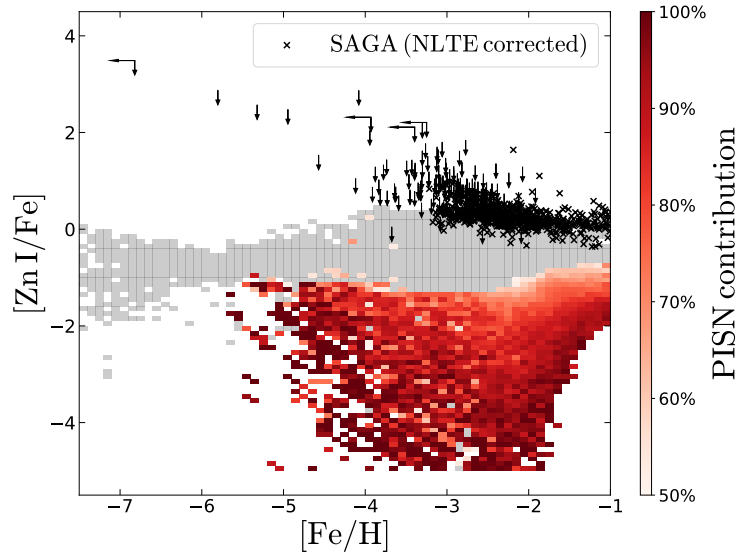


**Figure 4.2.** Predicted  $[\text{Zn I}/\text{Fe}]$  abundances for stars with  $> 50\%$  PISN enrichment is shown with red color bar, in the Milky Way halo. Other predicted stars are shown in grey, and black symbols are measured abundances corrected for NLTE effects. Adopted from Koutsouridou et al. (2025).

Clouds are most likely on their first infall (e.g. Besla et al. 2010), while Sagittarius shows clear evidence of tidal stripping (Ibata et al. 1994, 1995). With HRMOS we are thus able to identify and measure the effects that the interaction with the Milky Way has had on these galaxies.

Furthermore, through the identification of accreted systems, we can characterise the SFHs of small ancient systems that are now embedded within their hosts. This is a fundamental testbed for the star formation and chemical enrichment at the earliest times. In particular, in the Milky Way halo we see indications that the in-situ halo experienced a different chemical enrichment at earliest times compared to the surviving dSph galaxies (e.g. Skúladóttir et al. 2024b), but this needs further investigating. Finally, we can investigate how these merger events happened, and how the accreted stars were dissipated in the host galaxy, by looking at the current location of accreted stars from events occurring at different times in history.

Through the capabilities of HRMOS we can thus provide the complete history of these galaxies, through the evolution of the full age, chemical, and kinematical structures. Combined with our Milky Way, this will provide an invaluable benchmark of galaxy formation and evolution covering orders of magnitude in galaxy mass.

#### 4.1.3 Nucleosynthesis in the MW satellites

One of the key capabilities of HRMOS is the precise and accurate determination of stellar chemical abundances, essential for testing nucleosynthesis theories beyond the Milky Way across different astrophysical environments (see Chapter 3). Satellite galaxies are fundamental for a comprehensive understanding of these processes, as they provide a natural laboratory to probe environmental effects. The star formation in smaller galaxies is inefficient, which results in lower metallicities, and amplifies the impact of time-delayed nucleosynthetic sources (Hill et al. 2019; Kirby et al. 2019; Reichert et al. 2020; Skúladóttir & Salvadori 2020), such as SNIa, AGB stars, and neutron star mergers (NSM) via their kilonovae. This makes dwarf galaxies ideal to study the nucleosynthetic yields of such events, and to constrain their time-delay distributions, and their level of impact depending on environment, that is, star formation histories and mass loss due to stellar winds and SN explosions.

For this purpose, very high-resolution spectra at wavelengths shorter than 500 nm are essential, since this is where we find the key diagnostics for heavy elements (created through neutron-capture,  $Z > 30$ ) synthesised by AGB stars and NSM. For metal-poor stars, atomic lines at redder wavelengths become increasingly weak and most of the information can only be found in the blue region of the spectra. A large fraction of the needed information is thus not available in infrared studies such as APOGEE and MOONS. 4MOST will produce excellent catalogues of metallicities and lower-precision chemical abundances in both the Magellanic Clouds (The 1001MC survey; Cioni et al. 2019) and Sagittarius (4DWARFS; Skúladóttir et al. 2023), providing opportunities for very efficient follow up. HRMOS will thus be key in answering pressing scientific questions such as *Are there different dominant types of SN Ia in different galaxies?* (as suggested e.g. in Kirby et al. 2019; de los Reyes et al. 2020; Rigault et al. 2020; Nissen et al. 2024), and *What are the nucleosynthetic sites of the neutron-capture elements, their physical properties and delay-time distributions?* (see further discussion in e.g. Skúladóttir & Salvadori 2020; Schatz et al. 2022 and Chapter 3 in this White Paper).

#### 4.1.4 Descendants of zero-metallicity Pair-Instability Supernovae

The first stars created after the Big Bang were the sources of the first metals and ionizing radiation in the Universe, and were thus fundamental in starting reionization and shaping the early stages of galaxy formation (e.g., Bromm 2013). Various theoretical predictions and indirect observational evidence suggest that these stars were typically more massive than those formed today, up to  $1000 M_{\odot}$  (e.g., Hirano et al. 2014; Rossi et al. 2021; Klessen & Glover 2023). In particular, the zero-metallicity stars that formed in the mass range  $140\text{--}260 M_{\odot}$  are predicted to explode as Pair-Instability Supernovae (PISN), leaving behind a very unique abundance pattern characterised by a strong odd-even effect and extremely low abundances of Zn and Cu (Heger & Woosley 2002; Takahashi et al. 2018). Finding primitive stars with the abundance pattern from these stars would establish their existence. Understanding their fractions in various populations of the Milky Way and its satellite galaxies (e.g. Salvadori et al. 2015; Rossi et al. 2025) has been shown to be some of the most important observational constraints to determine the mass distribution of the first stars (Koutsouridou et al. 2024), which greatly impacts the following metal enrichment and the overall galaxy formation process (e.g. Brauer et al. 2025).

Despite decades long searches, no unambiguous descendant of zero-metallicity PISN has been found (e.g. Skúladóttir et al. 2024a; Thibodeaux et al. 2024; Bonifacio et al. 2025). However, with the advent of large spectroscopic surveys such as 4MOST and WEAVE, this is expected to change. Such surveys will likely find dozens, if not hundreds of candidates for PISN descendants that will need follow-up from other facilities. Most importantly, none of the upcoming spectroscopic surveys (4MOST, WEAVE, APOGEE) will be able to measure Zn in low-metallicity stars, which is the smoking gun for PISN enrichment (Salvadori et al. 2019; Vanni et al. 2024). This is clearly illustrated in Fig. 4.2. With HRMOS this can be done very efficiently, especially in the satellite galaxies where this can easily be combined with the aforementioned science cases. Following up these candidates is fundamental for identifying true descendants of PISN (see e.g. Aguado et al. 2023) but also to be able to exclude false positives, as finding no such PISN descendants in the very large samples of 4MOST will provide stringent constraints on the mass distribution of the first stars (Koutsouridou et al. 2024).

#### 4.1.5 Binary properties

More than half of the stars in the Galactic field are in binary systems (Duquennoy & Mayor 1991). These stellar systems have an important role in stellar astrophysics. The fraction and the

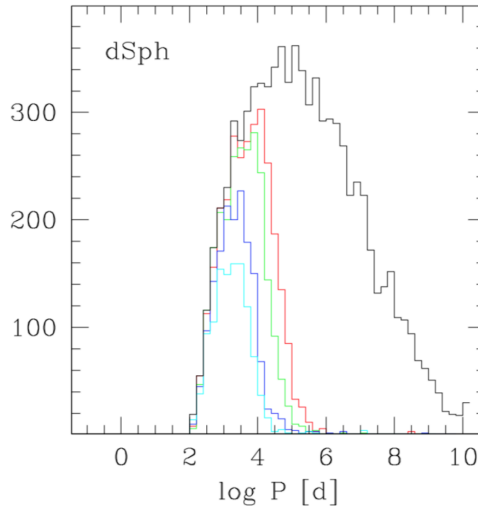


**Figure 4.3.** The number of detected binaries with period,  $P$ , during simulated 5-year mock observations with 5 epochs for a typical dSph galaxy (Sculptor). Black lines show the assumed underlying distributions while coloured lines show different assumption of the radial velocity precision,  $\sigma_o = 0.02$  (red),  $0.1$  (green),  $0.5$  (blue) and  $1 \text{ km s}^{-1}$  (cyan). *Credit: A. Sollima.*

characteristics (distribution of periods, mass-ratios, eccentricities) of a binary population is expected to depend on the environment where they live (e.g. Minor 2013). It is therefore of crucial importance to study the relative frequency and the characteristics of binary stars in different environments. However, to date, a thorough census of the properties of binary systems is available only in the Solar neighbourhood (e.g. Penoyre et al. 2022), and such studies are being expanded with *Gaia* data (e.g. El-Badry et al. 2021). Only sparse studies, performed using low- and intermediate-resolution radial velocity surveys on relatively small numbers ( $< 500$ ) of stars have been performed on stellar systems like star clusters and dwarf galaxies (Minor 2013; Spencer et al. 2018).

Dwarf galaxies provide an excellent environment for binary studies, as they are large and diffuse enough that their binary systems should remain mostly unaltered. These galaxies can thus be used as test-beds to understand star formation - especially at lower metallicities - and their binary fractions and orbital characteristics also provide information about the initial conditions under which the stars in the galaxy formed. Unfortunately, not much is known about the fraction and period distribution of binary star systems in dwarf galaxies. The most comprehensive studies were carried out by Minor (2013); Spencer et al. (2018) and Arroyo-Polonio et al. (2023) on between 4 and 7 of the “classical” dSph galaxies satellites of the Milky Way. These studies were based on multi-epoch data with radial velocity precision of  $1 - 3 \text{ km s}^{-1}$ , thus limited to binaries with periods  $P < 10$  years, and in general consisted of samples obtained with heterogeneous facilities and/or small number statistics.

With HRMOS, these studies can be drastically improved. Fig. 4.3 shows how the precision of line-of-sight velocities affect the detectable part of the binary period distributions. With HRMOS in satellite galaxies, we expect  $\sigma < 0.05 \text{ km s}^{-1}$  at the typical SNR obtained in these galaxies, meaning an improvement of an order of magnitude compared to the current state-of-the-art and what is expected from 4MOST ( $\sigma \sim 1 - 2 \text{ km s}^{-1}$ ), even when taking into account the effects of jitter,  $\sigma \sim 0.35 \text{ km s}^{-1}$  (see Magrini et al. 2023, Chapter 7.4). Importantly, 4MOST will provide a valuable baseline in the Satellite galaxies (expected start of surveys in 2026), which can be combined with the much higher precision of HRMOS about  $\sim 10$ -15 years later, and thereby drastically improve our knowledge of binary properties in different environments.

## 4.2 Simulations

The key requirement to be able to fulfil the science cases presented in this Chapter 4 are precise and accurate chemical abundance measurements (better than 0.05 dex). When it comes to identifying accreted events, there are several abundance ratios that are critical. The discovery of the last major merger of the Milky Way, *Gaia* Enceladus, (Nissen & Schuster 2010, 2011) showed that the chemical abundance ratios of the accreted galaxy separated from the Milky Way at the same [Fe/H]. The same is true also for other mergers (Mori et al. 2025). In particular, the abundance ratios of Na, Mg, Ni, Si, Ca, Ti, Cu, Zn, Y, and Ba differed substantially in their [X/Fe] ratios when comparing the accreted population to the stars formed in situ. Later works analysing the same sample have also shown clear differences in the abundances of C and O (Nissen et al. 2014; Amarsi et al. 2019b); Al (Skúladóttir et al. 2025; Ernandes et al. 2025); Sc, V, and Co (Nissen et al. 2024); as well as Zr and Eu (Fishlock et al. 2017). All of these elements will be accessible with HRMOS.<sup>1</sup>

The separation between galaxies in these chemical abundance ratios stems from the diverse star formation and chemical evolutionary history of these galaxies, and allow us to distinguish stars born in different in environment. Out of these elements, Mg is arguably the most important. The element Mg is unique in the sense that it purely traces the production of ccSN and it is relatively easy to measure (while the other pure ccSN  $\alpha$ -element, O, is more challenging).

This has two important consequences. Firstly, [Mg/Fe] ratios show a cleaner separation between galaxies compared to other  $\alpha$ -elements such as Si, Ca, and Ti which are produced both by ccSN and SNIa. In fact, high-precision abundances of [Mg/Fe] taking into account 3D NLTE effects (Nissen et al. 2024; Matsuno et al. 2024) have also been shown to separate not only between stars from different galaxies, but also between stars formed at different locations in the same, now-accreted galaxy (Skúladóttir et al. 2025). Secondly, the elemental ratios [X/Mg] are very sensitive to star formation histories, and can be used to constrain the time delay distribution of delayed processes such as SNIa, AGB, NSM (e.g. Skúladóttir & Salvadori 2020). These elemental ratios (e.g. [Y/Mg]) have further been shown to have very strong correlation with stellar age, and that each trend is dependent on the environment (e.g. Nissen 2015; Feltzing et al. 2017; Skúladóttir et al. 2019; Jofré et al. 2020).

In version 1 of the HRMOS white paper (Magrini et al. 2023, their Fig. 33), it was shown that for [Fe/H] a precision  $\lesssim 0.1$  dex was reached both in the green and blue spectra at SNR=20. By combining all three arms, this precision is then even further improved. For optimal identification of different merger events, a similar precision for Mg is preferred. Fig. 4.4 shows the precision of Mg that can be achieved as a function of SNR from the Mg<sub>I</sub> triplet at  $\sim 520$  nm. For a typical metallicities of the accreted galaxies of [Fe/H]  $\lesssim -1.0$ , such precision can be reached with  $SNR \gtrsim 40^2$  in the green arm of HRMOS for a K-type giant, in 2 h of exposure at  $G = 15.8$ , and is achievable down to  $G = 16.8$  in 6 h.

When it comes to the blue region, the high-resolution of HRMOS becomes even more important. The brightest and most suitable targets in the MCs and Sagittarius are evolved red giants, which means that the blue region is very dense with atomic and molecular lines. Thus, the continuum very challenging to determine in intermediate-resolution spectra such as 4MOST - especially at the modest SNR  $\sim 10 - 25 \text{ pix}^{-1}$  expected for these observations in the blue. This will greatly affect the precision and accuracy achievable with the 4MOST data in this region. Fig. 4.5 shows a comparison of the HRMOS spectra (top row) with that of 4MOST (lower row). Here we focus on two key elements, Al which is a very good tracer of accreted populations, and Eu which is the canonical

<sup>1</sup>In the case of C, accurate abundance measurements will only be accessible in a part of the expected metallicity and abundance range (through C I and CH), but CN molecular lines should always be present.

<sup>2</sup>The ETC results for HRMOS (see Fig. 1.1) are reported per resolution element

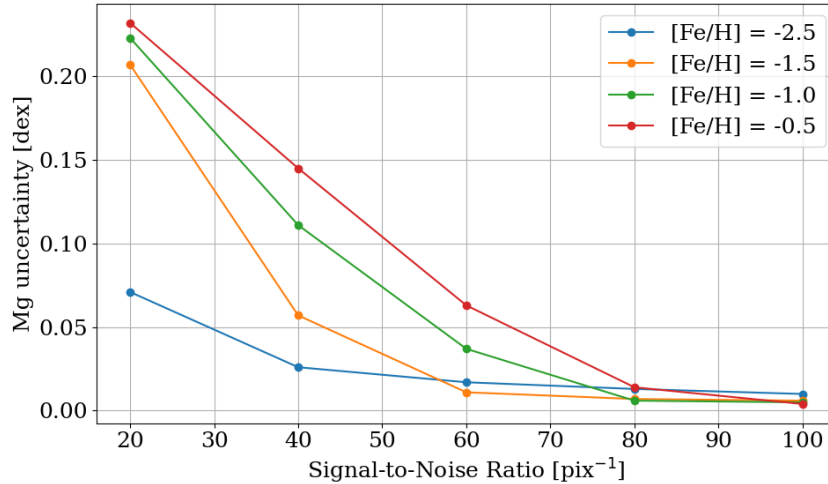


**Figure 4.4.** Precision of Mg measurements as a function of SNR, assuming a typical evolved giant with  $\log g = 1.5$ , and  $[\text{Mg}/\text{Fe}] = 0.0$ , measured from the two redder lines of the Mg i triplet at  $\sim 518$  nm. Strong wings of the lines at higher  $[\text{Fe}/\text{H}]$  result in less precision.

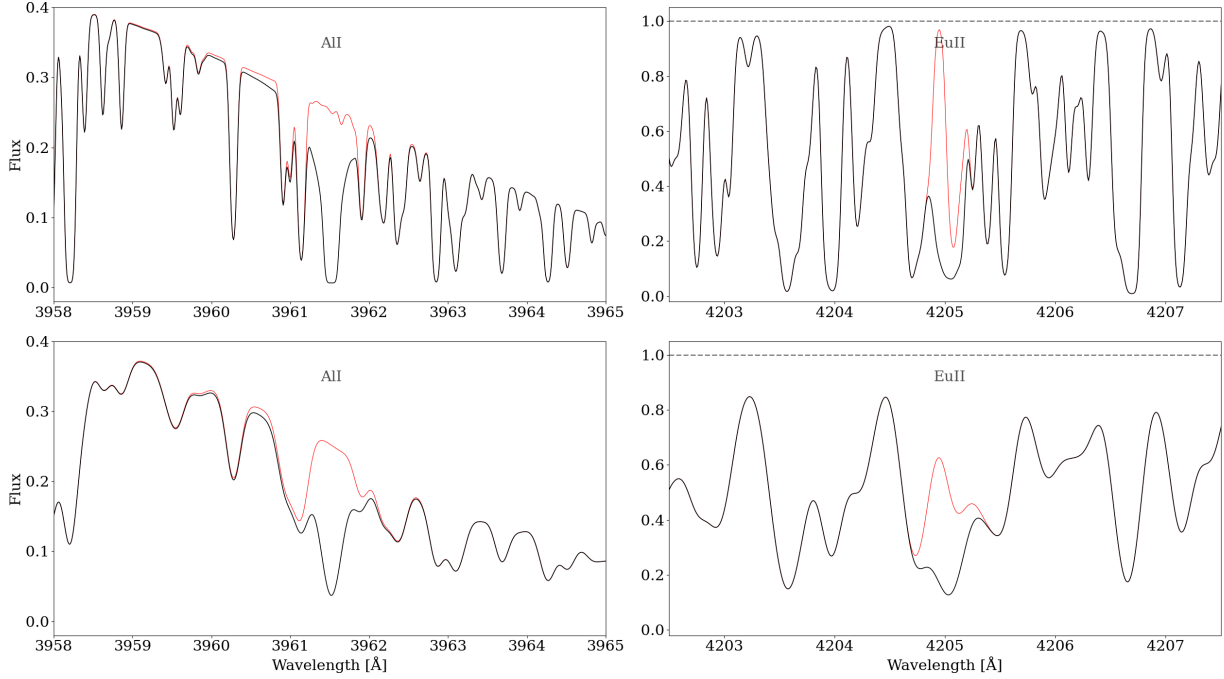
tracer of the rapid neutron-capture process (from ccSN and NSM). The degree of blending with other lines in the 4MOST spectra adds greatly to the uncertainties, but even more importantly the lower resolution spectra lacks reliable continuum points, which is expected to cause significant systematic errors as well as lower precision.

In addition, the 4MOST strategy is such that the entire survey plan is decided before start of operations for the whole 5 year survey (de Jong et al. 2019). This means that in the case of interesting discoveries, such as indication of merger events, they cannot be followed up for higher SNR in a focused way within the respective 4MOST survey. Finally, the more precise and accurate chemical abundances achievable with HRMOS will be an invaluable training set that can be used to improve the pipelines used to analyse the 4MOST data. Such a training set is greatly needed, as the abundance patterns of these galaxies are known to be significantly different from those observed in the Milky Way at similar  $[\text{Fe}/\text{H}]$ . The information that HRMOS will provide will thus be propagated onto the  $> 10^5$  RGB stars that will be targeted by the 4MOST surveys (Cioni et al. 2019; Skúladóttir et al. 2023), greatly improving the precision and accuracy of these large data.

### 4.3 Potential targets

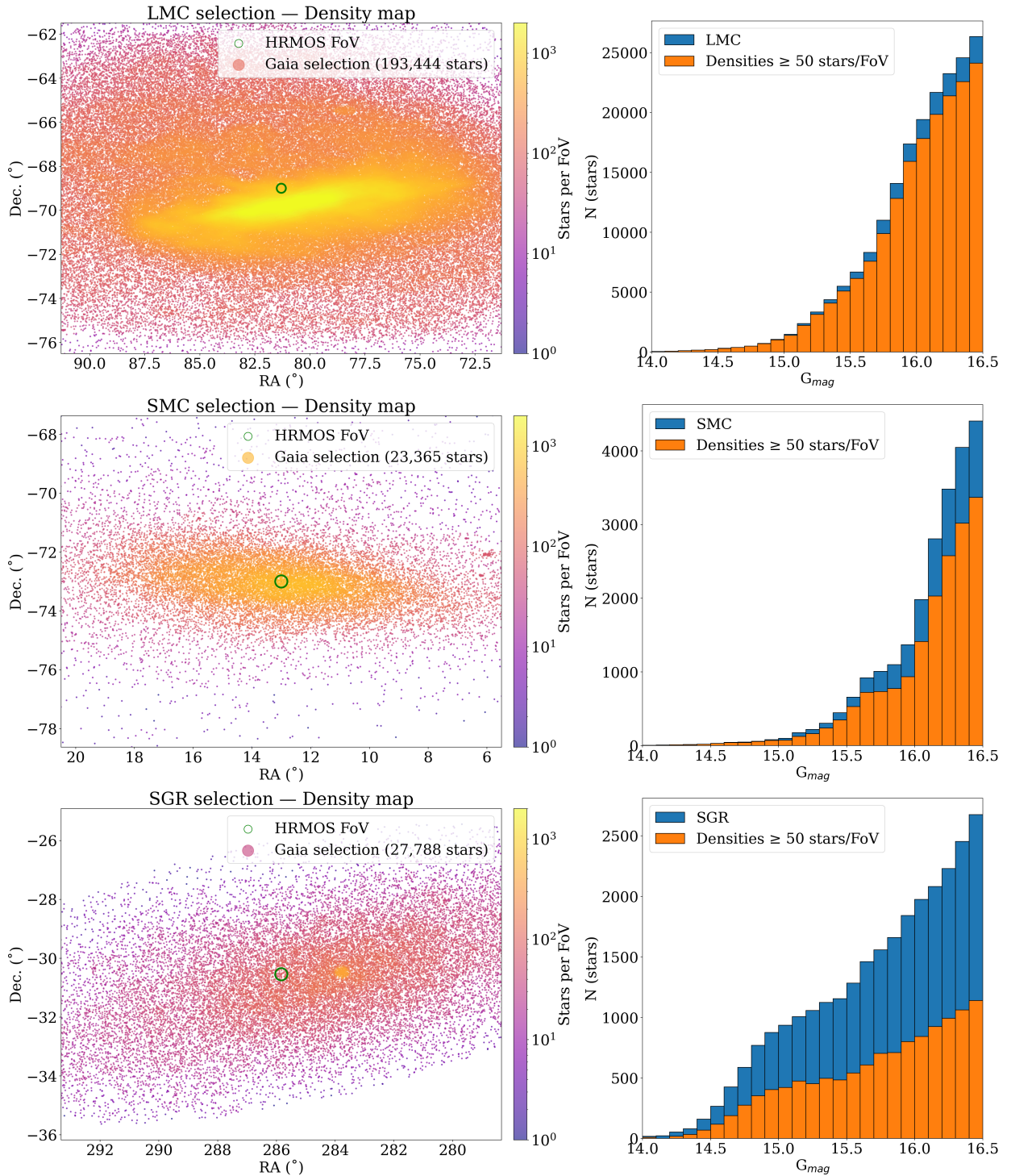
The key targets to study the hierarchical formation of external galaxies are the three large and nearby satellite galaxies of the Milky Way, see Table 4.1. Our science case relies on tracing old stellar populations (age  $\sim 1$ -14 Gyr). Getting high SNR is limited to the brightest stars in these galaxies, therefore the RGB stars will be the key targets. Thanks to its multi-object capability, HRMOS can very efficiently obtain high-quality spectra of 100s of stars. As an example, with 6h observations of one FoV covering 50-60 stars with  $G \leq 16.5$  using HRMOS, we can expect a  $\text{SNR} \approx (25, 70, 100)$  per resolution element for the faintest stars in the blue, green, and red arms, respectively. The brighter populations in the field,  $G = 15.5$ , will reach a  $\text{SNR} \approx (60, 130, 200)$  for the same exposure time.

Fig. 4.6 (left panels) shows the density of RGB stars with  $G \leq 16.5$  in the three target galaxies based on *Gaia* DR3, illustrating the need and benefits of a multi-object spectrograph. The densities in the central regions of the LMC and SMC reach as high as  $\sim 10^3$  stars per FoV of HRMOS. This means that there is substantial flexibility to focus on rare populations, and limit the targets to



**Figure 4.5.** Synthetic spectra (black) for a typical star representative of our samples ( $T_{\text{eff}} = 4500 \text{ K}$ ,  $\log g = 1.0$ ,  $[\text{Fe}/\text{H}] = -0.5$ ) around the Al I 396.1 nm line (left), and the Eu II 420.5 nm line (right) with HRMOS resolution ( $R=80,000$ ) at the top, compared to 4MOST resolution ( $R=20,000$ ) at the bottom. Red lines show the synthetic spectra without Al (left) or Eu (right) present.

brighter stars for shorter exposure times and/or higher SNR. The right panels of Fig. 4.6 show the histograms of stars as a function of  $G$  magnitude for the three large Milky Way Satellites, highlighting those in locations where the target density is  $\geq 50$  stars/FoV. The total number of potential targets in regions where all the HRMOS fibres can be exploited is  $> 10^5$  stars in the selected magnitude range of  $G \leq 16.5$ . However, we emphasise that even in the outer regions of the galaxy where there are only  $\sim 10$  stars/FoV, the multi-object capabilities of HRMOS are still crucial for making it possible to get the necessary number of stars ( $\sim 10^2 - 10^3$ ) for the science cases presented. Furthermore, any free fibres can always be used to target fainter stars for less detailed but still highly informative chemical abundance information. An example of a potential observational strategy is given in Section 11.3, where it is shown that the fibre configuration of HRMOS is very suitable for observations in these large satellites, where the density of potential targets is much less crowded than in the typical globular cluster.



**Figure 4.6.** The three large and nearby Milky Way satellite galaxies, RGB members with  $G \leq 16.5$ . *Left:* Spatial distribution of stars, colour coded by the number of stars per FoV (green circle,  $d = 25'$ ). *Right:* Histogram of all stars with  $G \leq 16.5$  (blue) and those located in regions with densities  $\geq 50$  stars/FoV (orange).

## 5 Nucleocosmochronology: Constraining Cosmology from the Ages of the Oldest Milky Way Stars

Stellar ages of the oldest populations provide a lower limit on the age of the Universe and a complementary probe of the Hubble constant, providing constraints to the Hubble tension. Nucleocosmochronology, based on the thorium (or uranium) over europium abundance ratio, offers an independent route to stellar ages, directly comparable to  $\Lambda$ CDM predictions for the cosmic age. HRMOS will enable large-scale application of this method through high-resolution spectroscopy of globular cluster stars, improving precision by averaging measurements over large numbers of cluster members. This will yield robust and precise ages for globular clusters, enabling a direct and stringent test of cosmological consistency.

### 5.1 Scientific context

Precise and accurate absolute age determinations of the oldest stars at  $z = 0$  provide a direct and largely model-independent lower limit on the age of the Universe (Cimatti & Moresco 2023; Tomasetti et al. 2026). In the current cosmological landscape, robust progress relies on the availability of multiple, complementary probes. Such measurements are required not only to place new constraints on key parameters—most notably the Hubble constant ( $H_0$ )—but also to identify, quantify, and mitigate systematic effects affecting different observational approaches (see e.g. Moresco et al. 2022). The present *Hubble tension*, reflecting the discrepancy between early-Universe measurements (e.g. from the CMB) and late-Universe determinations based on local distance ladders, strongly motivates the exploration of stellar age-based constraints.

In this context, the use of the oldest stellar populations as cosmic clocks offers a powerful approach, since stellar age determinations are independent of cosmological assumptions such as the underlying expansion history or the matter–energy content of the Universe. As such, they provide a lower bound on the age of the Universe that can be directly compared with cosmological age estimates inferred within the  $\Lambda$ CDM framework, offering a stringent consistency test of the standard cosmological model. Indeed, forecasts based on the covariance analysis presented by Cimatti & Moresco (2023) show that, by reducing uncertainties on age determinations below 0.5 Gyr (the lighter part of the matrix presented in their Figure 5), such measurements can lead to competitive constraints on  $H_0$ , potentially decreasing current uncertainties by a factor of three. In particular, an improved estimate of the cosmic age from stellar clocks directly translates into a constraint on the present-day expansion rate, providing a new handle on the origin of the Hubble tension.

Looking beyond  $H_0$ , age-based constraints from the oldest stellar populations also offer the possibility to probe a wider range of cosmological parameters, since combining stellar age measurements with other probes can help constrain extensions to the standard cosmological model and explore deviations in the early expansion history of the Universe. Age dating of ancient stars therefore represents not only a complementary tool for addressing the Hubble tension, but also a promising avenue for testing new physics in cosmology, without relying on traditional distance-based methods.

In recent years several studies have explored the use of stellar ages as cosmological probes,

employing a variety of techniques -mostly isochrone fitting- to derive ages (see Tomasetti et al. 2026, and references therein), highlighting that both precision and accuracy are key to this effort. In this Chapter we make the case that HRMOS has the potential to bring a transformative contribution to this field: it will indeed allow for the first time model-independent, direct age determination of a large number of old stars through precise measurements of the abundances of long-lived radioactive isotopes, such as those of thorium and uranium, formed in the astrophysical  $r$ -process of nucleosynthesis, the so called nucleocosmochronology (see, e.g. Meyer & Truran 2000).

We will also discuss that, in addition to its cosmological applications, nucleocosmochronology provides a crucial method to determine the absolute ages of field stars. This technique can be used to distinguish between stellar populations in the Galactic halo that formed in situ and those accreted through past merger events, thereby offering insights into the assembly history of the Galaxy (Hansen et al. 2018).

### Key Questions:

- How old is the Universe?
- How do *new, independent* age determinations contribute to the  $H_0$  tension?
- How do the ages of ancient, most metal-poor stars inform our understanding of the Milky Way halo's assembly?

## 5.2 The method: Nucleocosmochronology

Radioactive isotopes with half-lives of several Gyrs provide an independent route to measuring the time spanned between when the radioactive isotope was produced and today ( $\Delta t$ ). In old stars,  $\Delta t$  is a good proxy for the age of the star itself (see below), and the method is commonly referred to as nucleocosmochronology (pioneered by Butcher 1987). Among the isotopes that can be used are the heavy neutron-capture elements  $^{232}\text{Th}$  and  $^{238}\text{U}$  with half-lives  $\tau$  of 14.5 and 4.5 Gyr, respectively. The method typically relies on measuring the abundance ratio of thorium and/or uranium with respect to stable isotopes that are believed to be co-produced in a single nucleosynthetic process, such as, for example, europium (e.g. Goriely et al. 2011; Kratz et al. 2014; Hill et al. 2017). There is a consensus to attribute this production to the  $r$ -process (see Shah et al. 2026a, and references therein). The measured ratio is then compared to the initial one. The basic relation between the initial abundance ratio of a radioactive (Y, with a half-life  $\tau$ ) to stable (X) isotope is:

$$(Y/X)_{\text{today}} = (Y/X)_{\text{initial}} \times e^{-\ln 2 \Delta t / \tau},$$

which allows one to derive the  $\Delta t$  time between the production of the radioactive isotope and when it is observed, for Th and U:

$$\begin{aligned} \Delta t &= 46.67 \times (\log(\text{Th}/X)_{\text{initial}} - \log(\text{Th}/X)_{\text{today}}) \\ \Delta t &= 14.84 \times (\log(\text{U}/X)_{\text{initial}} - \log(\text{U}/X)_{\text{today}}) \\ \Delta t &= 21.83 \times (\log(\text{U}/\text{Th})_{\text{initial}} - \log(\text{U}/\text{Th})_{\text{today}}) \end{aligned} \tag{5.1}$$

The  $\Delta t$ , thus derived, is a measure of the time between production of the radioactive isotope and today, and is in fact the combination of the time spanned between the production time (i.e.

the birth of the star), and the current age of the star. In the oldest stars in the Milky Way, one can expect that the latter dominates largely. This has led to use the Th/X, U/X and Th/U to infer the ages of old (mostly *r*-process enhanced) metal-poor stars (e.g. Sneden et al. 1996; Cayrel et al. 2001; Hill et al. 2002; Mashonkina et al. 2014). Initial production ratios, which are critical for an accurate estimate of the age, are discussed in Section 5.5 below.

As it can be appreciated in Eq.5.1, exquisite abundance ratios are needed to allow precise age determinations, since even relatively low uncertainties of 0.1 dex in the abundance ratios of  $\log(\text{Th}/X)$  or  $\log(\text{U}/X)$  will turn into age uncertainties of 4.7 and 1.5 Gyr, respectively. Only with the highest resolution ( $R = 80,000$ ), along with extremely high signal-to-noise and statistical power allowed by HRMOS on an 8 m class telescope breakthrough results can be obtained in this field. While measurements of Th in field stars are available for less than 100 stars (Shah et al. 2026a), a small fraction of these are for globular cluster stars. As for U, it was first detected by Cayrel et al. (2001), and more than two decades later, is still only measured in a handful of stars (Cayrel et al. 2001; Hill et al. 2002; Cowan et al. 2002; Frebel et al. 2007; Hill et al. 2017; Placco et al. 2017; Holmbeck et al. 2018; Yong et al. 2021; Roederer et al. 2024).

The capability of HRMOS to systematically measure Th, and to some extent U, in cluster and field stars, opens up a new window into stellar ages of the oldest populations in the Milky-Way and, with implications for cosmology and the timescales for the first formation of low-mass stars in the Universe.

Below, we first assess the feasibility of Th and U abundance measurements with HRMOS using both synthetic and observed spectra. We then discuss the theoretical framework underlying these measurements, highlighting the key assumptions and limitations relevant to nucleocosmochronology. Finally, we present the selection criteria for suitable targets and outline a possible observing strategy for measuring Th in old field stars and globular clusters. We also provide estimates of the expected uncertainties in the derived stellar ages, emphasizing the unique capability of HRMOS to deliver precise nucleocosmochronology for a large and diverse sample of ancient stars. Particular attention is devoted to the discussion of systematic effects and accuracy limitations, which are crucial for establishing reliable absolute age determinations.

### 5.3 Feasibility of high-precision Th and Eu abundance measurements

#### 5.3.1 Thorium abundances

Thorium abundance measurements require analysis of highly blended absorption lines (e.g., Mishenina et al. 2022; Caffau et al. 2008; Hansen et al. 2018). This section demonstrates the capability of HRMOS in detecting Th abundances based on synthetic and real spectra. We focus on the strongest Th absorption line in the HRMOS spectral range: the line at 401.9 nm. An example of the spectral region covering this line is shown in Figure 5.1 for a metal-poor stars at different spectral resolutions.

We first test the detectability of the Th 401.9 nm line. The linelist is based on VALD, but modified according to Mishenina et al. (2022) for this transition. Detectability is quantified following Kordopatis et al. (2023a) using the On-the-fly line selection code<sup>1</sup>. Spectra are synthesised with Korg (Wheeler et al. 2023) and smoothed to  $R = 80,000$ . Our analysis indicates that the Th 401.9 nm line remains detectable down to  $[\text{Fe}/\text{H}] \sim -2$ , making spectral coverage of this feature essential (see, also Hansen et al. 2018). A very high signal-to-noise ratio is not strictly required for detection, whereas high spectral resolution is crucial for reliable line identification and deblending. The line is more severely blended in Sun-like stars than in giants, likely because the Th feature is

<sup>1</sup><https://github.com/tadmatsuno/SelectLinesOnthefly>

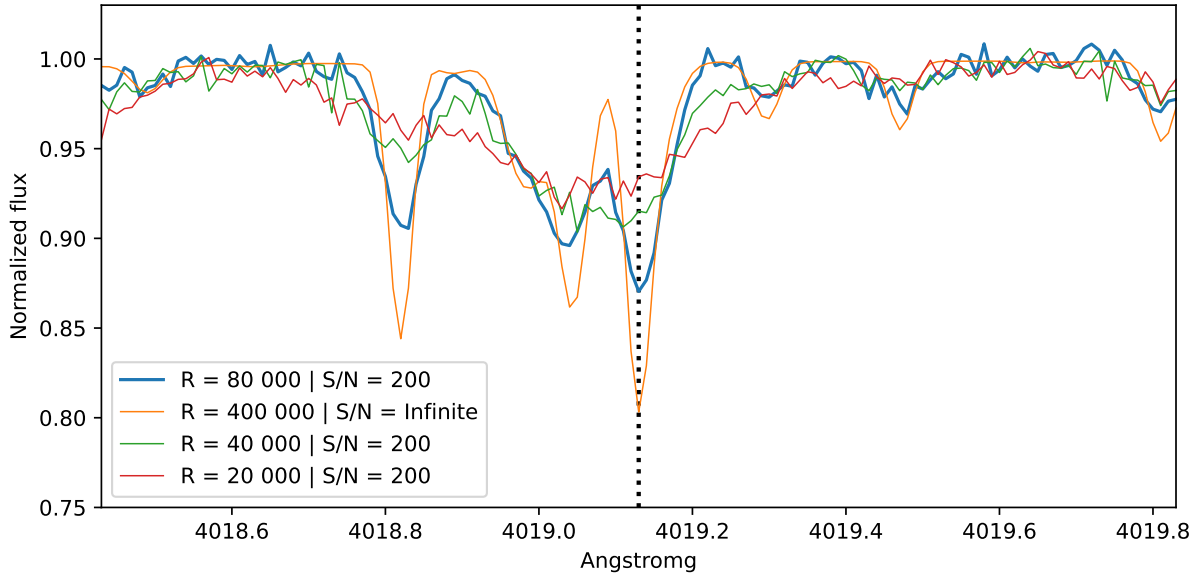


**Figure 5.1.** Simulated spectra in the region of the Th line (indicated with a vertical dotted line) at different resolution, as indicated in the legend.

intrinsically stronger in the latter. We note that continuum normalisation can be challenging in metal-rich giants; however, this does not affect our science case, which is focused on metal-poor stars.

We further investigate the abundance precision that can be achieved (Figure 12.1 in the Appendix). For this test, synthetic spectra were generated using the radiative transfer code *TURBOSPECTRUM* (Plez 2012) with MARCS model atmospheres (Gustafsson et al. 2008), assuming a UVES-like wavelength sampling of 0.0012 nm. The spectra were then degraded to a resolving power of  $R = 80\,000$  and injected with noise corresponding to representative S/N between 50 and 400. The input chemical composition adopted for the synthesis includes an  $\alpha$ -element enhancement of +0.4 dex, a carbon-to-iron ratio of  $[C/Fe] = 1$  dex with an isotopic ratio of  $^{12}C/^{13}C = 19$ , and  $[Ba/Fe]$ ,  $[Ce/Fe]$ , and  $[Nd/Fe]$  ratios of 0.5 dex.

Table 5.1 summarizes the uncertainties in the derived Th abundances for different stellar types, metallicities, and signal-to-noise ratios.

Thorium abundances can be recovered with a precision better than 0.05 dex in most cases where the line is enhanced ( $[Th/Fe] = 1.75, 0.75$ , or  $0.25$ ), as is commonly expected in the metal-poor regime. For very high-quality spectra ( $S/N = 400$ ), the precision can reach values as low as  $\sim 0.01$  dex. In cases without Th enhancement, achieving comparable precision requires substantially higher signal-to-noise ratios (typically  $S/N \gtrsim 200$ ).

Overall, giant stars provide systematically more precise measurements than dwarfs, owing to their stronger and less blended Th spectral features.

S/N	Stage	[Fe/H] = -1.0				[Fe/H] = -1.5				[Fe/H] = -2.0				[Fe/H] = -2.5				
		1.75	0.75	0.25	0	1.75	0.75	0.25	0	1.75	0.75	0.25	0	1.75	0.75	0.25	0	
100	6000 K - 4.5 dex	0.06	-	-	-	0.12	-	-	-	-	-	-	-	-	-	-	-	-
	6400 K - 4.1 dex	0.06	-	-	-	0.09	-	-	-	-	-	-	-	-	-	-	-	-
	5800 K - 3.7 dex	0.05	0.12	-	-	0.06	-	-	-	0.10	-	-	-	-	-	-	-	-
	5200 K - 2.5 dex	0.05	0.05	0.08	0.11	0.04	0.07	0.13	0.22	0.03	0.15	-	-	0.05	-	-	-	-
	5000 K - 2.0 dex	0.05	0.03	0.05	0.06	0.04	0.05	0.09	0.14	0.03	0.08	-	-	0.04	0.19	-	-	-
	4800 K - 1.2 dex	0.06	0.03	0.03	0.04	0.05	0.04	0.05	0.06	0.04	0.05	0.09	0.13	0.04	0.08	-	-	-
150	6000 K - 4.5 dex	0.04	-	-	-	0.08	-	-	-	0.20	-	-	-	-	-	-	-	-
	6400 K - 4.1 dex	0.03	0.20	-	-	0.06	-	-	-	0.16	-	-	-	-	-	-	-	-
	5800 K - 3.7 dex	0.03	0.08	-	-	0.04	0.22	-	-	0.07	-	-	-	0.17	-	-	-	-

S/N	Stage	[Fe/H] = -1.0				[Fe/H] = -1.5				[Fe/H] = -2.0				[Fe/H] = -2.5			
		1.75	0.75	0.25	0	1.75	0.75	0.25	0	1.75	0.75	0.25	0	1.75	0.75	0.25	0
	5200 K - 2.5 dex	0.03	0.03	0.06	0.08	0.03	0.05	0.12	0.23	0.03	0.10	-	-	0.04	-	-	-
	5000 K - 2.0 dex	0.04	0.03	0.04	0.05	0.04	0.04	0.06	0.09	0.04	0.05	0.13	0.22	0.03	0.12	-	-
	4800 K - 1.2 dex	0.04	0.03	0.03	0.04	0.04	0.03	0.04	0.04	0.04	0.04	0.06	0.09	0.03	0.05	0.13	-
200	6000 K - 4.5 dex	0.03	0.17	-	-	0.06	-	-	-	0.15	-	-	-	-	-	-	-
	6400 K - 4.1 dex	0.03	0.15	-	-	0.05	-	-	-	0.12	-	-	-	-	-	-	-
	5800 K - 3.7 dex	0.03	0.07	0.18	-	0.03	0.14	-	-	0.05	-	-	-	0.13	-	-	-
	5200 K - 2.5 dex	0.02	0.03	0.04	0.04	0.02	0.04	0.08	0.08	0.02	0.07	0.21	-	0.03	0.19	-	-
	5000 K - 2.0 dex	0.03	0.02	0.03	0.03	0.03	0.03	0.05	0.06	0.02	0.04	0.10	0.16	0.03	0.09	-	-
	4800 K - 1.2 dex	0.03	0.02	0.02	0.03	0.04	0.02	0.03	0.03	0.02	0.02	0.04	0.10	0.02	0.05	0.10	0.17
400	6000 K - 4.5 dex	0.02	0.09	-	-	0.04	-	-	-	0.08	-	-	-	0.21	-	-	-
	6400 K - 4.1 dex	0.01	0.08	0.19	-	0.03	0.19	-	-	0.06	-	-	-	0.17	-	-	-
	5800 K - 3.7 dex	0.01	0.03	0.09	0.09	0.02	0.08	-	-	0.02	0.21	-	-	0.07	-	-	-
	5200 K - 2.5 dex	0.01	0.01	0.03	0.03	0.02	0.03	0.04	0.06	0.02	0.04	0.11	0.16	0.02	0.09	-	-
	5000 K - 2.0 dex	0.01	0.01	0.01	0.02	0.02	0.02	0.03	0.03	0.02	0.03	0.06	0.08	0.02	0.04	0.13	-
	4800 K - 1.2 dex	0.01	0.01	0.01	0.01	0.02	0.02	0.02	0.02	0.02	0.02	0.03	0.03	0.02	0.03	0.06	0.08

Notes: The second row header indicates [Th/Fe]. Precision values exceeding 0.25 dex are clipped.

### 5.3.2 Uranium detection with HRMOS

While the primary goal of this program is the precise measurement of thorium abundances (with a target precision better than 0.05 dex), this capability extends to both weaker-line regimes (low Th abundances) and more challenging blended-line conditions (higher metallicities and/or lower  $r$ -process enhancement). In addition, it may enable uranium measurements in a limited number of favourable cases. Indeed, the strongest U line accessible to HRMOS, U II 385.9 nm, is exceedingly weak and requires a resolving power of at least  $R \sim 80\,000$  to be adequately separated from the neighbouring Fe I line. These requirements restrict its detectability to stars with strongly enhanced  $r$ -process abundances relative to lighter elements, i.e. the so-called  $r$ -process-enhanced metal-poor stars. Although thorium remains the primary focus of this survey, uranium provides a unique complementary chronometer that, in favourable cases, can yield highly precise stellar ages. Owing to its shorter half-life, uranium is more sensitive to the elapsed time since nucleosynthesis, making the U/Th ratio a particularly powerful chronometric probe. The main limitation, however, is its extreme observational weakness.

The first reliable detection of Uranium was achieved in the  $r$ -process-enhanced star CS 31082-001 (Hill et al. 2002), where the 385.9 nm U II feature is measurable due to its high  $r$ -process enrichment and relatively low molecular contamination. These conditions—strong actinide enhancement (including actinide-boost behaviour) combined with weak CH and CN molecular absorption—remain the key prerequisites for successful Uranium detection.

Within the HRMOS Th survey, Uranium measurements should therefore be regarded as a secondary opportunity rather than a primary science driver. Nevertheless, the combination of high spectral resolution and broad wavelength coverage, including the 385.9 nm, 405.0 nm, and 409.0 nm regions, may enable U detections in a small subset of actinide-boost stars. Even a handful of such measurements would have a major scientific impact, providing improved constraints on absolute ages of the oldest stars, on actinide yield variations in the  $r$ -process, and on Galactic age estimates based on radioactive chronometers.

### 5.4 Systematic uncertainties affecting Th and Eu abundance determinations

Precise Th and Eu abundance determinations require careful control of systematic uncertainties, which often dominate over statistical errors in high-quality spectra (see Ludwig et al. 2010, for a complete discussion). The main sources of systematics in Th and Eu abundance determinations can be grouped into four broad categories: (i) uncertainties in the adopted stellar parameters, which affect the atmospheric structure and line formation; (ii) uncertainties in the atomic data, in

particular oscillator strengths and line broadening parameters; (iii) modelling assumptions, such as the use of 1D LTE model atmospheres; (iv) observational effects, including line blending and continuum placement; (v) nuclear production rates; (vi) model atmospheres (Caffau et al. 2008).

Mitigation strategies for the systematic error budget involve several complementary approaches. First, careful line selection and synthesis, focusing on transitions that are minimally blended and well characterised (e.g. the Th II 401.9 nm line in metal-poor giants), reduce line-dependent systematics. Second, adopting consistent stellar parameters and state-of-the-art model atmospheres ensures that systematic offsets in derived abundances are minimised across the sample. In addition, the systematic uncertainty budget explicitly accounts for the propagation of errors in the adopted stellar parameters, such as effective temperature, surface gravity, and microturbulence, which directly affect the derived Th and Eu abundances. These uncertainties are typically of the order of  $\sim 0.03$  dex.

Further sources of systematics arise from the atomic data, in particular the uncertainty in the oscillator strength of the Th II line, as discussed in Chapter 8, which represents a critical limitation in the absolute abundance scale and for which the HRMOS consortium is working to improve the currently adopted value. Finally, possible departures from LTE should also be considered, with non-LTE corrections applied where available or included as an additional source of systematic uncertainty, especially for Eu lines, to ensure a more physically consistent abundance determination. These corrections amount to about 0.05 dex for Th in the typical target stars of HRMOS (see, e.g. Mashonkina et al. 2012). The uncertainty associated with the NLTE correction is estimated to be of the order of  $\sim 0.02$  dex, although this value is still being reassessed within the HRMOS consortium (see Chapter 9).

The final uncertainties, accounting for the effects of stellar parameters, line-profile fitting, possible NLTE corrections, model atmospheres and atomic data uncertainties (assumed to be 0.02, 0.03, 0.02, 0.03 and 0.02 dex, respectively), are expected to be of the order of  $\sim 0.04$  dex when added in quadrature for a single star observed under optimal conditions.

## 5.5 Theoretical considerations: the Th/Eu production ratio

As discussed above, reliable nucleocosmochronology critically depends on understanding the nucleosynthetic origin of the relevant radioactive and stable species, since this directly determines the initial production ratios adopted in the age estimates. These ratios can be derived either from theoretical  $r$ -process nucleosynthesis calculations (e.g. Cowan et al. 1991; Arnould et al. 2007) or empirically from observations of stars with independently determined ages, by reconstructing their initial abundance ratios prior to radioactive decay (e.g. Sneden et al. 2008; Roederer 2017; Azhari et al. 2025).

The dominant production site of Th, Eu, and U is the  $r$ -process, which operates under extremely neutron-rich conditions. Such environments are realised in the dynamical ejecta of neutron-star mergers (NSMs), where low electron fractions ( $Y_e \lesssim 0.1$ ) and high neutron-to-seed ratios allow repeated fission cycling and efficient actinide production (e.g. Goriely et al. 2011; Kasen et al. 2017; Kullmann et al. 2023). The resulting Th and Eu yields, and in particular their production ratio, are highly sensitive to the ejecta properties (entropy, expansion timescale, and  $Y_e$ ), as well as to nuclear-physics uncertainties in the trans-lead region. Observations of the kilonova associated with the GW170817 event have demonstrated that NSMs are robust sources of heavy  $r$ -process elements, including lanthanides and likely actinides, although the absolute actinide fraction remains model dependent due to opacity uncertainties (Deprince et al. 2025).

Recent observational studies (Shah et al. 2026b) have shown that Th and Eu are generally co-produced in a remarkably consistent way across a wide range of metallicities and  $r$ -process

enhancement levels. Nevertheless, a significant intrinsic dispersion remains in the observed  $\log \epsilon(\text{Th}/\text{Eu})$  ratios, with an intrinsic scatter of about  $\pm 0.11$  dex at low metallicity. This implies that while the majority of  $r$ -process events produce Th/Eu ratios within  $\sim 30\%$  of the mean value, a small fraction of events may exhibit variations exceeding factors of  $\sim 3$ – $10$ , the so-called *actinide-boost* stars, for which standard chronometer ratios would imply unphysical or even negative ages (Hill et al. 2002; Sneden et al. 2008; Holmbeck et al. 2018). However, when targets are carefully selected to exclude actinide-boost, Th/Eu ratios can provide robust estimates of the time elapsed since the nucleosynthetic event. In this regime, nucleocosmochronology remains a powerful and largely model-independent tool for stellar age dating and for constraining the minimum age of the Universe. Ongoing theoretical improvements in  $r$ -process nucleosynthesis calculations, nuclear reaction networks, and radioactive decay data are expected to substantially improve the determination of the initial production ratios over the coming decades, thereby progressively reducing the associated uncertainties. In parallel, observational strategies targeting highly  $r$ -process-enhanced metal-poor stars with independent age estimates, and evidence for a single dominant enrichment event (the so-called  $r$ -II stars), provide empirical constraints on the initial Th/Eu production ratio (e.g. Sneden et al. 2008; Roederer 2017; Holmbeck et al. 2018).

## 5.6 Possible targets: ages of globular clusters and of old stars in the field

In this Chapter, we focus on nucleocosmochronology as a tool for cosmology, aiming to derive accurate and precise, model-independent ages of the oldest stars. Globular clusters provide the highest precision in stellar ages due to their coeval populations, whereas observations of field giants offer complementary insights into the origin and chemical evolution of Th and Eu. We stress that the age differences between first- and second-generation stars within globular clusters are generally negligible compared to the overall cluster age uncertainties, and are not expected to significantly affect age determination from nucleocosmochronology (e.g. Gratton et al. 2012) –see below. On the other hand, for field stars, the achievable precision is largely limited by the uncertainties related to Th measurement and cannot be reduced in the same way as for clusters. Nonetheless, they remain a crucial resource for tracing the formation history of the Milky Way halo, allowing us to age date between populations formed in situ and those accreted through past mergers, and to reconstruct the Galaxy’s assembly history.

### 5.6.1 Globular Clusters

The best approach that maximises the precision in stellar ages, is to measure the [Th/Eu] ratio in globular clusters. These are among the oldest stellar populations in the Galaxy, and observing cluster members is particularly well-suited for HRMOS thanks to its multi-object capability and field of view optimised for crowded fields. Indeed, determining [Th/Eu] in a large coeval sample of giant stars within a cluster minimises the final random uncertainty on the mean cluster [Th/Eu] ratio.

We consider a single star with a typical, conservative measurement error of 0.06 dex on Th and 0.02 dex on Eu. The resulting uncertainty on the [Th/Eu] ratio is  $\sigma_{\log(\text{Th}/\text{Eu})} \approx 0.06$  dex. Using the standard radioactive decay relation for  $^{232}\text{Th}$  (see Eq.5.2), this translates into an age uncertainty of approximately 2 Gyr for a single star. When multiple stars are measured within the same GC, the statistical uncertainty on the cluster mean age decreases as  $\sigma_{\text{cluster}} = \sigma_{\text{single}}/\sqrt{N_{\text{stars}}}$ . For a typical cluster with 80 giant stars with the same [Th/Eu] ratio, this yields a reduced uncertainty of  $\sim 0.3$  Gyr. Extending this approach to a sample of 30 old clusters, with similar ages, each with 80 stars, further reduces the random uncertainty on the mean age across the sample to

$\sim 0.06$  Gyr. For context, the expected age difference between first- and second-generation stars within a typical GC is very small, of order 10–300 Myr (e.g. Oliveira et al. 2020), much smaller than both the statistical uncertainties for individual clusters and the absolute ages, emphasising that the multi-population nature of GCs does not significantly affect the determination of their mean ages. These calculations demonstrate the power of averaging over multiple stars and clusters to reduce statistical uncertainties. A possible observational strategy, including estimates of Th measurement errors and potential synergy with exoplanet searches, is discussed in Chapter 11. We recall that systematic uncertainties, especially those associated with the initial production ratio of [Th/Eu] must be considered separately in the total error budget. These are discussed in Sects. 5.4 and 5.5.

### 5.6.2 Giant stars in the Milky Way field

Targets suitable for measuring accurate stellar ages with nucleocosmochronology are also old giants in the Milky Way, where isochrone fitting is very uncertain, and bright enough for HRMOS to achieve high SNR in reasonable exposure times. Age dating these stars could provide further constraints to the lower limit to the age of the Universe and to cosmological parameters and, at the same time, allow insights on the earliest phases of Galaxy assembly.

Starting from the XGBoost catalogue (Andrae et al. 2023), and in particular its golden sample (consisting of giants with reliable parameters), we performed a cross-match with the *Gaia* RVS catalogue ( $G < 16$ , Katz et al. 2023). The effective temperature, surface gravity, metallicity, and de-reddened absolute *Gaia* and WISE magnitudes are projected onto PARSEC isochrones following Kordopatis et al. (2023b, 2025). De-reddening was performed using the Green et al. (2019) 3D extinction map when available, or a corrected Schlegel et al. (1998) map otherwise (corrections take into account stellar distance and high-extinction regions, see Kordopatis et al. 2015).

We then filtered out stars with  $\text{RUWE} > 1.4$ , parallax errors  $> 20\%$ , or derived mass errors equal to zero. We also removed stars with  $G > 15$ , to simplify the selection function, since for fainter stars the *Gaia* DR3 RVS catalogue becomes incomplete.

Figure 5.2 shows the target density per square degree for stars of different masses and metallicities. Selecting stars with  $[\text{Fe}/\text{H}] < -1$  naturally favours targets towards the bulge and bar, which is particularly interesting as it probes the transition between the inner halo and thick disc. In practice, in some fields we could fill up to half of the fibres to detect Th.

An alternative approach is to target old stars across the full metallicity range and investigate Th/Eu trends. This is largely unexplored in the literature, especially at high metallicities. For instance, targeting the thick disc population allows a selection in age, given the tight age-metallicity relation of the thick disc (e.g. Haywood et al. 2013).

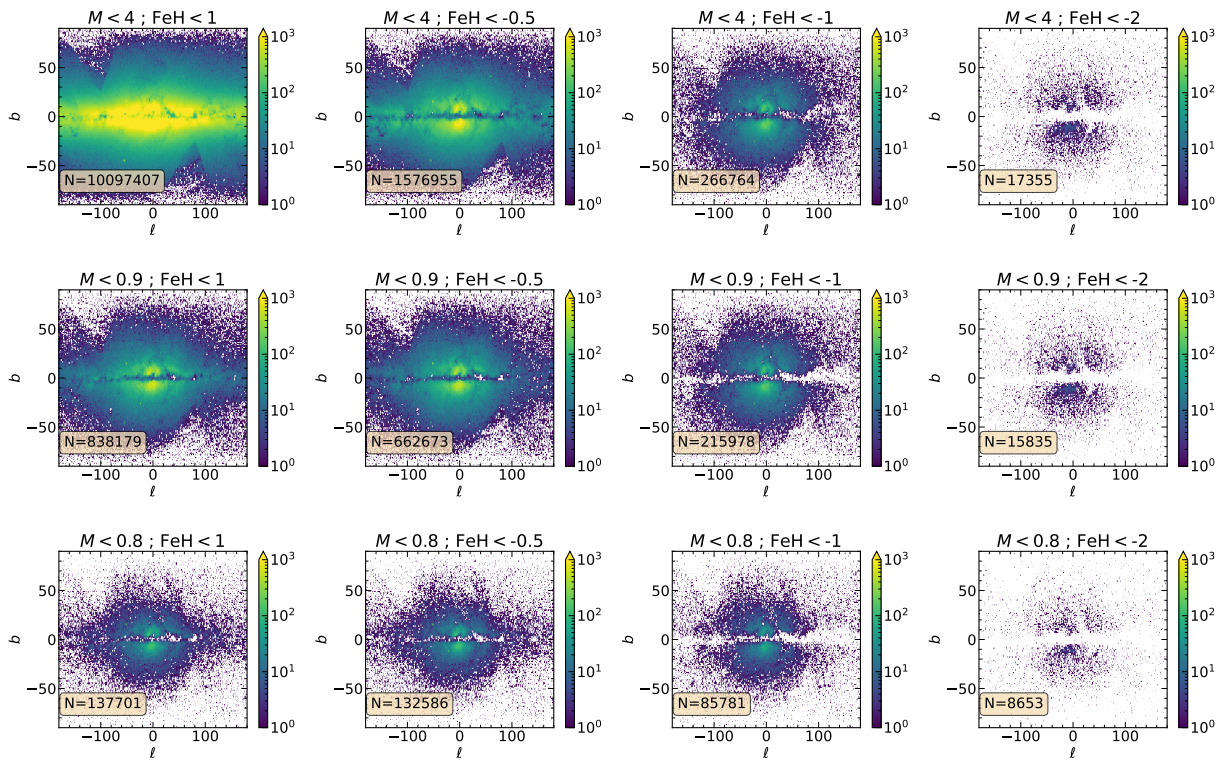


**Figure 5.2.** Target sky-density (in Galactic coordinates) for stars with different mass ranges (different rows) and metallicities (columns). Pixels are one square degree. A cut on the error in parallax, RUWE value and G magnitude  $G=15$  has been applied (see Sect. 5.6).

## 6 High-resolution spectroscopy of star clusters

Star clusters are key astrophysical laboratories, and the capabilities of HRMOS are ideally suited to open a new discovery space for their study through high-resolution, multiplexed spectroscopy and precise radial velocities. They will enable transformative investigations of stellar physics, including magnetic activity, accretion, internal mixing, and abundance variations across evolutionary phases and multiple stellar populations. At the same time, clusters provide unique benchmarks for testing stellar evolution models and for studying dynamical processes under well-constrained conditions.

### 6.1 Scientific context

Star clusters, open and globular, are mentioned several times throughout this white paper, as they are central to many of the proposed science cases. At the same time, the capabilities of HRMOS -its wavelength coverage, high spectral resolution and ability to deliver precise radial velocities for multiple objects simultaneously- open a qualitatively new discovery space for cluster studies themselves. Star clusters are, indeed, natural laboratories for astrophysical processes. Their approximately coeval nature make them ideal environments to test stellar evolution models and investigate complex physical processes under well-constrained conditions. For this reasons, we devote a dedicated chapter to star cluster science, bringing together the diverse scientific opportunities into a coherent framework and illustrating how the instrument will transform star clusters into fundamental benchmarks for precision astrophysics in the ELT era.

The chapter presents key stellar-physics science cases based on high-resolution spectroscopy of stars in open and globular clusters. These include the study of magnetic activity in young clusters through Doppler tomography, the characterization of multiple stellar populations in globular clusters via detailed abundance patterns, investigation of internal cluster dynamics, including the search for central black holes using precise radial velocities, and the analysis of atomic diffusion and internal mixing processes across different evolutionary stages. Together, these topics highlight the crucial role of HRMOS in advancing our understanding of stellar structure, evolution, and dynamics in dense stellar environments.

#### Key Questions:

- How do stellar dynamos control magnetic activity and planetary environments?
- How do young stars gain mass and lose angular momentum, and how are accretion, winds, and jets involved?
- How do diffusion and mixing shape surface abundances, and what does this imply for Galactic chemical evolution and chemical tagging?
- What are the different formation paths of Li-rich giants?

- What is the reason of the long standing issue of multiple populations in globular clusters, and what are the implications for the early Universe?
- How do internal dynamics shape stellar motions, mass segregation, and the evolution of star clusters?

## 6.2 Young clusters as tracers of magnetic activity

Dynamo-generated magnetic fields are crucial in the development of young stars and their planetary systems. They impact the atmospheres by causing non-radiative heating, regulate the accretion processes, shape stellar winds and jets, manage angular momentum loss, and possibly influence planetary habitability. HRMOS, with high spectral resolution and multiplexing capabilities, will enable Doppler tomography of starspots, prominences, magnetospheres, jets, and winds across large samples of cluster stars, offering a transformative view compared with previous studies limited to individual targets.

Young low-mass stars ( $0.1 - 1.5 M_{\odot}$ ) are rapidly rotating, magnetically active, and may accrete from circumstellar discs; as they age, discs disperse and stars spin down, feeding back on the dynamo (e.g. Weber & Davis 1967; Skumanich 1972; Durney & Latour 1978; Noyes et al. 1984; Koenigl 1991). Observations at millimetre and near-infrared wavelengths have resolved disc structure and planets on 1–100 au scales (e.g. Lagrange et al. 2010; Andrews et al. 2018; Gravity Collaboration et al. 2020; Benisty et al. 2022), but inner discs, magnetospheres, close-in planets, and stellar surfaces remain largely unresolved, requiring indirect imaging via Doppler tomography (e.g. Marsh 2001; Strassmeier 2009).

Young stars have chromospheres and coronae orders of magnitude stronger than the Sun (Stauffer et al. 1994; Brasseur et al. 2024), and prominences may influence angular momentum loss and flaring (e.g. Collier Cameron et al. 1990; Wood et al. 2005; Jardine & Collier Cameron 2019; Jardine et al. 2020), though mass ejections are often weaker than solar extrapolations (Odert et al. 2017; Maehara et al. 2021; Inoue et al. 2023). Large-scale magnetic geometry, crucial for angular momentum loss (e.g. Matt et al. 2012; Vidotto et al. 2014; Réville et al. 2015; See et al. 2018), varies with age, rotation, internal structure, and spectral type (e.g. Donati et al. 2008; Donati & Landstreet 2009; Donati et al. 2011; Gregory et al. 2016; Folsom et al. 2018), while the coupling of magnetism to accretion discs remains poorly understood (e.g. Koenigl 1991; Collier Cameron & Campbell 1993; Gallet et al. 2019).

Indeed, phenomenological models reproduce general trends in spin and activity evolution (e.g. Kawaler 1988; Denissenkov 2010; Reiners & Mohanty 2012; Gallet & Bouvier 2013, 2015), yet key questions remain. Dynamos in fast-rotating young stars are not simply scaled-up solar analogues: cool spots can appear at high or polar latitudes (e.g. Barnes et al. 2000; Barnes & Collier Cameron 2001), activity cycles are weak or absent, and dynamos operate even in fully convective stars, sometimes saturating at high rotation rates (Jeffries et al. 2011; Wright et al. 2011, 2018). The mechanism(s) responsible for activity saturation remain unclear (e.g. Reiners et al. 2014).

Observing low-mass stars to obtain spatial information on magnetic structures and their evolution over tens to hundreds of Myr is therefore crucial to understanding how rotation, magnetism, coronal and chromospheric activity, planet formation, migration, and star-planet interactions are regulated. Progress has been limited because nearby field stars can be studied individually, but their ages are uncertain, and large-scale synoptic monitoring requires prohibitive telescope time. HRMOS provides a transformational opportunity. Most young stars are in clusters or star-forming regions at  $> 100$  pc, where ages and masses can be more reliably assigned from the

HR diagram. Multiplexing allows efficient, time-resolved observations of statistically significant samples, mapping the mass/age plane and capturing the range of stellar behaviours. High resolution is essential for Doppler tomography, which resolves rotational profiles into discrete elements, increasing the number of viable targets beyond ultra-fast rotators. We briefly discuss below a few more specific aspects.

### 6.2.1 Doppler tomography

Doppler tomography tracks contrasts between emission from the stellar surface and features on or above it. Tomograms reveal starspot locations and extent (e.g. Strassmeier 2002, 2009), magnetic fields and abundance anomalies in early-type stars, prominence heights and physical conditions (Collier Cameron & Robinson 1989; Jeffries 1993; Collier Cameron et al. 1990; Dunstone et al. 2006), accretion hotspots and flows (Donati et al. 2013), and even confirm transiting planet orbits (e.g. Temple et al. 2019). Features moving across the spectral line profile as the star rotates can be forward-modelled to reconstruct surface maps (e.g. Vogt et al. 1987; Kuerster et al. 1994; Collier Cameron & Unruh 1994).

Doppler tomography has been performed on many 4-m+ class telescopes worldwide, but typically for bright, nearby stars at moderate resolving power ( $R \sim 50,000$ ) and one target at a time. Current 4-m multiplexing instruments such as WEAVE and 4MOST, and MOONS on the VLT, operate at  $R \lesssim 20,000$ , limiting tomographic resolution to only the fastest rotators and reducing the number of viable targets. Even the proposed 12-m Wide-field Spectroscopic Telescope (WST, Bacon et al. 2023), with its wide field and many fibres, would operate at  $R \sim 40,000$ , still offering lower spatial resolution and a restricted target range compared to HRMOS.

Tomographic methods indeed require sufficiently high resolution to divide a stellar rotation profile into many spectral elements,  $2v \sin i / \Delta v > 10$ , where  $v \sin i$  is the projected equatorial velocity and  $\Delta v = c/R$  is the spectrograph velocity resolution. Higher resolving power improves tomographic and spatial resolution, lowers the  $v \sin i$  threshold for resolvable features, and increases the number of viable targets per cluster. At  $R = 80,000$ , HRMOS can perform detailed Doppler tomography for  $\sim 20 - 40\%$  of solar-type stars in typical young clusters with  $v \sin i > 19 \text{ km s}^{-1}$ , producing well-resolved surface maps (e.g. Queloz et al. 1998). This is a much larger fraction than achievable with lower-resolution spectrographs, enabling simultaneous observations of many targets, including slower rotators in complementary programs such as exoplanet surveys.

Mapping spot distribution and extent as a function of age and mass probes stellar dynamos (e.g. Schuessler & Solanki 1992; Solanki & Unruh 2004). Synoptic monitoring captures activity cycles and spot migration, while short-term monitoring constrains spot lifetimes and differential rotation, essential for interpreting variability from *Kepler*, *TESS*, *CHEOPS*, and *PLATO*, and for mitigating activity signals in radial-velocity exoplanet searches (e.g. Collier Cameron 1995; Jeffers et al. 2007; Barnes et al. 2017). Simultaneous chromospheric diagnostics in HRMOS spectra (Ca II H&K, H $\alpha$ ) probe the coupling between photosphere and chromosphere, while monitoring circumstellar prominences constrains angular momentum loss, winds, flares, and disc/planet interactions (e.g. Dunstone et al. 2006; Jardine & Collier Cameron 2019; Waugh & Jardine 2022; Daley-Yates & Jardine 2024).

HRMOS will enable this at scale for cluster samples, producing population-level surface maps and chromospheric diagnostics, providing a comprehensive view of stellar magnetic activity and its evolution with mass and age (Fig. 6.1).

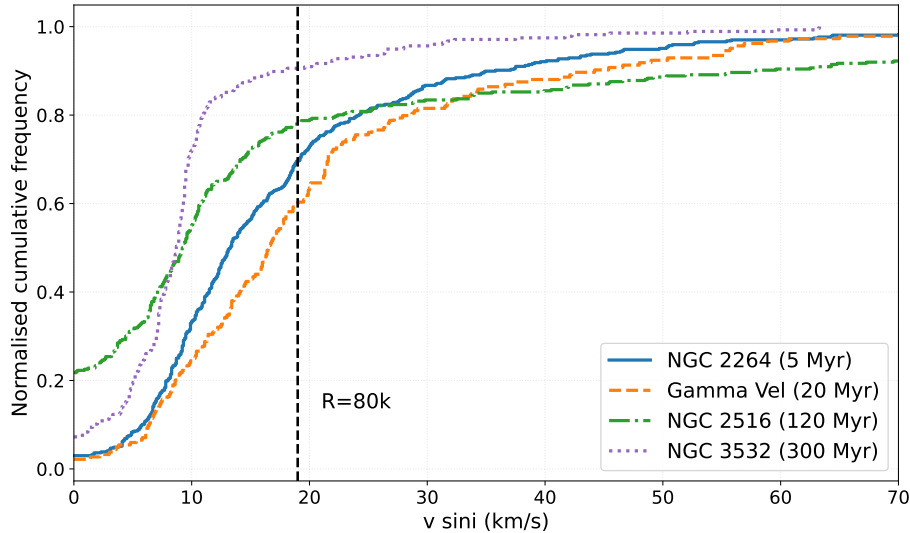


**Figure 6.1.** A normalised cumulative histogram of  $v \sin i$  for solar-type stars ( $4000 < T_{\text{eff}}/\text{K} < 6500$ ) in clusters with ages from 5 – 300 Myr (data from the *Gaia*-ESO Survey, Randich et al. 2022). The vertical line marks the threshold where the rotation profile can be resolved into 10 elements at  $R = 80\text{K}$ . Approximately 20 – 40% of stars are viable targets for Doppler imaging in clusters of age 5 – 300 Myr. Lower-resolution instruments with  $R \leq 40\text{K}$  (e.g., 4MOST, WEAVE, WST) reach only 5 – 15%.

## 6.2.2 Magnetic activity and planet detection

Magnetic activity can mimic radial-velocity and photometric signals from planets, introducing false positives or biases in mass and orbit determinations. Simultaneous monitoring of chromospheric and photospheric activity indicators in HRMOS spectra (e.g., Ca II H&K,  $H\alpha$ , line-profile variations) allows us to disentangle stellar variability from planetary signals. Combining these diagnostics with Doppler tomography of surface features ensures more reliable planet detection and characterization in young, active stars.

## 6.2.3 Impact of magnetic activity on abundance measurements

Stellar magnetic activity can significantly affect spectroscopic parameters and abundances determinations obtained with the standard analysis techniques. On the one hand, iron lines are found systematically deeper in young, active stars when compared with older counterparts, leading to an over-estimation of the micro-turbulence velocity parameter, and in turn to an underestimation of the metallicity (when using the equivalent width method, see e.g. Baratella et al. 2020; Spina et al. 2020). On the other hand, the over-abundance of Ba in young stars is found to correlate with stellar activity (Baratella et al. 2021) which could explain the presence of extreme Ba-rich young OCs. Cool starspots and chromospheric emission alter line depths and profiles, leading to biases if unaccounted for (Nordlander et al. 2024). Measuring abundances and stellar parameters in stars where magnetic activity is simultaneously characterised will allow us to correct for these effects, improving both precision and accuracy. Such strategy has also the potential to open the path for more rigorous modelling studies to create new tools dedicated to the analysis of young, active stars and to finally pinpoint the main responsible of these effects. HRMOS’s high-resolution, time-resolved spectra provide the ideal dataset. By combining Doppler tomography of surface features with line-profile analysis, we can quantify and correct the impact of magnetic activity on abundance determinations, enabling robust studies of chemical evolution in clusters across a wide range of stellar masses and ages.

### 6.3 Star-disc interaction and tests of magnetospheric accretion

Young stars accrete mass from circumstellar discs via magnetospheric accretion, where the stellar magnetic field truncates the disc near the co-rotation radius and channels material onto the stellar surface (e.g. Hartmann et al. 2016). This magnetospheric accretion model is supported by multiple indirect observational evidences, but direct spatially resolved observations are challenging due to the small scales involved ( $R_c \lesssim 0.01 \text{ au}$ ). High-resolution spectroscopy overcomes this limitation by observing features originating from hot gas in shocks at accretion hot spots, and from magnetically funnelled accretion columns linking the inner disc to the star (e.g. Bouvier et al. 2007a). Radial velocity and intensity variations of emission and absorption lines over the stellar rotation period, combined with techniques such as Doppler tomography, can recover the geometry of the magnetospheric accretion, locate hot spots and accretion funnel flows, providing indirect information on magnetic properties such as obliquity (e.g. Bouvier et al. 2007b; McGinnis et al. 2020).

However, these observations are time consuming, requiring monitoring over the stellar rotation period, and have been performed only on the brightest, nearby targets. Consequently, information on the evolution of accretion flows and their dependence on stellar mass, spectral type, radius, age, and disc properties remains sparse.

Disc dispersal, via magnetically driven or photo-evaporative (X-ray and FUV) winds, is the primary mechanism for gas removal in protoplanetary discs, terminating gas giant planet formation and constraining the timescale for orbital migration. Models predict that photo-evaporation can dissipate gas discs in a few Myr (e.g. Armitage et al. 2013; Pascucci et al. 2022), yet measurements in 10–20 Myr stars show significant accretion persists (e.g. Manara et al. 2020), indicating missing ingredients in disc evolution theories. The paradigm has shifted from viscous turbulence-driven accretion to magnetised disc wind-driven accretion (e.g. Bai 2016; Tabone et al. 2022), emphasizing the need for observational constraints on MHD and photo-evaporative winds across large PMS samples.

High-resolution observations of young clusters at different ages are essential to understand how accretion and wind processes evolve with disc evolution and depend on stellar and disc properties. Key spectroscopic diagnostics include:

#### 6.3.1 Magnetospheric accretion

Hot spots on the stellar surface produce veiling in photospheric lines and narrow emission in He I and Ca II infrared triplet lines, tracing shock-heated regions. Accretion columns funnel material from the inner disc to the star, producing rotationally modulated line profiles, sometimes with P-Cygni or inverse P-Cygni features. Doppler tomography and spectro-polarimetry can map these structures, providing constraints on magnetospheric geometry, obliquity, and the spatial distribution of accretion shocks (e.g. Donati et al. 2010; Bouvier et al. 2007b).

#### 6.3.2 Disc winds and jets

Material escaping from the disc surface or ejected in collimated jets is traced by forbidden emission lines such as [O I], [S II], and [N II]. Line profiles reveal the geometry, velocities, and launching regions of the outflows. Photo-evaporative winds produce narrow, low-velocity features, while magnetohydrodynamic winds generate broader, more blue-shifted profiles. High-resolution spectroscopy across clusters of different ages is essential to link wind properties to stellar and disc characteristics and to test models of disc dispersal, mass loss, and planet formation (e.g. Armitage et al. 2013; Bai 2016).

HRMOS, with its combination of high spectral resolution and multiplexing on an 8-m class telescope, is uniquely suited to this task. It enables time-resolved observations of large samples of young stars in clusters, extending Doppler tomography and accretion/wind diagnostics beyond the few nearby targets accessible today. These population-level studies will provide transformational insights into star-disc interactions, accretion physics, and disc wind evolution, directly informing models of early stellar evolution and planet formation.

#### 6.4 From cosmic dawn to today: the origin of multiple populations in globular clusters

One of the most active research topics in GC studies is the existence and origin of multiple stellar populations (MP), exhibiting correlated chemical anomalies (Bastian & Lardo 2018; Milone & Marino 2022). These populations are primarily characterised by star-to-star variations and (anti-)correlations in light elements, including He, C, N, O, F, Na, Mg, Al, and often Li (e.g. Gratton et al. 2004, 2012, 2019; D’Orazi et al. 2015; Schiappacasse-Ulloa et al. 2022), with additional spreads observed in Si, K, Ca, Sc, and in some cases in heavy neutron-capture elements (Mucciarelli et al. 2012a; Marino et al. 2009, 2015; Carretta & Bragaglia 2021). High-precision photometry from the *Hubble Space Telescope* has revealed that MPs also separate in colour–magnitude diagrams (Bedin et al. 2004; Piotto et al. 2007), a direct consequence of how light-element abundance variations modify stellar spectral energy distributions (Cassisi & Salaris 2020).

Multiple populations are observed in nearly all Milky Way GCs, as well as in clusters in the Magellanic Clouds and Fornax (Saracino et al. 2020; Martocchia et al. 2021; Cadelano et al. 2022), but are absent in open clusters (Bragaglia et al. 2017). Their origin remains debated. Most scenarios invoke multiple star-formation episodes, with later generations forming from material polluted by earlier stars. Proposed polluters include intermediate-mass AGB stars (Ventura et al. 2001), fast-rotating massive stars (Decressin et al. 2007), massive interacting binaries (de Mink et al. 2009), and, more recently, extremely massive stars (Gieles et al. 2025). However, no single model reproduces all observed abundance patterns. This is particularly evident in Type II clusters, which show internal Fe and CNO variations, and in the chemical inhomogeneities observed even within the primordial first population (1P) (Marino et al. 2019a,b; Legnardi et al. 2022; Lardo et al. 2023).

A major unresolved issue is the *mass-budget problem*: although 1P stars typically constitute 30–50% of present-day GC populations, most enrichment models require initial cluster masses 10–100 times larger to provide sufficient processed material for second-generation stars, implying extreme early mass loss that challenges cluster survival (Bastian & Lardo 2018). HST Treasury programs have mapped MPs in detail using “Chromosome Maps” (Milone et al. 2015, 2017), which efficiently separate populations photometrically but are not always fully consistent with spectroscopic abundance patterns (Carretta & Bragaglia 2024). Moreover, abundance spreads at the  $\sim 0.1$  dex level are observed even among 1P stars, suggesting either inhomogeneous natal gas or early supernova enrichment and highlighting the need for high-precision spectroscopy of large stellar samples.

The relevance of MPs extends beyond local GC formation. Recent JWST observations have identified strongly lensed *proto-globular clusters* at  $z > 6 - 10$ , observed only  $\sim 400$ – $500$  Myr after the Big Bang (Vanzella et al. 2023; Adamo et al. 2024). These compact, massive systems are likely progenitors of present-day GCs, and preliminary evidence for N/O and C/O anomalies suggests that multiple-population chemistry may already have been established during cosmic reionization. Multiple populations therefore provide a unique window on early star formation, feedback, and chemical enrichment in the young Universe, linking GC studies to galaxy formation at high redshift.

HRMOS will enable transformational studies by observing  $\sim 50$  stars per field in cluster outskirts, where 1P stars dominate, and by measuring 1P/2P ratios via light-element abundance

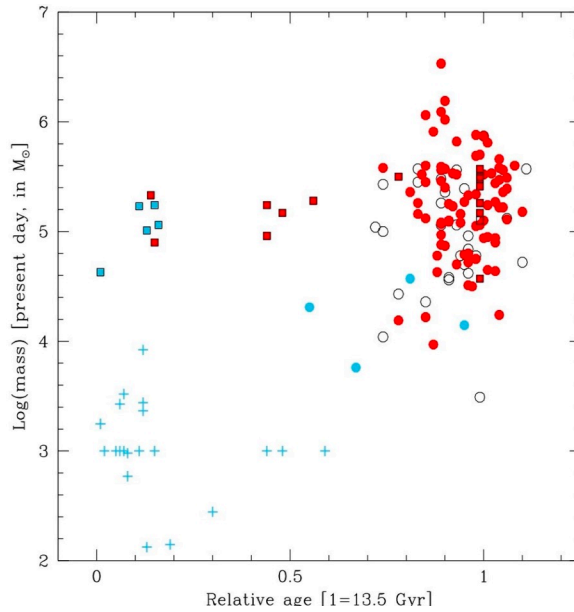


**Figure 6.2.** Age–mass diagram of star clusters. Plus signs: open clusters in the MW; circles: MW GCs; squares: Magellanic Clouds and Fornax GCs. Red: multiple populations; light blue: absent; white: unclassified (figure from Bragaglia et al. 2017).

tags. Combined with high-precision radial velocities, this will allow us to trace cluster dynamical evolution and test whether 1P stars were preferentially lost over time. Performing such an analysis with current instrumentation—either single-object spectrographs or multi-object spectrographs with limited multiplexing capability at high resolution—would require an impractically large amount of observing time. As a result, completing such a study with strong statistical significance would not be feasible with current facilities, even on a decadal timescale, and would require an instrument such as HRMOS.

#### 6.4.1 High-precision abundances of light and heavy elements in globular clusters

High-resolution, multiplexed spectroscopy of cluster centres is essential to probe all stellar populations. HRMOS enables simultaneous measurement of light elements (Li, C, N, O, Na, Mg, Al) and neutron-capture elements, particularly lead (Pb). Li should be measured in giants below the RGB bump to account for dilution, while Pb—previously largely unexplored due to limited blue coverage ( $<500$  nm)—constrains the polluter mass and metallicity via first- (Y, Zr), second- (Ba, La), and third-peak (Pb) element ratios. The strongest optical Pb line, Pb I 405.78 nm, falls within the HRMOS spectral range. MgH features in cool stars ( $T_{\text{eff}} < 4500$  K) can be compared to Mg I lines to infer He abundances, accounting for LTE deviations, granulation, and activity. Independent diagnostics (He I 587.6 nm in hotter stars, MgH in cool giants) break the He–metallicity degeneracy.

A comprehensive understanding requires large, homogeneous samples from each cluster, covering centre to outskirts, combined with photometry (sensitive to He, C, N, O) and asteroseismology (e.g., HAYDN; Miglio et al. 2021) to constrain mass, He, and rotation. HRMOS will deliver high-precision abundances in RGB, AGB, HB, SGB, and MSTO stars, allowing detailed study of pollution mechanisms, 1P metallicity spreads, and 2P inhomogeneities at  $\sim 0.05$  dex (Legnardi et al. 2022; Latour et al. 2025).

With its  $\sim 25$  arcmin FoV, HRMOS can observe GC centres down to  $G \sim 16.5$ , with a  $\text{SNR} \sim 40 - 50$ , while collecting  $\sim 50$ – $60$  stars per field at  $R \sim 80,000$ , with  $\text{SNR} \sim 100$  in 1 hr in the red spectral window for a giant star with  $G = 15$ . This allows achieving  $\sim 0.02$  dex precision in

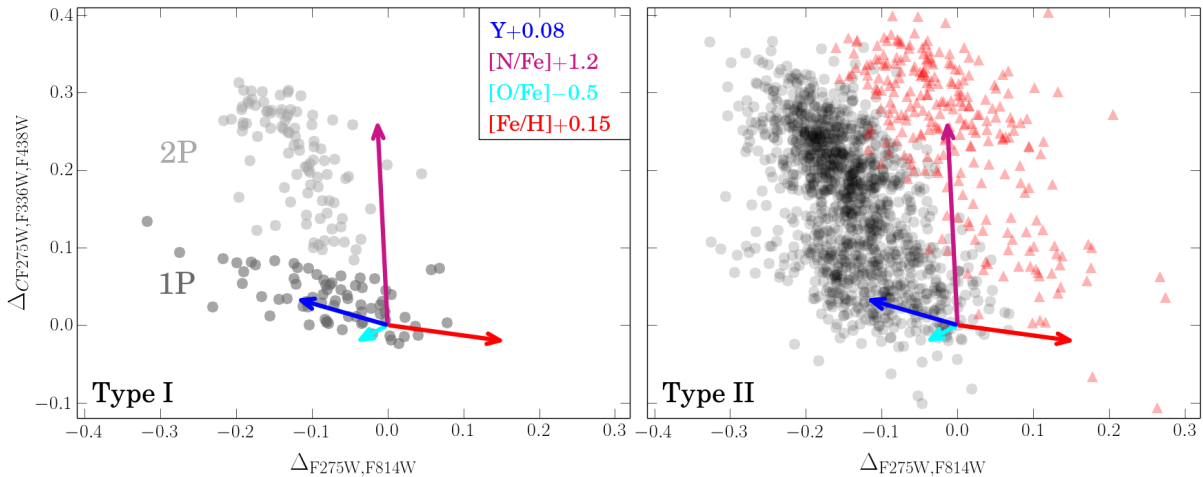


**Figure 6.3.** HST chromosome maps using F275W, F336W, F438W, and F814W bands (Milone et al. 2017). The pseudo-colour index  $\Delta CF_{275W, F336W, F438W} = \Delta[(F_{275W} - F_{336W}) - (F_{336W} - F_{438W})]$  is plotted against  $\Delta F_{275W} - F_{814W}$ . Left: NGC 3201 (Type I, classical 1P–2P dichotomy). Right: NGC 5286 (Type II) showing an additional subpopulation enriched in CNO and Fe (red triangles). Arrows indicate effects of specific abundance changes.

[Fe/H] while measuring all key light and neutron-capture elements, including Pb near 405.8 nm. The combination of high multiplexing, high resolution, and comprehensive elemental coverage enables truly transformational studies of multiple stellar populations, providing unprecedented constraints on cluster formation, early chemical enrichment, and the origin of MPs.

#### 6.4.2 Magnesium isotopes and the nature of globular-cluster polluters

The presence (or puzzling absence) of the Mg–Al anti-correlation in different globular-cluster populations provides one of the most sensitive diagnostics of multiple-population formation mechanisms (Carretta et al. 2009b; Mészáros et al. 2015; Pancino et al. 2017). For example, Carretta et al. (2009a); Pancino et al. (2017) found a dependency of the Mg–Al anti-correlation with both the metallicity and the mass of the clusters, but no significant trend with age. The Mg–Al anti-correlation disappears in the less massive or most metal-rich clusters. This abundance signature requires the activation of the hot Mg–Al cycle, offering strong constraints on the parent stellar source of the material (Prantzos et al. 2007; Denissenkov et al. 2015).

The Mg isotopic pattern can also be used to identify the origin of polluters in globular clusters (Ventura et al. 2018). The Mg element is made up of three stable isotopes,  $^{24}\text{Mg}$ ,  $^{25}\text{Mg}$ , and  $^{26}\text{Mg}$ , which have different nucleosynthetic origins (Vangioni & Olive 2019). The dominant isotope,  $^{24}\text{Mg}$ , is primarily produced during carbon and neon burning in massive stars before the supernova explosion. The other isotopes,  $^{25}\text{Mg}$  and  $^{26}\text{Mg}$ , each contributing about 10% of the Mg abundance in the Sun, can be produced in massive stars and also in stars of intermediate mass through  $\alpha$ -capture on Ne (Karakas & Lattanzio 2014; Pignatari et al. 2016). In globular clusters, the distribution of the relative abundances of the magnesium isotopes in second-generation stars, both with respect to the total magnesium abundance and the extension of the Mg–Al anti-correlation, offer important constraints for understanding the origin of the abundance anomalies (Ventura et al. 2018).

Yong et al. (2003) measured the Mg isotopic ratios in 20 red giants of NGC 6752, finding a decrease in  $^{24}\text{Mg}$  and an increase in  $^{26}\text{Mg}$  for extreme second-generation stars. Similar trends were found for four red giants in M13 and one giant in M71 by Yong et al. (2006) and seven giants of  $\omega$  Cen by Da Costa et al. (2013). On the other hand, in an analysis of 13 giants belonging to 47

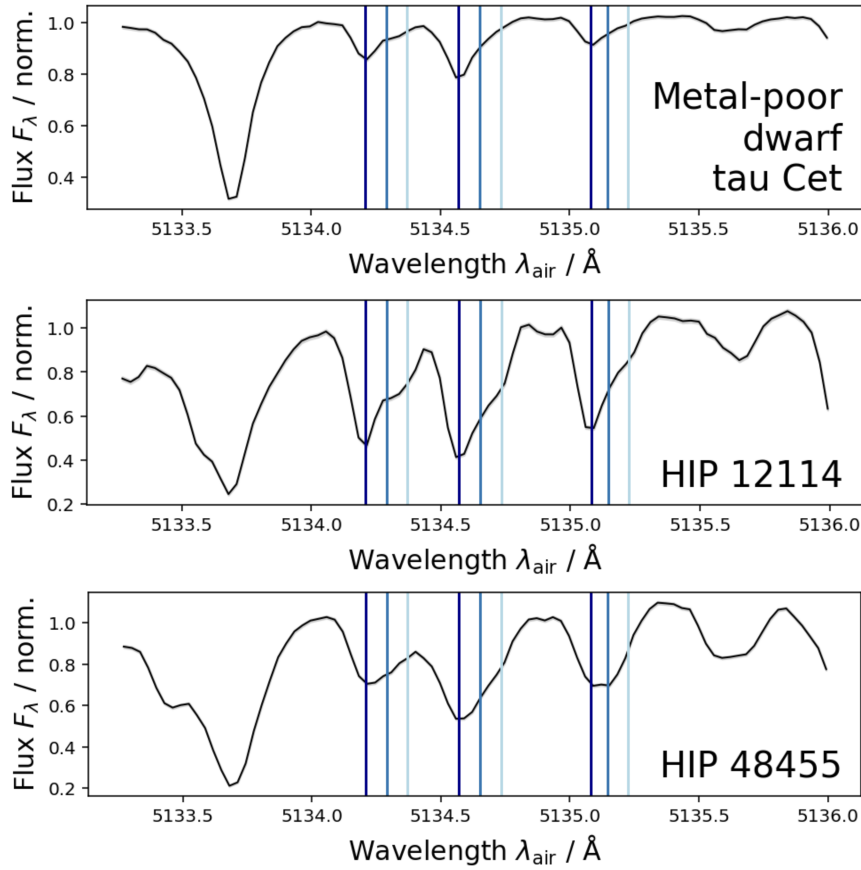


**Figure 6.4.** Expectations of HRMOS spectra around the MgH region tracing the three different Mg isotopes. Shown are spectra taken with the Veloce spectrograph at  $R = 80\,000$  of the metal-poor G dwarf Tau Cet (top), the K dwarf HIP 12114 (middle), and a red clump star (HIP48455, bottom) with solar metallicity.

Tuc, Thygesen et al. (2016) found no variation in isotopic ratios. More recently, McKenzie et al. (2024) analysed six giants in M 22, a globular cluster that also shows star-to-star variations in the abundances of s-process elements. Although differences were found in the Mg isotopic ratios between the stars, they do not correlate with the abundances of the s-process elements. This suggests that the nucleosynthetic source of the s-process enrichment in that cluster did not affect the Mg isotopic ratios and therefore still has to be identified. Furthermore, it is important to highlight that the works mentioned above stress that the observed behaviour of the isotopic ratios do not always agree with the expectations from theoretical models, suggesting that our understanding of the nucleosynthesis of Mg isotopes is incomplete.

As is clear from the above, the Mg isotopic ratios have been investigated so far only in a few stars of a small number of clusters. Given the variety of chemical anomalies seen in stars of different clusters, a lot of work remains to be done to fully understand how the variation in the  $^{24}\text{Mg}:^{25}\text{Mg}:^{26}\text{Mg}$  ratios correlates with other cluster properties. Only in this way can Mg isotopes be fully used to help solve the puzzle of globular cluster formation. HRMOS can play a strong role in this respect, thanks to its high resolution and multiplex, facilitating the observation of large samples in several globular clusters. The MgH features used for the determination of Mg isotopic ratios are located around 513-514 nm (Aicken Davies & Worley 2025) and therefore are included in the HRMOS 480-522 nm spectral window. Example of spectra in this region obtained with the Veloce échelle spectrograph at the 3.9m Anglo-Australian Telescope are shown in Fig. 6.4.

Moreover, like many molecules, we stress that MgH is best modelled with three-dimensional

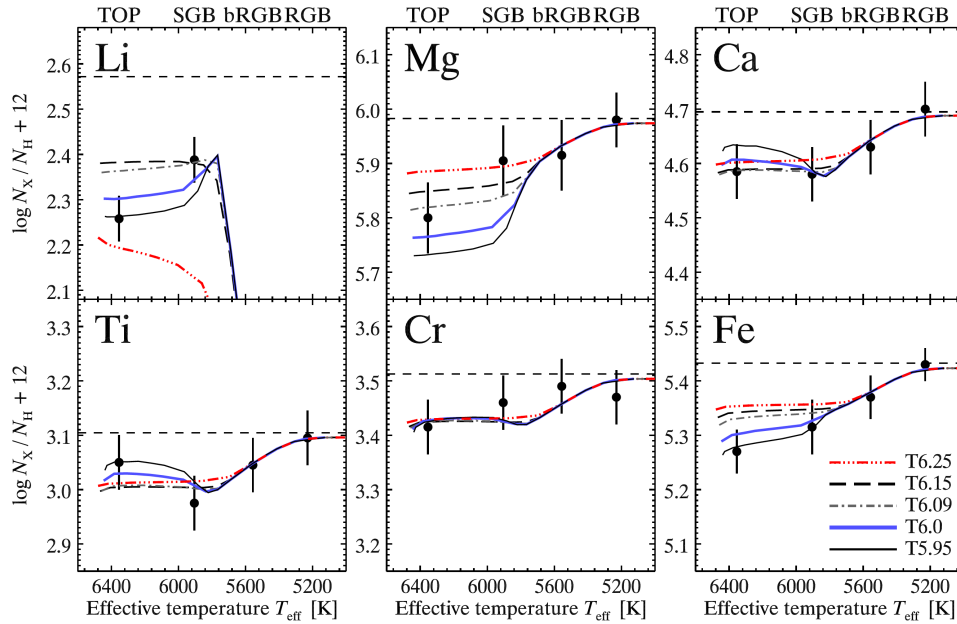


**Figure 6.5.** Fig. 2 of Nordlander et al. (2012) displaying inferred abundance trends from the MS turnoff point (TOP) to the red-giant branch (RGB) below the bump. The bullets represent the average abundances of 2-6 stars observed with VLT/FLAMES-UVES. Within the errors, all element-specific abundance trends can be described well with Richard et al. (2005) stellar-structure models treating atomic diffusion (gravitational settling, radiative acceleration) together with an intermediate efficiency of extra mixing (T6.0) at the bottom of the convective envelope.

model atmospheres (e.g., Thygesen et al. 2017). A homogeneous data set, like the one HRMOS will deliver, will therefore spur innovation in computational methods of state-of-the-art spectral modeling. For the analysis, a survey with HRMOS can further make progress by assembling many stars at similar temperatures and gravities within globular clusters. A small range of atmospheric parameters is ideal for a differential analysis (e.g., Yong et al. 2013). In such an analysis, errors in oscillator strengths and uncertainties from the assumptions, such as LTE, are mostly subtracted away. However, the typical observation scheme targets stars at a diversity of evolutionary states (i.e., the base and the tip of the RGB). With HRMOS it will be possible to target a tight grouping of red giants in temperature and gravity, yielding ultra-precise Mg isotopic abundances.

## 6.5 Cluster stars as tracers of surface-composition evolution

High-resolution spectroscopic studies of stellar photospheres, including both elemental and isotopic abundances, provide crucial insights into stellar evolution and the chemical history of their host galaxies. They allow us to probe a wide range of stellar properties, such as metallicity, age, and mass, across different Galactic populations. When combined with astrometric, asteroseismic, and interferometric data, spectroscopy enables detailed studies of magneto-hydrodynamic transport processes in stellar interiors and allows us to quantify their efficiency as a function of stellar properties. Improved constraints on these processes lead to more accurate stellar evolutionary models and yields, which, when incorporated into chemical evolution and chemo-dynamical simulations, enhance our understanding of galactic chemical enrichment. The combination of high spectral resolution and high multiplexing capability on an 8-m-class telescope makes HRMOS a uniquely powerful instrument for advancing our understanding of stellar evolution.

### 6.5.1 The role of atomic diffusion

The surface composition of evolved stars is often assumed to reflect the birth-cloud abundances, underpinning chemical tagging (Freeman & Bland-Hawthorn 2002). However, stellar evolution modifies surface abundances via processes such as convection, dredge-up, atomic diffusion, and extra mixing. While qualitatively understood (e.g., Deliyannis et al. 1990), quantitative constraints remain limited, especially in low-mass stars with poorly described outer convection zones. Clusters provide natural laboratories to compare stars across evolutionary phases along a single isochrone.

Atomic diffusion—gravitational settling and radiative levitation—causes heavy elements to sink or be pushed outward, establishing stratified abundance profiles (Michaud et al. 2015). In G- and F-type stars, shallow convection cannot fully suppress diffusion, affecting surface abundances, especially for He, Li, and light metals. Observationally, atomic-diffusion effects have been measured in globular (Gratton et al. 2001; Korn et al. 2007; Gruyters et al. 2014) and open clusters (Önehag et al. 2014; Bertelli Motta et al. 2018; Gao et al. 2018; Souto et al. 2019), with abundance variations of up to  $\sim 0.3$  dex for Li and Mg, and  $<0.1$  dex for heavier metals (Fig. 6.5). Studying turnoff-point and subgiant stars requires high SNR spectra at FLAMES-like resolution down to  $G \sim 18.5$ .

Lithium provides a striking example of diffusion in action. In NGC 6397 ( $[\text{Fe}/\text{H}] = -2.1$ ), Li abundances rise along the subgiant branch as previously settled Li is temporarily dredged up before the first dredge-up dilutes the surface by  $\sim 20$  (Korn et al. 2006, 2007; Lind et al. 2009). Accurate modelling requires high-quality spectra and 3D NLTE analysis (Wang et al. 2021). Extra mixing below the convective envelope moderates diffusion and is essential to reproduce observed trends such as the Spite plateau (Richard et al. 2005). Its physical nature remains uncertain but may involve boundary-layer processes like overshooting or shear turbulence.

Atomic-diffusion effects at metallicities below  $[\text{Fe}/\text{H}] \sim -2.5$  are largely unknown. Extending empirical corrections across a metallicity sequence from  $[\text{Fe}/\text{H}] = -1$  to  $-2.5$  can sharpen our understanding of stellar interiors and atomic processes, refine stellar ages by up to 1 Gyr, and determine how reliably we can use surface abundances for chemical tagging to reconstruct the formation and accretion history of the Milky Way (Dotter et al. 2017).

HRMOS, with its high spectral resolution, multi-object capability, and sensitivity to faint stars, will enable systematic studies of turnoff-point and subgiant stars across a wide metallicity range, providing the precision data needed to empirically constrain atomic diffusion, extra mixing, and their impact on Galactic archaeology.

### 6.5.2 Demographics of lithium-rich giants

Lithium has been one of the most studied chemical elements in stars and ISM absorption systems for many decades. It has two stable isotopes,  ${}^6\text{Li}$  and  ${}^7\text{Li}$ , with  ${}^7\text{Li}$  being by far the most abundant. It is one of the few elements produced during Big Bang nucleosynthesis (BBN, Cooke 2026), which yields only  ${}^7\text{Li}$ . As Galactic chemical evolution proceeds, delayed  ${}^7\text{Li}$  sources are added, although their dominant origin is still uncertain; novae are currently among the most promising candidates (Molaro et al. 2023b; Nguyen et al. 2025, and references therein). In the Solar system, such delayed production accounts for roughly 70% of meteoritic  ${}^7\text{Li}$  (Lodders 2003). The  ${}^6\text{Li}$  isotope is instead believed to be produced only by cosmic-ray spallation (Fields & Olive 2022), with a Solar system  ${}^6\text{Li}/{}^7\text{Li}$  ratio of  $\sim 0.08$  (Lodders 2003).

Lithium is fragile:  ${}^7\text{Li}$  is destroyed at temperatures of  $\sim 2.7 \times 10^6$  K, and  ${}^6\text{Li}$  at  $\sim 2 \times 10^6$  K. As a result, Li is depleted in stellar photospheres whenever convective envelopes reach layers hot enough to burn it.

Because convective envelopes deepen significantly as stars evolve off the main sequence and ascend the red giant branch, giant stars are typically strongly Li-depleted (Mucciarelli et al. 2012b;

Deliyannis et al. 2019, among many). Although the Li I 670.8 nm doublet strengthens at lower effective temperatures, Li is therefore often undetectable in evolved stars. Nevertheless, a small fraction of giants (about 1%, Sayeed et al. 2024) show very high lithium abundances, sometimes exceeding Solar System meteoritic values (giants are generally considered Li-rich for  $A(\text{Li}) \gtrsim 1.5$ ). This implies either recent lithium production or external enrichment after the last convective dilution episode. The rarity of these objects suggests either a short-lived enrichment phase or a rare production channel (or both).

Proposed mechanisms include (see Sayeed et al. 2024 for a review):

- Lithium production via the Cameron–Fowler mechanism (Cameron & Fowler 1971), possibly during thermal pulses on the asymptotic giant branch (AGB);
- Mass transfer from an evolved companion that has undergone Cameron–Fowler Li production (Sackmann & Boothroyd 1992);
- Engulfment of rocky planets: lithium is enhanced in refractory material, leading to temporary surface enrichment after planet destruction (Aguilera-Gómez et al. 2016).

None of these scenarios is fully satisfactory: the Cameron–Fowler mechanism operates only in specific evolutionary phases, whereas Li-rich giants are observed from the subgiant branch onward (e.g. Yan et al. 2022). Mass transfer requires binarity and should leave additional chemical signatures from AGB nucleosynthesis. Planet engulfment models appear unable to reach  $A(\text{Li}) \gtrsim 1.5$  (Aguilera-Gómez et al. 2016). Notably, both the Cameron–Fowler process and BBN produce only  ${}^7\text{Li}$ , whereas planet engulfment would introduce lithium with a composition reflecting the accreted material, although  ${}^6\text{Li}$  would be rapidly destroyed due to its lower dissociation temperature (Aguilera-Gómez et al. 2016, 2020).

The main limitation in understanding the origin of Li-rich giants is the uneven observational characterisation of their population. They are known to occur across the RGB/AGB phases and the red clump (e.g. Deepak & Lambert 2021; Singh et al. 2021, and references therein), but their overall fraction remains poorly constrained, as does its dependence on age and metallicity. It is also unclear whether such trends persist across the more than two orders of magnitude in observed Li enhancement. A fraction of Li-rich giants are binaries, although the overall binary fraction is still uncertain (Jorissen et al. 2020; Castro-Tapia et al. 2024). If mass transfer is the dominant channel, some overlap with s-process enhanced stars is expected, together with additional signatures from AGB nucleosynthesis in CNO abundances, C and Mg isotopic ratios, and related diagnostics (Aguilera-Gómez et al. 2023; Zhou et al. 2018).

This limited demographic information largely reflects the rarity of Li-rich giants and the need for high-resolution, high-S/N, and wide spectral coverage to trace multiple chemical indicators simultaneously. So far, this has required single-object echelle spectroscopy (Martell et al. 2021).

In this context, HRMOS represents a significant step forward. It will combine the above capabilities with multiplexing, enabling efficient demographic studies. Moreover, the identification and characterisation of Li-rich giants will effectively come “for free” in parallel with broader stellar chemical analyses: the Li I 670.8 nm doublet lies in a high-throughput region of the spectra for low-mass giants, so targets observed to reach  $S/N \sim 50$  in the blue will achieve even higher S/N at the Li feature, allowing robust detection of Li-rich stars and measurement of their abundances (see below and Fig. 6.6). At higher Li enhancement, lower  $T_{\text{eff}}$ , or higher S/N, the  ${}^6\text{Li}/{}^7\text{Li}$  ratio can also be measured (Fig. 6.6, 6.7). Current models predict that highly Li-enhanced giants should show no  ${}^6\text{Li}$ , whereas modestly enriched, metal-rich stars that recently engulfed a planet may retain detectable  ${}^6\text{Li}$ . The isotopic ratio therefore provides a powerful diagnostic of enrichment channels,

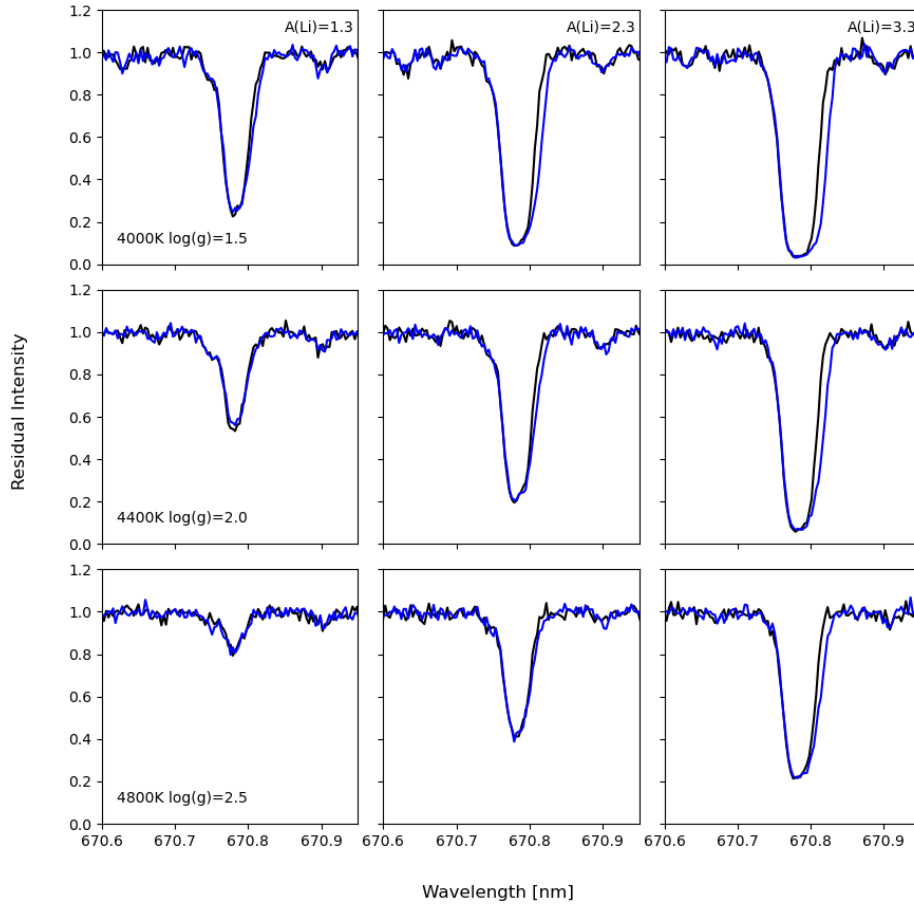


**Figure 6.6.** Simulated Li I 670.8 nm doublet in giants at varying Li abundances (rows) and stellar parameters, assuming  $[\text{Fe}/\text{H}] = -0.5$ ,  $[\alpha/\text{Fe}] = 0.0$ , and  $\text{SNR} = 50$ . Black line, pure  ${}^7\text{Li}$ , blue line  ${}^6\text{Li}/{}^7\text{Li} = 0.08$ .

enabled by the high resolution of HRMOS. Although Li-rich giants are found in both field and cluster environments, globular clusters are particularly well suited for demographic studies due to their coeval, dense, and chemically homogeneous populations, which also facilitate precise evolutionary phase determination.

**Li I 670.8 nm doublet in lithium-rich giants:** To demonstrate the capability of HRMOS to measure lithium abundances in cool giants and potentially derive  ${}^6\text{Li}/{}^7\text{Li}$  isotopic ratios, we computed synthetic spectra around the Li I 670.8 nm doublet for three representative sets of stellar parameters ( $T_{\text{eff}} = 4000, 4400, 4800$  K;  $\log g = 1.5, 2.0, 2.5$ ), and  $A(\text{Li}) = 1.3, 2.3, 3.3$ , corresponding approximately to the Spite plateau, the onset of Li-richness, and the meteoritic solar-system abundance. Two chemical compositions were considered:  $[\text{Fe}/\text{H}] = -1.5$  with  $[\alpha/\text{Fe}] = 0.4$ , and  $[\text{Fe}/\text{H}] = -0.5$  with  $[\alpha/\text{Fe}] = 0.0$ . We also assumed two isotopic mixtures: pure  ${}^7\text{Li}$  and  ${}^6\text{Li}/{}^7\text{Li} = 0.08$  (meteoritic). A microturbulence of  $2 \text{ km s}^{-1}$  was adopted. All calculations are based on ATLAS12 1D plane-parallel LTE models with SYNTH spectrum synthesis (Kurucz 2005; Sbordone et al. 2004; Sbordone 2005).

The synthetic spectra were convolved with a Gaussian profile corresponding to a total FWHM of  $6.25 \text{ km s}^{-1}$ , combining HRMOS resolution ( $R = 80\,000$ ) and  $5 \text{ km s}^{-1}$  macroturbulence, then resampled to 2.7 pixels per resolution element ( $0.00315 \text{ nm pixel}^{-1}$ ) and degraded with Poisson

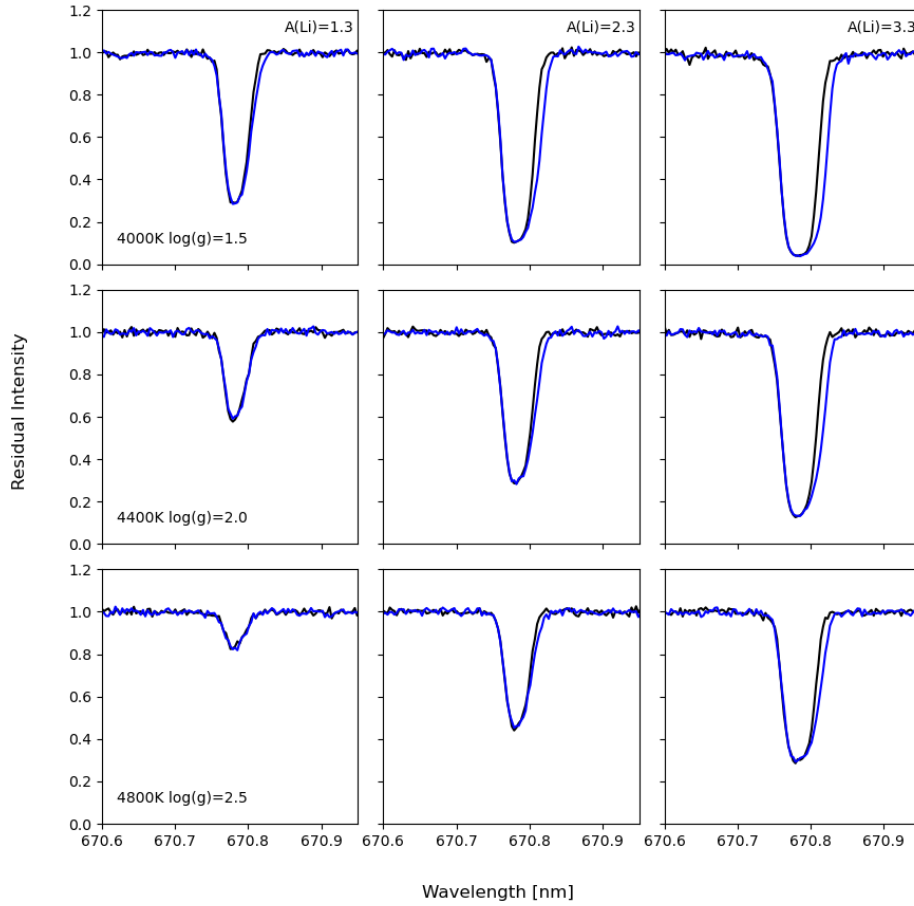


**Figure 6.7.** Same as in Fig. 6.6, but for  $[\text{Fe}/\text{H}] = -1.5$ ,  $[\alpha/\text{Fe}] = 0.4$ , and  $\text{SNR} = 100$

noise to  $\text{SNR} = 50$  and  $100$ . Figure 6.6 shows the most challenging case ( $[\text{Fe}/\text{H}] = -0.5$ ,  $\text{SNR} = 50$ ), where metallic blending is slightly enhanced, while Figure 6.7 shows the cleaner case ( $[\text{Fe}/\text{H}] = -1.5$ ,  $\text{SNR} = 100$ ). In both figures,  $A(\text{Li})$  increases left-to-right and  $T_{\text{eff}}$  increases top-to-bottom; black and blue spectra correspond to pure  ${}^7\text{Li}$  and meteoritic isotopic mixtures, respectively.

The Li feature appears as a single asymmetric profile due to thermal and turbulent broadening. The small redward shift of the  ${}^6\text{Li}$  component induces subtle changes in line asymmetry. The doublet strengthens significantly at lower temperatures and can be measured even below the classical Li-rich threshold. At high  $A(\text{Li})$  and low  $T_{\text{eff}}$ , the  ${}^7\text{Li}$  component becomes saturated, while the weaker  ${}^6\text{Li}$  contribution remains sensitive to abundance and temperature, enabling isotopic measurements in favourable cases.

Finally, the Li I doublet is sensitive to 3D and NLTE effects, and isotopic measurements rely critically on reproducing subtle line asymmetries, which are also affected by convective motions (e.g. Monaco et al. 2014). Accurate abundances and isotopic ratios therefore require 3D NLTE hydrodynamical synthesis. Such methods, together with reliable Li model atoms, are now well established and have been successfully applied over the past decade.

## 6.6 Dynamics and kinematics of star clusters

The last decade has been transformational for studies of the internal dynamics of star clusters. High precision proper motions have been used to derive velocity dispersion profiles for  $\sim 50$  globular cluster with HST (Libralato et al. 2022) and for  $\sim 100$  globular clusters with *Gaia* (Vasiliev & Baumgardt 2021). In addition, proper motions, in particular from *Gaia*, have been key in firmly establishing membership in the low-density outer regions of clusters. Combined with dedicated spectroscopic surveys (Ferraro et al. 2018; Kamann et al. 2018), this has provided new insight into dynamical properties of globular clusters, such as their masses and mass distribution (Baumgardt & Hilker 2018), their orbits in the Milky Way (Baumgardt et al. 2019), internal rotation (Bianchini et al. 2018; Sollima et al. 2019), velocity anisotropy (Vasiliev & Baumgardt 2021; Libralato et al. 2022), tidal tails (Sollima 2020), kinematics near the tidal radius (Wan et al. 2021), intermediate-mass black holes (Häberle et al. 2024), stellar-mass black holes (Dickson et al. 2024) and the stellar mass function below  $\sim 1 M_{\odot}$  (Baumgardt et al. 2023) and above  $\sim 1 M_{\odot}$  (Dickinson et al. 2023). This rapid increase in availability of kinematics has sparked the development of new mass models (Gieles & Zocchi 2015; Daniel et al. 2017) and evolutionary models of star clusters (Wang et al. 2020). Below we discuss several science cases that benefit from HRMOS.

### 6.6.1 Cluster rotation and anisotropy

The median half-light radius of Milky Way globular clusters is  $R_{\text{eff}} \simeq 3$  arcmin (Harris 2010). This means that, when centred on a cluster, the field-of-view of the VLT covers  $\sim 4 R_{\text{eff}}$ . This is a perfect coverage to assess rotation and the velocity dispersion away from the core. At large radii two-body relaxation has not yet erased imprints of the formation process. The velocity dispersion decreases with distance from the centre, such that sub  $\text{km s}^{-1}$  precision is needed to confidently establish rotation of anisotropy signatures. This is where HRMOS will offer significant progress to existing instruments, such as GIRAFFE/FLAMES. This precision will allow HRMOS to trace the primordial dynamical state of clusters, measure rotation and anisotropy across their extent, and constrain models of cluster formation and long-term evolution. The bottom-right panel of Fig. 6.8 shows the mean velocity along the line of sight as function of the projected distance from the cluster centre for a slow and fast rotating globular cluster as seen by HRMOS.

### 6.6.2 Dynamics of multiple populations

Different models for the origin of multiple populations in globular clusters predict different kinematic properties for the sub-populations, some of which survive a Hubble time of dynamical evolution (Hénault-Brunet et al. 2015; Tiongco et al. 2019). These kinematic signatures can be used in addition to the abundance imprints (§ 6.4). Imprints from formation are best preserved at large distances from the centre, where the velocity dispersion is low. It is for this reason that accurate line-of-sight velocities are required. Combined with the growing availability of photometric and spectroscopic data (e.g., Dondoglio et al. 2025), precise radial velocities can be key to distinguish different formation scenarios of the multiple populations.

### 6.6.3 Binaries

The presence of binary stars affects kinematics and can affect inference of dynamical properties (Rastello et al. 2020; Aros et al. 2021). Multi-epoch, precise kinematics can be used to identify binaries and assess their properties (Cottaar & Hénault-Brunet 2014). The binary fraction in globular clusters is significantly lower (few per cent) than for halo stars with the same metallicity. This is

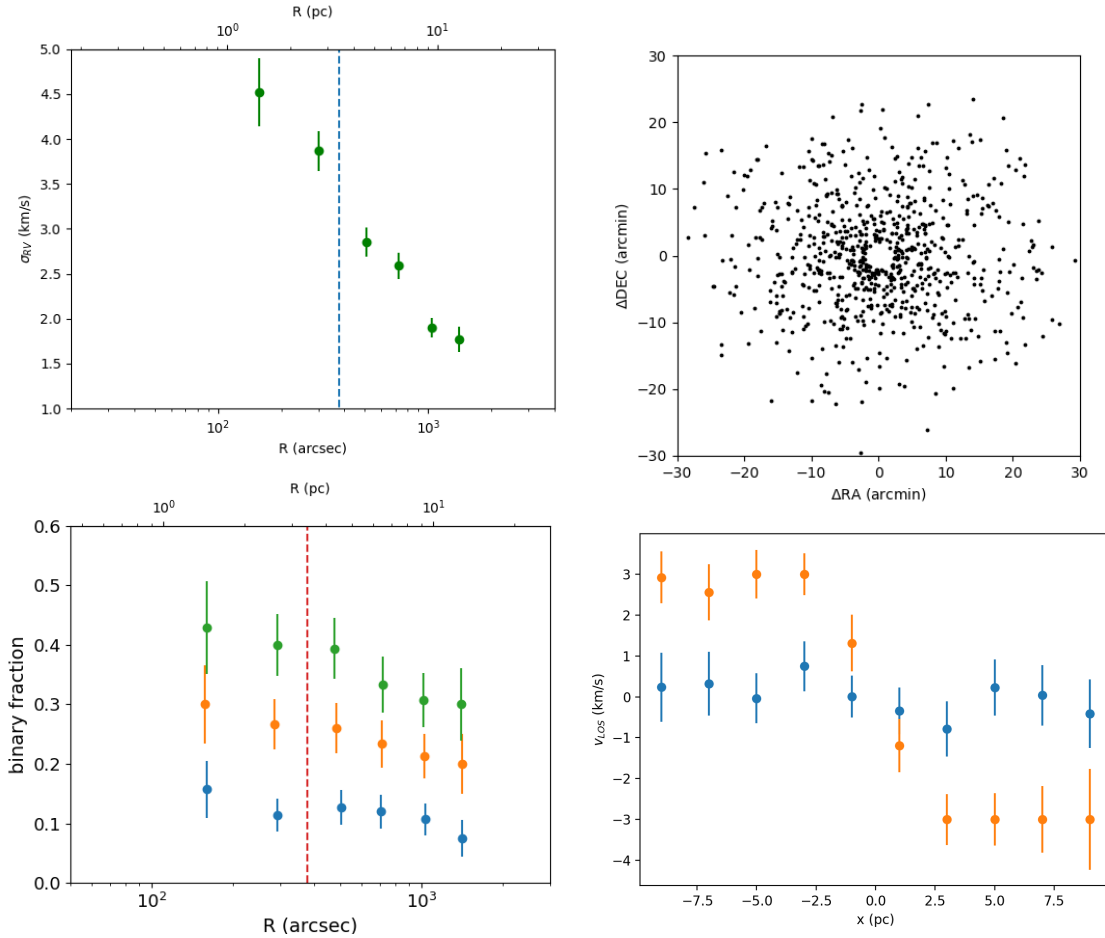


**Figure 6.8.** A simulated observation of the GC M4 with HRMOS. *Top-right:* the distribution of the observed stars. *Top-left:* the variation of the velocity dispersion  $\sigma_{RV}$  with the distance from the GC centre. *Bottom-left:* the observed binary fraction as a function of the distance of the GC, assuming a binary fraction  $f_{\text{bin}} = f_{\text{bin}}(0)(R/R_{HM})^{0.25}$ , with  $f_{\text{bin}}(0) = 0.1$  (blue dots), 0.2 (orange dots), 0.3 (green dots). *Bottom-right:* the mean velocity along the line of sight at different distances from the GC centre for a slow ( $v_{\text{rot}}/\sigma_{RV} = 0.04$ , blue dots) and a fast rotating GC ( $v_{\text{rot}}/\sigma_{RV} = 0.2$ , orange dots), where  $v_{\text{rot}}$  is the rotational velocity of the GC.

thought to be the result of dynamical evolution (Ivanova et al. 2005). Precise line-of-sight velocities, combined with photometric indicators of binarity (e.g., Milone et al. 2012), are a powerful way to assess the present-day properties of binaries in globular clusters, which guides our understanding of the formation and dynamical evolution of the clusters themselves.

#### 6.6.4 Simulations

To evaluate the performances of HRMOS, we simulated the observations of a globular cluster. We used a snapshot of the simulation carried out by Heggie (2014) and assumed the distance and the extinction of M4. In Fig. 6.8, we show the results of a simulated observation of 750 stars in the magnitude range  $15 < G < 18$  ( $10 < \text{SNR} < 90$  in one hour in the red window) in two different epochs, assuming a precision in RV of  $10 \text{ m s}^{-1}$ . In particular, we investigate the capabilities of this instrument to a) derive the velocity dispersion as function of the distance from the cluster centre; b) measure the rotational velocity of the cluster; c) estimate the binary fraction and the effects on the measurements of the velocity dispersion. The simulation probes that HRMOS is expected to be a powerful machine for kinematic studies of star clusters. In particular, the possibility to

observe simultaneously several stars with a precision below  $0.1 \text{ km s}^{-1}$  will significantly improve our capability to determine velocity dispersion of open clusters that usually ranges between  $0.3$  and  $1.0 \text{ km s}^{-1}$  and to identify the correct binary fraction including binaries with a high-mass ratio.

## 7 Galactic and extragalactic gas reservoirs

Ionised nebulae and extragalactic absorption systems probe complementary regimes of gaseous baryons, tracing respectively the impact of stellar feedback in star forming regions and in galaxies and the structure of gas in galactic and circumgalactic environments. HRMOS is ideally suited to exploit these diagnostics across large samples with high efficiency and precision.

### 7.1 Scientific context

The study of gaseous baryons across cosmic environments, from the Milky Way to distant galaxies, benefits significantly from high-resolution multi-object spectroscopy, which adds a crucial layer of physical information beyond what is accessible with lower spectral resolution or single-object observations. In the Galactic context, ionised nebulae trace the interaction between massive stars and the interstellar medium, where complex kinematics, sharp density variations, and strong spatial inhomogeneities require both high spectral resolution and multiplex capability to properly disentangle the underlying physical processes.

On extragalactic scales, absorption-line systems observed against bright background sources provide complementary probes of diffuse gas in galaxies and their halos. In these systems, the identification of multiple kinematic components and the accurate characterisation of line profiles are essential to derive reliable physical conditions, again requiring the combined power of high resolution and multi-object efficiency.

In both regimes, high-resolution MOS observations provide a key added value by enabling an efficient, detailed and physically meaningful decomposition of gas structures. This leads to a deeper understanding of the mechanisms governing gas dynamics, feedback, and gas cycling across a wide range of astrophysical environments. HRMOS, combining high spectral resolving power with multiplex capability, is therefore uniquely positioned to deliver this step-change in diagnostic capability.

#### Key Questions:

- How do massive stars shape ionized nebulae and ultimately cause the dispersal of their own parent cloud?
- Can we use the present-day dynamics and geometry of the ionized gas to derive the mechanical momentum imparted by high-mass star winds and radiation in their past lifetime, linking it to the star masses and evolutionary statuses?
- What is the kinematic structure of AGN-driven winds on nuclear to interstellar medium scales and what is the physics driving the winds?
- Do fundamental constants of physics vary on cosmological time-scales?

## 7.2 The interstellar medium in the Galaxy

The hot, ionised gas component of the Galaxy is prominently visible in optical-band images due to its numerous emission lines, which span most of the visual spectral range. These emission lines provide a wealth of information about the physical conditions of the emitting gas, including velocity fields, temperature, density, extinction (as inferred from the Balmer decrement), ionization parameter, and chemical composition (Osterbrock & Ferland 2006).

An ionised nebula, such as an HII region, receives a substantial energy input from the massive OB stars embedded within it, both in the form of mechanical momentum from stellar winds and of stellar radiation, predominantly in the ultraviolet. As a consequence, it is a highly dynamical environment, with physical properties that vary significantly from place to place. A proper spectroscopic study of these nebulae therefore requires adequate spatial sampling, achievable through either an integral field unit (IFU) or a multi-object spectrograph (MOS). Since filamentary nebular structures do not exhibit a characteristic length scale, finer spatial sampling leads to a progressively more accurate characterisation of the physical conditions of the nebula.

In this context, a fibre separation of 10–15 arcsec represents an effective baseline sampling scale for HRMOS observations, well matched to the typical spatial coherence of nebular structures. Since nebular emission is generally not time-variable, iterated (dithered) pointings over the same sky region can be used to progressively enhance the effective spatial sampling, yielding a finer reconstruction of the emission morphology. Owing to the strong feedback from massive stars, velocity fields can reach values of several tens of  $\text{km s}^{-1}$ . In the Carina Nebula, which hosts some of the most massive known O-type stars, doubly peaked emission lines have been observed, originating from large expanding gas shells surrounding these stars. In this way, the combined spatial and spectral mapping of the gas emission provides key information on the three-dimensional structure of the nebula and its interaction with the embedded massive stellar population (e.g., Damiani et al. 2016).

In the HRMOS wavelength ranges, i.e. [385–419 nm], [480–522 nm] and [623–677 nm], the dominant nebular emission lines include H $\alpha$  (656.3 nm), H $\beta$  (486.1 nm), [O I] (630.0 nm), the [N II] doublet (654.8, 658.4 nm), and the [O III] doublet (496.9, 500.7 nm). The density-sensitive [S II] doublet (671.3, 673.1 nm) will also be included in the red spectral range. Additional, fainter lines within the same spectral ranges include higher-order Balmer transitions such as H $\delta$  (410.2 nm), and H $\epsilon$  (397.0 nm), as well as [Ne III] (386.9 and 396.7 nm), [N I] (519.9 nm), He I (667.8, 501.6, 388.9, 402.6 nm), [Ar III] (519.2 nm), O II (407.2 nm), and [S III] (631.2 nm). In particular, the He I line at 388.9 nm is density-sensitive and coincides with H $\theta$ , but exhibits a smaller thermal width ( $\sim 0.03$  nm) owing to the higher atomic mass of helium compared to hydrogen. The high spectral resolution of HRMOS may therefore allow the separation of the two contributions within this blended feature. Similarly, resolving power is required to disentangle the [S II] lines at 406.9 and 407.6 nm from the nearby [O II] multiplet spanning 406.96–407.59 nm.

At  $R \sim 80,000$ , the thermal widths of nebular emission lines (typically 0.02–0.05 nm) will be spectrally resolved. This will provide an independent estimate of the gas temperature from individual line profiles, complementary to line-ratio diagnostics, which may not be sensitive across the full range of temperatures present within a nebula.

The ratio  $I_{671.6}/I_{673.1}$  of the [SII] doublet provides a robust diagnostic of the electron density, while the combined ratio  $(I_{671.6} + I_{673.1})/(I_{406.8} + I_{407.6})$  is sensitive to the electron temperature. The blue doublet ratio  $I_{406.8}/I_{407.6}$  constitutes an additional density diagnostic. These lines must be resolved from the neighbouring OII multiplet, a separation that will be enabled by the spectral resolution of HRMOS. For temperature measurements, the HRMOS data will enable the application of the Strong-Line Method (Arellano-Córdova & Rodríguez 2020), through the computation of the

$O_3N_2$  index using  $H\alpha$ ,  $H\beta$ ,  $[OIII]$  500.7 nm, and  $[NII]$  658.4 nm. High-ionisation emission lines may also reveal the presence of very hot ionising stars, even in regions of strong optical extinction that prevent direct detection of the stellar continuum in the blue spectral range. As an example, the so-called “Bajamar star” (Comerón & Pasquali 2005), which is responsible for the excitation of the NGC 7000 nebula, is optically obscured at visual wavelengths.

Emission from ionized nebulae is concentrated in a limited number of strong emission lines, with essentially no continuum contribution. This is particularly advantageous for spectroscopic observations, even in cases where nebulae appear faint in optical imaging compared to embedded stellar sources. If the specific intensity (flux per steradian) of a stellar image, broadened by seeing and the instrumental PSF, is comparable to the diffuse nebular surface brightness in the  $G$  band, the nebular signal is confined to only  $\sim 5$  nm when considering the main diagnostic lines, compared to  $\sim 5000$  nm for a stellar continuum over the same spectral range. This difference of roughly three orders of magnitude translates into a substantial gain in observational efficiency for nebular studies.

In this context, HRMOS is particularly well suited to exploit the high surface-brightness contrast of emission-line nebulae. The ability to perform repeated exposures with dithering provides a powerful strategy to overcome the limitations imposed by the finite number of fibres and their minimum separation, enabling a progressively finer reconstruction of the nebular structure.

The capability of multi-object spectroscopic surveys to deliver major advances in the study of H II regions has already been demonstrated by Gaia-ESO Survey observations of the Carina and M8 nebulae (Damiani et al. 2016, 2017).

### 7.2.1 Products, potential targets and synergies for the Galactic case

**Scientific products.** HRMOS observations of Galactic ionised regions will enable a comprehensive set of scientific products. These include detailed gas kinematics from high-resolution modelling of emission-line profiles, and three-dimensional structural reconstruction through spatially resolved velocity fields. In addition, spatially resolved maps of electron temperature and density will be obtained, together with constraints on the ionisation parameter and interstellar reddening independent of stellar-based estimates. These diagnostics will be derived across hundreds of sight-lines in each nebular complex, enabling statistically robust studies of their physical conditions and internal variations.

**Potential targets and observing strategy.** From a geographical perspective, a Southern Hemisphere facility provides privileged access to the most active star-forming regions of the Milky Way, including the Inner Galactic Plane, the Carina–Sagittarius Arm, the Vela/Puppis complexes, and the Orion/Monoceros regions. A particularly compelling objective is the systematic spectroscopic coverage of the hundreds of H II regions listed in the NGC, IC, RCW, and Sharpless catalogues accessible from Paranal.

**Synergies.** HRMOS observations will benefit from strong synergies with ongoing and upcoming large spectroscopic surveys. In particular, the WEAVE SCIP survey will provide complementary observations of similar astrophysical environments. Although no 4MOST survey is explicitly dedicated to nebular science, its stellar surveys of the Galactic plane—especially those targeting young clusters—will include a large number of sky fibres sampling diffuse emission, which will constitute a valuable ancillary dataset for nebular studies and cross-comparison with HRMOS results.

### 7.3 Extragalactic gas reservoirs

In addition to Galactic ionized gas, HRMOS can be used to investigate gaseous reservoirs in and around galaxies, traced through absorption features against bright background continuum sources such as active galactic nuclei (AGN) and quasars. These absorption systems can be broadly classified into three main categories, on their distance from the continuum source and on their kinematic properties:

- **Intrinsic / associated systems:** Absorption systems at  $z_{\text{abs}}$  within a velocity offset of a few hundred  $\text{km s}^{-1}$  from the emission redshift of the background source ( $z_{\text{abs}} \sim z_{\text{bkg}}$ ), generally associated with the interstellar medium of the host galaxy ( $\text{FWHM} \sim 20\text{--}500 \text{ km s}^{-1}$ ), including AGN-driven outflows. These features are observed in a significant fraction of Seyfert I galaxies in rest-frame UV resonance lines (up to  $\sim 50\%$ ; Crenshaw et al. 1999) and, more rarely, in He I and HI Balmer transitions. In quasars, narrow associated absorption systems can exhibit blueshifted velocities of  $1000\text{--}5000 \text{ km s}^{-1}$  relative to  $z_{\text{bkg}}$  (Hamann et al. 2001).
- **Broad absorption line systems (BALs):** Absorption features with typical  $\text{FWHM} > 2000 \text{ km s}^{-1}$  and blue-shifted velocities reaching up to  $\sim 0.2c$  with respect to  $z_{\text{bkg}}$ . They are commonly observed in both high-ionisation (C IV, N V) and low-ionization (Mg II) transitions. BALs are detected in  $\sim 10\text{--}50\%$  of high-redshift quasars (Gibson et al. 2009; Bischetti et al. 2022), and trace powerful outflows on sub-pc to kpc scales (Arav et al. 2018) capable of heating and depleting the interstellar medium of the host galaxy.
- **Intervening systems:** Absorption arising in (inter-)circumgalactic halos and galactic disks containing metals and, in some cases, molecules. These systems are characterized by  $z_{\text{abs}} \ll z_{\text{bkg}}$ , where  $z_{\text{abs}}$  and  $z_{\text{bkg}}$  denote the redshift of the absorber and of the background source, respectively. Metal absorption profiles typically exhibit  $\text{FWHM} \lesssim 20\text{--}200 \text{ km s}^{-1}$ , and high-resolution spectroscopy often reveals complex kinematic substructure in the absorbing gas (e.g. Werk et al. 2016).

These systems are illustrated in Figure 7.1.

High spectral resolution is advantageous for the study of all the absorption systems described above. As an example, observations at spectral resolving power  $R > 10\,000$  have revealed increasing complexity in the profiles of broad absorption line troughs (e.g. Dunn et al. 2010; Borguet et al. 2013). This complexity indicates that the observed absorption often arises from multiple, and in some cases several, distinct kinematic components in both Seyfert and quasar outflows.

The standard approach for analysing absorption features in quasar spectra is based on the apparent optical depth method. This requires the identification of individual kinematic components and the measurement of their optical depths for each atomic species. The resulting optical depths are converted into ionic column densities and compared with photoionisation models to infer the physical conditions of the gas along the line of sight. However, in cases where kinematic components are blended, this method can only provide lower limits to the column densities, leading to weak constraints on the gas density and on its distance from the continuum source (Choi et al. 2020).

Studies at  $R \approx 80,000$  have so far remained limited due to the long exposure times required for distant quasars, while UV investigations of nearby objects have been primarily carried out with *HST*. Although ground-based observations, for instance from X-shooter, confirm a high level of kinematic complexity also in quasars (Vietri et al. 2025), current theoretical models of AGN winds still largely rely on the assumption of homogeneous gas, thereby preventing a realistic description

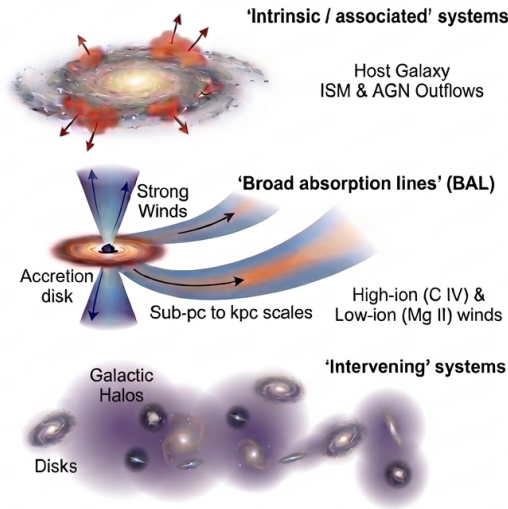


**Figure 7.1.** Three types of absorption systems that could be studied with HRMOS observations of extragalactic sources like quasars and AGN (see text for details). This image was created using generative large-language model Gemini 3, using the description of absorption systems as prompt.

of AGN feedback. HRMOS observations, at a spectral resolution corresponding to  $3\text{--}5\text{ km s}^{-1}$ , will enable the disentangling of these kinematic components. This capability is essential to (i) build a realistic picture of the kinematic structure of the interstellar and circumgalactic medium, and (ii) break the degeneracy between partial covering and optical depth in optically thin absorption profiles, thereby enabling robust measurements of the physical conditions of the gas. Emerging correlations between the properties of winds detected in absorption and those of emission-line winds on scales from parsecs to galactic scales are beginning to provide key constraints for AGN feedback prescriptions in galaxy evolution models (e.g. Brazzini et al. 2025; Temple et al. 2024).

Intervening absorption systems constrain the cosmic history of metal enrichment, complementing similar studies referenced in Chapter 3. The same data can be used to test extensions of the  $\Lambda$ CDM cosmological model through measurements of the values of fundamental physical constants in the early Universe. In many such models, new degrees of freedom (e.g. a scalar or a vector field, compactified spatial dimensions, etc.) couple to the matter fields of the Standard Model of particle physics, manifesting as temporal or spatial variations of constants such as the fine-structure constant ( $\alpha = e^2/4\pi\epsilon_0\hbar c$ ) or proton-to-electron mass ratio  $\mu = m_p/m_e$  (see the review by Uzan 2025). The most precise method for high redshift measurement of  $\alpha$  from metal absorption (the “many-multiplet” method Dzuba et al. 1999; Webb et al. 1999) and  $\mu$  from molecular absorption (Thompson 1975; Ubachs 2018), both require from high resolution spectroscopy ( $R > 40\,000$ ) and accurate wavelength calibration of astronomical spectrographs (relative uncertainty on wavelengths,  $\sigma_\lambda/\lambda$ , should be better than  $\lesssim 10\text{ ms}^{-1}$  to match uncertainties on laboratory wavelength measurements). With the current baseline performance, HRMOS will be able to measure  $\Delta\alpha/\alpha$  and  $\Delta\mu/\mu$  with a precision of several parts per million, provided that its line-spread function is well characterised.

### 7.3.1 Products, potential targets, and synergies for the extragalactic case

**Products.** New spectral analysis tools, such as AI-VPFIT Lee et al. (2021a); Webb et al. (2021); Milaković et al. (2023), can be employed for the automatic modelling of HRMOS spectra. These

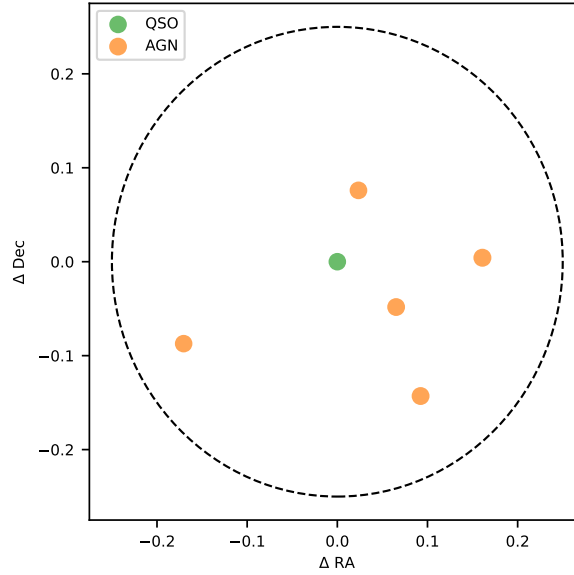


**Figure 7.2.** HRMOS can be used to study extragalactic gas in absorption towards quasars and other AGN. Based on known luminosity functions, a typical VLT field of view contains on average  $\sim 8$  AGN, including approximately one quasar. The figure illustrates a representative fibre allocation strategy.

tools provide measurements of line widths, column densities, and redshifts of absorption systems, which can be used to constrain the physical properties of the intervening gas, including potential constraints on  $\Delta\alpha/\alpha$ . In validation tests, AI-VPFIT has been shown to recover unbiased simulated input parameters in 99% of cases Lee et al. (2021b); Webb et al. (2022).

**Potential targets and observing strategy.** Although intrinsically luminous, quasars and other AGN appear faint due to their large distances, with most objects fainter than  $G = 20$ . At  $G \sim 18$  a  $\text{SNR} > 5$  in the red window can be achieved, as shown in Fig. 1.1.

Using the SDSS quasar luminosity function (Palanque-Delabrouille et al. 2016), we estimate a surface density of 0.79 (7.16) quasars per  $\text{deg}^2$  brighter than  $G < 18$  (19), corresponding to only a few quasars per HRMOS field of view (Fig. 7.2). Type-I AGN are expected to be roughly an order of magnitude more numerous (e.g. Bongiorno et al. 2007), providing additional background continuum sources beyond quasars.

A natural observing strategy is therefore to allocate  $\sim 10$  HRMOS fibres to quasars and AGN within the field of view, while distributing remaining fibres to sky positions for systematics control and/or to nearby stars of comparable magnitude. A preliminary cross-match with Gaia indicates the presence of several hundred suitable stellar sources per field, enabling efficient and flexible fibre allocation (Fig. 7.2).

**Synergies.** A key advantage of HRMOS, compared to other multi-object spectrographs on large telescopes (e.g. 4MOST, WEAVE, and MOONS), is its significantly higher spectral resolving power. The resolution of  $R = 80,000$  enables a much more detailed physical characterisation of absorbing gas, particularly in terms of kinematic decomposition and line-profile structure. This advantage is, however, partially offset by the non-continuous wavelength coverage of HRMOS, which requires prior identification of suitable targets through complementary spectroscopic surveys. In this context, HRMOS is ideally positioned as a follow-up instrument for large surveys such as 4MOST, WEAVE, and MOONS.

## 8 Atomic data for high-precision spectroscopy

Accurate atomic data are essential to correctly interpret high-resolution astrophysical spectra, as they determine the reliability of derived abundances, kinematics, and plasma diagnostics. HRMOS will critically depend on improved laboratory and theoretical atomic data to fully exploit its resolving power. For the first time, before an instrument is operational, a coordinated effort between spectroscopy and laboratory astrophysics is therefore foreseen to enable its full scientific potential.

### 8.1 Scientific context

In high-precision, high-resolution astrophysical spectroscopy, the accuracy of the extracted astrophysical information is fundamentally determined by the quality of the underlying atomic data. Wavelengths, energy levels, transition probabilities, and hyperfine and isotopic structures govern the formation and appearance of spectral lines and thus directly affect the derivation of plasma parameters and chemical abundances. Accurate atomic data therefore constitute the indispensable foundation of astrophysical spectroscopy.

Despite the importance of accurate atomic data to all astrophysical spectroscopy, most existing data, especially for elements beyond the iron-group, derive from low-resolution laboratory experiments measured in the mid-20th century or from theoretical calculations with limited experimental calibration or validation. For example, the situation for heavy neutron-capture elements, which dominate the opacity in kilonova ejecta and shape the spectra of chemically peculiar stars, is stark. Transition probabilities often disagree by factors of ten or more between sources; energy level structures have high uncertainties and are fragmentary, often with critical configurations missing; and isotopic and hyperfine components are completely absent from most lists. Uncertainties in oscillator strengths propagate directly into abundance determinations, and the absence of hyperfine components alters line shapes, causing radial velocity shifts at the meter-per-second scale, which are critical in the context of exoplanet searches and stellar kinematics.

The blue spectral region (385 - 419 nm), where HRMOS will operate, exemplifies the challenge. This domain is crowded with transitions from complex species such as the lanthanides, whose atomic structures produce dense forests of overlapping spectral lines. Without complete and accurate laboratory data, even basic line identification becomes uncertain. The consequences cascade: isotopic ratios cannot be measured, weak neutron-capture lines remain inaccessible, and abundance determinations fail to reach the accuracies demanded.

These shortcomings are not isolated; they reflect a systemic underinvestment in laboratory astrophysics. As discussed, many datasets critical for HRMOS science cases date back over half a century, and for numerous species relevant to nucleosynthesis and chemical evolution, no modern measurements exist at all. The cost of inaction is clear: without a coordinated programme to expand the atomic database, HRMOS risks producing spectra that remain under-analysed for decades, diminishing the scientific return on this flagship instrument. Atomic data are not ancillary, they are critical infrastructure. Planning for atomic data research must be embedded from the outset, funded and prioritised alongside hardware development. Only by coupling HRMOS' observational capabilities with a sustained, systematic effort to deliver high-accuracy atomic data

can we guarantee that its spectra fulfil their scientific promise.

**Key Quantities:** Experimental and theoretical values of the following atomic data for key elements are essential for enabling accurate interpretation of high-resolution spectra and maximising the scientific return of HRMOS:

- Wavelengths
- Energy levels
- $\log(gf)$ s
- Hyperfine structure constants
- Isotope structure components

## 8.2 Capabilities: Delivering Atomic Data at the Accuracy HRMOS Demands

High-resolution spectroscopy has advanced dramatically since large sections of the atomic databases currently in use were determined. The perception of completeness is misleading: for many species the available datasets are fragmentary, inconsistent, and in some cases fundamentally unreliable. Without new, accurate laboratory measurements of wavelengths, transition probabilities, and hyperfine and isotope structures, many HRMOS spectra risk becoming archives of unresolved information instead of engines driving breakthroughs in stellar and Galactic physics.

The following sections detail the capabilities of modern laboratory measurements and demonstrate the necessity of experimental atomic data for high-resolution astrophysical spectroscopy.

### 8.2.1 Experimental atomic data

#### Wavelengths and Energy Levels

Fourier Transform Spectroscopy (FTS) is the benchmark technique for large-scale, high-resolution laboratory analyses of wavelengths and energy levels. FTS combines ultra-high resolving powers ( $R > 10^6$ ) with broad spectral coverage, recording thousands of lines simultaneously at high resolution from the ultraviolet to the infrared (Concepcion et al. 2023). This capability is indispensable for constructing complete energy level systems for complex species, where transitions often span multiple spectral regions.

In the visible range, uncertainties for strong, unblended lines are typically in the sub-mK region ( $\sim 10^{-3} \text{cm}^{-1}$ ), corresponding to radial velocity uncertainties of about  $10 \text{ m s}^{-1}$ . This level of accuracy is essential as HRMOS aims to measure stellar radial velocities and chemical signatures at sensitivities where systematic errors from atomic data would otherwise dominate. If laboratory wavelengths are inaccurate by even a few  $10^{-4} \text{ nm}$ , derived velocities can be biased by tens of  $\text{m s}^{-1}$ , comparable to the signal of an Earth-like exoplanet or the internal kinematics of stellar clusters. Such biases could lead to incorrect conclusions about stellar dynamics, planet detection, or chemical identification.

Accurate energy levels are equally critical. HRMOS spectra will contain thousands of blended lines, especially for heavy elements, where complex atomic structures produce dense forests of transitions (Ding 2025). Large-scale energy level analysis using FTS data enables least-squares optimisation of level values, resulting in Ritz wavelengths that surpass the accuracy of individual

observed measurements. These optimised values provide the high accuracy foundation for astrophysical line lists, ensuring reliable species identification in environments where blending from overlapping lines and Doppler broadening severely complicates interpretation.

The scientific stakes are high: HRMOS aims for radial velocity precision at the  $10 \text{ m s}^{-1}$  level and abundance uncertainties below 0.05 dex. Achieving these goals requires laboratory wavelengths accurate to better than  $2.5 \cdot 10^{-3} \text{ nm}$ , which is achievable with high-resolution FTS. Inaccuracies at this scale propagate directly into astrophysical interpretation, affecting measurements of stellar motions, nucleosynthetic signatures, and age-dating techniques based on radioactive chronometers. Next-generation surveys will push to fainter stars and more metal-rich environments, where line blending is extreme and high-accuracy laboratory data will be essential for disentangling these spectra.

### Transition Probabilities

Transition probabilities (Einstein coefficients for spontaneous emission, oscillator strengths, or  $f$ -values) are fundamental atomic parameters that link observed line strengths to chemical abundances. Uncertainties in transition probabilities propagate directly into abundance uncertainties: for example, a 50% uncertainty in a transition probability corresponds to  $\sim 0.2$  dex in abundance, large enough to obscure nucleosynthetic signatures. HRMOS science cases, such as tracing  $r$ - and  $s$ -process enrichment or age-dating stars via radioactive chronometers, require abundance uncertainties well below 0.05 dex and achieving this demands laboratory measurements with accuracies of 5–10%.

Transition probabilities are derived from calibrated line intensities. After recording spectra, intensity calibration is performed using standard lamps (deuterium for UV, tungsten for visible/IR, and xenon for bridging the UV-visible gap). The region between 350 and 380 nm is particularly challenging due to low lamp output in this region, but this can be mitigated by xenon lamps or calibration using well-known argon lines (Belmonte et al. 2025; Lawler & Den Hartog 2019).

Two main experimental approaches to determine transition probabilities from calibrated line intensities are used:

**Branching Fraction Method.** This technique measures the relative intensities of all lines originating from a common upper energy level to determine branching fractions (defined as the ratio between the intensity of a particular line over the sum of intensities of all spectral lines from the same upper energy level), which are then combined with the level's radiative lifetime (typically measured by laser-induced fluorescence (Bergstrom et al. 1988)) to obtain transition probabilities. This technique's main advantage is that it does not require any assumptions about source plasma conditions and yields highly accurate results when all decay channels are observed. However, it does demand complete spectral coverage across multiple regions if transitions from the given upper level lie in those regions and access to reliable lifetime data which is often unavailable for heavy ions.

**Boltzmann-Plot Technique.** This method assumes local thermodynamic equilibrium (LTE) in the plasma source and uses the distribution of calibrated line intensities versus upper energy level to infer transition probabilities. This technique is particularly useful when lifetime measurements are unavailable, as tends to be the case for high-lying energy levels. Another advantage is that only the lines of interest need to be measured rather than all lines originating from a given upper energy level. However, the reliability of this technique depends on the validity of local thermodynamic equilibrium and on the existence of a set of reference lines with accurate known transition probabilities. These reference lines are used to determine the population temperature of the plasma.

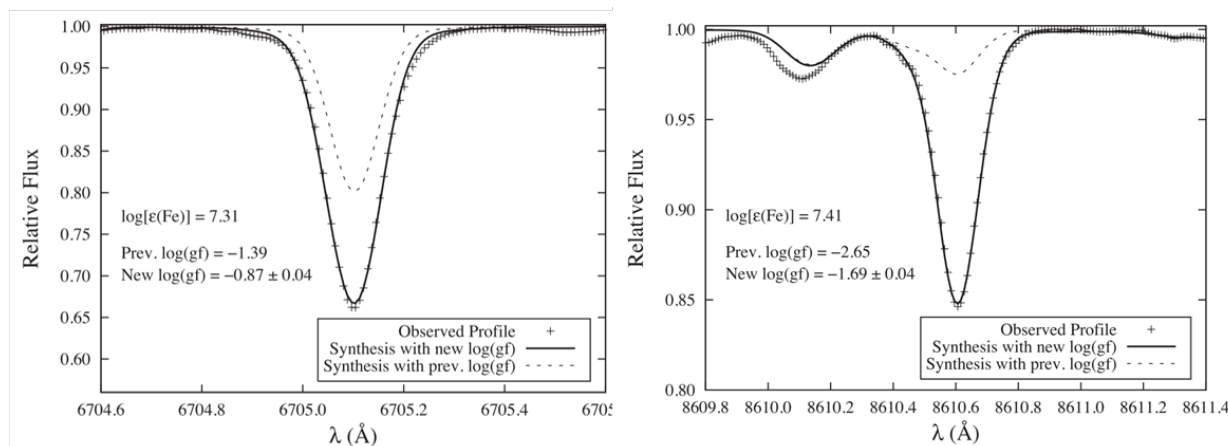


**Figure 8.1.** Improvement in the synthesis of neutral iron (Fe I) solar lines when using new values of  $\log(gf)$  measured by Ruffoni et al. (2014) with a high-resolution Fourier transform spectrometer. The dotted lines show the synthesis using the previous best values.

The importance of accurate laboratory transition probabilities is illustrated in Figure 8.1. Here, the synthesis of two neutral iron (Fe I) solar lines is shown using newly measured  $\log(gf)$  values obtained with a high-resolution Fourier transform spectrometer by Ruffoni et al. (2014). The improved oscillator strengths produce a much better match between the observed and synthetic spectra compared to the previous best values (dotted line). These examples demonstrate how inaccurate atomic data can lead to systematic discrepancies in spectral modelling, directly impacting abundance determinations. For HRMOS, which aims to detect subtle chemical signatures, such improvements are critical to achieving its science goals.

### Nuclear Broadening Effects: Hyperfine and Isotope Structure

Hyperfine and isotope structures are nuclear broadening effects that introduce small shifts in atomic energy levels and spectral line positions. Hyperfine structure (HFS) originates from the interaction between the nuclear magnetic dipole and electric quadrupole moments with the electromagnetic field of the electrons, resulting in the splitting of fine structure energy levels. Isotope structure (IS) arises from differences in nuclear mass and volume among isotopes of the same element, which lead to shifts in spectral line positions for each isotope.

Both hyperfine and isotope shifts alter line profiles and, if neglected, introduce systematic errors in both radial velocity and abundance analyses of astrophysical spectra. Fig. 8.2 demonstrates the effects of neglecting nuclear broadening on line profiles, resulting in substantial discrepancies for resultant abundances (Lundqvist, M. et al. 2007). Hyperfine and isotope structures are subtle but critical effects that must be accounted for in high-resolution spectroscopy. Their impact on line profiles, radial velocities, and abundance determinations is non-negligible and can have large effects on interpretation of astrophysical spectra. Accurate laboratory measurements of these structures are therefore essential to meet HRMOS science goals and avoid systematic errors that would compromise chemical abundances and isotopic studies.

For species such as Ba, Eu, and Pb, which are key tracers of neutron-capture processes, these effects can distort line centres by tens of  $\text{m s}^{-1}$  and change equivalent widths significantly. HRMOS aims for meter-per-second radial velocity stability and precise isotopic ratios; without laboratory measurements of HFS/IS components the introduced systematic biases will exceed these precisions and compromise exoplanet detection and isotopic studies.

Fig. 8.3 illustrates the resolving power of laboratory spectroscopy in capturing hyperfine

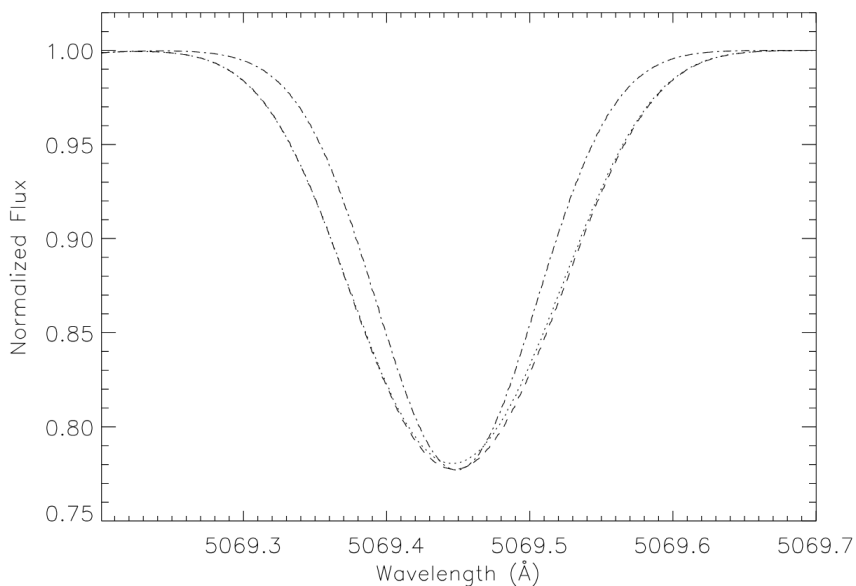


**Figure 8.2.** Synthetic spectra of Sm II  $\lambda 5069$  showing the impact of both hyperfine and isotope structure on line profile (Lundqvist, M. et al. 2007). The dotted profile includes both HFS and IS, the dashed profile is IS only and the dot-dashed profile is without either HFS or IS. The difference between the lines with structure and without is  $\sim 0.1$  dex.

structure in complex ions. The Co II line at 261.51 nm is shown with its observed profile (black) and fitted profile (red dashed), where individual hyperfine components are resolved and their relative intensities indicated by red lines (Ding & Pickering 2020). At the top, the transition diagram details the splitting pattern governed by the hyperfine  $A$  and  $B$  constants. This level of detail enables accurate determination of hyperfine constants and isotope shifts from laboratory spectra, providing the data needed to model high-resolution astrophysical spectra accurately. Without these measurements, synthetic spectra would fail to reproduce observed line asymmetries and widths, introducing systematic errors in radial velocities and abundance analyses. For HRMOS, which targets meter-per-second precision and isotopic ratio determinations, laboratory-resolved hyperfine and isotope structures are indispensable.

### Plasma Sources

Producing complete and accurate atomic data requires tailored plasma conditions to generate and populate multiple ionisation stages of different species. Hollow cathode and Penning discharge lamps are the workhorses for generating intense, stable emission spectra across the IR–UV range. Hollow cathode lamps (HCL) can be both commercial, which operate at low currents of up to 30 mA and so only populate low-lying energy level of low ionisation species, or custom, high-powered (up to 2 A) lamps which can populate high-lying levels of neutral (I), singly- (II) and doubly-ionised (III) species. This second lamp type is far more versatile and has several advantages (Sarma et al. 2024): the lamp can be fitted with a cathode made of many different elements, the carrier gas can be chosen too to excite the upper energy levels of interest and the signal-to-noise ratio of lines coming from different upper energy levels can be optimised by changing the pressure of the carrier gas and the current.

Penning lamps use the same mechanism of radiation generation as hollow cathode lamps, but with the addition of a permanent magnetic field which increases the number of collisions within the plasma. Penning lamps can be fitted with cathodes of different elements to produce up to triply

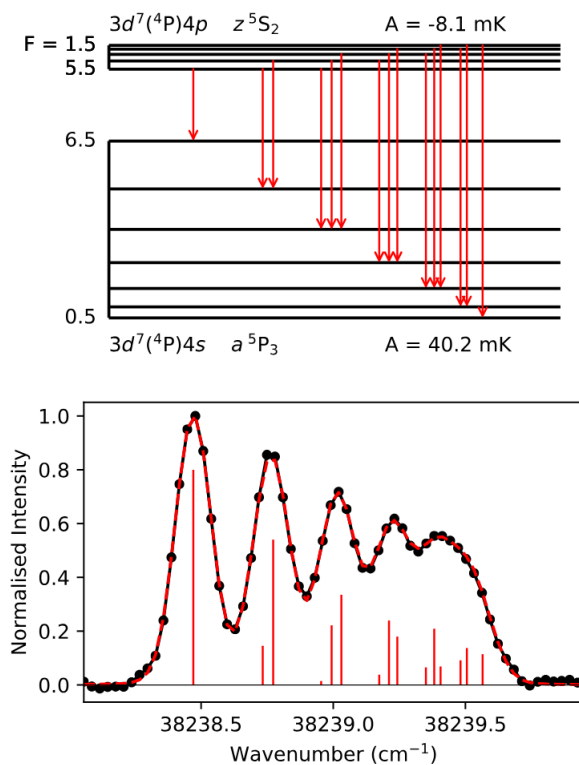


**Figure 8.3.** Observed (black) and fitted (red dashed) line profile of the Co II 261.51 nm transition from Ding & Pickering (2020). The relative intensities of the individual HFS components are given by red lines. The transition diagram detailing individual hyperfine transitions is shown at the top of the figure.

ionised (iv) atoms (Heise et al. 1994). A third way of getting emission spectra, in this case from neutral and singly ionised elements, is using laser-induced breakdown spectroscopy (LIBS). This technique can be used to measure Stark widths and shifts (Manrique et al. 2025) and transition probabilities (Rehse & Ryder 2009; Kodangil et al. 2026). The accuracy of the measurements will depend of the resolving power of the instrument used to record the radiation.

These three light sources enable measurements of thousands of lines for species such as iron-peak elements or the very important lanthanides which dominate kilonova spectra and are central to nucleosynthesis science cases of HRMOS. Without these light sources, laboratory data would remain incomplete, limiting the ability of HRMOS to interpret complex stellar and transient spectra.

### 8.2.2 Theoretical atomic data

While experimental measurements remain the benchmark for high-accuracy atomic data, theoretical calculations will play an indispensable role in meeting the science requirements of HRMOS. Their importance is twofold: firstly, theory provides the framework for interpreting complex laboratory spectra, enabling level assignments, predicting unknown levels, and providing estimates of transition probabilities, without which deciphering dense atomic spectra would be almost impossible; secondly, theory can deliver predictions of atomic parameters in cases where experiments are incomplete or impractical. For HRMOS, which targets species with complex atomic structures and elements of multiple ionisation stages, the synergy between theory and experiment is essential.

Modern atomic structure theory has advanced significantly, leveraging relativistic and correlation effects to achieve accuracies that were unattainable in earlier decades. State-of-the-art approaches include multi-configuration Dirac–Hartree–Fock (MCDHF) and relativistic configura-

tion interaction (RCI) methods (Fischer et al. 2016), implemented in widely used codes such as GRASP (Jönsson et al. 2013), FAC (Gu 2008), and AUTOSTRUCTURE (Badnell 2016), as well as semi-empirical techniques based on least-squares fitting of observed energy levels combined with theoretical transition probabilities, such as the orthogonal operator method (Uylings & Raassen 2019) or the Cowan code (Cowan 2023). These methods allow the calculation of key atomic quantities: energy levels, oscillator strengths ( $\log(gf)$ ), radiative lifetimes, and branching ratios, across large systems where experimental coverage is difficult.

The accuracy of theoretical data depends strongly on the quantity being calculated and the complexity of the atomic system. For energy levels, *ab initio* methods typically achieve energy level and wavelength uncertainties on the order of 1% (e.g. Ghosh & Sharma 2026), far larger than the parts in  $10^8$  precision attainable in modern laboratory measurements (Concepcion et al. 2023). This makes calculated level values unsuitable for line identification in high-resolution spectra, where blended features require high-accuracy wavelengths to disentangle. Semi-empirical methods fine-tuned to accurate experimental levels can reduce uncertainties to  $\sim 0.1$ – $0.5\%$  (Uylings & Raassen 2019), making them more useful for term analyses and the prediction of unknown energy levels. While theory cannot replace experiment for wavelength-critical applications, it is invaluable for opacity determinations and large-scale modelling, where completeness of data is more critical than absolute precision.

Calculations for transition probabilities are in general more accurate than for energy levels, especially for simpler systems or strong transitions from levels with little eigenvector mixing. For these cases, theoretical oscillator strengths can approach experimental uncertainties of about 5–10%. Semi-empirical fine-tuning further improves accuracy by refining eigenvector compositions, which in turn strongly govern calculated transition probabilities (Clear et al. 2023b). However, for weaker transitions or those involving significant configuration interaction, uncertainties degrade rapidly, reaching 50–100%, and for very weak lines, often exceed 200%. This behaviour reflects the sensitivity of transition probabilities to wavefunction composition and correlation effects.

### The neodymium example

Neodymium is one of the elements of interest for the science cases of HRMOS and is a good example of the strengths and limitations of theoretical atomic data, as well as its complementarity with experimental data. Alongside experimental efforts, a significant amount of theoretical atomic data on neodymium has been produced in recent years, driven by the astrophysical community's keen interest in interpreting kilonova spectra (Fontes et al. 2017; Tanaka et al. 2020). Due to the vast number of levels and transitions in lanthanides such as neodymium, comprehensive theoretical datasets are frequently the sole source of atomic structure information across broad wavelengths and ionisation ranges relevant to transient spectra. However, the surge in interest from kilonova studies has stimulated renewed experimental campaigns to obtain accurate atomic data for these complex elements.

Several theoretical groups have contributed such datasets, employing various theoretical methodologies and scopes. Gaigalas et al. (2019) calculated atomic data for Nd II, III and IV using multiconfiguration Dirac–Hartree–Fock and relativistic configuration interaction methods to perform extended calculations of energy levels and transition rates. These methods were implemented using modern relativistic atomic structure codes, such as versions of the GRASP2K package (Jönsson et al. 2013). These calculations showed improved agreement with experimental data compared to earlier calculations, but also highlighted persistent uncertainties in level energies that affect wavelength-dependent opacities in kilonova models. Similarly, Tanaka et al. (2018) have employed fully relativistic atomic structure codes (e.g. HULLAC, Bar-Shalom et al. (2001))

to obtain energy levels and transition probabilities and integrated these data into opacity and light-curve simulations. These approaches all demonstrated that atomic structure uncertainties propagate directly into kilonova observables. Simultaneous efforts by a group at Los Alamos (Fontes et al. 2020; Even et al. 2020) have produced a large-scale opacity database (NIST-LANL Lanthanide/Actinide Opacity Database, Ralchenko et al. (2021)) that includes Nd and other lanthanides across multiple ionisation stages. A Portuguese–German collaboration have obtained atomic data for Nd III (Silva et al. 2022) using FAC (The Flexible Atomic Code, (Gu 2008)). They compared these results with those obtained with GRASK2K and investigated the impact of atomic structure choices on opacity estimates. This work again underscored the significant dependencies of models on wavelength-dependent opacity. This diversity of approaches clearly illustrates the importance of theoretical atomic data for astrophysical modelling, as well as the intrinsic difficulty of modelling heavy elements with open f-shells and extremely complex atomic structures.

From a laboratory spectroscopy perspective, these theoretical datasets are crucial for guiding experimental strategies and prioritising spectral regions and transitions of interest. However, neodymium’s high level density leads to extremely dense spectra, particularly for the lower ionisation stages. Consequently, the uncertainties in theoretical wavelengths are usually far greater than the separation between neighbouring spectral lines. This makes it impossible to use theoretical wavelengths alone to identify lines in laboratory emission spectra.

The situation differs significantly when theoretical transition probabilities are calculated using semi-empirical approaches based on the Cowan code, which is parameterised using known experimental energy levels. This method has been employed in recent high-resolution spectroscopic studies, such as those conducted by (Ding et al. 2024b). Preliminary comparisons between these theoretical transition probabilities and new experimental measurements (currently in preparation) reveal reasonable overall agreement for many strong lines. This is probably due to the experimental wavelengths of (Ding et al. 2024b) accurate to parts in  $10^8$ .

In this context, theoretical transition probabilities are a valuable laboratory tool, providing guidance on expected relative line strengths and helping to separate blended features in crowded spectra, even when theoretical wavelengths are not accurate enough for direct identification.

### **Synergy Between Theory and Experiment**

It is important to emphasise that theoretical atomic data are not only complementary, but also often essential for a complete understanding of atomic spectra. Many spectral lines cannot be measured in the laboratory, including forbidden transitions, very weak lines and lines that fall outside the range of accessible light sources. Experimental methods for determining transition probabilities often require either the lifetime of the upper energy level or previously measured transition probabilities for a set of reference lines. In many cases, lifetimes are simply unavailable, and they may be impossible to measure for high-lying energy levels with current laboratory setups. The closure of specialised laboratories that historically provided lifetime measurements, such as the one at the University of Lund (Sweden), has exacerbated this limitation in recent years. In such circumstances, theoretical calculations become indispensable, offering the only practical source of atomic data and informing both experimental design and astrophysical modelling.

The most robust atomic datasets therefore arise from iterative refinement between theory and experiment. Laboratory wavelengths and energy levels constrain theoretical models, reducing uncertainties in predicted transition probabilities. Conversely, theoretical calculations extend experimental results by filling gaps in line lists and providing estimates for unobserved transitions. This interplay is critical for HRMOS, where the complexity of stellar spectra demands comprehensive, high-accuracy atomic data. Coordinated efforts between atomic theory groups and laboratory

teams will ensure that HRMOS line lists combine the best available measurements with validated theoretical predictions.

### 8.3 State of the field and data needs for HRMOS

To achieve the main scientific goals of HRMOS, more accurate atomic data than what currently available are required for both the iron-group elements, which define the overall metallicity scale, and the neutron-capture elements, which trace the nucleosynthetic pathways responsible for the production of heavy elements.

#### Iron group elements

Iron-group species (Sc to Zn) dominate the optical spectra of late-type stars and are used to determine stellar parameters and reference abundances. Improved experimental and theoretical data for neutral and singly ionised states, particularly Fe, Ni, Cr, Ti, and Co, have already directly enhanced the precision and reliability of stellar abundance analyses. Our laboratories, working together with theoretical groups, can provide accurate measurements of wavelengths, oscillator strengths, and hyperfine/isotopic structures for these elements, ensuring that HRMOS spectra can be analysed with unprecedented fidelity.

Over the last 25 years, different laboratories have carried out extensive work to measure high-quality atomic data of iron group elements within the FERRUM project (Johansson et al. 2002). Focusing on the last 10 years, the *Atomic and Molecular Spectroscopy Group at Imperial College London* (United Kingdom) (Concepcion et al. 2023) has conducted extensive work on wavelengths and energy levels of species of the iron-group, including Co II (Ding & Pickering 2020), Mn II (Liggins et al. 2021b,a), Ni II (Clear et al. 2022, 2023b,a) and Fe II (Ding et al. 2025), as well as oscillator strengths such as V I (Holmes et al. 2016) and Fe I (Belmonte et al. 2017). A lot of this work has been performed in collaboration with the *Atomic Spectroscopy Group at the National Institute of Standards and Technology* (NIST), which in the last 10 years has also worked on hyperfine structure constants, e.g. Mn II (Townley-Smith et al. 2016), reference wavelengths, e.g. Fe I and Ni II (Nave & Clear 2021) and transition probabilities, e.g. Cr II (Ward et al. 2023). The *spectroscopy group at Lund University (Sweden)* (now based in Malmö), has also been very active in measuring the lifetimes and oscillator strengths of iron peak elements for example Sc I (Pehlivan et al. 2015) and Sc II (Rhodin et al. 2017), Fe II (Hartman et al. 2015), Ti II (Lundberg et al. 2016), Co II (Quinet et al. 2016), Ni II (Hartman et al. 2017) and V II (Nilsson et al. 2019).

Despite the work carried out by laboratories to improve atomic data for iron group elements, there are still many spectral lines and ionisation states (e.g. doubly ionised) for which no data exist or for which the existing data are of low accuracy and completeness, stemming from measurements made in the 1960s and 1970s with instruments and detectors whose capabilities were more limited than those of today's high-resolution instruments (see Fig. 8.4). The atomic data group will be able to provide the data necessary for the analysis of spectra obtained by HRMOS, ensuring that the potential of HRMOS due to its high resolution is fully exploited.

#### Neutron-capture elements

HRMOS offers a unique opportunity to observe the weak and frequently blended lines of neutron-capture elements within the 385–675 nm spectral range (see Chapters 5 and 3).

**First peak r-process elements**, such as Sr, Y and Zr lines, constrain multiple enrichment channels in metal-poor stars. However, their analysis is often limited by incomplete oscillator strengths and poorly characterised hyperfine structures. For singly ionised strontium (Sr II), the

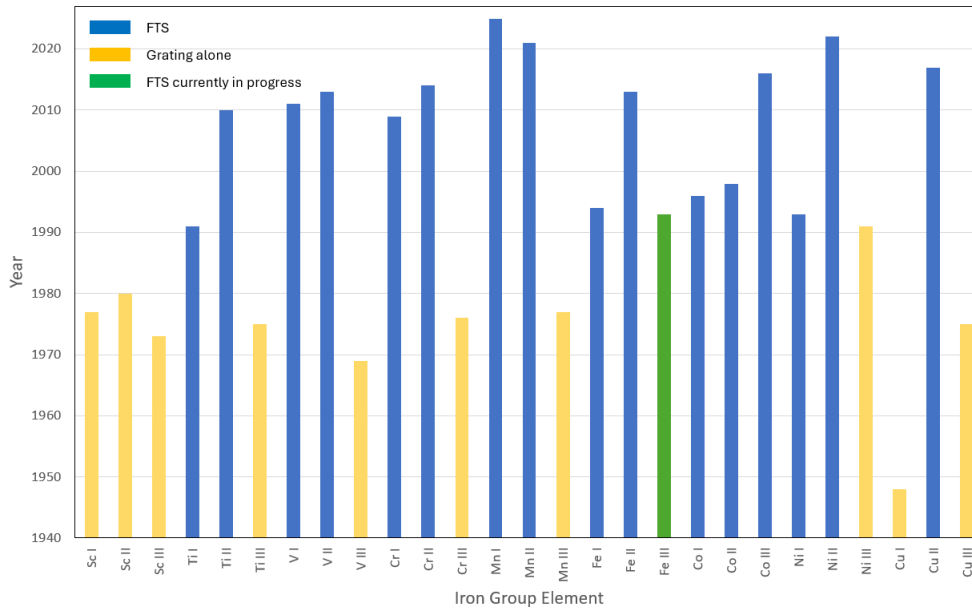


**Figure 8.4.** Year of last large-scale energy level analysis of low-ionisation iron group elements.

NIST Atomic Spectral Database (ASD, Kramida et al. (2024)) contains 40 lines in the HRMOS spectral region, only 12 of which include  $\log(gf)$  values. Of these, only the two resonant lines (Sr II 407.77 and 421.55 nm) have accurate  $\log(gf)$  values (0.004 dex). The remaining ten lines, one of which (Sr II 416.18 nm) is of interest to the nucleosynthesis working group in HRMOS, have  $\log(gf)$  values from Wiese & Martin (1980) with uncertainties of 0.2 dex (uncertainty in the transition probability of 50%). The increasing need for non-local-thermodynamic-equilibrium simulations of elements in the first peak of neutron capture for the analysis of kilonovae has led to new theoretical and experimental work on elements such as yttrium (see, for example, Mulholland et al. (2024); Dowd et al. (2025)).

**Elements from the second peak**, such as barium (Ba), lanthanum (La), cerium (Ce), and neodymium (Nd), enable the quantitative determination of r/s-process fractions in Galactic halo and disc populations. Over the past 25 years, the *Atomic Spectroscopy Laboratory at University of Wisconsin-Madison* (USA) has produced a considerable amount of data on transition probabilities for neutral and singly-ionised atoms using the branching fraction method and commercial hollow cathode lamps. Amongst many others, they have produced accurate transition probabilities of La I (Hartog et al. 2015) and Hf II (Hartog et al. 2021), energy levels of Hf I and II (Lawler et al. 2022) and hyperfine structure constants of Lu II (Hartog et al. 2020). More recently, other groups have measured new transition probabilities using laser-induced breakdown spectroscopy (LIBS) combined with the Boltzmann-plot method (Kodangil et al. 2024, 2025). In both cases, the light sources used produce neutral and once-ionised atoms, but not doubly-ionised species, which explains the significant lack of data for doubly ionised species. This lack of data can be remedied by using high-current hollow cathode and Penning discharge lamps, which are capable of producing twice-ionised atoms. Using these versatile lamps, an extended term analysis of doubly ionised neodymium (Nd III) has been recently carried out at Imperial College London, both for the low-lying (Ding et al. 2024a) and the high-lying configurations (Ding et al. 2024b) yielding 788 Nd III spectral lines in the spectral range 185.2 nm to 307.7 nm with uncertainties of a few parts in  $10^8$ . New experimental work on transition probabilities of Nd is also in process at the Atomic Spectroscopy Laboratory at the University of Valladolid, ASTroLab-UVa (Spain) (Sarma et al. 2024,

2025) (article in preparation). New transition probabilities for other second peak elements, such as singly ionised xenon ( $\text{Xe II}$ ) needed for the analysis of chemically peculiar stars (Yuce et al. 2011) have been recently measured using pulsed discharge lamps where the assumption of local thermodynamic equilibrium holds (Belmonte et al. 2025).

As for Barium (Ba), which has seven stable isotopes, the strong Ba II 493.4 nm resonance line, which lies within the HRMOS spectral range, is one of the most widely used diagnostic tools for identifying the chemical signatures of AGB stars and distinguishing between s- and r-process contributions in stellar populations. Another important line is the resonant Ba II line at 455.4 nm, which is used to determine barium abundances due to its lower sensitivity to isotopic ratios. In both cases, accurate laboratory data, including hyperfine and isotopic structure measurements for Ba II, are essential to exploit the full diagnostic potential of these lines and quantify s/r fractions through detailed line profile analysis. The  $\log(g_l f_l)$ s of these two lines included at the Atomic Spectra Database (ASD) from the National Institute of Standards and Technology (NIST) date back to 1992 (Davidson et al. 1992), and the last critical compilation for transition probabilities was performed in 2002 by Klose et al. (2002). These lines are an example of cases in which the high resolving power capabilities of modern atomic spectroscopy laboratories could have a significant impact on the HRMOS project, improving current atomic data and measuring new values for other spectral lines of interest that are currently unavailable due to a lack of data. It is important to note that the three-dimensional (3D) stellar atmosphere models (Lind & Amarsi 2024) required to improve the interpretation of Ba lines necessitate a substantial amount of atomic data, some of which may currently be unavailable.

At the opposite end of the neutron-capture distribution, in the **third peak**, thorium (Th) plays a crucial role. The Th II 401.9 nm line is the main feature that can be observed in the optical range to determine the abundance of actinides. Compared with stable r-process elements such as Europium (Eu), this line makes it possible to derive radioactive decay ages for stars with very low metallicity. This provides direct constraints on the timescales of early nucleosynthetic events. However, the Th II line is intrinsically weak and lies in a complex spectral region where it blends with transitions from Fe-group and rare-earth elements. High spectral resolution and precise laboratory atomic data, such as the measurement of the  $\log(g_l f_l)$  for the Th II 401.9 nm line as measured by Nilsson et al. (2002), are indispensable for reliable analysis and interpretation of high resolving power spectra recorded by HRMOS, capabilities that will be provided by HRMOS and coordinated laboratory efforts.

### 8.3.1 Synergies and products

High-resolution astrophysical spectroscopy provides the most powerful tool for tracing the chemical and dynamical evolution of the Galaxy. Extracting precise elemental abundances from observed spectra, however, critically depends on the availability of accurate and complete atomic data. Without reliable laboratory measurements of wavelengths, transition probabilities, and hyperfine and isotopic structures, spectra cannot be quantitatively interpreted, and the physical information encoded in them remains inaccessible.

Despite this fundamental dependence, the need for new or improved atomic data is often recognised only after astrophysical spectra have been collected, once the instruments are built and the observational campaigns have already consumed significant resources. This reactive approach delays scientific exploitation and limits the return on investment of large-scale spectroscopic projects. The HRMOS initiative offers a unique opportunity to invert this sequence. By engaging laboratory atomic physicists from the earliest stages of the project, HRMOS ensures that, by the time the first spectra are acquired, the necessary atomic data will already be available and validated

for immediate inclusion in the data processing pipelines.

Furthermore, over the past two decades, the field of experimental atomic spectroscopy has suffered from a marked decline in funding and institutional support. Several specialised laboratories have closed, and the continuity of expertise has become fragile as senior researchers retire without replacement. The involvement of active atomic data groups in HRMOS is therefore not only scientifically necessary but also strategically important to sustain this vital capability within Europe. This proactive integration of laboratory spectroscopy and observational astronomy represents a novel and forward-looking model for maximising the scientific impact of major instruments.

## 9 Advanced stellar atmosphere and radiative transfer models for high-precision spectroscopy

HRMOS science cases require very high precision, driving the development of advanced 3D non-LTE and radiative-hydrodynamic modelling. Systematic grids of 3D models and improved model atoms are rapidly expanding, enabling more accurate and reliable stellar parameters and abundances. The consortium is actively preparing for these requirements by fostering coordinated developments in these areas. Together, these efforts ensure that HRMOS can fully exploit its high-resolution capabilities for transformative science.

### 9.1 Scientific context

Many science cases presented here require precisions of 0.05 dex, and in some cases as fine as 0.03 dex (e.g., Eu and Th for nucleocosmochronology; Chapter 5). While HRMOS is expected to provide spectra of sufficient quality to achieve these *precision* levels, the *accuracy* of the results depends critically on modelling assumptions and post-processing methods. Continued development of spectral line formation methods is therefore essential to unlock the full scientific potential of HRMOS.

The majority of stellar spectroscopic analyses today are based on one dimensional (1D), hydrostatic, radiative-equilibrium model atmospheres, that are post-processed under the assumption of local thermodynamic equilibrium (LTE). Even with their array of fudge parameters (in particular mixing length, microturbulence, and macroturbulence), the traditional 1D approach is unable to closely reproduce the line strengths, shifts, and asymmetries that are either a direct or indirect consequence of stellar surface convection (e.g. Allende Prieto et al. 2002); while LTE can over- or underestimate the populations of absorbers and emitters implied by statistical equilibrium (e.g. Takeda 1991). The two assumptions, which may couple together, thereby might give rise to systematic errors in spectroscopic analyses that routinely exceed nominal precision levels (e.g. Nissen & Gustafsson 2018).

Key products in the next eight to ten years to support HRMOS science cases:

- Expanded grids of 3D RHD model atmospheres.
- Reliable model atoms for species of astrophysical interest across the periodic table.
- 1D non-LTE departure coefficients for species of astrophysical interest across the periodic table and full FGK-type parameter space.
- 3D non-LTE synthetic spectra and abundance corrections for select elements across the full FGK-type parameter space.

If not accounted for, 1D LTE errors can distort both the abundance patterns of individual stars and the global trends of chemical enrichment, potentially leading to erroneous conclusions when comparing observations with theoretical stellar evolution and galaxy formation models (e.g. Storm

et al. 2025; Koutsouridou et al. 2025). For example, analyses that attempt to correct for 1D LTE errors have been shown to recover chemically distinct stellar populations that are otherwise blurred by star-to-star scatter (Nissen et al. 2024; Matsuno et al. 2024; Ernandes et al. 2025); these signatures can be linked to past merger events and used to study the hierarchical formation of our Galaxy (Chapter 4).

In particular, an important characteristic of 1D LTE errors is that they usually have a strong dependence on the stellar parameters (effective temperature, surface gravity, metallicity), as well as on the specific spectral line considered. Their magnitude can range from negligible to over an order of magnitude and their sign may change, even within the same atomic, ionic, or molecular species. Consequently, it is ambiguous to talk about the 1D LTE errors on iron, for example, without qualifying the discussion with details about the star and the line in question. Even for a single spectral line, the 1D LTE errors may in extreme cases span from negligible to as much as 0.6 dex across the stellar parameter space and the corrections may vary rapidly enough to even impact differential analyses of similar types of stars (e.g. Gustafsson 2025).

Thus, 1D LTE errors have to be contended with when the science case requires a comparison of different types of stars. A canonical example is the use of abundance ratio trends such as  $[X/Fe]$  versus  $[Fe/H]$ , to study hierarchical galaxy formation in the local Universe or to infer the origin of elements (Chapters 4 and 3). A related application is investigating the relationship between stellar metallicity and planet formation (Chapter 2). These studies inherently involve stars spanning a range of metallicities; yet, 1D LTE errors are often strongly correlated with metallicity (e.g. Amarsi et al. 2019b). The problem is exacerbated by the need to use different spectral lines, having different 1D LTE errors, depending on the stellar parameters of the star. This is especially relevant when comparing stars at different evolutionary stages, for example within stellar clusters, where abundance patterns across the colour-magnitude diagram can be used, for example, to constrain internal stellar processes (Chapters 6). In all these cases, unaccounted for 1D LTE systematics can introduce spurious trends or mask real astrophysical signatures.

The 1D LTE errors may also indirectly affect elemental abundance determinations, via their influence on atmospheric parameter inferences. Excitation and ionisation balance of neutral and singly ionised iron, commonly used to estimate precise effective temperatures, surface gravities, and metallicities from stellar spectra, is well known to be susceptible to biases from 1D LTE errors (e.g. Ruchti et al. 2013).

Thus, it is necessary to develop more advanced stellar atmosphere and radiative transfer models. So-called “3D non-LTE” models (e.g. Lind & Amarsi 2024) are arguably the gold-standard for current spectroscopic analyses of FGK-type dwarfs and K-type giants. This approach typically employs “box-in-a-star” radiation-hydrodynamics (RHD) simulations (Figure 9.1) with a vertical depth of the order ten pressure scale heights and a horizontal area of the order ten granules (e.g. Freytag et al. 2012; Magic et al. 2013). Synthetic spectra and related observables are generated via post-processing radiative transfer in three dimensions, that relaxes the assumption of LTE by iteratively solving for the populations of all interconnected energy levels together with the radiation field (e.g. Rybicki & Hummer 1992). Stellar convection naturally arises in the RHD models, meaning that the mixing length as well as microturbulence and macroturbulence free parameters never enter into the spectroscopic analyses. In all, this approach is expected to give the most accurate results currently attainable (e.g. Nissen & Gustafsson 2018).

## 9.2 Grids of 3D RHD model atmospheres expanded across stellar parameter space

Spectroscopic analyses can take advantage of 3D RHD model atmosphere grids that are fairly extensive in up to three stellar parameters: effective temperature, surface gravity, and metallicity.

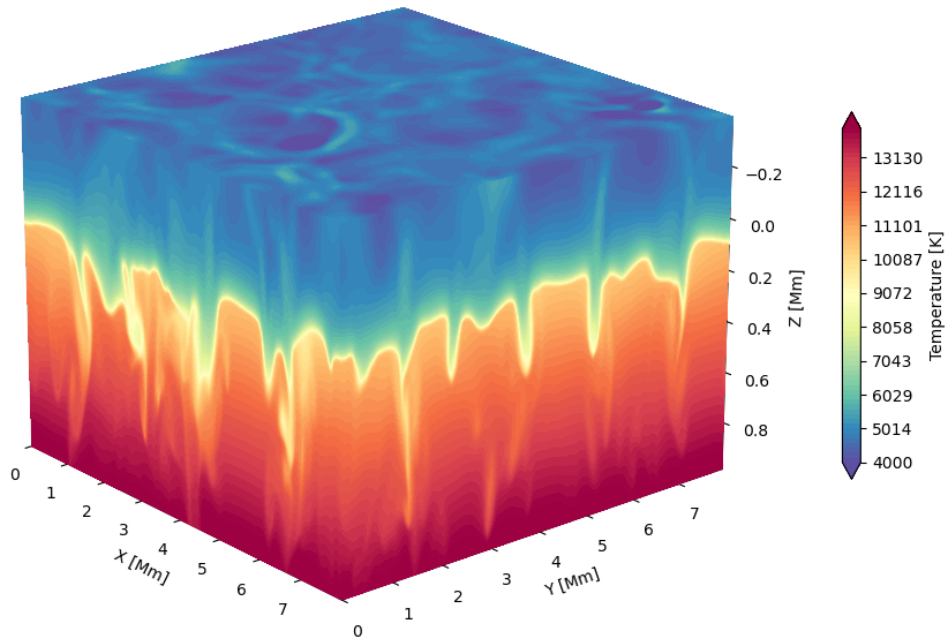


**Figure 9.1.** Example of the temperature structure of a 3D box-in-a-star Stagger-model for the Sun. The colour is capped at 13000 K to improve the visual clarity of the surface inhomogeneities. Based on data presented in Rodríguez Díaz et al. (2024). Full movie available at <https://warwick.ac.uk/fac/sci/physics/research/astro/people/cislagae>.

The most commonly used grids are the Stagger-grid (Magic et al. 2013; Rodríguez Díaz et al. 2024) based on the code Stagger (Stein et al. 2024); and the CIFIST-grid (Ludwig et al. 2009; Bertran de Lis et al. 2022) based on the code C0<sup>5</sup>BOLD (Freytag et al. 2012). More recently, there is development of a new grid, the M3DIS-grid (Eitner et al. 2024, 2025), based on the DISPATCH framework (Nordlund et al. 2018).

However, the aforementioned grids of 3D model atmospheres do not have the same coverage as their 1D counterparts. This leads to complications with interpolation for stars near the peripheries of these grids (Wang et al. 2021). This is particularly the case for metal-poor stars, which are bluer than their metal-rich counterparts. There is a particular need for additional models at the warm edge of the giant branch, to increase the accuracy of spectrum interpolation (Figure 9.2). This is especially problematic since the majority of known metal-poor stars in globular clusters occupy these regions in the HR-diagram (e.g. Usman et al. 2025). The CIFIST-grid does extend slightly further to the blue and up to  $\log g \leq 1$ , but is still not sufficiently dense to allow for accurate interpolation near the grid edge.

In addition, the effect of chemical composition on the structure of 3D model atmospheres is relatively unexplored. Introducing a fourth dimension  $[\alpha/\text{Fe}]$  to capture the alpha enhancement may, for example, impact studies of different stellar populations (Chapter 4). We highlight that Stagger-grid has expanded significantly over the past five years, with 116 existing models updated and 14 new models computed (Rodríguez Díaz et al. 2022, 2024), demonstrating that further targeted extensions are realistic, in particular considering the timeline for HRMOS.

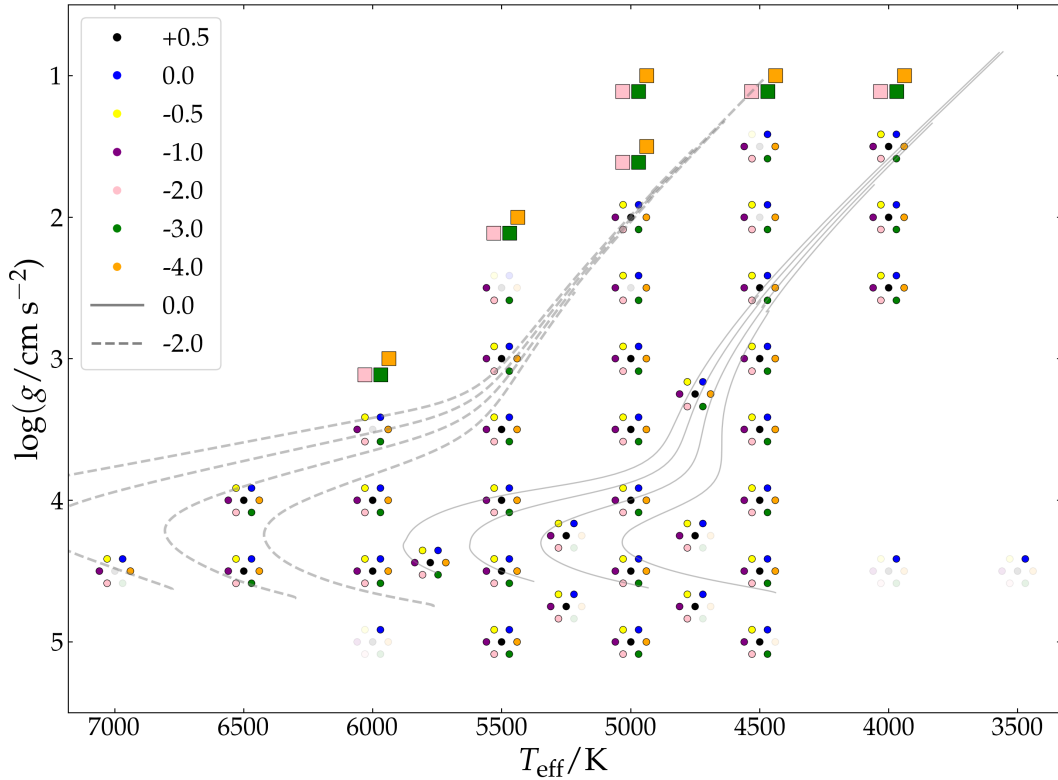


**Figure 9.2.** The Stagger-grid of 3D model atmospheres. Existing models are circles colour-coded by metallicity, missing models are made transparent. Overplotted are MIST stellar evolutionary tracks (Dotter 2016; Choi et al. 2016; Paxton et al. 2011, 2013, 2015) for two metallicities,  $[\text{Fe}/\text{H}] = 0, -2$ , and four stellar masses:  $0.7 - 1.0 M_{\odot}$  in steps of  $0.1 M_{\odot}$ . Priority models for an expanded grid are solid squares. Adapted from Lagae et al. (2025).

### 9.3 Model atoms with more complete and more accurate atomic data

Generating 1D non-LTE or 3D non-LTE spectra requires an assortment of critically compiled and linked atomic data, commonly referred to as the model atom (e.g. Lind & Amarsi 2024). The reliability of non-LTE analyses are often limited by the reliability of the model atom (e.g. Dixon et al. 2025). The treatment of inelastic collisions with neutral hydrogen remains a major uncertainty in non-LTE modelling (e.g. Barklem et al. 2011), as different prescriptions can lead to significantly different synthetic spectra and, consequently, different astrophysical interpretations (Figure 9.3). Modern asymptotic models for low-lying levels (e.g. Barklem 2016) are supported by recent experiments (e.g. Schmidt-May et al. 2024). In parallel, astrophysical evidence motivates the inclusion of an additional free-electron momentum-transfer channel for high-lying levels (e.g. Amarsi et al. 2018a, 2019a). This combined “asymptotic+free” approach is now widely adopted (e.g. Bergemann et al. 2019; Canocchi et al. 2024; Caliskan et al. 2025).

Inelastic collisions with free electrons also play an important role, particularly in warmer and more metal-rich stars where their relative contribution increases compared to hydrogen collisions. Calculations based on the B-spline R-matrix and convergent close-coupling methods are generally in good agreement, indicating a high level of reliability (e.g. Reggiani et al. 2019), although the number of available studies remains limited. In this context, recent progress in the kilonova community beyond traditional approximations (e.g. van Regemorter 1962) is providing improved

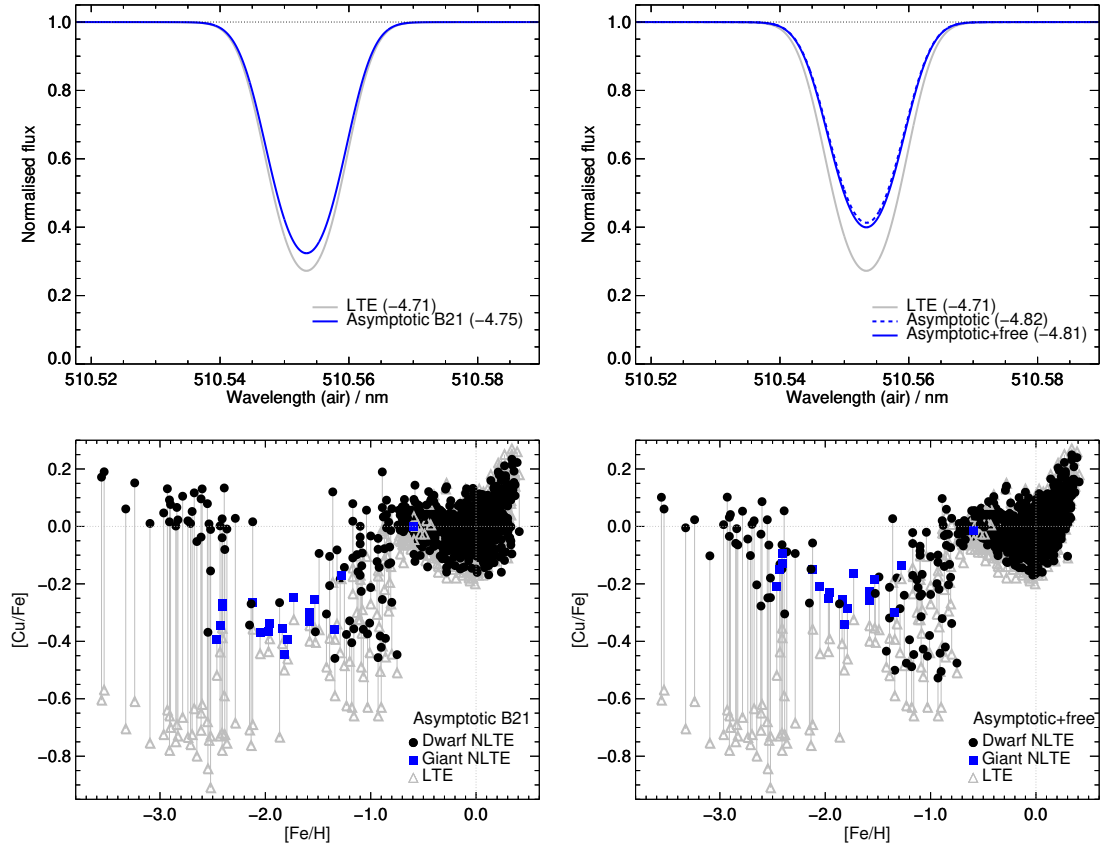


**Figure 9.3.** Impact of the model atom on spectral line strengths and thus on the  $[X/Fe]$  versus  $[Fe/H]$  plane (e.g. Chapters 4 and 3). Top: synthesis of the Cu I 510 nm line for a typical metal-poor red giant branch star in LTE, and in non-LTE with different prescriptions for the inelastic hydrogen collisions (left and right). Logarithmic reduced equivalent widths indicated in parentheses. Gaussian broadening corresponding to  $R = 80\,000$  applied; rotational broadening and macroturbulence have been neglected. Bottom:  $[Cu/Fe]$  versus  $[Fe/H]$  trends in LTE, and in non-LTE with different prescriptions for the inelastic hydrogen collisions (left and right). Based on data presented in Caliskan et al. (2025).

atomic data (e.g. McCann et al. 2025) that are also relevant for stellar atmosphere modelling.

For heavy elements, incomplete atomic models and uncertain transition probabilities remain a significant source of systematic uncertainty (e.g. Velichko et al. 2011). Progress in this area relies strongly on collaborations with atomic physicists, particularly those performing large-scale relativistic calculations (e.g. Li et al. 2021). Similar developments in the kilonova community (e.g. Deprince et al. 2025) are also promising, although stellar applications often require additional Rydberg levels and improved energy-level ordering (e.g. Caliskan et al. 2024). It is also important to move beyond hydrogenic approximations for bound-free photoionisation rates, for instance using B-spline R-matrix methods (e.g. Zatsariny et al. 2019), since inaccurate overionisation can significantly bias inferred abundances (e.g. Mashonkina et al. 2022).

From a broader perspective, Asplund et al. (2021) identified Li, C, N, O, Na, Mg, Al, Si, K, Ca, Fe, and Ba as elements with “full 3D non-LTE” analyses based on relatively complete model atoms and realistic treatments of hydrogen collisions. Consistent model atoms are now also available for Be and S (Korotin & Kučinskas 2022; Korotin & Kiselev 2024; cf. Amarsi et al. 2024, 2025). In addition, similar approaches have been extended to a growing number of heavier species, including Ti (Mallinson et al. 2022), Mn (Bergemann et al. 2019), Co (Yakovleva et al. 2020), Ni (Eitner et al.

2023), Cu (Caliskan et al. 2025), Zn (Sitnova et al. 2022), Rb (Korotin 2020), Sr (Yakovleva et al. 2022), Y (Alexeeva et al. 2023), Ag (Caliskan et al. 2026), and Eu (Storm et al. 2024).

However, several elements relevant for HRMOS science cases still lack complete model atoms with realistic hydrogen-collision data, including Zr, La, Nd, Pb, Th, and U. Reinvestigating existing model atoms is also important, since different assumptions can lead to qualitatively different astrophysical interpretations (Figure 9.3), particularly for Fe (Amarsi et al. 2022; Mashonkina et al. 2023). While the theoretical framework and computational methods are already well established, further effort is needed to critically assess available data and build internally consistent model atoms for non-LTE calculations. Given the rapid progress of the past decade, it is realistic to expect robust atomic data and model atoms for at least six key elements to be available in time to fully exploit HRMOS observations.

#### 9.4 1D non-LTE and 3D LTE grids expanded across the periodic table

The large computational costs, combined with the absence of reliable atomic data or compiled model atoms, generally explain the sparsity of existing 3D non-LTE results. In their absence, the much cheaper theoretical 1D non-LTE approach is often to be preferred; results from averaged-3D models (that are also of 1D geometry) may be less reliable (Lind & Amarsi 2024). Nevertheless, it should be stressed that 1D non-LTE may still not be sufficient for achieving the precise and accurate abundances at the expected level, especially when 3D effects dominate (e.g. Matsuno et al. 2024), and so 3D non-LTE should remain the ultimate goal.

Grids of 1D non-LTE departure coefficients may be calculated for the whole set of elements with reliable model atoms. Indeed, pre-computed grids of 1D non-LTE departure coefficients now exist for around fifteen (mainly light) elements (e.g. Amarsi et al. 2020; Gerber et al. 2023). These can be used with 1D LTE codes such as SME (Piskunov & Valenti 2017; Wehrhahn et al. 2023) and Turbospectrum (Plez 2012; Gerber et al. 2023) for on-the-fly 1D non-LTE analyses, with the caveat that these grids are coupled to a particular family of 1D model atmospheres and that the results are only as reliable as the atomic data and model atoms that they are based upon. With modern computers and parallelised codes such calculations are feasible across extended 1D model atmosphere grids such as MARCS (Gustafsson et al. 2008). This approach is well-suited to studies of large numbers of elements in large samples of stars (e.g. Bijavara Seshashayana et al. 2025; Nunnari et al. 2025). Abundance corrections can be calculated from such grids (e.g. Lind et al. 2022; Mohorian et al. 2025), and abundance corrections may also be used to correct large data sets (e.g. Koutsouridou et al. 2025). It should also be kept in mind that 3D LTE may be more realistic than 1D non-LTE in some cases. This is often the case for certain key species such as Fe II (e.g. Amarsi et al. 2022) and CH (e.g. Hoppe et al. 2026).

Extended 1D non-LTE departure coefficient grids are now routinely computed even for complex species (e.g., Mallinson et al. 2024; Caliskan et al. 2025), and so the main limitation is the availability of high-quality model atoms. In contrast, 3D LTE grids are  $\sim 10^4$ – $10^5$  times more computationally expensive (e.g., Lind & Amarsi 2024). Nevertheless, 3D snapshots and analysis tools are publicly available. A focused effort on the most critical species, such as CH and MgH isotopologues (Chapter 3), is feasible in time for HRMOS, enabling high-fidelity modelling of key molecular and atomic features.

#### 9.5 Full 3D non-LTE calculations

Given the model atmosphere and model atom, 3D non-LTE radiative transfer codes such as Multi3D (Leenaarts & Carlsson 2009) and its offshoot Balder (Amarsi et al. 2018b) can be used to generate

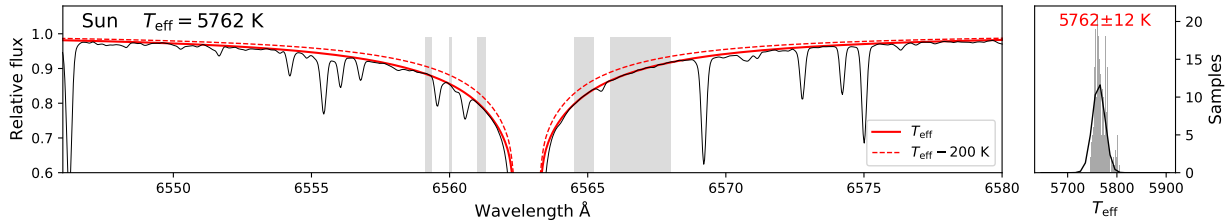


**Figure 9.4.** Solar  $H\alpha$  line profile fit. The observational spectrum (black line) has a resolving power  $R = 86\,000$ , taken from the MELCHORS public database (Royer et al. 2024) normalised as in Giribaldi et al. (2019). Vertical shaded regions indicate the portions of the spectrum used for fitting. The best-fit 3D non-LTE synthetic profile is shown as a solid red line, with the corresponding temperature labelled in the plot. A dashed red line represents a synthetic profile for an effective temperature that is 200 K cooler. The right-hand panel displays a histogram of the temperatures associated with each pixel within the fitting regions. A Gaussian fit to the histogram is over-plotted in black, with its median and  $1\sigma$  dispersion indicated, representing the derived effective temperature and its associated uncertainty.

3D non-LTE stellar spectra, typically for one species or element at a time. Grids of 3D non-LTE spectra, equivalent widths, or abundance corrections now exist for a handful of elements and spanning FG-dwarfs, and sometimes also K-dwarfs and K-giants, of a range of metallicities.

Stellar parameter determinations may benefit from the grid of 3D non-LTE Balmer line profiles across the FGK-type parameter space (Amarsi et al. 2018b), and from 3D non-LTE abundance corrections for Fe I lines across a more limited parameter space (Amarsi et al. 2022). The former have been systematically tested using the Sun (Figure 9.4) and other benchmark stars having non-spectroscopic stellar parameter estimates (Giribaldi et al. 2021, 2023).

Given an extended grid of 3D RHD model atmospheres and reliable model atoms, it would be worthwhile to compute homogeneous 3D non-LTE synthetic spectra and/or abundance corrections for key elements of interest to HRMOS science cases. A pertinent strategy would be to first focus on extending the existing grids listed above of 3D non-LTE stellar spectra and abundance corrections, to encompass the full FGK parameter space.

For stellar parameters, elements of high priority include H and Fe. For stellar abundances, elements of importance crucially include, among others, neutron-capture ones such as Zr, Ba, Eu, Pb (e.g. origins of heavy elements, Chapter 3), and Th (e.g. nucleocosmochronology, Chapter 5). Since 2019, significant progress has been made in the production of grids of 3D non-LTE spectra and abundance corrections. Currently, eleven such grids exist for mainly light elements as described above. By extrapolating forward, it is not unreasonable to expect this number to double by the time HRMOS observes first light.

## 10 Synergies and complementarities with present and forthcoming instrumentation

HRMOS will work in synergy with major spectroscopic surveys (4MOST, WEAVE, MOONS), space missions (*Gaia*, TESS, PLATO), and future or proposed ground-based and space facilities (WST, ELT instruments such as ANDES and MOSAIC, MICADO, HAYDN). It will provide very high-resolution follow-up, benchmark spectra, precise abundances, and radial velocities, enabling full exploitation of their data and science potential.

Over the next decade, stellar and exoplanet astronomy will be transformed by the combination of large spectroscopic surveys and space missions delivering high-precision astrometry, photometry, time-domain observations, along with spectroscopy for millions of targets.

HRMOS is uniquely positioned to complement these efforts. Thanks to its combination of high-resolution and multi-object capabilities, it will serve as a key high-fidelity spectroscopic facility, providing the precision data required to fully exploit discoveries from the next generation of surveys and missions. The following sections highlight several major areas in which these synergies will be particularly powerful.

### 10.1 Large spectroscopic surveys follow-up

Several major wide-field spectroscopic facilities—including 4MOST@VISTA, WEAVE@WHT, and MOONS@VLT— have just started or will very soon begin operations. These surveys will obtain millions of stellar spectra across large areas of the sky, delivering homogeneous measurements of radial velocities, stellar parameters, metallicities, and elemental abundances. Their primary strengths are survey efficiency, large multiplexing capability, and systematic coverage of stellar populations spanning a wide range of ages and environments.

HRMOS will operate in a complementary observational regime, providing much higher spectral resolution, excellent stability, and superior measurement precision, albeit with a smaller multiplex. This naturally creates a strong synergy between the large surveys and HRMOS: surveys efficiently identify and classify targets and place them in their broader astrophysical context, while HRMOS delivers the detailed spectroscopic characterisation required for the precision studies on selected sub-samples. To mention a concrete example, the science case for detailed chemical abundances in Milky Way satellites depends strongly on forthcoming releases from *Gaia* and the large spectroscopic surveys that will precede HRMOS. Future *Gaia* releases will improve astrometry and spectrophotometry, providing strong priors on stellar atmospheric parameters and metallicities. In parallel, 4MOST (Bensby et al. 2019; Skúladóttir et al. 2023) and MOONS (Cirasuolo et al. 2020) will deliver metallicities and abundance measurements that enable efficient selection of candidate accreted stars, that will be the targets for HRMOS.

Together, *Gaia*, 4MOST, and MOONS will make target selection for HRMOS highly efficient and reliable, enabling science cases that are currently inaccessible and that critically depend on the combination of precise astrometry, large-scale survey spectroscopy, and much higher-resolution multi-object observations.

Beyond the specific science cases, HRMOS will play an important role in calibrating the data-driven methodologies that underpin modern spectroscopic surveys. Techniques such as *The*

*Cannon, The Payne*, and neural-network approaches rely on high-quality reference spectra to infer stellar parameters and abundances for vast datasets. HRMOS observations will provide these benchmark spectra with unprecedented precision, increasing the number of measurable elements and isotopic species while improving the validation of data-driven methods.

In the 2030s, HRMOS will therefore provide a high-resolution calibration framework for surveys such as 4MOST and MOONS, enabling applications including chemical tagging, isotopic abundance studies, and the identification of Galactic substructures.

Strong synergies are also expected between HRMOS and facilities such as the proposed Wide-field Spectroscopic Telescope (WST; Bacon et al. 2024). While WST will survey vastly larger stellar samples over a wider field of view at lower spectral resolution ( $R \sim 40,000$ ), HRMOS will provide the higher-resolution benchmark spectra required for precision calibration. Machine-learning approaches trained on HRMOS observations will enable the extraction of precise chemical abundances and isotopic ratios across the much larger WST datasets. In this context, HRMOS will act as a critical pathfinder for the scientific exploitation of WST in studies of the Milky Way and the Local Group.

## 10.2 Present and future space missions

### 10.2.1 TESS

The Transiting Exoplanet Survey Satellite (TESS; Ricker et al. 2015) is a NASA all-sky mission dedicated to discovering transiting exoplanets around bright stars ( $G \lesssim 13\text{--}14$ ). Since 2018, TESS has observed the sky in a sequence of sectors lasting approximately 27 days, covering a field of view of  $24^\circ \times 96^\circ$ . Regions near the ecliptic poles, known as the Continuous Viewing Zones (CVZs), benefit from more than 300 days of cumulative coverage.

TESS observes a selected set of high-priority targets at short cadence, while simultaneously acquiring Full Frame Images (FFIs) of the entire field. Over the course of the mission, the FFI cadence has improved from 30 minutes during the primary mission to 200 seconds in the current extended mission.

As an all-sky survey covering more than 95% of the sky, TESS has observed most known star clusters and associations for at least one 27-day sector, and often multiple times over several years. This has created an unprecedented archive for studies of stellar variability and exoplanets in stellar populations of different ages and environments.

Although the relatively low spatial resolution of the FFIs complicates observations in crowded fields, specialised approaches such as PSF-based photometry and difference imaging analysis (Nardiello et al. 2019, 2020; Bouma et al. 2019, 2020) have enabled the discovery of numerous exoplanet candidates and variable stars in clusters, associations, and moving groups. Many of these systems are now included among the TESS Objects of Interest (TOIs) and Community TOIs (CTOIs).

Cross-matching these detections with the open-cluster catalogue of Cantat-Gaudin et al. (2020) reveals 29 TOIs and 85 CTOIs orbiting main-sequence stars in open clusters. Most of these systems ( $\sim 95\%$ ) have orbital periods shorter than 30 days, while approximately 45% have radii below  $\sim 2.5 R_J$ . These properties make them excellent targets for HRMOS follow-up.

By the time HRMOS becomes operational, TESS is expected to have discovered many additional planets in clusters and associations through the increased sensitivity provided by multi-sector observations. HRMOS will be ideally suited for efficient spectroscopic follow-up of these systems. Its multiplexing capability will enable simultaneous observations of many cluster members, dramatically reducing the telescope time required for stellar and planetary characterisation.

Clusters such as NGC 2516 (Nardiello et al. 2020) already contain multiple stars hosting candidate or confirmed exoplanets and represent prime HRMOS targets. High-resolution follow-up will refine stellar parameters, measure chemical abundances, and characterise planetary systems through radial velocities. In systems hosting hot or warm Jupiters identified by TESS, HRMOS will also enable searches for additional outer giant planets through long-term radial-velocity monitoring, thereby providing a more complete view of planetary system architectures.

### 10.2.2 PLATO

PLAnetary Transits and Oscillations of stars (PLATO; Rauer et al. 2014) is an ESA mission scheduled for launch in January 2027. Its primary objective is to discover habitable Earth-like planets around nearby bright solar-type stars using the transit technique. Equipped with 26 wide-field telescopes, PLATO will monitor its first southern long-duration field (LOPS2; Nascimbeni et al. 2025) for at least two years almost continuously, delivering ultra-high precision light curves for more than 200,000 FGK dwarfs and subgiants across 2150 deg<sup>2</sup>.

PLATO is optimised for bright nearby stars and asteroseismology, but it is less well suited for observing the Galactic bulge and dense stellar systems. Nevertheless, the LOPS2 field contains approximately 400 open clusters, including benchmark systems such as NGC 2516 and IC 2391 (Nascimbeni et al. 2025, see Sect. 3.5). PLATO will therefore enable extensive searches for transiting planets in cluster environments while simultaneously providing detailed characterisation of stellar variability and activity.

For the brightest stars, PLATO will also deliver highly precise stellar parameters and ages through asteroseismology (Goupil et al. 2024). In addition, thousands of giant stars observed for Science Calibration and Validation purposes will have their light curves rapidly released to the community.

HRMOS provides the essential spectroscopic complement to these observations, particularly for the fainter members of stellar clusters. In rich clusters, it will enable homogeneous high-resolution spectroscopy of stars hosting transiting planet candidates identified by PLATO. These observations will provide radial-velocity confirmation of giant planets and identify spectroscopic binaries or activity-related signals that could complicate transit and seismic interpretations, especially in young and rapidly rotating stars.

Beyond planet confirmation, HRMOS will deliver homogeneous and extremely precise chemical abundances, placing the detected planetary systems within a robust chemical and evolutionary framework. These measurements are essential for interpreting PLATO's transit and asteroseismic observables and for connecting planetary properties to host-star composition and evolutionary stage.

In particular, together, PLATO and HRMOS will establish nearby young clusters as benchmark laboratories for stellar and planetary astrophysics. PLATO will provide the time-domain photometric foundation, while HRMOS will deliver the high-resolution spectroscopic characterisation required to connect stellar properties, chemical composition, and planet occurrence in young stellar environments.

### 10.2.3 *Gaia*

*Gaia*'s major contribution to exoplanet science will be its unbiased astrometric census of planetary systems around hundreds of thousands of nearby stars spanning a broad range of spectral types and stellar populations. While DR3 contained 214 exoplanet candidates, DR4 will deliver a substantially larger catalogue based on 66 months of observations, and DR5 will exploit the full 10.5-year baseline of the extended mission.

By the end of the decade, *Gaia* is expected to provide an astrometric survey of  $10^6$ – $10^7$  stars. Thousands of planets below  $15 M_{\text{Jup}}$  are anticipated in DR4, with *Gaia* particularly sensitive to long-period Jupiter-mass companions. The longer baseline of DR5 will extend sensitivity to giant planets on Solar-System-like orbits and may increase the total planet yield by a factor of three for stars with  $G \sim 16$  (Brown 2025). Recent predictions suggest approximately  $7500 \pm 2100$  planet candidates in DR4 and up to 120,000 in DR5, dominated by super-Jupiters ( $3$ – $13 M_{\text{Jup}}$ ) orbiting GKM stars at separations of 2–5 au within 500 pc (Lammers & Winn 2026). In open clusters, *Gaia* may detect long-period super-Jupiters around bright stars out to distances of  $\sim 200$  pc (Perryman et al. 2014).

However, astrometric detections alone do not always provide complete orbital solutions. Radial-velocity follow-up is essential to break degeneracies, reduce false positives, and refine orbital parameters. Ground-based spectroscopy will also be required to improve phase coverage, extend the observational time baseline, and identify additional short-period or lower-mass planets below *Gaia*'s detection threshold.

This is where HRMOS offers a transformative capability. Its multiplexed, high-resolution spectroscopy enables efficient large-scale radial-velocity follow-up of the *Gaia* astrometric sample. In addition to confirming planetary systems and excluding false positives, HRMOS will characterise the detailed chemistry of host stars, enabling comprehensive studies of planetary architectures and stellar composition across an unbiased stellar population.

Importantly, HRMOS probes a complementary parameter space to astrometry, with strong sensitivity to closer-in giant planets inaccessible to *Gaia*. Together, the two facilities will provide a far more complete picture of giant planet demographics across the Galaxy.

#### 10.2.4 The ESO Extremely Large Telescope

HRMOS and ANDES (Marconi et al. 2022b) on the Extremely Large Telescope (ELT) are highly complementary facilities for the study of exoplanetary systems. HRMOS, operating at high multiplexing efficiency and high spectral resolution, is particularly well suited for the discovery and characterisation of exoplanet host stars in large stellar samples. Its capability to obtain precise radial velocities and accurate stellar parameters for large numbers of targets enables the identification of planetary candidates across a wide range of Galactic environments. Once suitable systems are identified, ANDES will provide ultra-high-resolution, high signal-to-noise spectroscopy of selected targets, enabling detailed investigations of exoplanet atmospheres through transmission and emission spectroscopy, including measurements of chemical abundances, isotopic ratios, and potential biosignature tracers. In this framework, HRMOS serves as a discovery and target-selection facility, while ANDES delivers the detailed atmospheric follow-up. Together, the two instruments provide a powerful end-to-end approach to exoplanet science on the ELT, linking large-scale population studies with detailed atmospheric characterization. For the brighter targets, follow up with ESPRESSO at the VLT can also be performed.

HRMOS will be also complementary to MOSAIC (Hammer et al. 2014), which will probe much fainter stellar populations throughout the Local Group at lower spectral resolution, extending stellar population studies beyond the reach of current high-resolution spectroscopic surveys. HRMOS, by contrast, will focus on the brightest stars, providing detailed chemical abundances and precise radial velocities. The combination of the two facilities will connect depth and spectral detail, extending investigations from the Milky Way to nearby galaxies.

A further key synergy exists with MICADO (Trippe et al. 2010), which will deliver high-precision astrometry and diffraction-limited imaging in crowded and distant stellar fields. Accurate proper motions, parallaxes, and photometric measurements from MICADO will provide an ideal target

database for HRMOS spectroscopy. Combining MICADO astrometry with HRMOS radial velocities and chemical abundances will enable full six-dimensional phase-space analyses together with chemical tagging, offering a powerful tool to investigate the assembly history and dynamical evolution of stellar populations. For exoplanet studies, MICADO will identify and characterize stellar hosts through its astrometric capabilities, while HRMOS will provide the spectroscopic information required to determine stellar parameters, chemical compositions, and radial-velocity signatures. The combined capabilities of MICADO and HRMOS will create a unique framework linking astrometry, imaging, and spectroscopy, maximising the scientific return of ELT observations across both Galactic and extragalactic science cases.

### 10.2.5 HAYDN

The proposed ESA M8 candidate mission HAYDN (Miglio et al. 2024) is specifically designed to provide key and precise information on stellar interiors. Through high-cadence, high-precision photometry with arcsecond spatial sampling, HAYDN will obtain asteroseismic diagnostics—including  $\nu_{\max}$ ,  $\Delta\nu$ , mixed-mode period spacings, individual mode frequencies, and rotational splittings—for thousands of stars in dense clusters spanning a wide range of ages and metallicities. These measurements probe core masses, mean stellar densities, buoyancy-frequency profiles, and internal differential rotation, directly constraining processes such as convective-boundary mixing, angular-momentum transport, rotational mixing, and RGB mass loss. HAYDN will also deliver precise stellar ages and search for exoplanets through transits in a number of selected star clusters and crowded stellar environments, enabling studies of how environment influences planet formation and evolution.

HRMOS provides the complementary and fundamental surface perspective, linking internal stellar physics to observable photospheric signatures. Abundances and isotopic ratios of C, N, and Li trace mixing and diffusion processes, while precise radial velocities reveal binaries, mass-transfer systems, and dynamical interactions that may also produce anomalous seismic signatures. Incorporating seismic  $\log g$  measurements, accurate to  $\lesssim 0.03$  dex (Morel & Miglio 2012; Morel et al. 2014), will significantly reduce degeneracies in spectroscopic analyses and improve abundance determinations across entire cluster sequences.

Together, HAYDN and HRMOS will enable a complete and transformative core-to-photosphere characterisation of stars: asteroseismology will probe internal structure and dynamics, while spectroscopy will trace chemical and kinematic signatures at the stellar surface. This combination will provide stringent and self-consistent tests of stellar evolution models in benchmark stellar populations, with direct implications for Galactic archaeology, chemical evolution, and exoplanet science.

Several clusters targeted by HAYDN—including M67, NGC 6121, NGC 6656, NGC 2243, NGC 2506, NGC 6397, NGC 6705, and NGC 2818 can be efficiently targeted with HRMOS targets. High-resolution spectroscopy of the same stars will provide detailed and precise abundances and radial velocities. The multiplexing capability of HRMOS also enables efficient Doppler surveys for giant planets in clusters, while activity diagnostics and chemical tagging help disentangle stellar jitter, particularly in young and rapidly rotating systems.

Combined with HAYDN's seismic and transit measurements, HRMOS will enable robust planet detection and characterisation in dense stellar environments, providing statistically significant samples of exoplanets orbiting stars with well-constrained ages, masses, and chemical compositions.

Although HRMOS is expected to achieve first light several years before HAYDN, this timing is advantageous. HRMOS can establish a rich spectroscopic legacy database for future HAYDN targets, enabling immediate cross-matching and combined analyses once seismic and transit

measurements become available. The synergy between HAYDN and HRMOS will therefore provide a uniquely multidimensional view of stellar evolution, cluster dynamics, and exoplanet demographics across diverse Galactic environments.

## 11 Target selection: Crowded stellar fields in the Milky Way and nearby dwarf galaxies

HRMOS will be best positioned to target crowded stellar fields in the Milky Way and nearby satellites, including open and globular clusters, the Galactic bulge, the Sagittarius dwarf galaxy, and the Magellanic Clouds, and will also open new opportunities for observations of Galactic nebulae and extragalactic targets.

The primary targets for HRMOS are crowded stellar fields in the Milky Way and its nearby dwarf satellites. As discussed in detail in the Chapters of this paper, open and globular clusters, the Galactic bulge, the Sagittarius dwarf galaxy, and the Magellanic clouds contain complex stellar populations that are key to understanding stellar evolution, chemical enrichment, and the formation history of the Milky Way and its satellites. They also enable the detection and study of exoplanets across a wide range of stellar densities, ages, and chemical compositions, offering new insights into how planets form and survive in different galactic environments.

HRMOS is exceptionally well suited to such dense fields, as its ability to simultaneously observe many stars at high spectral resolution enables the precise and detailed chemical and kinematic analyses needed to disentangle their diverse populations.

### 11.1 Open clusters

Focusing on hot Jupiters (Chapter 2), HRMOS will enable a comprehensive assessment of planet occurrence rates around stars formed in diverse environments. The selection of open cluster targets and of members within each cluster is beyond the scopes of this paper. We just recall that a general discussion was provided in Magrini et al. (2023) (Chapter 4.5), which highlighted that a very large number of clusters, covering the age range between 0.1 and 6.5 Gyr, exist where efficient exoplanet searches among FGK-type main sequence and giant stars could efficiently be performed. We add here that the sample can be extended to younger clusters; also, the number of suitable clusters has increased after *Gaia* DR3 (Hunt & Reffert 2023, e.g.) and it may be further refined with future *Gaia* releases, allowing a more solid selection function, well covering the parameter space. Very well studied clusters from the *Gaia*-ESO Survey (Gilmore et al. 2022; Randich et al. 2022) may also represent primary targets, also to enable calibration synergies. Finally, as already mentioned, clusters observed by the HAYDN mission will also be targeted with HRMOS

#### 11.1.1 Observational strategy in a Benchmark open cluster

To illustrate a possible observational strategy, we selected the benchmark open cluster M67 as a case study for assessing the feasibility of exoplanet detection and detailed stellar characterisation. M67 is also a primary target of the HAYDN mission.

The minimum SNR required for giant-planet detection is  $\sim 25$  (Green band, Table 2.1) and Brucalassi et al. (see, e.g., 2014, 2016), which can be achieved for stars with  $G \approx 16$  in both the blue and red spectral ranges. A robust detection typically requires between 20 and 30 exposures of 1 hr each (Brucalassi et al. 2017, and Chapter 2 of the White Paper). To avoid fibre cross-talk, we adopted two magnitude bins— $13.5 < G < 16.5$  (faint) and  $G < 13.5$  (bright)—following the

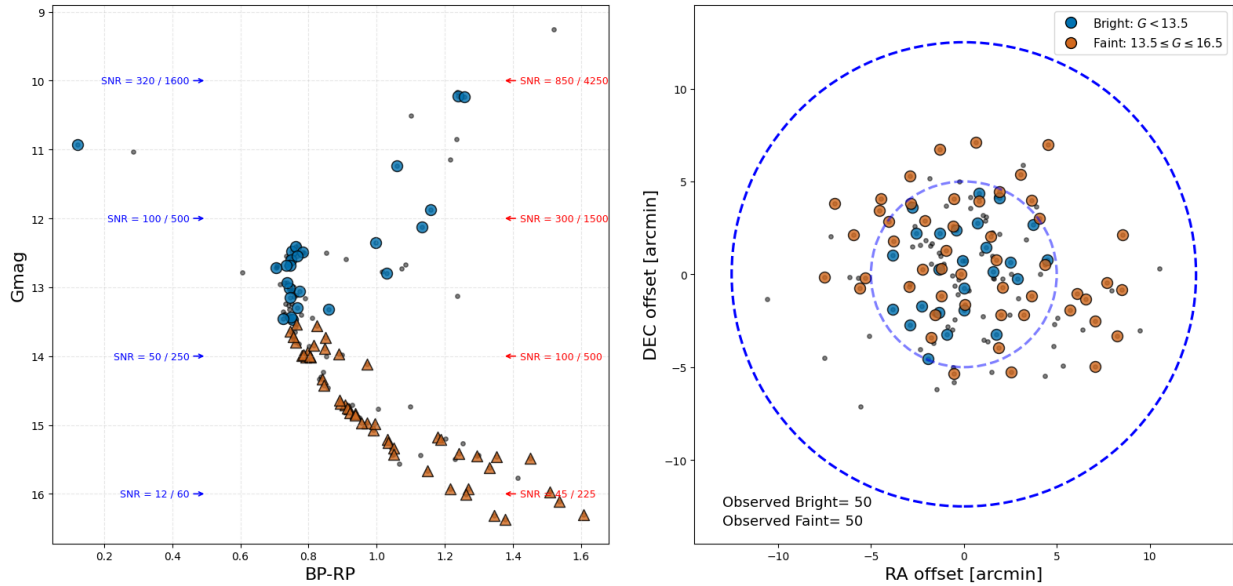


**Figure 11.1.** Two possible telescope pointings of member stars in M67, divided into two  $G$  magnitude bins (in orange the faint sample, with  $16.5 < G < 13.5$ , in blue the bright sample, with  $G < 13.5$ ). The minimum distance between stars within the inner and external regions are 15 arcsec and 30 arcsec, respectively, and the number of allocated fibres is 50 per magnitude bin. In the left panel, the CMD of M67 (stars with membership probability  $>0.9$ ) is shown. The blue and red arrows indicate the SNR achievable in 1 hr and 25 hr of observing time in the blue and red spectral ranges, respectively. In the right panel, the spatial distribution of the selected stars is presented. The dark and light blue dashed circles represent the FoV of VLT and the inner FoV where the instrument fibres can be closer.

approach used in the *Gaia*-ESO Survey (Randich et al. 2022; Gilmore et al. 2022). Assuming a minimum fibre separation of 30 arcsec (which can be reduced to 15 arcsec in the central regions; see Section 1.3), we allocate 50 fibres to each bin, targeting main-sequence stars in the faint sample and turn-off/giant stars in the bright sample. Figure 11.1 illustrates the selected targets on both the colour–magnitude diagram and the sky. The SNRs achievable in 1 hr (first number) and 25 hr (second number) for four different  $G$  magnitudes, in both the blue and red ranges, are shown in Fig. 11.1. Using 20–30 exposures with appropriate cadence, the combined spectra reach SNRs of  $\sim 1600$  (blue) and  $\sim 4250$  (red) for the brightest stars, and  $\sim 60$  and  $\sim 225$  for the faintest ones.

Thus, an observational campaign targeting hot Jupiters in one cluster (two pointings, each totalling 25 hr, which is about six nights) yields time-series spectra for  $\sim 100$  stars and cumulative high-SNR spectra. These enable chemical abundance analyses, including differential abundances, with precisions of  $0.01 \sim 0.02$  dex, allowing studies of atomic diffusion, stellar mixing, abundance inhomogeneities, and isotopic ratios such as Ba (see Chapters 6 and 3). The individual spectra also enable Doppler Tomography to trace magnetic-activity variations and distinguish them from planetary signals (see Chapter 6).

## 11.2 Globular clusters

In the previous chapters it has been shown that globular clusters will serve as key laboratories for studying multiple stellar populations, planet formation in crowded regions, and the precise dating of the Galaxy’s early assembly (see Chapters 5, 2, and 6). To achieve these goals, we investigated which are the possible targets, which span a wide range of metallicities, masses, spatial locations, origins, and degrees of multiple-population complexity.

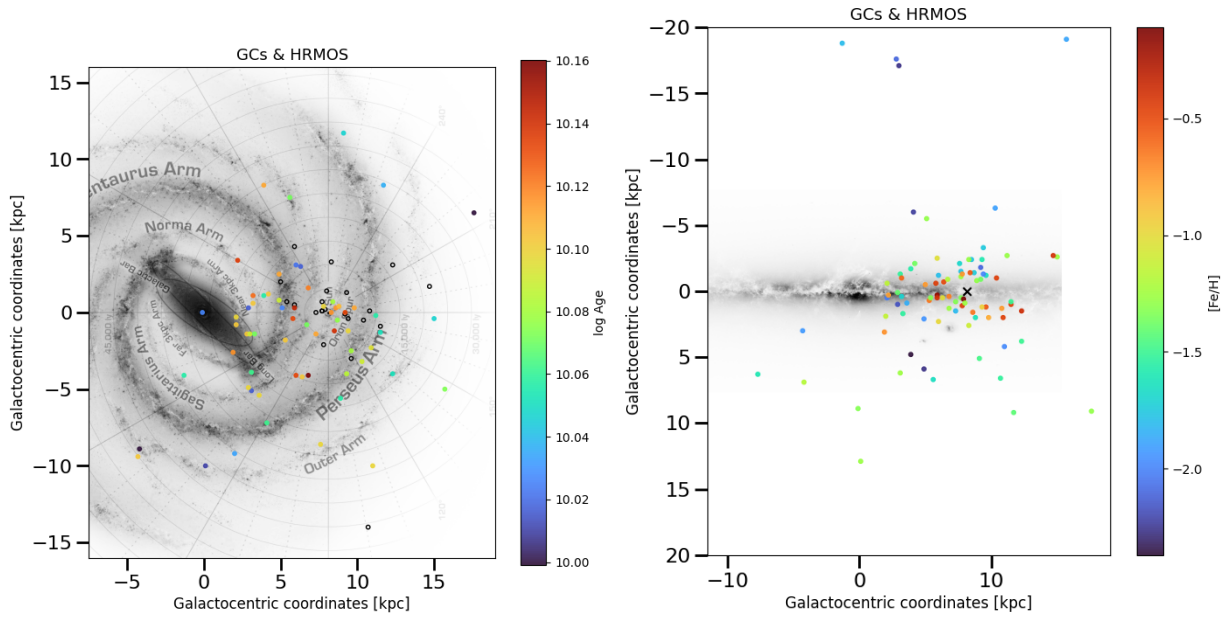


**Figure 11.2.** Spatial distribution of the globular clusters observable with HRMOS, projected onto the Milky Way. The left panel shows the top-down view, while the right panel displays the edge-on view.

As a starting point, we compiled potential targets from the Harris Catalogue<sup>1</sup> (Harris 2010), which lists 157 Galactic GCs. We selected clusters observable from the Southern hemisphere ( $DEC < 20^\circ$ ) and with horizontal-branch magnitudes  $V < 18$ , ensuring practical accessibility for HRMOS. For each cluster, we extracted photometric and astrometric data from *Gaia* DR3<sup>2</sup> (Gaia Collaboration et al. 2023) within 15 arcmin of the cluster centre. We cross-matched this sample with membership probabilities from Vasiliev & Baumgardt (2021) and retained only stars with membership probability  $> 0.95$  to minimise contamination from foreground and background stars.

To maximise scientific return of HRMOS, we focused this possible selection on FGK-type stars, which provide the most reliable abundance measurements across a wide metallicity range. We retained only clusters with at least 30 high-probability FGK members. The final dataset includes a large number of targetable stars ( $> 40,000$ ) across several dozens of GCs, spanning a range of magnitudes and evolutionary stages, providing a robust foundation for HRMOS science. Figure 11.2 shows the spatial distribution of the clusters in both top-down and edge-on Galactic projections, covering the bulge as well as the inner and outer halo. Ages from isochrone fitting and metallicities are also indicated. This GC sample complements the open clusters, spanning  $[Fe/H]$  from  $\sim -2.5$  to  $-0.5$  dex and extending to much older stellar populations. Among the 65 clusters with age estimates (Forbes & Bridges 2010), all exceed 10 Gyr, highlighting their role as fossil remnants of the earliest phases of Galactic formation. Precise ages remain a major challenge and a core HRMOS objective. Using the classification of Massari et al. (2019), the sample includes both in-situ and likely accreted clusters.

In summary, HRMOS will enable observations of globular clusters spanning a broad range of spatial, chemical, dynamical, and evolutionary properties, thereby addressing key astrophysical questions. When combined with *Gaia* astrometry and photometry, HRMOS spectroscopy will provide unprecedented insights into globular cluster physics and the formation history of the Milky Way.

<sup>1</sup>Harris catalog webpage: <https://physics.mcmaster.ca/~harris/mwgc.dat>

<sup>2</sup>*Gaia* Data Release 3 webpage: <https://www.cosmos.esa.int/web/gaia/dr3>

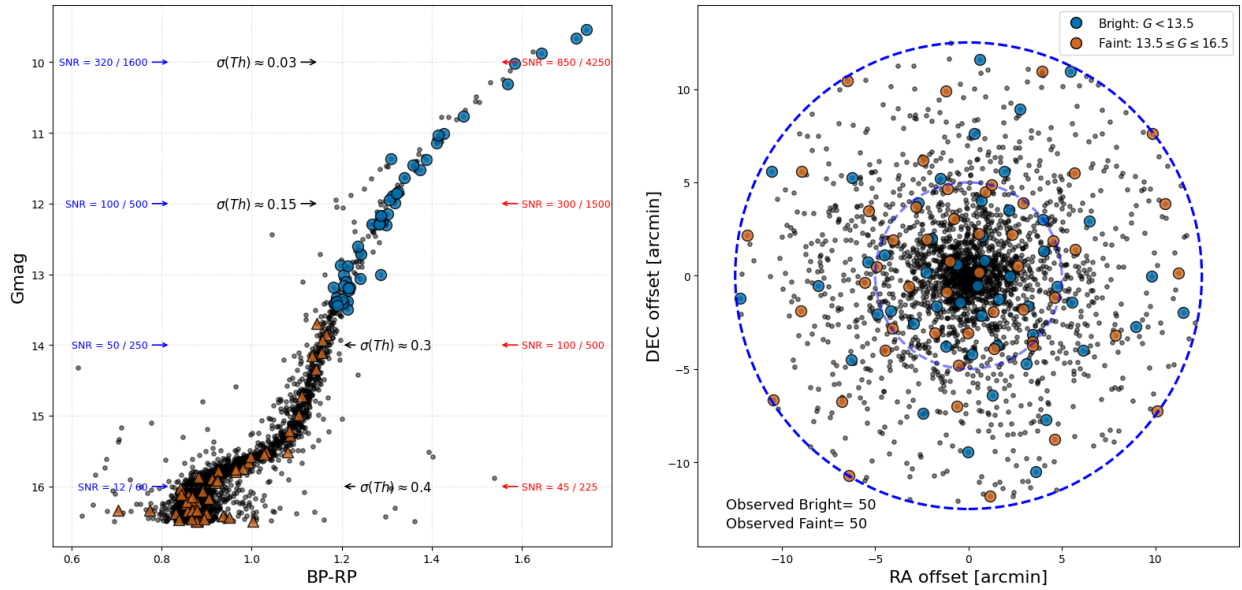


**Figure 11.3.** Two possible telescope pointings of member stars in NGC6397, divided into two G magnitude bins (in orange the faint sample, with  $16.5 < G < 13.5$ , in blue the bright sample, with  $G < 13.5$ ). The minimum distance between stars is 30 arcsec, while the number of allocated fibres is 50 per magnitude bin. In the left panel, the CMD of NGC6397 (stars with membership probability  $> 0.9$ ) is shown. In the right panel, the spatial distribution of the selected stars is presented. Colors and symbols follow the same description as Fig.11.1. In the left panel, the uncertainty on the measurement of the abundance of Th,  $\sigma(\text{Th})$ , is indicated for the combined observations along the sequence of the cluster.

### 11.2.1 Observational strategy in a Benchmark globular cluster

Following the same approach as for M67, we tested the observational strategy on the benchmark globular cluster NGC6397, located at 2.3 kpc (Harris 1996) and well populated along both the MS and RGB. Its magnitude range is similar to M67, so we again divide the targets into faint and bright samples. Owing to stronger crowding, we can allocate 50 fibres per sample in the whole FoV, yielding 100 stars observed in two pointings.

Figure 11.3 shows the selected targets in the CMD and on the sky. The SNRs achievable with 1 hr exposures (first number) and 25 hr combined exposures (second number) for four G magnitudes, in both the blue and red spectral ranges, are also shown.

As in M67, a hot-Jupiter search campaign (two pointings totalling 25hr, which is about six nights) will provide time-series spectra for  $\sim 70$  stars and high-SNR combined spectra. In the blue, SNRs of 250 – 600 can be reached for RGB stars, enabling measurements of neutron-capture elements such as Th and Eu.

Specifically, for NGC6397, the SNR is sufficient to measure Th in roughly 40 giant stars, substantially improving the precision of ages derived from Th/Eu.

## 11.3 The Galactic bulge and nearby dwarf galaxies

As described in Chapter 6, HRMOS will enable unprecedented chemical studies of stellar populations in three Milky Way satellite galaxies—the Magellanic Clouds and the Sagittarius dwarf—surpassing the capabilities of upcoming large spectroscopic surveys (e.g., 4MOST and WEAVE). As outlined in Chapter 4, HRMOS can deliver precise elemental abundances to identify signatures of hierarchical galaxy formation in these low-mass systems, analogous to how current surveys are revealing merger debris in the Galactic halo (see, e.g., Helmi et al. 1999, 2018; Horta

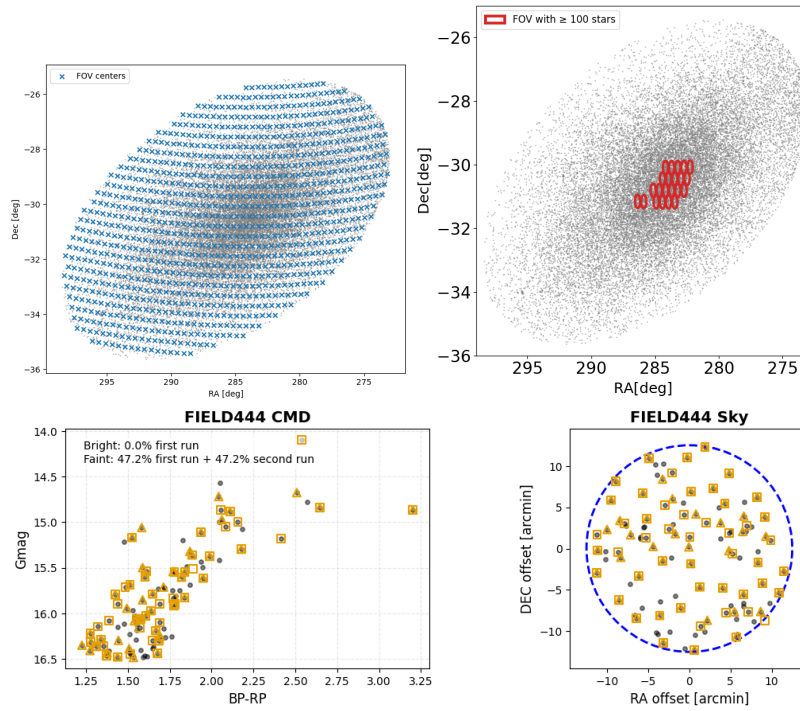


**Figure 11.4.** Upper left: Center of the FOV allocated (blue crosses) in the Sagittarius dwarf galaxy. Upper right: 25 arcmin FOV in the Sagittarius dwarf galaxy, containing at least 100 stars. Lower left: Color–magnitude diagram of one of the fields in the Sagittarius dwarf galaxy. Lower right: Position on the sky of the Sagittarius field with targeted stars in orange symbols.

et al. 2023).

By adopting an observational strategy similar to that used for clusters (i.e., repeated visits for planet detection), we can optimise both exoplanet and chemical-evolution science. This will allow, for the first time, searches for extragalactic massive planets and binaries around the brightest stars in the Magellanic Clouds, Sagittarius, and even in bulge populations. The combined spectra from repeated visits will provide extremely high signal-to-noise ratios, enabling very precise and detailed chemical abundance measurements.

### 11.3.1 Observational strategies in the Sagittarius dwarf galaxy and the LMC

Given that these galaxies are distant, faint, and spatially extended, we adopted a unified observational strategy for all of them. To minimise contamination from field stars, candidate targets were first selected using *Gaia* DR3 proper motions, parallaxes, and photometric colours. The regions of interest were then divided into individual fields matching the HRMOS field of view. Figure 11.4 show the field centres for the Sagittarius dwarf galaxy, covering more than 1,000 fields; only those containing at least 100 stars (highlighted in blue in the upper left panel) were retained. The corresponding layout and selected fields for the Large Magellanic Cloud. are shown in Fig. 11.5

Unlike Galactic open and globular clusters, these galaxies contain no stars brighter than  $G = 13.5$ , making observations more challenging and requiring longer exposure times to reach sufficient SNR. Example colour–magnitude diagrams for selected fields are shown in the upper right panels of Figs. 11.4 and 11.5, where red symbols indicate the chosen targets for Sagittarius and the LMC. The right panels display their spatial distribution, demonstrating that the HRMOS field of view enables efficient sampling of dense stellar regions.

This strategy maximises the number of genuine member stars while limiting contamination,

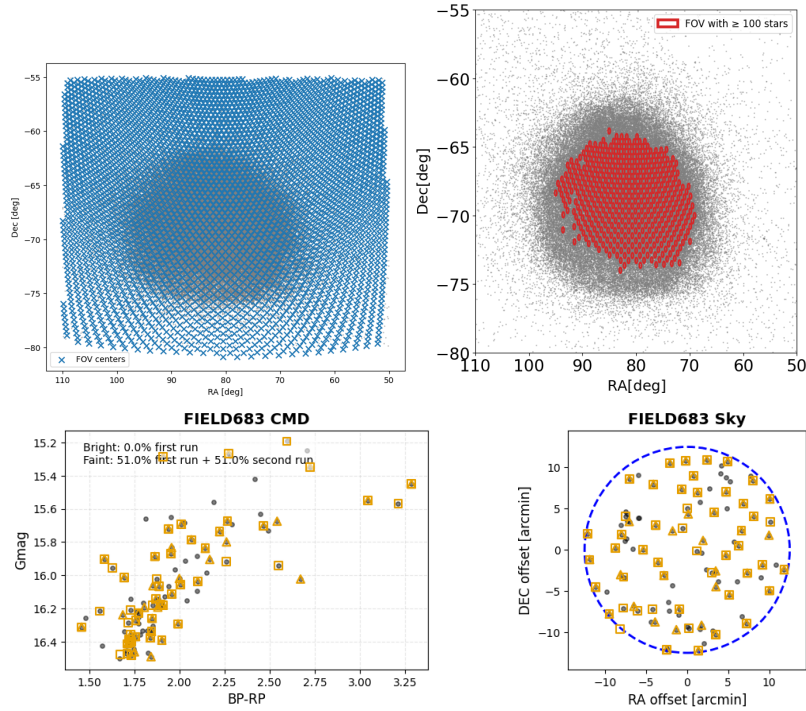


**Figure 11.5.** Upper left: Center of the FOV allocated (blue crosses) in the LMC. Upper right: 25 arcmin FOV in the LMC, containing at least 100 stars. Lower left: Color–magnitude diagram of one of the fields in the LMC. Lower right: Position on the sky of the LMC with targeted stars in orange symbols.

providing a solid basis for detailed chemical and kinematic studies of these extended systems. Even a limited set of strategically chosen fields, as discussed in Chapter 4, will significantly advance our understanding of the hierarchical formation of low-mass galaxies. High-precision abundances from HRMOS will allow identification of merger debris with a level of detail unattainable by forthcoming intermediate-resolution surveys such as 4MOST and WEAVE on 4-m class telescopes.

### 11.3.2 Observational strategy in the Galactic bulge

Another key region for HRMOS observations is the Galactic bulge, particularly Baade’s window. Owing to its comparatively low interstellar extinction, this field provides rare access to one of the most crowded and least explored components of the Milky Way. HRMOS observations here would enable detailed chemical analyses of bulge stars and offer new insight into the central Galactic structure.

To define suitable targets, we selected stars from *Gaia* DR3 within Baade’s window. The HRMOS field of view allows four distinct pointings, positioned to cover the densest areas; their central coordinates are shown in Fig. 11.6. As in previous cases, each field contains more than 100 viable targets. Figure 11.6 shows an example colour–magnitude diagram for one field, along with the spatial distribution of the selected stars.

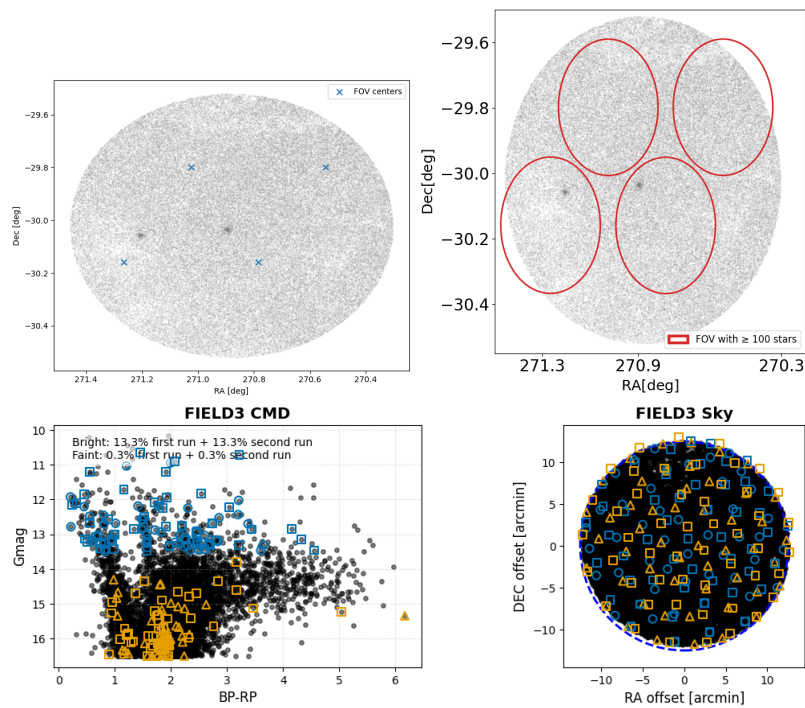


**Figure 11.6.** Upper left: Center of the FOV allocated (blue crosses) in the Baade's window area. Upper right: 25 arcmin FOV in the Baade's window area. Each of them contains at least 100 stars. Lower left: Color-magnitude diagram of one of the fields in Baade's window area. Lower right: Position on the sky of the Baade's window field with targeted stars in orange symbols.

## 12 Appendix

### 12.1 Estimating the precision in abundances and abundance ratios

In this appendix, we report the estimated uncertainties on the derived abundances of various elements and isotopic ratios as a function of the expected abundance, signal-to-noise ratio (SNR), and surface gravity in spectra typical of HRMOS-like instruments. The errors were evaluated using synthetic spectra covering a wide range of stellar parameters representative of our survey targets, taking into account both photon noise and continuum placement uncertainties.

Figure 12.1 illustrates the dependence of the abundance uncertainty on the intrinsic abundance and SNR for [Th/Fe], adopting the following stellar parameters:  $T_{\text{eff}}\text{-log } g$  pairs of 5800 K–3.7 dex, 6400 K–4.1 dex, and 6000 K–4.5 dex for dwarf main-sequence stars, and 4800 K–1.2 dex, 5000 K–2.0 dex, and 5200 K–2.5 dex for red giant branch stars. Microturbulence values of  $v_{\text{mic}} = 1.2 \text{ km s}^{-1}$  and  $2.0 \text{ km s}^{-1}$  were adopted for dwarfs and giants, respectively.

In a similar manner, Figures 12.2, 12.3, and 12.4 show the uncertainties in the abundance ratios [La/Fe], [Eu/Fe], and [Pb/Fe], respectively. Finally, Figure 12.5 presents the estimated errors on the isotopic fractions of Ba.

These results provide a quantitative guide to the achievable precision in chemical abundance studies across different stellar populations observed with HRMOS-class instruments, and are particularly useful for planning high-resolution multi-object spectroscopic surveys and for interpreting detailed chemical patterns in stars of varying evolutionary stages.

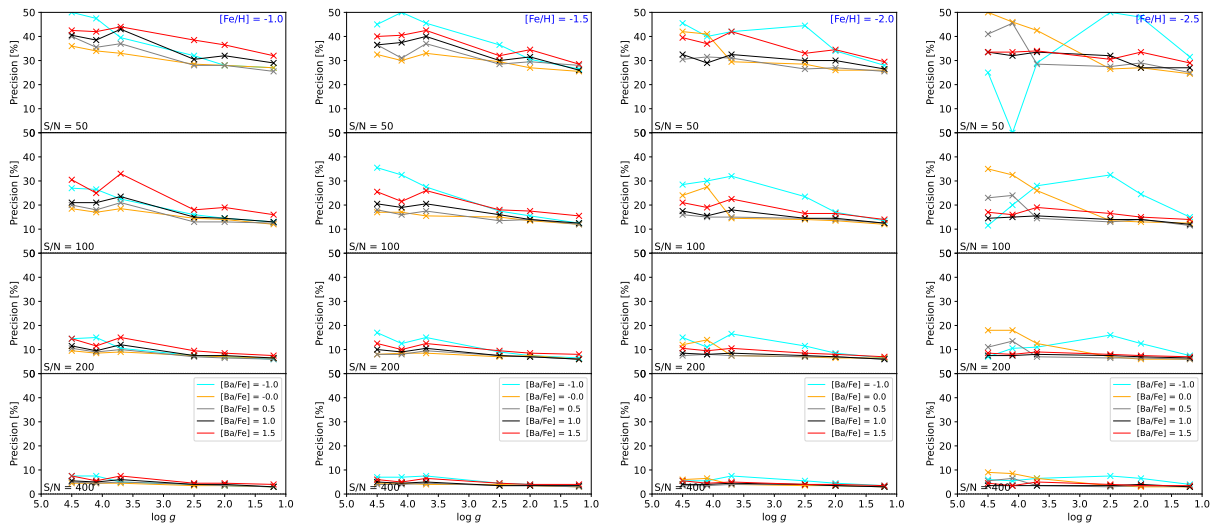


**Figure 12.1.** Precision in the measurement of Th abundances as a function of metallicity and of SNR. The adopted stellar parameters are the  $T_{\text{eff}}\text{-log } g$  pairs of 5800 K–3.7 dex, 6400 K–4.1 dex, and 6000 K–4.5 dex for dwarf main sequence stars, and 4800 K–1.2 dex, 5000 K–2.0 dex, and 5200 K–2.5 dex for the red giant branch stars. For dwarfs and giants, microturbulence values of  $v_{\text{mic}} = 1.2$  and  $2.0 \text{ km s}^{-1}$ , respectively, are assumed.

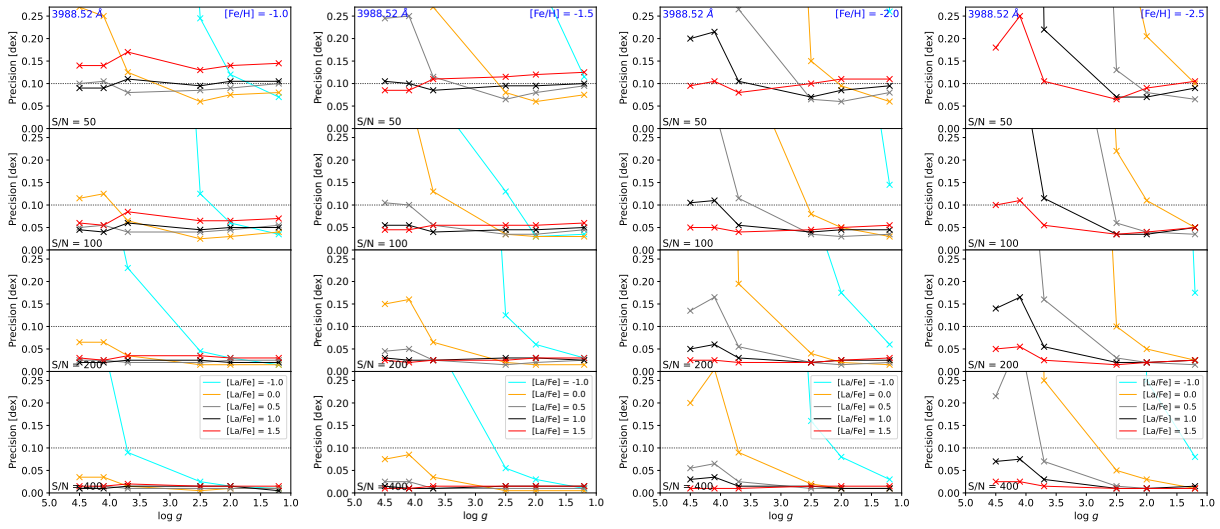


**Figure 12.2.** Precision in the measurement of La abundances as a function of metallicity and of SNR. Stellar parameters are as in Fig. 12.1.

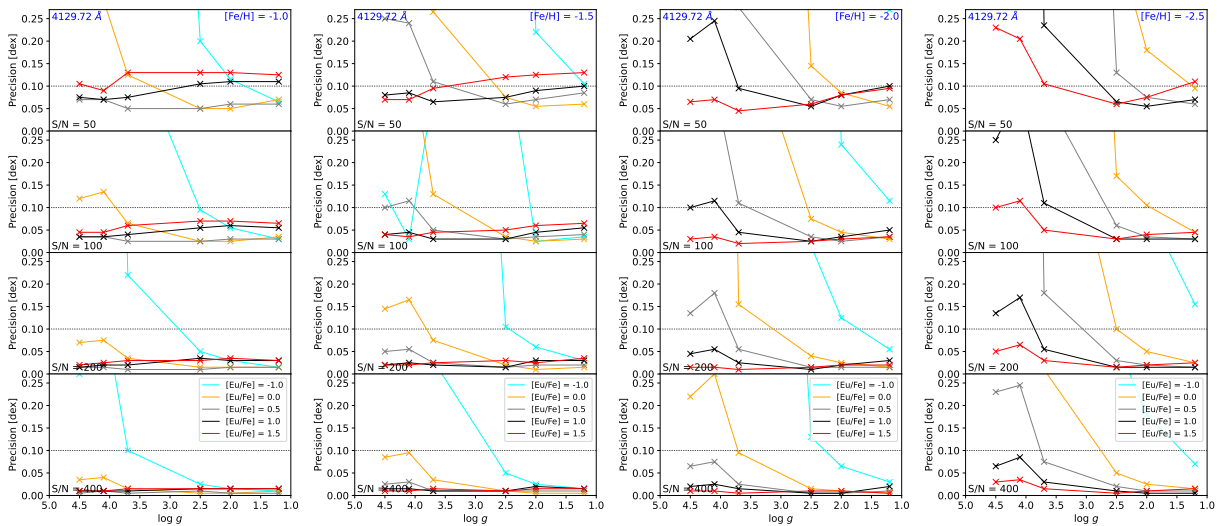


**Figure 12.3.** Precision in the measurement of Eu abundances as a function of metallicity and of SNR. Stellar parameters are as in Fig. 12.1.

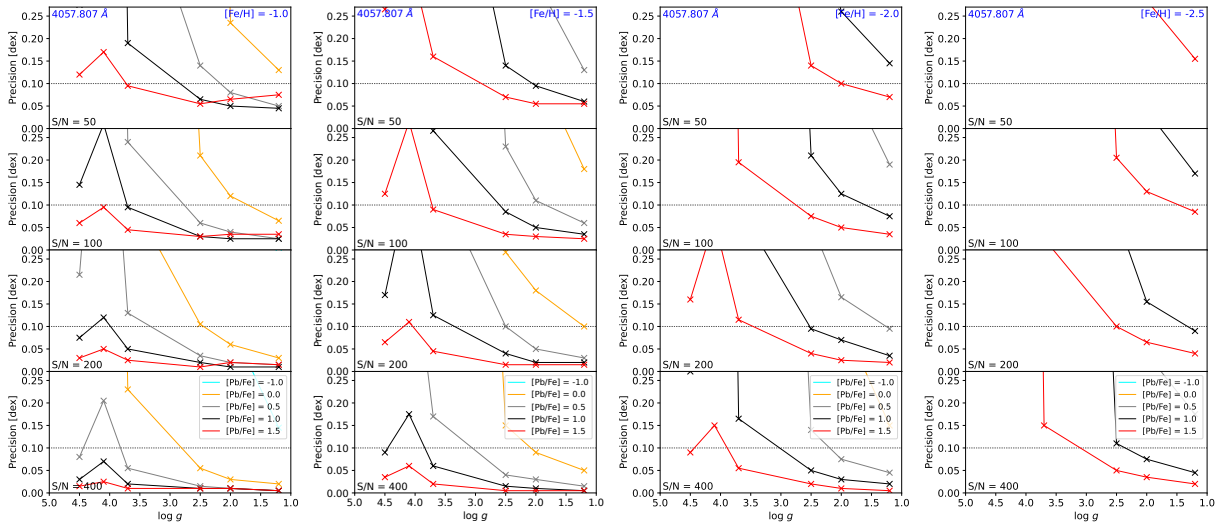


**Figure 12.4.** Precision in the measurement of Pb abundances as a function of metallicity and of SNR. Stellar parameters are as in Fig. 12.1.

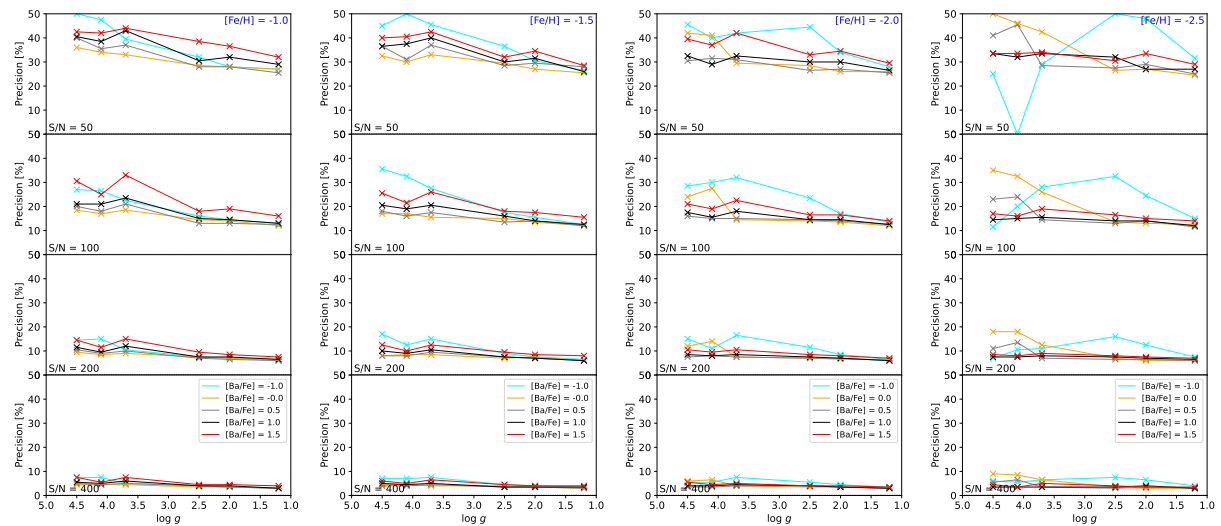


**Figure 12.5.** Precision in the measurement of Ba isotopic ratio as a function of metallicity and of SNR. Stellar parameters are as in Fig. 12.1.

**List of acronyms**

1D - One dimensional  
2D - Two dimensional  
3D - Three dimensional  
4MOST - 4-metre Multi-Object Spectroscopic Telescope  
AAT - Anglo-Australian Telescope  
ADC - Atmospheric dispersion corrector  
AGB - Asymptotic giant branch  
AGN- Active Galactic Nucleus  
ANDES - AmazoNES high Dispersion Echelle Spectrograph  
APOGEE - Apache Point Observatory Galactic Evolution Experiment  
ASD - Atomic Spectra Database  
BEBOP - Binaries Escorted By Orbiting Planets  
CA - Core Accretion  
CBP - Circumbinary planet  
CCD - Charge-coupled device  
CCF - Cross-Correlation Function  
ccSN - Core-Collapse SuperNovae  
CDM - Cold Dark Matter  
CDPS - the Cluster Difference Imaging Photometric Survey  
CEMP - Carbon-enhanced metal-poor  
CEMP-rs - Carbon-enhanced metal-poor with r- and s- elements  
CHEOPS - CHaracterising ExOPlanet Satellite  
CMB - Cosmic Microwave Background  
CMOS - Complementary Metal–Oxide–Semiconductor  
CTL - Candidate Target List  
CRIRES+ - CRyogenic high-resolution InfraRed Echelle Spectrograph  
CVZ - Continuous Viewing Zone  
DAZ - D = White Dwarf, A = hydrogen-dominated atmosphere, Z = metals present.  
DBZ - D = White Dwarf, B = helium-dominated atmosphere, Z = metals present.  
DESI - Dark Energy Spectroscopic Instrument  
DI - Disc Instability  
DM - Dark Matter  
DSPH - Dwarf spheroidal  
DZ - D = White Dwarf, Z = metals present  
ELT - Extremely Large Telescope  
EMP - Extremely metal-poor  
EP - Excitation potential  
ESA - European Space Agency  
ESO - European Southern Observatory  
ESPRESSO - Echelle SPectrograph for Rocky Exoplanet and Stable Spectroscopic Observations  
EUV- Extreme UltraViolet  
EW - Equivalent Width  
FLAMES - Fibre Large Array Multi Element Spectrograph  
FDM - Fuzzy Dark Matter  
FFIs - Full Frame Images  
FOV - Field-Of-View

FTS - Fourier Transform Spectroscopy  
FUV - Far UltraViolet  
FNX - Fornax  
FWHM - Full Width Half Maximum  
GALAH - GALactic Archaeology with HERMES  
GAPS - Global Architecture of Planetary Systems  
GC - Globular Cluster  
GEMS - Galaxy Evolution via Montecarlo Sampling  
HARPS - The High Accuracy Radial velocity Planet Searcher  
HAYDN - High-precision Asteroseismology of DeNse stellar fields  
HB- Horizontal Branch  
HCL- Hollow cathode lamps  
HERMES - The high efficiency and resolution Mercator echelle spectrograph  
HR - High Resolution  
HRMOS - High-Resolution Multi-Object Spectrograph  
HST - Hubble Space Telescope  
K2 - Kepler Extended Mission  
KMOS - K-band Multi Object Spectrograph  
IC - Index Catalogue  
iCCF - Interpolated Cross-Correlation Function  
LAMOST - The Large Sky Area Multi-Object Fibre Spectroscopic Telescope  
LBT - The Large Binocular Telescope  
LFC - Laser Frequency Comb  
LIM - Low- and intermediate-mass  
LMC - Large Magellanic Cloud  
LR - Low Resolution  
LSST - Large Synoptic Survey Telescope  
LTE- Local Thermodynamic Equilibrium  
MARCS - Model Atmospheres with a Radiative and Convective Scheme  
mas - milliarcsecond  
MCDHF - Multi-Configuration Dirac–Hartree–Fock  
MDF - Metallicity Distribution Function  
MHD - Magneto-HydroDynamics  
MICADO - Multi-AO Imaging Camera for Deep Observations  
MOONS - Multi-Object Optical and Near-infrared Spectrograph  
MOS - Multi-Object Spectrograph  
MOSAIC - the Multi-Object Spectrograph for the ELT  
MP - Multiple Population  
MS - Main Sequence  
MSE - Maunakea Spectroscopic Explorer  
MSTO - Main Sequence Turn Off  
MW - Milky Way  
MWM- Milky Way Mapper  
NIR - Near InfraRed  
NIST - National Institute of Standards and Technology  
NGC- New General Catalogue  
NLTE- Non Local Thermodynamic Equilibrium

NSM - Neutron star merger  
OC - Open cluster  
PATHOS - A PSF-based Approach to TESS High quality data Of Stellar clusters  
PEPSI - Potsdam Echelle Polarimetric and Spectroscopic Instrument  
PIE - Proton-Ingestion Event  
PISN - Pair-instability SuperNova  
PLATO - PLANetary Transits and Oscillations of stars  
PMS - Pre-main sequence  
PSF - Point Spread Function  
R - Resolving power  
RAVE - The Radial Velocity Experiment  
RC - Red Clump  
RCI- Relativistic Configuration Interaction  
RCW - Rodgers, Campbell, Whiteoak Catalogue  
RGB - Red Giant Branch  
RHD - Radiation-HydroDynamics  
RV - Radial velocity  
SB1 - Spectroscopic Binary Type 1  
SB2 - Spectroscopic Binary Type 2  
SDSS - Sloan Digital Sky Survey  
SEGUE - Sloan Extension for Galactic Understanding and Exploration  
SGB - Sub Giant Branch  
SGR - Sagittarius  
SMC - Small Magellanic Cloud  
SMHM - Stellar Mass-Halo Mass  
SN - SuperNova  
SNIa - SuperNova Type Ia  
SNR - Signal-to-noise ratio  
STC - Science and Technical Committee  
TATOOINE -The Attempt to Observe Outer-planets In Non-single-stellar Environments  
TESS - Transiting Exoplanet Survey Satellite  
TLR - Top Level Requirements  
TOIs - TESS Objects of Interest  
TNG - Telescopio Nazionale Galileo  
THYME - TESS Hunt for Young and Maturing Exoplanets  
UES - The Utrecht Echelle Spectrograph  
UCLES - University College London Echelle Spectrograph  
UFD - Ultra-faint dwarf  
UVES - The UltraViolet-Visual Echelle Spectrograph  
VLT - Very Large Telescope  
VPH - Volume Phase Holographic  
WEAVE - WHT Enhanced Area Velocity Explorer  
WD -White Dwarf  
WDM - Warm Dark Matter  
WFIRST - The Wide Field Infrared Survey Telescope  
WHT - William Herschel Telescope  
WST - The Wide-Field Spectroscopic telescope

ZAMS - Zero-age main sequence

# Bibliography

- Abazajian, K. N., Adelman-McCarthy, J. K., Agüeros, M. A., et al. 2009, *ApJS*, 182, 543
- Abbott, B. P., Abbott, R., Abbott, T. D., et al. 2017, *Phys. Rev. Lett.*, 119, 161101
- Adamo, A., Bradley, L. D., Vanzella, E., et al. 2024, *Nature*, 632, 513
- Adams, F. C. 2010, *ARA&A*, 48, 47
- Adams, F. C., Hollenbach, D., Laughlin, G., & Gorti, U. 2004, *ApJ*, 611, 360
- Adibekyan, V. 2019, *Geosciences*, 9, 105
- Aguado, D. S., Molaro, P., Caffau, E., et al. 2022, *A&A*, 668, A86
- Aguado, D. S., Salvadori, S., Skúladóttir, Á., et al. 2023, *MNRAS*, 520, 866
- Aguilera-Gómez, C., Chanamé, J., & Pinsonneault, M. H. 2020, *ApJ*, 897, L20
- Aguilera-Gómez, C., Chanamé, J., Pinsonneault, M. H., & Carlberg, J. K. 2016, *ApJ*, 829, 127
- Aguilera-Gómez, C., Jones, M. I., & Chanamé, J. 2023, *A&A*, 670, A73
- Aicken Davies, Q. & Worley, C. C. 2025, arXiv e-prints, arXiv:2510.22487
- Alencastro Puls, A., Kuske, J., Hansen, C. J., et al. 2025, *A&A*, 693, A294
- Alexeeva, S., Wang, Y., Zhao, G., et al. 2023, *ApJ*, 957, 10
- Allende Prieto, C., Asplund, M., García López, R. J., & Lambert, D. L. 2002, *ApJ*, 567, 544
- Almeida, A., Anderson, S. F., Argudo-Fernández, M., et al. 2023, *ApJS*, 267, 44
- Amarsi, A. M., Barklem, P. S., Asplund, M., Collet, R., & Zatsarinny, O. 2018a, *A&A*, 616, A89
- Amarsi, A. M., Barklem, P. S., Collet, R., Grevesse, N., & Asplund, M. 2019a, *A&A*, 624, A111
- Amarsi, A. M., Li, W., Grevesse, N., & Jurewicz, A. J. G. 2025, *A&A*, 703, A35
- Amarsi, A. M., Liljegren, S., & Nissen, P. E. 2022, *A&A*, 668, A68
- Amarsi, A. M., Lind, K., Osorio, Y., et al. 2020, *A&A*, 642, A62
- Amarsi, A. M., Nissen, P. E., & Skúladóttir, Á. 2019b, *A&A*, 630, A104
- Amarsi, A. M., Nordlander, T., Barklem, P. S., et al. 2018b, *A&A*, 615, A139
- Amarsi, A. M., Ogneva, D., Buldgen, G., et al. 2024, *A&A*, 690, A128
- Andrae, R., Rix, H.-W., & Chandra, V. 2023, *ApJS*, 267, 8
- Andrews, S. M., Huang, J., Pérez, L. M., et al. 2018, *ApJ*, 869, L41
- Arav, N., Liu, G., Xu, X., et al. 2018, *ApJ*, 857, 60
- Arcones, A. & Thielemann, F.-K. 2023, *A&A Rev.*, 31, 1
- Arellano-Córdova, K. Z. & Rodríguez, M. 2020, *MNRAS*, 497, 672
- Armitage, P. J., Simon, J. B., & Martin, R. G. 2013, *ApJ*, 778, L14
- Armstrong, D. J., Osborn, H. P., Brown, D. J. A., et al. 2014, *MNRAS*, 444, 1873
- Arnould, M. & Goriely, S. 2003, *Phys. Rep.*, 384, 1
- Arnould, M., Goriely, S., & Takahashi, K. 2007, *Phys. Rep.*, 450, 97
- Aros, F. I., Sippel, A. C., Mastrobuono-Battisti, A., et al. 2021, *MNRAS*, 508, 4385
- Arroyo-Polonio, J. M., Battaglia, G., Thomas, G. F., et al. 2023, *A&A*, 677, A95
- Asplund, M., Amarsi, A. M., & Grevesse, N. 2021, arXiv e-prints, arXiv:2105.01661

- Azhari, A., Matsuno, T., Aoki, W., Ishigaki, M. N., & Tolstoy, E. 2025, *A&A*, 699, A276
- Bacon, R., Mainieri, V., Randich, S., et al. 2024, in *Society of Photo-Optical Instrumentation Engineers (SPIE) Conference Series*, Vol. 13094, *Ground-based and Airborne Telescopes X*, ed. H. K. Marshall, J. Spyromilio, & T. Usuda, 130941O
- Bacon, R., Roth, M. M., Amico, P., Hernandez, E., & WST Consortium, t. 2023, arXiv e-prints, arXiv:2308.16064
- Badnell, N. R. 2016, *AUTOSTRUCTURE: General program for calculation of atomic and ionic properties*, *Astrophysics Source Code Library*
- Bai, X.-N. 2016, *ApJ*, 821, 80
- Balsalobre-Ruza, O., Lillo-Box, J., Silva, A. M., et al. 2025, *A&A*, 694, A15
- Banerjee, P., Qian, Y.-Z., & Heger, A. 2018, *ApJ*, 865, 120
- Bar-Shalom, A., Klapisch, M., & Oreg, J. 2001, *Journal of Quantitative Spectroscopy and Radiative Transfer*, 71, 169
- Baranne, A., Queloz, D., Mayor, M., et al. 1996, *A&AS*, 119, 373
- Baratella, M., D’Orazi, V., Carraro, G., et al. 2020, *A&A*, 634, A34
- Baratella, M., D’Orazi, V., Sheminova, V., et al. 2021, *A&A*, 653, A67
- Barklem, P. S. 2016, *A&A Rev.*, 24, 9
- Barklem, P. S., Belyaev, A. K., Guitou, M., et al. 2011, *A&A*, 530, A94
- Barnes, J. R. & Collier Cameron, A. 2001, *MNRAS*, 326, 950
- Barnes, J. R., Collier Cameron, A., James, D. J., & Donati, J. F. 2000, *MNRAS*, 314, 162
- Barnes, J. R., Jeffers, S. V., Anglada-Escudé, G., et al. 2017, *MNRAS*, 466, 1733
- Barnes, J. R., Jeffers, S. V., & Jones, H. R. A. 2011, *MNRAS*, 412, 1599
- Barragán, O., Aigrain, S., Kubyschkina, D., et al. 2019, *MNRAS*, 490, 698
- Barragán, O., Yu, H., Freckelton, A. V., et al. 2024, *MNRAS*, 531, 4275
- Bastian, N. & Lardo, C. 2018, *ARA&A*, 56, 83
- Baumgardt, H., Hénault-Brunet, V., Dickson, N., & Sollima, A. 2023, *MNRAS*, 521, 3991
- Baumgardt, H. & Hilker, M. 2018, *MNRAS*, 478, 1520
- Baumgardt, H., Hilker, M., Sollima, A., & Bellini, A. 2019, *MNRAS*, 482, 5138
- Baycroft, T. A., Santerne, A., Triaud, A. H. M. J., et al. 2025, *MNRAS*, 541, 2801
- Bedin, L. R., Piotto, G., Anderson, J., et al. 2004, *ApJ*, 605, L125
- Belmonte, M. T., Mar, S., Djurović, S., Menéndez, J. A., & Gavanski, L. 2025, *Spectrochimica Acta Part B: Atomic Spectroscopy*, 107190
- Belmonte, M. T., Pickering, J. C., Ruffoni, M. P., et al. 2017, arXiv
- Belokurov, V., Erkal, D., Evans, N. W., Koposov, S. E., & Deason, A. J. 2018, *MNRAS*, 478, 611
- Benisty, M., Dominik, C., Follette, K., et al. 2022, arXiv e-prints, arXiv:2203.09991
- Benito, M., Criado, J. C., Hütsi, G., Raidal, M., & Veermäe, H. 2020, *Phys. Rev. D*, 101, 103023
- Benito, M., Hütsi, G., Mürsepp, K., et al. 2025, *Physics of the Dark Universe*, 49, 102010
- Bensby, T., Bergemann, M., Rybizki, J., et al. 2019, *The Messenger*, 175, 35
- Berdyugina, S. V., Berdyugin, A. V., Fluri, D. M., & Piirola, V. 2008, *ApJ*, 673, L83
- Bergemann, M., Gallagher, A. J., Eitner, P., et al. 2019, *A&A*, 631, A80
- Bergstrom, H., Faris, G., Hallstadius, H., et al. 1988, *Zeitschrift für Physik D Atoms, Molecules and Clusters*, 8, 17
- Bernabò, L. M., Turrini, D., Testi, L., Marzari, F., & Polychroni, D. 2022, *ApJ*, 927, L22
- Bertelli Motta, C., Pasquali, A., Richer, J., et al. 2018, *MNRAS*, 478, 425
- Bertran de Lis, S., Allende Prieto, C., Ludwig, H. G., & Koesterke, L. 2022, *A&A*, 661, A76

- Besla, G., Kallivayalil, N., Hernquist, L., et al. 2010, *ApJ*, 721, L97
- Bianchini, P., van der Marel, R. P., del Pino, A., et al. 2018, *MNRAS*, 481, 2125
- Biazzo, K., D’Orazi, V., Desidera, S., et al. 2022, *A&A*, 664, A161
- Bijavara Seshashayana, S., Jönsson, H., D’Orazi, V., et al. 2025, arXiv e-prints, arXiv:2511.05115
- Bischetti, M., Feruglio, C., D’Odorico, V., et al. 2022, *Nature*, 605, 244
- Bongiorno, A., Zamorani, G., Gavignaud, I., et al. 2007, *A&A*, 472, 443
- Bonifacio, P., Caffau, E., François, P., & Spite, M. 2025, *A&A Rev.*, 33, 2
- Borguet, B. C. J., Arav, N., Edmonds, D., Chamberlain, C., & Benn, C. 2013, *ApJ*, 762, 49
- Borucki, W. J., Koch, D., Basri, G., et al. 2010, *Science*, 327, 977
- Botelho, R. B., Milone, A. d. C., Meléndez, J., et al. 2020, *MNRAS*, 499, 2196
- Bouchy, F., Pepe, F., & Queloz, D. 2001, *A&A*, 374, 733
- Bouma, L. G., Hartman, J. D., Bhatti, W., Winn, J. N., & Bakos, G. Á. 2019, *ApJS*, 245, 13
- Bouma, L. G., Hartman, J. D., Brahm, R., et al. 2020, *AJ*, 160, 239
- Bouvier, J. 2008, *A&A*, 489, L53
- Bouvier, J., Alencar, S. H. P., Boutelier, T., et al. 2007a, *A&A*, 463, 1017
- Bouvier, J., Alencar, S. H. P., Harries, T. J., Johns-Krull, C. M., & Romanova, M. M. 2007b, in *Protostars and Planets V*, ed. B. Reipurth, D. Jewitt, & K. Keil, 479
- Bowen, D. V., Jenkins, E. B., Pettini, M., & Tripp, T. M. 2005, *ApJ*, 635, 880
- Bragaglia, A., Carretta, E., D’Orazi, V., et al. 2017, *A&A*, 607, A44
- Bramich, D. M. & Horne, K. 2006, *MNRAS*, 367, 1677
- Brasseur, C. E., Jardine, M. M., & Hussain, G. A. J. 2024, *MNRAS*, 530, 2442
- Brauer, K., Mead, J., Wise, J. H., et al. 2025, *ApJ*, 993, 2
- Brazzini, M., D’Odorico, V., Bischetti, M., et al. 2025, *A&A*, 698, A145
- Bromm, V. 2013, *Reports on Progress in Physics*, 76, 112901
- Brown, A. G. A. 2025, arXiv e-prints, arXiv:2503.01533
- Brucalassi, A., Koppenhoefer, J., Saglia, R., et al. 2017, *A&A*, 603, A85
- Brucalassi, A., Pasquini, L., Saglia, R., et al. 2014, *A&A*, 561, L9
- Brucalassi, A., Pasquini, L., Saglia, R., et al. 2016, *A&A*, 592, L1
- Brucalassi, A., Tozzi, A., Oliva, E., et al. 2022, in *Society of Photo-Optical Instrumentation Engineers (SPIE) Conference Series*, Vol. 12184, *Ground-based and Airborne Instrumentation for Astronomy IX*, ed. C. J. Evans, J. J. Bryant, & K. Motohara, 121841A
- Bruntt, H., Grundahl, F., Tingley, B., et al. 2003, *A&A*, 410, 323
- Buder, S., Buck, T., Skúladóttir, Á., et al. 2025, arXiv e-prints, arXiv:2510.11284
- Burbidge, E. M., Burbidge, G. R., Fowler, W. A., & Hoyle, F. 1957, *Reviews of Modern Physics*, 29, 547
- Burke, C. J., Gaudi, B. S., DePoy, D. L., & Pogge, R. W. 2006, *AJ*, 132, 210
- Burn, R. & Mordasini, C. 2024, in *Handbook of Exoplanets* (Springer International Publishing), 143–2
- Busso, M., Gallino, R., & Wasserburg, G. J. 1999, *ARA&A*, 37, 239
- Butcher, H. R. 1987, *Nature*, 328, 127
- Cadelano, M., Dalessandro, E., Salaris, M., et al. 2022, *ApJ*, 924, L2
- Caffau, E., Bonifacio, P., Faraggiana, R., et al. 2005a, *A&A*, 441, 533
- Caffau, E., Bonifacio, P., Faraggiana, R., & Sbordone, L. 2005b, *A&A*, 436, L9
- Caffau, E., Monaco, L., Spite, M., et al. 2014, *A&A*, 568, A29
- Caffau, E., Sbordone, L., Ludwig, H. G., Bonifacio, P., & Spite, M. 2010, *Astronomische Nachrichten*,

- 331, 725
- Caffau, E., Sbordone, L., Ludwig, H.-G., et al. 2008, *A&A*, 483, 591
- Caliskan, S., Amarsi, A. M., Jönsson, P., Grevesse, N., & Sahoo, B. K. 2026, arXiv e-prints, arXiv:2605.05356
- Caliskan, S., Amarsi, A. M., Racca, M., et al. 2025, *A&A*, 696, A210
- Caliskan, S., Grumer, J., & Amarsi, A. M. 2024, *Journal of Physics B Atomic Molecular Physics*, 57, 055003
- Cameron, A. G. W. 1957, *PASP*, 69, 201
- Cameron, A. G. W. & Fowler, W. A. 1971, *ApJ*, 164, 111
- Canocchi, G., Lind, K., Lagae, C., et al. 2024, *A&A*, 683, A242
- Cantat-Gaudin, T., Anders, F., Castro-Ginard, A., et al. 2020, *A&A*, 640, A1
- Carleo, I., Desidera, S., Nardiello, D., et al. 2021, *A&A*, 645, A71
- Carretta, E. & Bragaglia, A. 2021, *A&A*, 646, A9
- Carretta, E. & Bragaglia, A. 2024, *A&A*, 690, A158
- Carretta, E., Bragaglia, A., Gratton, R., & Lucatello, S. 2009a, *A&A*, 505, 139
- Carretta, E., Bragaglia, A., Gratton, R. G., et al. 2009b, *A&A*, 505, 117
- Cassisi, S. & Salaris, M. 2020, *A&A Rev.*, 28, 5
- Castro-González, A., Bouchy, F., Correia, A. C. M., et al. 2025, *A&A*, 699, A344
- Castro-Tapia, M., Aguilera-Gómez, C., & Chanamé, J. 2024, *A&A*, 690, A367
- Cayrel, R., Hill, V., Beers, T. C., et al. 2001, *Nature*, 409, 691
- Cehula, J., Thompson, T. A., & Metzger, B. D. 2024, *MNRAS*, 528, 5323
- Cescutti, G., Morossi, C., Franchini, M., et al. 2021, *A&A*, 654, A164
- Cescutti, G., Romano, D., Matteucci, F., Chiappini, C., & Hirschi, R. 2015, *A&A*, 577, A139
- Chen, H.-Y., Landry, P., Read, J. S., & Siegel, D. M. 2025, *ApJ*, 985, 154
- Choi, H., Leighly, K. M., Terndrup, D. M., Gallagher, S. C., & Richards, G. T. 2020, *ApJ*, 891, 53
- Choi, J., Dotter, A., Conroy, C., et al. 2016, *ApJ*, 823, 102
- Chopin, A., Siess, L., Goriely, S., & Martinet, S. 2024, *Galaxies*, 12, 66
- Cimatti, A. & Moresco, M. 2023, *ApJ*, 953, 149
- Cioni, M., R. L., Storm, J., Bell, C. P. M., et al. 2019, *The Messenger*, 175, 54
- Cirasuolo, M., Fairley, A., Rees, P., et al. 2020, *The Messenger*, 180, 10
- Clarkson, O., Herwig, F., & Pignatari, M. 2018, *MNRAS*, 474, L37
- Clear, C. P., Pickering, J. C., Nave, G., Uylings, P., & Raassen, T. 2022, *The Astrophysical Journal Supplement Series*, 261, 35
- Clear, C. P., Pickering, J. C., Nave, G., Uylings, P., & Raassen, T. 2023a, *The Astrophysical Journal Supplement Series*, 269, 36
- Clear, C. P., Uylings, P., Raassen, T., Nave, G., & Pickering, J. C. 2023b, *Monthly Notices of the Royal Astronomical Society*, 519, 4040
- Colless, M., Dalton, G., Maddox, S., et al. 2001, *MNRAS*, 328, 1039
- Collier Cameron, A. 1995, *MNRAS*, 275, 534
- Collier Cameron, A. & Campbell, C. G. 1993, *A&A*, 274, 309
- Collier Cameron, A., Duncan, D. K., Ehrenfreund, P., et al. 1990, *MNRAS*, 247, 415
- Collier Cameron, A. & Robinson, R. D. 1989, *MNRAS*, 236, 57
- Collier Cameron, A. & Unruh, Y. C. 1994, *MNRAS*, 269, 814
- Columba, G., Danielski, C., Dorozsmai, A., Toonen, S., & Lopez Puertas, M. 2023, *A&A*, 675, A156
- Comerón, F. & Pasquali, A. 2005, *A&A*, 430, 541

- Concepcion, F., Clear, C. P., Ding, M., & Pickering, J. C. 2023, *European Physical Journal D*, 77
- Cooke, R. 2026, in *Encyclopedia of Astrophysics*, Volume 5, Vol. 5, 159–183
- Cooper, A. P., Kuposov, S. E., Allende Prieto, C., et al. 2023, *ApJ*, 947, 37
- Coria, D. R., Crossfield, I. J. M., Lothringer, J., et al. 2023, *ApJ*, 954, 121
- Cosentino, R., Lovis, C., Pepe, F., et al. 2012, in *Society of Photo-Optical Instrumentation Engineers (SPIE) Conference Series*, Vol. 8446, *Ground-based and Airborne Instrumentation for Astronomy IV*, ed. I. S. McLean, S. K. Ramsay, & H. Takami, 84461V
- Côté, B., Eichler, M., Arcones, A., et al. 2019, *ApJ*, 875, 106
- Cottaar, M. & Hénault-Brunet, V. 2014, *A&A*, 562, A20
- Covino, E., Esposito, M., Barbieri, M., et al. 2013, *A&A*, 554, A28
- Cowan, J. J. & Rose, W. K. 1977, *ApJ*, 212, 149
- Cowan, J. J., Sneden, C., Burles, S., et al. 2002, *ApJ*, 572, 861
- Cowan, J. J., Sneden, C., Lawler, J. E., et al. 2021, *Reviews of Modern Physics*, 93, 015002
- Cowan, J. J., Thielemann, F.-K., & Truran, J. W. 1991, *ARA&A*, 29, 447
- Cowan, R. D. 2023, *The theory of atomic structure and spectra*, Vol. 3 (Univ of California Press)
- Crenshaw, D. M., Kraemer, S. B., Boggess, A., et al. 1999, *ApJ*, 516, 750
- Curtis, J. L., Vanderburg, A., Torres, G., et al. 2018, *AJ*, 155, 173
- Da Costa, G. S., Norris, J. E., & Yong, D. 2013, *ApJ*, 769, 8
- da Silva, A. R. & Smiljanic, R. 2023, *A&A*, 677, A74
- Dai, Y.-Z., Liu, H.-G., Pang, X., et al. 2025, arXiv e-prints, arXiv:2512.07029
- Daley-Yates, S. & Jardine, M. M. 2024, *MNRAS*, 534, 621
- Dalton, G., Trager, S., Abrams, D. C., et al. 2014, in *SPIE Conf. Ser.*, Vol. 9147, 91470L
- Damasso, M., Polychroni, D., Locci, D., et al. 2024, *A&A*, 688, A15
- Damiani, F., Bonito, R., Magrini, L., et al. 2016, *A&A*, 591, A74
- Damiani, F., Bonito, R., Prisinzano, L., et al. 2017, *A&A*, 604, A135
- Daniel, K. J., Heggie, D. C., & Varri, A. L. 2017, *MNRAS*, 468, 1453
- Davidson, M. D., Snoek, L. C., Volten, H., & Doenszelmann, A. 1992, *Astronomy and Astrophysics* (ISSN 0004-6361), 255
- Davies, M. B., Adams, F. C., Armitage, P., et al. 2014, in *Protostars and Planets VI*, ed. H. Beuther, R. S. Klessen, C. P. Dullemond, & T. Henning, 787
- de Blok, W. J. G. 2010, *Advances in Astronomy*, 2010, 789293
- de Jong, R. S., Agertz, O., Berbel, A. A., et al. 2019, *The Messenger*, 175, 3
- de los Reyes, M. A. C., Kirby, E. N., Seitzzahl, I. R., & Shen, K. J. 2020, *ApJ*, 891, 85
- de Mink, S. E., Pols, O. R., Langer, N., & Izzard, R. G. 2009, *A&A*, 507, L1
- De Silva, G. M., Freeman, K. C., Bland-Hawthorn, J., et al. 2015, *MNRAS*, 449, 2604
- Deason, A. J., Bose, S., Fattahi, A., et al. 2022, *MNRAS*, 511, 4044
- Debes, J. H. & Sigurdsson, S. 2002, *ApJ*, 572, 556
- Decressin, T., Charbonnel, C., & Meynet, G. 2007, *A&A*, 475, 859
- Deepak & Lambert, D. L. 2021, *MNRAS*, 507, 205
- Dekker, H., D’Odorico, S., Kaufer, A., Delabre, B., & Kotzlowski, H. 2000, in *Society of Photo-Optical Instrumentation Engineers (SPIE) Conference Series*, Vol. 4008, *Optical and IR Telescope Instrumentation and Detectors*, ed. M. Iye & A. F. Moorwood, 534–545
- Delgado Mena, E., Bertrán de Lis, S., Adibekyan, V. Z., et al. 2015, *A&A*, 576, A69
- Delgado Mena, E., Gomes da Silva, J., Faria, J. P., et al. 2023, *A&A*, 679, A94
- Delgado Mena, E., Lovis, C., Santos, N. C., et al. 2018, *A&A*, 619, A2

- Deliyannis, C. P., Anthony-Twarog, B. J., Lee-Brown, D. B., & Twarog, B. A. 2019, *AJ*, 158, 163
- Deliyannis, C. P., Demarque, P., & Kawaler, S. D. 1990, *ApJS*, 73, 21
- Denissenkov, P. A. 2010, *ApJ*, 723, 563
- Denissenkov, P. A., Herwig, F., Woodward, P., et al. 2019, *MNRAS*, 488, 4258
- Denissenkov, P. A., VandenBerg, D. A., Hartwick, F. D. A., et al. 2015, *MNRAS*, 448, 3314
- Deprince, J., Wagle, G., Ben Nasr, S., et al. 2025, *A&A*, 696, A32
- Dessauges-Zavadsky, M., Calura, F., Prochaska, J. X., D’Odorico, S., & Matteucci, F. 2007, *A&A*, 470, 431
- Dickinson, D., Smith, N., Andrews, J., et al. 2023, in *American Astronomical Society Meeting Abstracts*, Vol. 241, *American Astronomical Society Meeting Abstracts #241*, 207.16
- Dickson, N., Smith, P. J., Hénault-Brunet, V., Gieles, M., & Baumgardt, H. 2024, *MNRAS*, 529, 331
- Diehl, R., Korn, A. J., Leibundgut, B., Lugaro, M., & Wallner, A. 2022, *Progress in Particle and Nuclear Physics*, 127, 103983
- Ding, M. 2025, *Atoms*, 13, 35
- Ding, M., Kozuki, H., Concepcion, F., Nave, G., & Pickering, J. C. 2025, *Monthly Notices of the Royal Astronomical Society*, 536, 274
- Ding, M., Pickering, J., Ryabtsev, A., Kononov, E., & Ryabchikova, T. 2024a, *Astronomy & Astrophysics*, 149, 1
- Ding, M. & Pickering, J. C. 2020, *The Astrophysical Journal Supplement Series*, 251, 24
- Ding, M., Ryabtsev, A. N., Kononov, E. Y., Ryabchikova, T., & Pickering, J. C. 2024b, *Astronomy and Astrophysics*, 692
- Dixon, J. D., Ezzeddine, R., Li, Y., et al. 2025, *ApJ*, 994, 44
- Donati, J. F., Gregory, S. G., Alencar, S. H. P., et al. 2011, *MNRAS*, 417, 472
- Donati, J. F., Gregory, S. G., Alencar, S. H. P., et al. 2013, *MNRAS*, 436, 881
- Donati, J. F. & Landstreet, J. D. 2009, *ARA&A*, 47, 333
- Donati, J. F., Morin, J., Petit, P., et al. 2008, *MNRAS*, 390, 545
- Donati, J. F., Skelly, M. B., Bouvier, J., et al. 2010, *MNRAS*, 409, 1347
- Dondoglio, E., Marino, A. F., Milone, A. P., et al. 2025, *A&A*, 697, A135
- D’Orazi, V., Gratton, R. G., Angelou, G. C., et al. 2015, *MNRAS*, 449, 4038
- D’Orazi, V., Magrini, L., Randich, S., et al. 2009, *ApJ*, 693, L31
- Dorn, R. J., Bristow, P., Smoker, J. V., et al. 2023, *A&A*, 671, A24
- Dotter, A. 2016, *ApJS*, 222, 8
- Dotter, A., Conroy, C., Cargile, P., & Asplund, M. 2017, *ApJ*, 840, 99
- Dowd, K., Doyle, E., & Dunne, P. 2025, *Experimental Astronomy*, 60
- Duffau, S., Caffau, E., Sbordone, L., et al. 2017, *A&A*, 604, A128
- Duncan, D. K., Vaughan, A. H., Wilson, O. C., et al. 1991, *ApJS*, 76, 383
- Dunn, J. P., Bautista, M., Arav, N., et al. 2010, *ApJ*, 709, 611
- Dunstone, N. J., Collier Cameron, A., Barnes, J. R., & Jardine, M. 2006, *MNRAS*, 373, 1308
- Duquennoy, A. & Mayor, M. 1991, *A&A*, 248, 485
- Durney, B. R. & Latour, J. 1978, *Geophysical and Astrophysical Fluid Dynamics*, 9, 241
- Dzuba, V. A., Flambaum, V. V., & Webb, J. K. 1999, *Phys. Rev. Lett.*, 82, 888
- Eistrup, C., Walsh, C., & van Dishoeck, E. F. 2016, *A&A*, 595, A83
- Eistrup, C., Walsh, C., & van Dishoeck, E. F. 2018, *A&A*, 613, A14
- Eitner, P., Bergemann, M., Hoppe, R., et al. 2024, *A&A*, 688, A52
- Eitner, P., Bergemann, M., Hoppe, R., et al. 2025, *arXiv e-prints*, arXiv:2509.24555

- Eitner, P., Bergemann, M., Ruiter, A. J., et al. 2023, *A&A*, 677, A151
- El-Badry, K., Rix, H.-W., & Heintz, T. M. 2021, *MNRAS*, 506, 2269
- Ernandes, H., Feuillet, D., Feltzing, S., & Skúladóttir, Á. 2024, *A&A*, 691, A333
- Ernandes, H., Skúladóttir, Á., Feltzing, S., & Feuillet, D. 2025, *A&A*, 703, A256
- Even, W., Korobkin, O., Fryer, C. L., et al. 2020, *The Astrophysical Journal*, 899, 24
- Fakhouri, O., Ma, C.-P., & Boylan-Kolchin, M. 2010, *MNRAS*, 406, 2267
- Faria, J. P., Santos, N. C., Figueira, P., & Brewer, B. J. 2018, *The Journal of Open Source Software*, 3, 487
- Feltzing, S., Howes, L. M., McMillan, P. J., & Stonkutė, E. 2017, *MNRAS*, 465, L109
- Ferraro, F. R., Mucciarelli, A., Lanzoni, B., et al. 2018, *ApJ*, 860, 50
- Fields, B. D. & Olive, K. A. 2022, *J. Cosmology Astropart. Phys.*, 2022, 078
- Fields, B. D., Olive, K. A., Yeh, T.-H., & Young, C. 2020, *J. Cosmology Astropart. Phys.*, 2020, 010
- Filomeno, S., Biazzo, K., Baratella, M., et al. 2024, *A&A*, 690, A370
- Fischer, C. F., Godefroid, M., Brage, T., Jónsson, P., & Gaigalas, G. 2016, *Journal of Physics B: Atomic, Molecular and Optical Physics*, 49, 182004
- Fischer, D. A. & Valenti, J. 2005, *ApJ*, 622, 1102
- Fishlock, C. K., Yong, D., Karakas, A. I., et al. 2017, *MNRAS*, 466, 4672
- Fitzpatrick, M., Placco, V., Bolton, A., et al. 2024, *arXiv e-prints*, arXiv:2401.01982
- Folsom, C. P., Bouvier, J., Petit, P., et al. 2018, *MNRAS*, 474, 4956
- Fontes, C. J., Fryer, C. L., & Hungerford, A. L. 2017, in *AIP Conference Proceedings*, Vol. 1811 (American Institute of Physics Inc.)
- Fontes, C. J., Fryer, C. L., Hungerford, A. L., Wollaeger, R. T., & Korobkin, O. 2020, *Monthly Notices of the Royal Astronomical Society*, 493, 4143
- Forbes, D. A. & Bridges, T. 2010, *MNRAS*, 404, 1203
- Fortney, J. J., Marley, M. S., & Barnes, J. W. 2007, *ApJ*, 659, 1661
- Frebel, A., Christlieb, N., Norris, J. E., et al. 2007, *ApJ*, 660, L117
- Freeman, K. & Bland-Hawthorn, J. 2002, *ARA&A*, 40, 487
- Freytag, B., Steffen, M., Ludwig, H. G., et al. 2012, *Journal of Computational Physics*, 231, 919
- Fröhlich, C., Martínez-Pinedo, G., Liebendörfer, M., et al. 2006, *Phys. Rev. Lett.*, 96, 142502
- Gaia Collaboration, Vallenari, A., Brown, A. G. A., et al. 2023, *A&A*, 674, A1
- Gaidos, E., Mann, A. W., Rizzuto, A., et al. 2017, *MNRAS*, 464, 850
- Gaigalas, G., Kato, D., Rynkun, P., Rada, L., & Tanaka, M. 2019, *The Astrophysical Journal Supplement Series*, 240, 29
- Gallagher, A. J., Ryan, S. G., Hosford, A., et al. 2012, *A&A*, 538, A118
- Gallet, F. & Bouvier, J. 2013, *A&A*, 556, A36
- Gallet, F. & Bouvier, J. 2015, *A&A*, 577, A98
- Gallet, F., Zanni, C., & Amard, L. 2019, *A&A*, 632, A6
- Gao, X., Lind, K., Amarsi, A. M., et al. 2018, *MNRAS*, 481, 2666
- Gerber, J. M., Magg, E., Plez, B., et al. 2023, *A&A*, 669, A43
- Ghosh, N. & Sharma, L. 2026, *Radiation Physics and Chemistry*, 239, 113273
- Gibson, R. R., Jiang, L., Brandt, W. N., et al. 2009, *ApJ*, 692, 758
- Gieles, M., Padoan, P., Charbonnel, C., Vink, J. S., & Ramírez-Galeano, L. 2025, *MNRAS*, 544, 483
- Gieles, M. & Zocchi, A. 2015, *MNRAS*, 454, 576
- Gilliland, R. L., Brown, T. M., Guhathakurta, P., et al. 2000, *ApJ*, 545, L47
- Gilmore, G., Randich, S., Worley, C. C., et al. 2022, *A&A*, 666, A120

- Giribaldi, R. E., da Silva, A. R., Smiljanic, R., & Cornejo Espinoza, D. 2021, *A&A*, 650, A194
- Giribaldi, R. E., Magrini, L., Schiappacasse-Ulloa, J., Randich, S., & Merle, T. 2025, *A&A*, 702, A65
- Giribaldi, R. E. & Smiljanic, R. 2023, *Experimental Astronomy*, 55, 117
- Giribaldi, R. E., Ubaldo-Melo, M. L., Porto de Mello, G. F., et al. 2019, *A&A*, 624, A10
- Giribaldi, R. E., Van Eck, S., Merle, T., et al. 2023, *A&A*, 679, A110
- Giribaldi, R. E., Vescovi, D., Magrini, L., et al. 2026, arXiv e-prints, arXiv:2605.11074
- Gomes da Silva, J., Bensabat, A., Monteiro, T., & Santos, N. C. 2022, *A&A*, 668, A174
- Gomes da Silva, J., Santos, N. C., Adibekyan, V., et al. 2021, *A&A*, 646, A77
- Gonzalez, G. 2015, *MNRAS*, 446, 1020
- Gonzalez, O. A., Mucciarelli, A., Origlia, L., et al. 2020, *The Messenger*, 180, 18
- González Picos, D., Snellen, I., & de Regt, S. 2025, *Nature Astronomy*, arXiv:2508.18424
- Goriely, S., Bauswein, A., & Janka, H.-T. 2011, *ApJ*, 738, L32
- Goupil, M. J., Catala, C., Samadi, R., et al. 2024, *A&A*, 683, A78
- Gratton, R., Bragaglia, A., Carretta, E., et al. 2019, *A&A Rev.*, 27, 8
- Gratton, R., Sneden, C., & Carretta, E. 2004, *ARA&A*, 42, 385
- Gratton, R. G., Bonifacio, P., Bragaglia, A., et al. 2001, *A&A*, 369, 87
- Gratton, R. G., Carretta, E., & Bragaglia, A. 2012, *A&A Rev.*, 20, 50
- Gravity Collaboration, Garcia Lopez, R., Natta, A., et al. 2020, *Nature*, 584, 547
- Gray, D. F. 1977, *ApJ*, 218, 530
- Green, G. M., Schlafly, E., Zucker, C., Speagle, J. S., & Finkbeiner, D. 2019, *ApJ*, 887, 93
- Gregory, S. G., Adams, F. C., & Davies, C. L. 2016, *MNRAS*, 457, 3836
- Griffith, E., Weinberg, D. H., Johnson, J. A., et al. 2021, *ApJ*, 909, 77
- Gruyters, P., Nordlander, T., & Korn, A. J. 2014, *A&A*, 567, A72
- Gu, M. F. 2008, *Canadian Journal of Physics*, 86, 675
- Gustafsson, B. 2025, *A&A Rev.*, 33, 3
- Gustafsson, B., Edvardsson, B., Eriksson, K., et al. 2008, *A&A*, 486, 951
- Häberle, M., Neumayer, N., Seth, A., et al. 2024, *Nature*, 631, 285
- Hamann, F. W., Barlow, T. A., Chaffee, F. C., Foltz, C. B., & Weymann, R. J. 2001, *ApJ*, 550, 142
- Hamers, A. S. & Tremaine, S. 2017, *AJ*, 154, 272
- Hammer, F., Barbuy, B., Cuby, J. G., et al. 2014, in *Society of Photo-Optical Instrumentation Engineers (SPIE) Conference Series*, Vol. 9147, *Ground-based and Airborne Instrumentation for Astronomy V*, ed. S. K. Ramsay, I. S. McLean, & H. Takami, 914727
- Hammer, F., Morris, S., Cuby, J.-G., et al. 2021, *The Messenger*, 182, 33
- Hansen, C. J., El-Souri, M., Monaco, L., et al. 2018, *ApJ*, 855, 83
- Hansen, C. J., Montes, F., & Arcones, A. 2014, *ApJ*, 797, 123
- Harris, W. E. 1996, *AJ*, 112, 1487
- Harris, W. E. 2010, arXiv e-prints, arXiv:1012.3224
- Hartman, H., Engstrom, L., Lundberg, H., et al. 2017, *Astronomy and Astrophysics*, 600
- Hartman, H., Nilsson, H., Engstrom, L., & Lundberg, H. 2015, *Astronomy and Astrophysics*, 584
- Hartman, J. D., Bakos, G. Á., Torres, G., et al. 2009, *ApJ*, 706, 785
- Hartmann, L., Herczeg, G., & Calvet, N. 2016, *ARA&A*, 54, 135
- Hartog, E. A., Palmer, A. J., & Lawler, J. E. 2015, *Journal of Physics B: Atomic, Molecular and Optical Physics*, 48
- Hartog, E. A. D., Lawler, J. E., & Roederer, I. U. 2020, *The Astrophysical Journal Supplement Series*, 248, 10

- Hartog, E. A. D., Lawler, J. E., & Roederer, I. U. 2021, *The Astrophysical Journal Supplement Series*, 254, 5
- Haywood, M., Di Matteo, P., Lehnert, M. D., Katz, D., & Gómez, A. 2013, *A&A*, 560, A109
- Heger, A. & Woosley, S. E. 2002, *ApJ*, 567, 532
- Heggie, D. C. 2014, *MNRAS*, 445, 3435
- Heise, C., Hollandt, J., Kling, R., Kock, M., & Kühne, M. 1994, *Applied Optics*, 33, 5111
- Helled, R., Bodenheimer, P., Podolak, M., et al. 2014, in *Protostars and Planets VI*, ed. H. Beuther, R. S. Klessen, C. P. Dullemond, & T. Henning, 643–665
- Helmi, A., Babusiaux, C., Koppelman, H. H., et al. 2018, *Nature*, 563, 85
- Helmi, A., White, S. D. M., de Zeeuw, P. T., & Zhao, H. 1999, *Nature*, 402, 53
- Hénault-Brunet, V., Gieles, M., Agertz, O., & Read, J. I. 2015, *MNRAS*, 450, 1164
- Hill, V., Christlieb, N., Beers, T. C., et al. 2017, *A&A*, 607, A91
- Hill, V., Lecureur, A., Gómez, A., et al. 2011, *A&A*, 534, A80
- Hill, V., Plez, B., Cayrel, R., et al. 2002, *A&A*, 387, 560
- Hill, V., Skúladóttir, Á., Tolstoy, E., et al. 2019, *A&A*, 626, A15
- Hirano, S., Hosokawa, T., Yoshida, N., et al. 2014, *ApJ*, 781, 60
- Holmbeck, E. M., Beers, T. C., Roederer, I. U., et al. 2018, *ApJ*, 859, L24
- Holmes, C. E., Pickering, J. C., Ruffoni, M. P., et al. 2016, *The Astrophysical Journal Supplement Series*, 224, 35
- Homma, D., Chiba, M., Komiyama, Y., et al. 2024, *PASJ*, 76, 733
- Hoppe, R., Bergemann, M., Eitner, P., et al. 2026, *MNRAS*, 546, staf2085
- Horta, D., Schiavon, R. P., Mackereth, J. T., et al. 2023, *MNRAS*, 520, 5671
- Hoyle, F. 1946, *MNRAS*, 106, 343
- Hunt, E. L. & Reffert, S. 2023, *A&A*, 673, A114
- Ibata, R., Malhan, K., Martin, N., et al. 2021, *ApJ*, 914, 123
- Ibata, R. A., Gilmore, G., & Irwin, M. J. 1994, *Nature*, 370, 194
- Ibata, R. A., Gilmore, G., & Irwin, M. J. 1995, *MNRAS*, 277, 781
- Ida, S. & Lin, D. N. C. 2004, *ApJ*, 616, 567
- Inoue, S., Maehara, H., Notsu, Y., et al. 2023, *ApJ*, 948, 9
- Israelian, G., Delgado Mena, E., Santos, N. C., et al. 2009, *Nature*, 462, 189
- Israelian, G. & Rebolo, R. 2001, *ApJ*, 557, L43
- Israelian, G., Santos, N. C., Mayor, M., & Rebolo, R. 2004, *A&A*, 414, 601
- Ivanova, N., Belczynski, K., Fregeau, J. M., & Rasio, F. A. 2005, *MNRAS*, 358, 572
- Jardine, M. & Collier Cameron, A. 2019, *MNRAS*, 482, 2853
- Jardine, M., Collier Cameron, A., Donati, J. F., & Hussain, G. A. J. 2020, *MNRAS*, 491, 4076
- Jeffers, S. V., Donati, J. F., & Collier Cameron, A. 2007, *MNRAS*, 375, 567
- Jeffries, R. D. 1993, *MNRAS*, 262, 369
- Jeffries, R. D., Jackson, R. J., Briggs, K. R., Evans, P. A., & Pye, J. P. 2011, *MNRAS*, 411, 2099
- Jin, S., Trager, S. C., Dalton, G. B., et al. 2022, *arXiv e-prints*, arXiv:2212.03981
- Jofré, P., Jackson, H., & Tucci Maia, M. 2020, *A&A*, 633, L9
- Johansson, S., Derkach, A., Donnelly, M. P., et al. 2002, *Phys. Scr*, 71
- Johnson, J. A., Dong, S., & Gould, A. 2010, *ApJ*, 713, 713
- Jones, M. I., Brahm, R., Espinoza, N., et al. 2018, *A&A*, 613, A76
- Jones, M. I., Jenkins, J. S., Brahm, R., et al. 2016a, *A&A*, 590, A38
- Jones, M. I., Wittenmyer, R., Aguilera-Gómez, C., et al. 2021, *A&A*, 646, A131

- Jones, S., Ritter, C., Herwig, F., et al. 2016b, *MNRAS*, 455, 3848
- Jönsson, P., Gaigalas, G., Bieroń, J., Froese Fischer, C., & Grant, I. P. 2013, *Computer Physics Communications*, 184, 2197
- Jorissen, A., Van Winckel, H., Siess, L., et al. 2020, *A&A*, 639, A7
- Jung, M., Roca-Fàbrega, S., Kim, J.-H., et al. 2024, *ApJ*, 964, 123
- Kacharov, N., Koch, A., Caffau, E., & Sbordone, L. 2015, *A&A*, 577, A18
- Kamann, S., Husser, T. O., Dreizler, S., et al. 2018, *MNRAS*, 473, 5591
- Kanehisa, K. J., Pawlowski, M. S., Heesters, N., & Müller, O. 2024, *A&A*, 686, A280
- Käppeler, F., Gallino, R., Bisterzo, S., & Aoki, W. 2011, *Reviews of Modern Physics*, 83, 157
- Karakas, A. I. & Lattanzio, J. C. 2014, *PASA*, 31, e030
- Kasen, D., Metzger, B., Barnes, J., Quataert, E., & Ramirez-Ruiz, E. 2017, *Nature*, 551, 80
- Katz, D., Sartoretti, P., Guerrier, A., et al. 2023, *A&A*, 674, A5
- Kawaler, S. D. 1988, *ApJ*, 333, 236
- King, G. W. & Wheatley, P. J. 2021, *MNRAS*, 501, L28
- Kirby, E. N., Lanfranchi, G. A., Simon, J. D., Cohen, J. G., & Guhathakurta, P. 2011, *ApJ*, 727, 78
- Kirby, E. N., Xie, J. L., Guo, R., et al. 2019, *ApJ*, 881, 45
- Klessen, R. S. & Glover, S. C. O. 2023, *ARA&A*, 61, 65
- Klose, J. Z., Fuhr, J. R., & Wiese, W. L. 2002, *Journal of Physical and Chemical Reference Data*, 31, 217–230
- Kobayashi, C., Karakas, A. I., & Lugaro, M. 2020, *ApJ*, 900, 179
- Kobayashi, C., Mandel, I., Belczynski, K., et al. 2023, *ApJ*, 943, L12
- Koch, A. & Caffau, E. 2011, *A&A*, 534, A52
- Kodangil, S., Domoto, N., Tanaka, M., et al. 2024, *Journal of Quantitative Spectroscopy and Radiative Transfer*, 322, 109011
- Kodangil, S., Tanaka, M., Kato, D., et al. 2025, *European Physical Journal D*, 79
- Kodangil, S., Tanaka, M., Kato, D., et al. 2026, *Journal of Quantitative Spectroscopy and Radiative Transfer*, 348, 109692
- Koenigl, A. 1991, *ApJ*, 370, L39
- Koester, D., Gänsicke, B. T., & Farihi, J. 2014, *A&A*, 566, A34
- Konacki, M., Muterspaugh, M. W., Kulkarni, S. R., & Hełminiak, K. G. 2009, *ApJ*, 704, 513
- Kordopatis, G., Feuillet, D., Lehmann, C., et al. 2025, *A&A*, 703, A151
- Kordopatis, G., Hill, V., & Lind, K. 2023a, *A&A*, 674, A104
- Kordopatis, G., Schultheis, M., McMillan, P. J., et al. 2023b, *A&A*, 669, A104
- Kordopatis, G., Wyse, R. F. G., Gilmore, G., et al. 2015, *A&A*, 582, A122
- Korn, A. J., Grundahl, F., Richard, O., et al. 2006, *Nature*, 442, 657
- Korn, A. J., Grundahl, F., Richard, O., et al. 2007, *ApJ*, 671, 402
- Korotin, S. & Kučinskas, A. 2022, *A&A*, 657, L11
- Korotin, S. A. 2020, *Astronomy Letters*, 46, 541
- Korotin, S. A. & Kiselev, K. O. 2024, *Astronomy Reports*, 68, 1159
- Kostov, V. B., Moore, K., Tamayo, D., Jayawardhana, R., & Rinehart, S. A. 2016, *ApJ*, 832, 183
- Koutsouridou, I., Salvadori, S., & Skúladóttir, Á. 2024, *ApJ*, 962, L26
- Koutsouridou, I., Skúladóttir, Á., & Salvadori, S. 2025, *A&A*, 699, A32
- Kramida, A., Yu. Ralchenko, Reader, J., & and NIST ASD Team. 2024, *NIST Atomic Spectra Database (ver. 5.12)*, [Online]. Available: <https://physics.nist.gov/asd> [2025, November 17]. National Institute of Standards and Technology, Gaithersburg, MD.

- Kratz, K.-L., Farouqi, K., & Möller, P. 2014, *ApJ*, 792, 6
- Kuerster, M., Schmitt, J. H. M. M., & Cutispoto, G. 1994, *A&A*, 289, 899
- Kullmann, I., Goriely, S., Just, O., Bauswein, A., & Janka, H.-T. 2023, *MNRAS*, 523, 2551
- Kurucz, R. L. 2005, *Memorie della Societa Astronomica Italiana Supplementi*, 8, 14
- Kuske, J., Arcones, A., & Reichert, M. 2025, *ApJ*, 990, 37
- Lagae, C., Amarsi, A. M., & Lind, K. 2025, *A&A*, 697, A60
- Lagarde, N., Minkevičiūtė, R., Drazdauskas, A., et al. 2024, *A&A*, 684, A70
- Lagrange, A. M., Bonnefoy, M., Chauvin, G., et al. 2010, *Science*, 329, 57
- Lammers, C. & Winn, J. N. 2026, *AJ*, 171, 18
- Lanza, A. F. 2009, *A&A*, 505, 339
- Lardo, C., Salaris, M., Cassisi, S., et al. 2023, *A&A*, 669, A19
- Latour, M., Kamann, S., Martocchia, S., et al. 2025, *A&A*, 694, A248
- Lawler, J. E. & Den Hartog, E. A. 2019, *Journal of Quantitative Spectroscopy and Radiative Transfer*, 237, 106620
- Lawler, J. E., Schmidt, J. R., & Hartog, E. A. D. 2022, *The Astrophysical Journal Supplement Series*, 258, 27
- Ledda, S., Danielski, C., & Turrini, D. 2023, *A&A*, 675, A184
- Lee, C.-C., Webb, J. K., Carswell, R. F., & Milaković, D. 2021a, *MNRAS*, 504, 1787
- Lee, C.-C., Webb, J. K., Milaković, D., & Carswell, R. F. 2021b, *MNRAS*, 507, 27
- Leenaarts, J. & Carlsson, M. 2009, in *Astronomical Society of the Pacific Conference Series*, Vol. 415, *The Second Hinode Science Meeting: Beyond Discovery-Toward Understanding*, ed. B. Lites, M. Cheung, T. Magara, J. Mariska, & K. Reeves, 87
- Legnardi, M. V., Milone, A. P., Armillotta, L., et al. 2022, *MNRAS*, 513, 735
- Li, W., Amarsi, A. M., & Jönsson, P. 2026, *A&A*, 707, A141
- Li, W., Amarsi, A. M., Papoulia, A., Ekman, J., & Jönsson, P. 2021, *MNRAS*, 502, 3780
- Libralato, M., Bedin, L. R., Nardiello, D., & Piotto, G. 2016a, *MNRAS*, 456, 1137
- Libralato, M., Bellini, A., Vesperini, E., et al. 2022, *ApJ*, 934, 150
- Libralato, M., Nardiello, D., Bedin, L. R., et al. 2016b, *MNRAS*, 463, 1780
- Liggins, F. S., Pickering, J. C., Nave, G., et al. 2021a, *The Astrophysical Journal*, 907, 69
- Liggins, F. S., Pickering, J. C., Nave, G., Ward, J. W., & Tchang-Brillet, W. L. 2021b, *The Astrophysical Journal Supplement Series*, 252, 10
- Lillo-Box, J., Barrado, D., Moya, A., et al. 2014, *A&A*, 562, A109
- Limongi, M. & Chieffi, A. 2003, *ApJ*, 592, 404
- Lind, K. & Amarsi, A. M. 2024, *ARA&A*, 62, 475
- Lind, K., Asplund, M., & Barklem, P. S. 2009, *A&A*, 503, 541
- Lind, K., Nordlander, T., Wehrhahn, A., et al. 2022, *A&A*, 665, A33
- Liu, F., Yong, D., Asplund, M., et al. 2018, *A&A*, 614, A138
- Liu, N., Alexander, C. M. O., Meyer, B. S., et al. 2024, *ApJ*, 961, L22
- Lodders, K. 2003, *ApJ*, 591, 1220
- Lodders, K. 2010, in *Astrophysics and Space Science Proceedings*, Vol. 16, *Principles and Perspectives in Cosmochemistry*, ed. A. Goswami & B. E. Reddy, 379
- Lovis, C. & Mayor, M. 2007, *A&A*, 472, 657
- Lucertini, F., Monaco, L., Caffau, E., Bonifacio, P., & Mucciarelli, A. 2022, *A&A*, 657, A29
- Ludwig, H. G., Behara, N. T., Steffen, M., & Bonifacio, P. 2009, *A&A*, 502, L1
- Ludwig, H.-G., Caffau, E., Steffen, M., Bonifacio, P., & Sbordone, L. 2010, *A&A*, 509, A84

- Lugaro, M., Pignatari, M., Reifarh, R., & Wiescher, M. 2023, *Annual Review of Nuclear and Particle Science*, 73, 315
- Lundberg, H., Hartman, H., Engström, L., et al. 2016, *Monthly Notices of the Royal Astronomical Society*, 460, 356
- Lundqvist, M., Wahlgren, G. M., & Hill, V. 2007, *A&A*, 463, 693
- Maehara, H., Notsu, Y., Namekata, K., et al. 2021, *PASJ*, 73, 44
- Magic, Z., Collet, R., Asplund, M., et al. 2013, *A&A*, 557, A26
- Magrini, L., Bensby, T., Brucalassi, A., et al. 2023, arXiv e-prints, arXiv:2312.08270
- Magrini, L., Danielski, C., Bossini, D., et al. 2022, *A&A*, 663, A161
- Magrini, L., Vescovi, D., Casali, G., et al. 2021, *A&A*, 646, L2
- Majewski, S. R., Schiavon, R. P., Frinchaboy, P. M., et al. 2017, *AJ*, 154, 94
- Malavolta, L., Mayo, A. W., Loudon, T., et al. 2018, *AJ*, 155, 107
- Malavolta, L., Nascimbeni, V., Piotto, G., et al. 2016, *A&A*, 588, A118
- Mallinson, J. W. E., Lind, K., Amarsi, A. M., et al. 2022, *A&A*, 668, A103
- Mallinson, J. W. E., Lind, K., Amarsi, A. M., & Youakim, K. 2024, *A&A*, 687, A5
- Manara, C. F., Natta, A., Rosotti, G. P., et al. 2020, *A&A*, 639, A58
- Mann, A. W., Gaidos, E., Vanderburg, A., et al. 2017, *AJ*, 153, 64
- Mann, A. W., Vanderburg, A., Rizzuto, A. C., et al. 2018, *AJ*, 155, 4
- Manrique, J., Pace, D. M. D., Aguilera, J. A., & Aragón, C. 2025, *Spectrochimica Acta - Part B Atomic Spectroscopy*, 234
- Mantovan, G., Malavolta, L., Desidera, S., et al. 2024, *A&A*, 682, A129
- Marconi, A., Abreu, M., Adibekyan, V., et al. 2022a, in *Society of Photo-Optical Instrumentation Engineers (SPIE) Conference Series*, Vol. 12184, *Ground-based and Airborne Instrumentation for Astronomy IX*, ed. C. J. Evans, J. J. Bryant, & K. Motohara, 1218424
- Marconi, A., Abreu, M., Adibekyan, V., et al. 2022b, in *Society of Photo-Optical Instrumentation Engineers (SPIE) Conference Series*, Vol. 12184, *Ground-based and Airborne Instrumentation for Astronomy IX*, ed. C. J. Evans, J. J. Bryant, & K. Motohara, 1218424
- Marino, A. F., Milone, A. P., Karakas, A. I., et al. 2015, *MNRAS*, 450, 815
- Marino, A. F., Milone, A. P., Piotto, G., et al. 2009, *A&A*, 505, 1099
- Marino, A. F., Milone, A. P., Renzini, A., et al. 2019a, *MNRAS*, 487, 3815
- Marino, A. F., Milone, A. P., Sills, A., et al. 2019b, *ApJ*, 887, 91
- Marsh, T. R. 2001, in *Astrotomography, Indirect Imaging Methods in Observational Astronomy*, ed. H. M. J. Boffin, D. Steeghs, & J. Cuypers, Vol. 573 (Springer Berlin, Heidelberg), 1
- Martell, S. L., Simpson, J. D., Balasubramanian, A. G., et al. 2021, *MNRAS*, 505, 5340
- Martin, D. V. 2018, in *Handbook of Exoplanets*, ed. H. J. Deeg & J. A. Belmonte (Springer International Publishing), 156
- Martin, D. V., Triaud, A. H. M. J., Udry, S., et al. 2019, *A&A*, 624, A68
- Martocchia, S., Lardo, C., Rejkuba, M., et al. 2021, *MNRAS*, 505, 5389
- Mashonkina, L., Christlieb, N., & Eriksson, K. 2014, *A&A*, 569, A43
- Mashonkina, L., Pakhomov, Y., Sitnova, T., et al. 2023, *MNRAS*, 524, 3526
- Mashonkina, L., Ryabtsev, A., & Frebel, A. 2012, *A&A*, 540, A98
- Mashonkina, L., Sitnova, T., & Korotin, S. 2022, *Astronomy Letters*, 48, 303
- Massari, D., Koppelman, H. H., & Helmi, A. 2019, *A&A*, 630, L4
- Masseron, T., Plez, B., Van Eck, S., et al. 2014, *A&A*, 571, A47
- Matsuno, T., Amarsi, A. M., Carlos, M., & Nissen, P. E. 2024, *A&A*, 688, A72

- Matt, S. P., MacGregor, K. B., Pinsonneault, M. H., & Greene, T. P. 2012, *ApJ*, 754, L26
- Matteucci, F. 2021, *A&A Rev.*, 29, 5
- Matteucci, F., Molaro, P., & Vladilo, G. 1996, arXiv e-prints, astro
- Matteucci, F., Romano, D., Arcones, A., Korobkin, O., & Rosswog, S. 2014, *MNRAS*, 438, 2177
- Mayo, A. W., Dressing, C. D., Vanderburg, A., et al. 2023, *AJ*, 165, 235
- Mayor, M., Pepe, F., Queloz, D., et al. 2003, *The Messenger*, 114, 20
- Mayor, M. & Queloz, D. 1995, *Nature*, 378, 355
- McCann, M., Ballance, C. P., McNeill, F., Sim, S. A., & Ramsbottom, C. A. 2025, *MNRAS*, 540, 2923
- McConnachie, A. W. 2012, *AJ*, 144, 4
- McGinnis, P., Bouvier, J., & Gallet, F. 2020, *MNRAS*, 497, 2142
- McKenzie, M., Yong, D., Karakas, A. I., et al. 2024, *MNRAS*, 527, 7940
- Mérand, A., Andreani, P., Cirasuolo, M., et al. 2021, *The Messenger*, 184, 8
- Merrill, P. W. 1952, *ApJ*, 116, 21
- Mészáros, S., Martell, S. L., Shetrone, M., et al. 2015, *AJ*, 149, 153
- Meyer, B. S. & Truran, J. W. 2000, *Phys. Rep.*, 333, 1
- Michaud, G., Alecian, G., & Richer, J. 2015, *Atomic Diffusion in Stars* (Springer International Publishing)
- Miglio, A., Girardi, L., Grundahl, F., et al. 2021, *Experimental Astronomy*, 51, 963
- Miglio, A., Mosser, B., Girardi, L., et al. 2024, in 8th TESS/15th Kepler Asteroseismic Science Consortium Workshop, 51
- Milaković, D., Lee, C. C., Molaro, P., & Webb, J. K. 2023, in *Memorie della Societa Astronomica Italiana*, Vol. 94, 270
- Miller, D. R., Caiazzo, I., Heyl, J., et al. 2026, *ApJ*, 996, 69
- Milone, A. P. & Marino, A. F. 2022, *Universe*, 8, 359
- Milone, A. P., Marino, A. F., Piotto, G., et al. 2015, *ApJ*, 808, 51
- Milone, A. P., Piotto, G., Bedin, L. R., et al. 2012, *Memorie della Societa Astronomica Italiana Supplementi*, 19, 173
- Milone, A. P., Piotto, G., Renzini, A., et al. 2017, *MNRAS*, 464, 3636
- Minor, Q. E. 2013, *ApJ*, 779, 116
- Mishenina, T., Kovtyukh, V., Soubiran, C., & Adibekyan, V. Z. 2016, *MNRAS*, 462, 1563
- Mishenina, T., Pignatari, M., Gorbaneva, T., et al. 2022, *MNRAS*, 516, 3786
- Mochejska, B. J., Stanek, K. Z., Sasselov, D. D., et al. 2006, *AJ*, 131, 1090
- Mohorian, M., Kamath, D., Menon, M., et al. 2025, *PASA*, 42, e151
- Molaro, P., Aguado, D. S., Caffau, E., et al. 2023a, *A&A*, 679, A72
- Molaro, P., Izzo, L., Selvelli, P., et al. 2023b, *MNRAS*, 518, 2614
- Molero, M., Magrini, L., Matteucci, F., et al. 2023, *MNRAS*, 523, 2974
- Monaco, L., Boffin, H. M. J., Bonifacio, P., et al. 2014, *A&A*, 564, L6
- Montalto, M., Piotto, G., Desidera, S., et al. 2007, *A&A*, 470, 1137
- Monty, S., Belokurov, V., Sanders, J. L., et al. 2024, *MNRAS*, 533, 2420
- Morbidelli, A., Lunine, J. I., O'Brien, D. P., Raymond, S. N., & Walsh, K. J. 2012, *Annual Review of Earth and Planetary Sciences*, 40, 251
- Morel, T. & Miglio, A. 2012, *MNRAS*, 419, L34
- Morel, T., Miglio, A., Lagarde, N., et al. 2014, *A&A*, 564, A119
- Moresco, M., Amati, L., Amendola, L., et al. 2022, *Living Reviews in Relativity*, 25, 6
- Mori, A., Di Matteo, P., Salvadori, S., et al. 2025, arXiv e-prints, arXiv:2509.13408

- Mösta, P., Roberts, L. F., Halevi, G., et al. 2018, *ApJ*, 864, 171
- Mucciarelli, A., Bellazzini, M., Ibata, R., et al. 2012a, *MNRAS*, 426, 2889
- Mucciarelli, A., Salaris, M., & Bonifacio, P. 2012b, *MNRAS*, 419, 2195
- Mulholland, L. P., McElroy, N. E., McNeill, F. L., et al. 2024, *Monthly Notices of the Royal Astronomical Society*, 532, 2289
- Mustill, A. J. & Villaver, E. 2012, *ApJ*, 761, 121
- Mustill, A. J., Villaver, E., Veras, D., Gänsicke, B. T., & Bonsor, A. 2018, *MNRAS*, 476, 3939
- Myers, N., Donor, J., Spoo, T., et al. 2022, *AJ*, 164, 85
- Naponiello, L., Bonomo, A. S., Mancini, L., et al. 2025, *A&A*, 693, A7
- Nardiello, D., Bedin, L. R., Nascimbeni, V., et al. 2015, *MNRAS*, 447, 3536
- Nardiello, D., Borsato, L., Piotto, G., et al. 2019, *MNRAS*, 490, 3806
- Nardiello, D., Libralato, M., Bedin, L. R., et al. 2016, *MNRAS*, 463, 1831
- Nardiello, D., Malavolta, L., Desidera, S., et al. 2022, *A&A*, 664, A163
- Nardiello, D., Piotto, G., Deleuil, M., et al. 2020, *MNRAS*, 495, 4924
- Nascimbeni, V., Bedin, L. R., Piotto, G., De Marchi, F., & Rich, R. M. 2012, *A&A*, 541, A144
- Nascimbeni, V., Piotto, G., Cabrera, J., et al. 2025, *A&A*, 694, A313
- Nave, G. & Clear, C. 2021, *Monthly Notices of the Royal Astronomical Society*, 502, 5679
- Newton, E. R., Mann, A. W., Kraus, A. L., et al. 2021, *AJ*, 161, 65
- Newton, E. R., Mann, A. W., Tofflemire, B. M., et al. 2019, *ApJ*, 880, L17
- Nguyen, C. T., Cescutti, G., Matteucci, F., et al. 2025, *A&A*, 703, A204
- Nguyen, M. & Adibekyan, V. 2025, *AJ*, 170, 334
- Nilsson, H., Andersson, J., Engstrom, L., Lundberg, H., & Hartman, H. 2019, *Astronomy and Astrophysics*, 622
- Nilsson, H., Zhang, Z. G., Lundberg, H., Johansson, S., & Nordstrom, B. 2002, *Astronomy and Astrophysics*, 382, 368
- Nissen, P. E. 2015, *A&A*, 579, A52
- Nissen, P. E., Akerman, C., Asplund, M., et al. 2007, *A&A*, 469, 319
- Nissen, P. E., Amarsi, A. M., Skúladóttir, Á., & Schuster, W. J. 2024, *A&A*, 682, A116
- Nissen, P. E., Chen, Y. Q., Asplund, M., & Pettini, M. 2004, *A&A*, 415, 993
- Nissen, P. E., Chen, Y. Q., Carigi, L., Schuster, W. J., & Zhao, G. 2014, *A&A*, 568, A25
- Nissen, P. E. & Gustafsson, B. 2018, *A&A Rev.*, 26, 6
- Nissen, P. E. & Schuster, W. J. 2010, *A&A*, 511, L10
- Nissen, P. E. & Schuster, W. J. 2011, *A&A*, 530, A15
- Nomoto, K., Kobayashi, C., & Tominaga, N. 2013, *ARA&A*, 51, 457
- Nordlander, T., Baratella, M., Spina, L., & D’Orazi, V. 2024, *MNRAS*, 535, 2863
- Nordlander, T., Korn, A. J., Richard, O., & Lind, K. 2012, *ApJ*, 753, 48
- Nordlund, Å., Ramsey, J. P., Popovas, A., & Küffmeier, M. 2018, *MNRAS*, 477, 624
- Norris, J. E., Bessell, M. S., Yong, D., et al. 2013, *ApJ*, 762, 25
- Noyes, R. W., Hartmann, L. W., Baliunas, S. L., Duncan, D. K., & Vaughan, A. H. 1984, *ApJ*, 279, 763
- Nunnari, A., D’Orazi, V., Fiorentino, G., et al. 2025, *arXiv e-prints*, arXiv:2511.22491
- Odert, P., Leitzinger, M., Hanslmeier, A., & Lammer, H. 2017, *MNRAS*, 472, 876
- Oliveira, R. A. P., Souza, S. O., Kerber, L. O., et al. 2020, *ApJ*, 891, 37
- Önehag, A., Gustafsson, B., & Korn, A. 2014, *A&A*, 562, A102
- Orosz, J. A., Welsh, W. F., Carter, J. A., et al. 2012, *Science*, 337, 1511
- Osterbrock, D. E. & Ferland, G. J. 2006, *Astrophysics of gaseous nebulae and active galactic nuclei*

(University Science Books)

- Owen, J. E. & Wu, Y. 2013, *ApJ*, 775, 105
- Pöder, S., Pata, J., Benito, M., Alonso Asensio, I., & Dalla Vecchia, C. 2025, *A&A*, 693, A227
- Pacetti, E., Schisano, E., Turrini, D., et al. 2025, *A&A*, 701, A194
- Pacetti, E., Turrini, D., Schisano, E., et al. 2022, *ApJ*, 937, 36
- Palanque-Delabrouille, N., Magneville, C., Yèche, C., et al. 2016, *A&A*, 587, A41
- Palla, M., Molero, M., Romano, D., & Mucciarelli, A. 2025, *A&A*, 699, A209
- Pancino, E., Romano, D., Tang, B., et al. 2017, *A&A*, 601, A112
- Pascucci, I., Cabrit, S., Edwards, S., et al. 2022, arXiv e-prints, arXiv:2203.10068
- Pascucci, I., Testi, L., Herczeg, G. J., et al. 2016, *ApJ*, 831, 125
- Pasquini, L., Brucalassi, A., Ruiz, M. T., et al. 2012, *A&A*, 545, A139
- Patel, A., Metzger, B. D., Cehula, J., et al. 2025, *ApJ*, 984, L29
- Paxton, B., Bildsten, L., Dotter, A., et al. 2011, *ApJS*, 192, 3
- Paxton, B., Cantiello, M., Arras, P., et al. 2013, *ApJS*, 208, 4
- Paxton, B., Marchant, P., Schwab, J., et al. 2015, *ApJS*, 220, 15
- Pehlivan, A., Nilsson, H., & Hartman, H. 2015, *Astronomy and Astrophysics*, 582
- Penny, M. T., Gaudi, B. S., Kerins, E., et al. 2019, *ApJS*, 241, 3
- Penoyre, Z., Belokurov, V., & Evans, N. W. 2022, *MNRAS*, 513, 5270
- Pepe, F., Cristiani, S., Rebolo, R., et al. 2021, *A&A*, 645, A96
- Pepe, F., Mayor, M., Galland, F., et al. 2002, *A&A*, 388, 632
- Perets, H. B. 2010, arXiv e-prints, arXiv:1001.0581
- Perryman, M., Hartman, J., Bakos, G. Á., & Lindegren, L. 2014, *ApJ*, 797, 14
- Pian, E., D'Avanzo, P., Benetti, S., et al. 2017, *Nature*, 551, 67
- Pignatari, M., Gallino, R., Heil, M., et al. 2010, *ApJ*, 710, 1557
- Pignatari, M., Herwig, F., Hirschi, R., et al. 2016, *ApJS*, 225, 24
- Pignatari, M., Zinner, E., Hoppe, P., et al. 2015, *ApJ*, 808, L43
- Pillitteri, I., Wolk, S. J., Sciortino, S., & Antoci, V. 2014, *A&A*, 567, A128
- Piotto, G., Bedin, L. R., Anderson, J., et al. 2007, *ApJ*, 661, L53
- Pirani, S., Johansen, A., Bitsch, B., Mustill, A. J., & Turrini, D. 2019, *A&A*, 623, A169
- Piskunov, N. & Valenti, J. A. 2017, *A&A*, 597, A16
- Placco, V. M., Holmbeck, E. M., Frebel, A., et al. 2017, *ApJ*, 844, 18
- Plez, B. 2012, *Turbospectrum: Code for spectral synthesis*
- Pollack, J. B., Hubickyj, O., Bodenheimer, P., et al. 1996, *Icarus*, 124, 62
- Polychroni, D., Turrini, D., & Pirani, S. 2023, *GroMiT: Planet Growth and Migration Track code*
- Poppenhaeger, K. & Wolk, S. J. 2014, *A&A*, 565, L1
- Prantzos, N., Aubert, O., & Audouze, J. 1996, *A&A*, 309, 760
- Prantzos, N., Charbonnel, C., & Iliadis, C. 2007, *A&A*, 470, 179
- Przyłuski, R., Rickman, H., Wajer, P., et al. 2025, *Universe*, 11, 240
- Queloz, D., Allain, S., Mermilliod, J. C., Bouvier, J., & Mayor, M. 1998, *A&A*, 335, 183
- Queloz, D., Henry, G. W., Sivan, J. P., et al. 2001, *A&A*, 379, 279
- Quinet, P., Fivet, V., Palmeri, P., et al. 2016, *Monthly Notices of the Royal Astronomical Society*, 462, 3912
- Rajpaul, V., Aigrain, S., Osborne, M. A., Reece, S., & Roberts, S. 2015, *MNRAS*, 452, 2269
- Ralchenko, Y., Fontes, C. J., et al. 2021, *NIST-LANL Lanthanide/Actinide Opacity Database*, National Institute of Standards and Technology and Los Alamos National Laboratory

- Ramírez, S. H., Gänsicke, B. T., Koester, D., Lafarga, M., & Gentile-Fusillo, N. P. 2025, *MNRAS*, 539, 2884
- Randich, S. 2019, in *The Very Large Telescope in 2030*, 11
- Randich, S., Bianco, A., Caito, L., et al. 2026, in *VLT Beyond 2030*, 44
- Randich, S., Gilmore, G., Magrini, L., et al. 2022, *A&A*, 666, A121
- Rastello, S., Carraro, G., & Capuzzo-Dolcetta, R. 2020, *ApJ*, 896, 152
- Rauer, H., Catala, C., Aerts, C., et al. 2014, *Experimental Astronomy*, 38, 249
- Reggiani, H., Amarsi, A. M., Lind, K., et al. 2019, *A&A*, 627, A177
- Rehse, S. J. & Ryder, C. A. 2009, *Spectrochimica Acta - Part B Atomic Spectroscopy*, 64, 974
- Reichert, M., Hansen, C. J., Hanke, M., et al. 2020, *A&A*, 641, A127
- Reichert, M., Obergaulinger, M., Aloy, M. Á., et al. 2023, *MNRAS*, 518, 1557
- Rein, H. & Liu, S.-F. 2012, *A&A*, 537, A128
- Reiners, A. & Mohanty, S. 2012, *ApJ*, 746, 43
- Reiners, A., Schüssler, M., & Passegger, V. M. 2014, *ApJ*, 794, 144
- Réville, V., Brun, A. S., Matt, S. P., Strugarek, A., & Pinto, R. F. 2015, *ApJ*, 798, 116
- Rhodin, A. P., Belmonte, M. T., Engstrom, L., et al. 2017, *Monthly Notices of the Royal Astronomical Society*, 472, 3337
- Richard, O., Michaud, G., & Richer, J. 2005, *ApJ*, 619, 538
- Ricker, G. R., Winn, J. N., Vanderspek, R., et al. 2015, *Journal of Astronomical Telescopes, Instruments, and Systems*, 1, 014003
- Rickman, H., Wajer, P., Przyłuski, R., et al. 2023, *MNRAS*, 520, 637
- Rigault, M., Brinnel, V., Aldering, G., et al. 2020, *A&A*, 644, A176
- Riva, M., Bianco, A., Randich, S., et al. 2026, in *VLT Beyond 2030*, 54
- Rizzuti, F., Cescutti, G., Molaro, P., et al. 2025, *A&A*, 698, A118
- Rizzuto, A. C., Newton, E. R., Mann, A. W., et al. 2020, *AJ*, 160, 33
- Roberts, L. F., Woosley, S. E., & Hoffman, R. D. 2010, *ApJ*, 722, 954
- Rodríguez Díaz, L. F., Bigot, L., Aguirre Børsen-Koch, V., et al. 2022, *MNRAS*, 514, 1741
- Rodríguez Díaz, L. F., Lagae, C., Amarsi, A. M., et al. 2024, *A&A*, 688, A212
- Roederer, I. U. 2017, *ApJ*, 835, 23
- Roederer, I. U., Beers, T. C., Hattori, K., et al. 2024, *ApJ*, 971, 158
- Roederer, I. U., Karakas, A. I., Pignatari, M., & Herwig, F. 2016, *ApJ*, 821, 37
- Rogers, L. K., Debes, J., Anslow, R. J., et al. 2024, *MNRAS*, 527, 977
- Romano, D. 2022, *A&A Rev.*, 30, 7
- Romano, D. & Matteucci, F. 2003, *MNRAS*, 342, 185
- Rossi, M., Salvadori, S., & Skúladóttir, Á. 2021, *MNRAS*, 503, 6026
- Rossi, M., Salvadori, S., Skúladóttir, Á., Vanni, I., & Koutsouridou, I. 2025, *ApJ*, 987, 121
- Royer, P., Merle, T., Dsilva, K., et al. 2024, *A&A*, 681, A107
- Ruchti, G. R., Bergemann, M., Serenelli, A., Casagrande, L., & Lind, K. 2013, *MNRAS*, 429, 126
- Ruffoni, M. P., Hartog, E. A. D., Lawler, J. E., et al. 2014, *Monthly Notices of the Royal Astronomical Society*, 3127
- Rybicki, G. B. & Hummer, D. G. 1992, *A&A*, 262, 209
- Sackmann, I.-J. & Boothroyd, A. I. 1992, *ApJ*, 392, L71
- Saffe, C., Jofré, E., Martioli, E., et al. 2017, *A&A*, 604, L4
- Sairam, L., Triaud, A. H. M. J., Baycroft, T. A., et al. 2024, *MNRAS*, 527, 2261
- Salpeter, E. E. 1952, *ApJ*, 115, 326

- Salvadori, S., Bonifacio, P., Caffau, E., et al. 2019, *MNRAS*, 487, 4261
- Salvadori, S., Skúladóttir, Á., & Tolstoy, E. 2015, *MNRAS*, 454, 1320
- Saracino, S., Kamann, S., Usher, C., et al. 2020, *MNRAS*, 498, 4472
- Sarma, P. R. S., Belmonte, M. T., Llorente, S., & Mar, S. 2025, *Spectrochimica Acta Part B: Atomic Spectroscopy*, 107342
- Sarma, P. R. S., Belmonte, M. T., & Mar, S. 2024, *European Physical Journal D*, 78
- Sato, B., Izumiura, H., Toyota, E., et al. 2007, *ApJ*, 661, 527
- Saunders, N., Grunblatt, S. K., Huber, D., et al. 2025, *AJ*, 169, 75
- Savvidou, S. & Bitsch, B. 2023, *A&A*, 679, A42
- Sayeed, M., Ness, M. K., Montet, B. T., et al. 2024, *ApJ*, 964, 42
- Sbordone, L. 2005, *Memorie della Societa Astronomica Italiana Supplementi*, 8, 61
- Sbordone, L., Bonifacio, P., Castelli, F., & Kurucz, R. L. 2004, *Memorie della Societa Astronomica Italiana Supplementi*, 5, 93
- Sbordone, L., Limongi, M., Chieffi, A., et al. 2009, *A&A*, 503, 121
- Schatz, H., Becerril Reyes, A. D., Best, A., et al. 2022, *Journal of Physics G Nuclear Physics*, 49, 110502
- Schiappacasse-Ulloa, J., Lucatello, S., Rain, M. J., & Pietrinferni, A. 2022, *MNRAS*, 511, 231
- Schlegel, D. J., Finkbeiner, D. P., & Davis, M. 1998, *ApJ*, 500, 525
- Schmidt, S. P. & Schlafman, K. C. 2026, *AJ*, 171, 157
- Schmidt-May, A. F., Barklem, P. S., Grumer, J., et al. 2024, *Phys. Rev. A*, 109, 052820
- Schneider, A. 2015, *MNRAS*, 451, 3117
- Schofield, J., Pignatari, M., Stancliffe, R. J., & Hoppe, P. 2022, *MNRAS*, 517, 1803
- Schuessler, M. & Solanki, S. K. 1992, *A&A*, 264, L13
- See, V., Jardine, M., Vidotto, A. A., et al. 2018, *MNRAS*, 474, 536
- Shah, S. P., Ezzeddine, R., Holmbeck, E. M., et al. 2026a, arXiv e-prints, arXiv:2604.12892
- Shah, S. P., Ezzeddine, R., Holmbeck, E. M., et al. 2026b, arXiv e-prints, arXiv:2604.12892
- Siegel, D. M., Barnes, J., & Metzger, B. D. 2019, *Nature*, 569, 241
- Silva, R. F., Sampaio, J. M., Amaro, P., et al. 2022, *Atoms*, 10, 18
- Simon, J. D. 2019, *ARA&A*, 57, 375
- Singh, R., Reddy, B. E., Campbell, S. W., Kumar, Y. B., & Vvard, M. 2021, *ApJ*, 913, L4
- Sirono, S.-i. & Turrini, D. 2025, *Scientific Reports*, 15, 30919
- Sitnova, T. M., Lombardo, L., Mashonkina, L. I., et al. 2025, *A&A*, 699, A262
- Sitnova, T. M., Yakovleva, S. A., Belyaev, A. K., & Mashonkina, L. I. 2022, *MNRAS*, 515, 1510
- Skúladóttir, Á., Andrievsky, S. M., Tolstoy, E., et al. 2015, *A&A*, 580, A129
- Skúladóttir, Á., Ernandes, H., Feuillet, D. K., et al. 2025, *ApJ*, 986, L21
- Skúladóttir, Á., Hansen, C. J., Salvadori, S., & Choplin, A. 2019, *A&A*, 631, A171
- Skúladóttir, Á., Koutsouridou, I., Vanni, I., et al. 2024a, *ApJ*, 968, L23
- Skúladóttir, Á., Puls, A. A., Amarsi, A. M., et al. 2023, *The Messenger*, 190, 19
- Skúladóttir, Á. & Salvadori, S. 2020, *A&A*, 634, L2
- Skúladóttir, Á., Vanni, I., Salvadori, S., & Lucchesi, R. 2024b, *A&A*, 681, A44
- Skumanich, A. 1972, *ApJ*, 171, 565
- Smiljanic, R., Gauderon, R., North, P., et al. 2009, *A&A*, 502, 267
- Snedden, C., Cowan, J. J., & Gallino, R. 2008, *ARA&A*, 46, 241
- Snedden, C., McWilliam, A., Preston, G. W., et al. 1996, *ApJ*, 467, 819
- Solanki, S. K. & Unruh, Y. C. 2004, *MNRAS*, 348, 307

- Sollima, A. 2020, *MNRAS*, 495, 2222
- Sollima, A., Baumgardt, H., & Hilker, M. 2019, *MNRAS*, 485, 1460
- Souto, D., Allende Prieto, C., Cunha, K., et al. 2019, *ApJ*, 874, 97
- Sozzetti, A., Torres, G., Latham, D. W., et al. 2006, *ApJ*, 649, 428
- Spencer, M. E., Mateo, M., Olszewski, E. W., et al. 2018, *AJ*, 156, 257
- Spina, L., Nordlander, T., Casey, A. R., et al. 2020, *ApJ*, 895, 52
- Spina, L., Sharma, P., Meléndez, J., et al. 2021, *Nature Astronomy*, 5, 1163
- Standing, M. R., Barnes, J. R., Haswell, C. A., et al. 2026, *Monthly Notices of the Royal Astronomical Society*, 547
- Standing, M. R., Sairam, L., Martin, D. V., et al. 2023, *Nature Astronomy*, 7, 702
- Standing, M. R., TriAUD, A. H. M. J., Faria, J. P., et al. 2022, *MNRAS*, 511, 3571
- Stauffer, J. R., Caillault, J.-P., Gagne, M., Prosser, C. F., & Hartmann, L. W. 1994, *ApJS*, 91, 625
- Stein, R. F., Nordlund, Å., Collet, R., & Trampedach, R. 2024, *ApJ*, 970, 24
- Steinmetz, M., Matijević, G., Enke, H., et al. 2020, *AJ*, 160, 82
- Storm, N., Barklem, P. S., Yakovleva, S. A., et al. 2024, *A&A*, 683, A200
- Storm, N., Bergemann, M., Eitner, P., et al. 2025, *MNRAS*, 538, 3284
- Strassmeier, K. G. 2002, *Astronomische Nachrichten*, 323, 309
- Strassmeier, K. G. 2009, *A&A Rev.*, 17, 251
- Suárez-Andrés, L., Israelian, G., González Hernández, J. I., et al. 2016, *A&A*, 591, A69
- Suárez-Andrés, L., Israelian, G., González Hernández, J. I., et al. 2017, *A&A*, 599, A96
- Tabone, B., Rosotti, G. P., Cridland, A. J., Armitage, P. J., & Lodato, G. 2022, *MNRAS*, 512, 2290
- Takahashi, K., Yoshida, T., & Umeda, H. 2018, *ApJ*, 857, 111
- Takeda, Y. 1991, *A&A*, 242, 455
- Takeda, Y. & Takada-Hidai, M. 2011, *PASJ*, 63, 537
- Tanaka, M., Kato, D., Gaigalas, G., & Kawaguchi, K. 2020, *Monthly Notices of the Royal Astronomical Society*, 496, 1369
- Tanaka, M., Kato, D., Gaigalas, G., et al. 2018, *The Astrophysical Journal*, 852, 109
- Tanvir, N. R., Levan, A. J., González-Fernández, C., et al. 2017, *ApJ*, 848, L27
- Tassis, K., Gnedin, N. Y., & Kravtsov, A. V. 2012, *ApJ*, 745, 68
- Tatischeff, V. & Gabici, S. 2018, *Annual Review of Nuclear and Particle Science*, 68, 377
- Temple, L. Y., Hellier, C., Anderson, D. R., et al. 2019, *MNRAS*, 490, 2467
- Temple, M. J., Rankine, A. L., Banerji, M., et al. 2024, *MNRAS*, 532, 424
- Testi, L., Natta, A., Manara, C. F., et al. 2022, *A&A*, 663, A98
- Thibodeaux, P., Ji, A. P., Cerny, W., Kirby, E. N., & Simon, J. D. 2024, *The Open Journal of Astrophysics*, 7, 66
- Thompson, R. I. 1975, *Astrophys. Lett.*, 16, 3
- Thygesen, A. O., Kirby, E. N., Gallagher, A. J., et al. 2017, *ApJ*, 843, 144
- Thygesen, A. O., Sbordone, L., Ludwig, H.-G., et al. 2016, *A&A*, 588, A66
- Tiongco, M. A., Vesperini, E., & Varri, A. L. 2019, *MNRAS*, 487, 5535
- Tolstoy, E. 2019, in *The Very Large Telescope in 2030*, 8
- Tomasetti, E., Chiappini, C., Nepal, S., et al. 2026, *A&A*, 707, A111
- Townley-Smith, K., Nave, G., Pickering, J. C., & Blackwell-Whitehead, R. J. 2016, *Monthly Notices of the Royal Astronomical Society*, 461, 73
- Travaglio, C., Gallino, R., Busso, M., & Gratton, R. 2001, *ApJ*, 549, 346
- Tremblay, P.-E., Bédard, A., O'Brien, M. W., et al. 2024, *New A Rev.*, 99, 101705

- Trippe, S., Davies, R., Eisenhauer, F., et al. 2010, *MNRAS*, 402, 1126
- Tsantaki, M., Magrini, L., Danielski, C., et al. 2025, *A&A*, 697, A102
- Tsuji, T. 2016, *PASJ*, 68, 84
- Turrini, D. 2023, *The Compositional Dimension of Planet Formation* (World Scientific Publishing), 1–47
- Turrini, D., Codella, C., Danielski, C., et al. 2022, *Experimental Astronomy*, 53, 225
- Turrini, D., Miguel, Y., Zingales, T., et al. 2018, *Experimental Astronomy*, 46, 45
- Ubachs, W. 2018, *Space Sci. Rev.*, 214, 3
- Usman, S. A., Ji, A. P., Rodriguez, J., et al. 2025, *The Open Journal of Astrophysics*, 8, 86
- Uylings, P. & Raassen, T. 2019, *Atoms*, 7
- Uzan, J.-P. 2025, *Living Reviews in Relativity*, 28, 6
- Valenti, S., Sand, D. J., Yang, S., et al. 2017, *ApJ*, 848, L24
- Van der Swaelmen, M., Viscasillas Vázquez, C., Cescutti, G., et al. 2023, *A&A*, 670, A129
- Van Eck, S., Shetye, S., & Siess, L. 2022, *Universe*, 8, 220
- van Regemorter, H. 1962, *ApJ*, 136, 906
- Vanderburg, A., Rappaport, S. A., Xu, S., et al. 2020, *Nature*, 585, 363
- Vangioni, E. & Olive, K. A. 2019, *MNRAS*, 484, 3561
- Vanni, I., Salvadori, S., D’Odorico, V., Becker, G. D., & Cupani, G. 2024, *ApJ*, 967, L22
- Vanzella, E., Claeysens, A., Welch, B., et al. 2023, *ApJ*, 945, 53
- Vasiliev, E. & Baumgardt, H. 2021, *MNRAS*, 505, 5978
- Velichko, A. B., Mashonkina, L. I., & Nilsson, H. 2011, *Astronomy Letters*, 37, 440
- Ventura, P., D’Antona, F., Imbriani, G., et al. 2018, *MNRAS*, 477, 438
- Ventura, P., D’Antona, F., Mazzitelli, I., & Gratton, R. 2001, *ApJ*, 550, L65
- Veras, D. 2016, *Royal Society Open Science*, 3, 150571
- Veras, D. 2021, in *Oxford Research Encyclopedia of Planetary Science* (Oxford University Press), 1
- Veras, D., Tremblay, P.-E., Hermes, J. J., et al. 2020, *MNRAS*, 493, 765
- Veras, D., Wyatt, M. C., Mustill, A. J., Bonsor, A., & Eldridge, J. J. 2011, *MNRAS*, 417, 2104
- Vidotto, A. A., Gregory, S. G., Jardine, M., et al. 2014, *MNRAS*, 441, 2361
- Vietri, G., Rodríguez Hidalgo, P., Rankine, A., et al. 2025, *A&A*, 704, A166
- Villaver, E. & Livio, M. 2007, *ApJ*, 661, 1192
- Viscasillas Vázquez, C., Magrini, L., Casali, G., et al. 2022, *A&A*, 660, A135
- Vogt, S. S., Allen, S. L., Bigelow, B. C., et al. 1994, in *Society of Photo-Optical Instrumentation Engineers (SPIE) Conference Series*, Vol. 2198, *Instrumentation in Astronomy VIII*, ed. D. L. Crawford & E. R. Craine, 362
- Vogt, S. S., Penrod, G. D., & Hatzes, A. P. 1987, *ApJ*, 321, 496
- Wagner-Carena, S., Lee, J., Pennington, J., et al. 2024, *ApJ*, 975, 297
- Wan, Z., Oliver, W. H., Baumgardt, H., et al. 2021, *MNRAS*, 502, 4513
- Wang, E. X., Nordlander, T., Asplund, M., et al. 2021, *MNRAS*, 500, 2159
- Wang, L., Iwasawa, M., Nitadori, K., & Makino, J. 2020, *MNRAS*, 497, 536
- Ward, J. W., Li, J. J., Schwartz, J., et al. 2023, *The Astrophysical Journal*, 959, 8
- Watson, D., Hansen, C. J., Selsing, J., et al. 2019, *Nature*, 574, 497
- Waugh, R. F. P. & Jardine, M. M. 2022, *MNRAS*, 514, 5465
- Webb, J. K., Flambaum, V. V., Churchill, C. W., Drinkwater, M. J., & Barrow, J. D. 1999, *Phys. Rev. Lett.*, 82, 884
- Webb, J. K., Lee, C.-C., Carswell, R. F., & Milaković, D. 2021, *MNRAS*, 501, 2268

- Webb, J. K., Lee, C.-C., & Milaković, D. 2022, *Universe*, 8, 266
- Weber, E. J. & Davis, Leverett, J. 1967, *ApJ*, 148, 217
- Wehrhahn, A., Piskunov, N., & Ryabchikova, T. 2023, *A&A*, 671, A171
- Welsh, W. F., Orosz, J. A., Carter, J. A., et al. 2012, *Nature*, 481, 475
- Werk, J. K., Prochaska, J. X., Cantalupo, S., et al. 2016, *ApJ*, 833, 54
- Wheeler, A. J., Abruzzo, M. W., Casey, A. R., & Ness, M. K. 2023, *AJ*, 165, 68
- Wiedeking, M., Goriely, S., Guttormsen, M., et al. 2025, *Nature Reviews Physics*, 7, 696
- Wiescher, M., Görres, J., Uberseder, E., Imbriani, G., & Pignatari, M. 2010, *Annual Review of Nuclear and Particle Science*, 60, 381
- Wiese, W. L. & Martin, G. A. 1980, *Wavelengths and transition probabilities for atoms and atomic ions* :, Tech. rep., National Bureau of Standards
- Winn, J. N. & Fabrycky, D. C. 2015, *ARA&A*, 53, 409
- Wolthoff, V., Reffert, S., Quirrenbach, A., et al. 2022, *A&A*, 661, A63
- Wood, B. E., Müller, H. R., Zank, G. P., Linsky, J. L., & Redfield, S. 2005, *ApJ*, 628, L143
- Woosley, S. E. & Hoffman, R. D. 1992, *ApJ*, 395, 202
- Wright, N. J., Drake, J. J., Mamajek, E. E., & Henry, G. W. 2011, *ApJ*, 743, 48
- Wright, N. J., Newton, E. R., Williams, P. K. G., Drake, J. J., & Yadav, R. K. 2018, *MNRAS*, 479, 2351
- Xiao, G.-Y., Teng, H.-Y., Zhou, J., et al. 2024, *AJ*, 167, 59
- Xuan, J. W., Wang, J., Finnerty, L., et al. 2024, *ApJ*, 962, 10
- Yakovleva, S. A., Belyaev, A. K., & Bergemann, M. 2020, *Atoms*, 8, 34
- Yakovleva, S. A., Belyaev, A. K., & Mashonkina, L. I. 2022, *Atoms*, 10, 33
- Yan, T.-S., Shi, J.-R., Wang, L., et al. 2022, *ApJ*, 929, L14
- Yong, D., Aoki, W., & Lambert, D. L. 2006, *ApJ*, 638, 1018
- Yong, D., Grundahl, F., Lambert, D. L., Nissen, P. E., & Shetrone, M. D. 2003, *A&A*, 402, 985
- Yong, D., Kobayashi, C., Da Costa, G. S., et al. 2021, *Nature*, 595, 223
- Yong, D., Meléndez, J., Grundahl, F., et al. 2013, *MNRAS*, 434, 3542
- Yuce, K., Castelli, F., & Hubrig, S. 2011, *Astronomy and Astrophysics*, 528, 1
- Zatsarinny, O., Bartschat, K., Fernandez-Mencherero, L., & Tayal, S. S. 2019, *Phys. Rev. A*, 99, 023430
- Zhao, G., Zhao, Y.-H., Chu, Y.-Q., Jing, Y.-P., & Deng, L.-C. 2012, *Research in Astronomy and Astrophysics*, 12, 723
- Zhou, Y. T., Shi, J. R., Yan, H. L., et al. 2018, *A&A*, 615, A74
- Zuckerman, B., Melis, C., Klein, B., Koester, D., & Jura, M. 2010, *ApJ*, 722, 725

## Affiliations

- [1] INAF - Osservatorio Astrofisico di Arcetri, Largo E. Fermi 5, 50125 Firenze, Italy
- [2] Lund Observatory, Division of Astrophysics, Department of Physics, Lund University, Sweden
- [3] INAF - Osservatorio Astronomico di Brera, Via Bianchi 46, 23807, Merate, Italy
- [4] UK Astronomy Technology Centre, Edinburgh, United Kingdom
- [5] Facultad de Física, Universidad de La Laguna, Avda. Astrofísico Fco. Sánchez s/n, 38206, La Laguna, Santa Cruz de Tenerife, Spain
- [6] Instituto de Astrofísica de Canarias, C. Vía Láctea, s/n, 38205 La Laguna, Santa Cruz de Tenerife, Spain
- [7] Instituto de Astrofísica e Ciências do Espaço, Universidade do Porto, CAUP, Rua das Estrelas, 4150-762 Porto, Portugal
- [8] INAF- Direzione Scientifica- Viale del Parco Mellini, 84, Roma, Italy
- [9] Departamento de Física e Astronomia, FCUP, Rua do Campo Alegre 687, Porto, Portugal
- [10] Theoretical Astrophysics, Department of Physics and Astronomy, Uppsala University, Uppsala, Sweden
- [11] Departamento de Física Teórica, Atómica y Óptica, Universidad de Valladolid, Valladolid, Spain
- [12] Department of Physics, Imperial College London, London, UK
- [13] Departament d'Astronomia i Astrofísica, Universitat de València, Burjassot, Spain
- [14] Dept. of Physics, University of Rome Tor Vergata, Rome, Italy
- [15] Goethe University Frankfurt, Institute for Applied Physics, Max-von-Laue-Str. 12, 60438, Frankfurt am Main, Germany
- [16] Observatoire de la Côte d'Azur, Université Côte d'Azur, CNRS, Laboratoire Lagrange, Nice, France
- [17] Keele University, Keele, ST5 5BG, UK
- [18] Dipartimento di Fisica e Astronomia, Università di Bologna, Via Gobetti 93/2, Bologna, Italy
- [19] INAF - Osservatorio di Astrofisica e Scienza dello Spazio di Bologna, Via Gobetti 93/3, Bologna, Italy
- [20] INAF - Osservatorio Astronomico di Trieste, via Tiepolo 11, 34143, Trieste, Italy
- [21] IFPU – Institute for Fundamental Physics of the Universe, via Beirut 2, I-34151 Trieste, Italy
- [22] Dipartimento di Fisica e Astronomia, Università degli Studi di Firenze, Via G. Sansone 1, Sesto Fiorentino, Italy
- [23] Nicolaus Copernicus Astronomical Center, Polish Academy of Sciences, ul. Bartycka 18, Warsaw, Poland
- [24] Technische Universität Darmstadt, Department of Physics, 64289 Darmstadt, Germany
- [25] GSI Helmholtzzentrum für Schwerionenforschung GmbH, 64291 Darmstadt, Germany
- [26] Max-Planck-Institut für Kernphysik, Saupfercheckweg 1, 69117 Heidelberg, Germany
- [27] ESO European Southern Observatory, Alonso de Córdova 3107, Vitacura, Santiago, Chile
- [28] Universidade de São Paulo, IAG, Rua do Matão 1226, São Paulo, Brazil
- [29] School of Physical Sciences, The Open University, Walton Hall, Milton Keynes, MK7 6AA, UK
- [30] School of Mathematics and Physics, The University of Queensland, St Lucia, QLD 4072, Australia
- [31] INAF - Osservatorio Astronomico di Roma, Via Frascati 88, I-00040 Monte Porzio Catone (RM), Italy
- [32] Dipartimento di Fisica "Enrico Fermi", Università di Pisa, Largo Bruno Pontecorvo 3, Pisa, I-56127, Italy
- [33] Interdisciplinary Center for Scientific Computing (IWR), University of Heidelberg, Im Neuenheimer Feld 205, 69120, Heidelberg, Germany
- [34] Universität Heidelberg, Zentrum für Astronomie, Institut für Theoretische Astrophysik, Albert-Ueberle-Strasse 2, 69120, Heidelberg, Germany
- [35] Australian National University; ARC Centre of Excellence for All Sky Astrophysics in 3 Dimensions

(ASTRO 3D)

[36] Space sciences, Technologies and Astrophysics Research (STAR) Institute, Université de Liège, Liège, Belgium

[37] Dipartimento di Fisica, Università degli Studi di Trieste, via Tiepolo 11, 34143, Trieste, Italy

[38] SUPA School of Physics and Astronomy, University of St Andrews, North Haugh, St Andrews KY16 9SS, UK

[39] Centre for Extragalactic Astronomy, Durham University, South Road, Durham DH1 3LE, UK

[40] Department of Physics, Durham University, South Road, Durham DH1 3LE, UK

[41] INAF, Osservatorio Astronomico d'Abruzzo, Via Mentore Maggini Snc, 64100 Teramo, Italy

[42] Sezione di Perugia, Istituto Nazionale di Fisica Nucleare, Perugia, Italy

[43] INAF - Osservatorio Astronomico di Palermo G.S.Vaiana, Piazza del Parlamento 1, 90134, Palermo, Italy

[44] Vilnius University, Faculty of Physics, Institute of Theoretical Physics and Astronomy, Sauletekio av. 3, 10257 Vilnius, Lithuania

[45] INAF - Osservatorio Astrofisico di Catania, via S. Sofia, 78, 95128, Catania, Italy

[46] ICREA, Pg. Lluís Companys 28, E-08010 Barcelona, Spain; Institut de Ciències del Cosmos (ICCUB), Universitat de Barcelona (UB), c. Martí i Franques, 1, E-08028 Barcelona, Spain

[47] Institut d'Estudis Espacials de Catalunya (IEEC), Edifici RDIT, Campus UPC, E-08860 Castelldefels (Barcelona), Spain

[48] Department of Physics and Astronomy, University of Notre Dame, 225 Nieuwland Science Hall, Notre Dame, IN 46556, USA

[49] Department of Physics, University of Warwick, Gibbet Hill Road, Coventry CV4 7AL, UK

[50] Centre for Exoplanets and Habitability, University of Warwick, Gibbet Hill Road, Coventry CV4 7AL, UK

[51] Laboratoire d'Astrophysique de Bordeaux, Université Bordeaux, CNRS, B18N, Allée Geoffroy Saint-Hilaire, 33615, Pessac, France

[52] Dipartimento di Fisica e Astronomia "Galileo Galilei", Università degli Studi di Padova, Vicolo dell'Osservatorio 3, 35122 Padova, Italy

[53] Astronomisches Rechen-Institut, Zentrum für Astronomie der Universität Heidelberg, Mönchhofstraße 12-14, 69120, Heidelberg, Germany

[54] Institut d'Astronomie et d'Astrophysique, Université Libre de Bruxelles (ULB), CP 226, Boulevard du Triomphe, 1050, Bruxelles, Belgium

[55] Royal Observatory of Belgium, Avenue Circulaire 3, 1180 Brussels, Belgium

[56] Space Telescope Science Institute

[57] INAF - Osservatorio Astronomico di Padova, Vicolo dell'Osservatorio 5, 85122, Padova, Italy

[58] INAF - Osservatorio Astrofisico di Torino, Via Osservatorio 20, 10025, Pino Torinese (TO), Italy

[59] HUN REN Konkoly Observatory, CSFK, H-1121, Budapest, Konkoly Thege M. ut 15-17, Hungary

[60] CSFK, MTA Centre of Excellence, Budapest, Konkoly Thege Miklos ut 15-17, H-1121, Hungary

[61] University of Bayreuth, BGI, Universitätsstrasse 30, 95447 Bayreuth, Germany

[62] Heidelberger Institut für Theoretische Studien, Schloss-Wolfsbrunnenweg 35, D-69118 Heidelberg, Germany

[63] European Space Agency (ESA), European Space Astronomy Centre (ESAC), Camino Bajo del Castillo s/n, E-28692 Villanueva de la Cañada, Madrid, Spain

[64] Department of Astronomy, The Ohio State University, Columbus, OH 43210, USA

[65] Center for Cosmology and AstroParticle Physics (CCAPP), The Ohio State University, Columbus, OH

43210, USA

[66] Max-Planck-Institut für Astronomie, Königstuhl 17, D-69117 Heidelberg, Germany

[67] University of Victoria (Canada)

[68] School of Physical and Chemical Sciences - Te Kura Matu, University of Canterbury, Private Bag 4800, Christchurch, 8140, New Zealand

[69] Centre for Astrophysics Research, University of Hertfordshire, Hatfield, AL10 9AB, UK

[70] Department of Physics, University of Surrey, Stag Hill, Guildford, GU2 7XH, UK

[71] Department of Astrophysics, University of Vienna, Turkenschanzstrasse 17, 1180, Vienna

[72] University of Southern Queensland

[73] Research School of Astronomy and Astrophysics, The Australian National University, Canberra, ACT 2611, Australia

[74] Centro de Astrobiología (CAB), CSIC-INTA, Camino Bajo del Castillo s/n, 28692, Villanueva de la Cañada (Madrid), Spain

[75] Instituto de Astrofísica, Facultad de Física, Pontificia Universidad Católica de Chile, Campus San Joaquín, Av. Vicuña Mackenna 4860, Macul, Santiago, 7820436, Chile

[76] INAF-IAPS, Via del Fosso del Cavaliere 100, Roma, Italy

[77] Purple Mountain Observatory, Chinese Academy of Sciences, Nanjing, 210023, PR China

[78] Department of Astronomy, Stockholm University, AlbaNova University Centre, Stockholm, Sweden

[79] Materials Science and Applied Mathematics, Malmö University, 20506, Malmö, Sweden

[80] Department of Astronomy, The University of Texas at Austin, 2515 Speedway Boulevard, Austin, TX 78712, USA

[81] Institut d'astrophysique de Paris, CNRS

[82] Sorbonne Université, UMR 7095, 98bis Boulevard Arago, 75014, Paris, France

[83] Laboratoire d'astrophysique, École Polytechnique Fédérale de Lausanne (EPFL), Observatoire, 1290, Versoix, Switzerland

[84] GEPI, Observatoire de Paris, CNRS, Université de Paris Diderot, 92195, Meudon Cedex, France

[85] Centre for Astrophysics Research, Department of Physics, Astronomy and Mathematics University of Hertfordshire, College Lane, AL10 9AB, Hatfield, UK

[86] Sapienza - University of Rome, Physics department, Piazzale Aldo Moro 5, 00185, Rome, Italy

[87] Tartu Observatory, University of Tartu, Tõravere, Estonia

[88] INAF - Osservatorio Astronomico di Capodimonte, Via Salita Moiariello 16, 80131, Napoli, Italy

[89] University of New South Wales - School of Physics, Sydney, Australia

[90] Institute of Astronomy, University of Cambridge, Madingley Road, Cambridge CB3 0HA, UK

[91] Centre for Astrophysics and Supercomputing, Swinburne University of Technology, Hawthorn, Victoria 3122, Australia

[92] Centre for Astrophysics, University of Southern Queensland, Toowoomba, QLD 4350, Australia

[93] Sub-department of Astrophysics, University of Oxford, Keble Rd, Oxford OX13RH, UK

[94] Physique Atomique et Astrophysique, Université de Mons - UMONS, 7000, Mons, Belgium

[95] European Southern Observatory, Garching, Germany

[96] Physique Atomique et Astrophysique, Université de Mons, B-7000 Mons, Belgium

[97] IPNAS, Université de Liège, Sart Tilman, B-4000 Liège, Belgium

[98] Université de Strasbourg, CNRS UMR 7550, Observatoire astronomique de Strasbourg, 11 rue de l'Université, 67000 Strasbourg, France

[99] University of Insubria

[100] Institute of Astrophysics and Space Sciences (IA)

[101] Centre for Advanced Instrumentation, Department of Physics, Durham University, South Road,  
Durham

## Acknowledgements

L.M., S.R., R.E.G., J.S.H., M.T. R.E.G., F.R., G.C. acknowledge support from INAF through the Large Grants EPOCH and WST, funding for the WEAVE project, the Mini-Grants Checs (1.05.23.04.02), and financial support under the National Recovery and Resilience Plan (PNRR), Mission 4, Component 2, Investment 1.1, Call for tender No. 104 published on 2 February 2022 by the Italian Ministry of University and Research (MUR), funded by the European Union – NextGenerationEU, through the Project ‘Cosmic POT’ (Grant Assignment Decree No. 2022X4TM3H, MUR). M.R.S. acknowledges support from the European Space Agency as an ESA Research Fellow; D.N. acknowledges support from PLATO ASI-INAF agreements n. 2022-28-HH.0; S.G.S. acknowledge support from FCT through FCT contract nr. CEECIND/00826/2018 and POPH/FSE (EC) and through the Scientific Employment Stimulus programme (reference 2024.08008.CEECIND). This work was supported by FCT - Fundação para a Ciência e a Tecnologia through national funds and by FEDER through COMPETE2020 through through national funds under the research grant UID/04434/2025 (DOI 10.54499/UID/04434/2025); V.A. acknowledges support from FCT through a work contract funded by the FCT Scientific Employment Stimulus program (reference 2023.06055.CEECIND/CP2839/CT0005, DOI:10.54499/2023.06055.CEECIND/CP2839/CT0005); C.D. acknowledges financial support from the grant RYC2023-044903-I funded by MCIU/AEI/10.13039/501100011033 and by the ESF+; D.T. acknowledge support from the ASI-INAF, grant no. 2021-5-HH.0, plus addenda no. 2021-5-HH.1-2022 and 2021-5-HH.2-2024, and from the European Research Council via the Horizon 2020 Framework Programme ERC Synergy ‘‘ECOGAL’’ Project GA-855130; D.P. is supported by the Fondazione ICSC, Spoke 3 ‘‘Astrophysics and Cosmos Observations’’, National Recovery and Resilience Plan (Piano Nazionale di Ripresa e Resilienza, PNRR) Project ID CN\_00000013 ‘‘Italian Research Center on High-Performance Computing, Big Data and Quantum Computing’’ funded by MUR Missione 4 Componente 2 Investimento 1.4: Potenziamento strutture di ricerca e creazione di ‘‘campioni nazionali di R&S (M4C2-19)’’ - Next Generation EU (NGEU); J.S.U., thanks to INAF for its support through the Mini-Grant (1.05.24.07.02); M.M. and A.A. thank the financial support from the Deutsche Forschungsgemeinschaft (DFG, German Research Foundation) – Project-ID 279384907 – SFB 1245; A.C.C. acknowledges support from UKRI/ERC Synergy Grant EP/Z000181/1 (REVEAL); V.G. acknowledges financial support from INAF under the program ‘‘Giovani Astrofisiche ed Astrofisici di Eccellenza – IAF: INAF Astrophysics Fellowships in Italy’’ (Project: GalacticA, ‘‘Galactic Archaeology: reconstructing the history of the Galaxy’’) F.Z.M. acknowledges support from the ASI-INAF Agreement no. 2021-12-HH.0 and Addendum 2021-12-HH.1-2024 ‘‘Missione Solar-C EUVST-Supporto scientifico di Fase B/C/D’’; M.M.J. acknowledges support from STFC consolidated grant number ST/R000824/1; S.B. acknowledges support from the Australian Research Council under grant number DE240100150; T.B.’s contribution to this project was made possible by funding from the Carl-Zeiss-Stiftung. T.B. is funded by the Deutsche Forschungsgemeinschaft (DFG, German Research Foundation) – 573580088. AE received the support of a fellowship from ‘‘La Caixa’’ Foundation (ID 100010434) with fellowship code LCF/BQ/PI23/11970031; T.C. is supported by FCT in the form of a work contract (2023.08117.CEECIND/CP2839/CT0004). This work was supported by national funds through FCT under project 2024.15303.PEX; IMC acknowledges funding from Agencia Nacional de Investigación y Desarrollo / Fondo ALMA 2025 / 31250023; This study has received funding from the Research Council of Lithuania, agreement No P-MIP-24-652; H.R. acknowledges ESA Estonia research infrastructure funded by the Estonian Research Council grant TARISTU24-TK3; T.B. acknowledges financial support by grants No. 2018-04857 and 2024-04990 from the Swedish Research Council; E.F.A and G.B. acknowledge support from the Agencia Estatal de Investigación del Ministerio de Ciencia, Innovación y Universidades (MCIU/AEI) under grant ‘‘En la Frontera De La Arqueología Galáctica: Evolución De La Materia Luminosa y Oscura De La Vía Láctea Y Las Galaxias Enanas Del Grupo Local En La Era De Gaia: los aspectos químicos’’ (FOGALERA-Chem) and the European Regional Development Fund (ERDF) with reference PID2023-150319NB-C22/10.13039/501100011033. This work is supported by the ERC Grant (ERC Advanced Grant ChronoGal, GA 101201412. Funded by the European Union; A.M.A. acknowledges support from the Swedish Research Council (VR 2020-03940, VR 2025-05167) and the Crafoord Foundation via the Royal Swedish Academy of Sciences (CR 2024-0015); M.T.B. thanks the Ministerio de Ciencia, Innovación y Universidades of the Spanish Government for her Beatriz Galindo Fellowship and acknowledges funding from MICIU/AEI /10.13039/501100011033 and by FEDER (UE) under project PID2021-127786NA-100; A.M. acknowledges support from the ERC Consolidator Grant funding scheme (project ASTEROCHRONOMETRY, G.A. n. 772293); M.M. acknowledges the financial

contribution from the grant PRIN-MUR 2022 2022NY2ZRS 001 “Optimizing the extraction of cosmological information from Large Scale Structure analysis in view of the next large spectroscopic surveys” supported by NextGenerationEU and the financial contribution from the grant ASI n. 2024-10-HH.0 “Attività scientifiche per la missione Euclid – fase E” A.F. acknowledges funding from the Large Grant INAF-2024 “Spectral Key features of Young stellar objects: Wind-Accretion Links Explored in the infraRed (SKYWALKER)”. M.B. is funded by the European Union (ERA Fellowship, DiaLoGues, 101180670). M.P. acknowledges support from HORIZON-INFRA-2024-DEV-01-01 – Research Infrastructure Concept Development, through the project WST: The Wide-Field Spectroscopic Telescope (Grant No. 101183153). T.M. is granted by the BELSPO Belgian federal research program FED-tWIN under the research profile Prf-2020-033\_BISTRO. S.C. and D.V. acknowledge funding by the European Union - NextGenerationEU RFF M4C2 1.1 PRIN 2022 project “2022RJLWHN URKA” and by INAF 2023 Theory Grant ObFu 1.05.23.06.06 “Understanding R-process & Kilonovae Aspects”. M.P. thanks the European Union’s Horizon 2020 research and innovation programme (ChETEC-INFRA – Project no. 101008324), the Lendület Program LP2023-10 of the Hungarian Academy of Sciences, the Hungarian NKFIH via K-project 138031 and NKKP Advanced grant 153697, the IReNA network by NSF AccelNet (Grant No. OISE-1927130) and the ERC Synergy Grant Programme (Geoastrometry, grant agreement number 101166936, Germany). I.C. acknowledges funding from the Italian National Recovery and Resilience Plan (PNRR), funded by the European Union – NextGenerationEU (Mission 4, Component 2, Investment 1.2; CUP: C23C24001360006). I.K. acknowledges ERC support (grant agreement No. 101117455). F.R. is a fellow of the Alexander von Humboldt Foundation, and acknowledges support by the Klaus Tschira Foundation. F.R. also acknowledges I.N.A.F. for the 1.05.24.07.02 Mini grant 2024 “GALoMS - Galactic Archaeology for Low Mass Stars” (PI: C.T. Nguyen). C.L. acknowledges funding from a UKRI Future Leader Fellowship (grant numbers MR/S035214/1 and MR/Y011759/1). D.R. research was supported by the Italian National Institute for Astrophysics (INAF) through the program “Finanziamento della Ricerca Fondamentale”, projects “An in-depth theoretical study of CNO element evolution in galaxies” Fu. Ob. 1.05.12.06.08 (PI: D. Romano). R.S. acknowledges support from the National Science Centre, Poland, research grant 2022/47/I/ST9/02358. K.L. acknowledges funds from the Knut and Alice Wallenberg Foundation. J.R.B. was funded by STFC under consolidated grants ST/T000295/1 and ST/X001164/1.